Study and development of Terahertz coherent imaging techniques

Yuchen Zhao

Supervisor: Dr. Marc Georges

Faculty of Science
University of Liège

This dissertation is submitted for the degree of
Doctor of Philosophy in Science

2022

Acknowledgements

This Ph.D. thesis is a joyful and challenging adventure. It is a once-in-a-lifetime opportunity and one of the most valuable experiences that ever happened in my life. I want to express my sincere gratitude to people who have helped me and kept me accompanied during this journey.

My deepest gratitude goes to my supervisor as well as my mentor, Dr. Marc Georges. Marc, thank you for being constantly supportive in every aspects. Thank you for your guidance and encouragement during this bumpy adventure of seeking the (invisible) light. Thank you for your helpful feedback on my publications, presentations and manuscripts.

I am lucky enough to be able to carry out the Ph.D. study in Centre Spatial de Liège (CSL), with my brilliant and genuine colleagues. I would like to thank them for their outstanding knowledge, inspiring advice and warming support during the thesis. Many thanks go to Dr. Vandenrijt Jean-François and Dr. Kirkove Murielle, who have worked closely with me on the TERA4ALL project. I would like to thank my colleagues Dr. Gailly Patrick, Rosin Julien and Rosato Natanaële for their help on sample fabrications.

I want to thank Dr. Dinh Nguyen for her guide on conducting many measurements using the THz time-domain spectroscopy in Mutitel at the beginning of my thesis. I want to thank Dr. Rong Lu and Tang Chao from the Beijing University of Technology for our collaboration on THz reflective ptychography. I want to thank Prof. Knap Wojciech and Dr. But Dmytro for helping me conducting the sub-THz digital holography experiment in CENTERA.

I am grateful to my defense jury members: Prof. Denis Grodent, Prof. Serge Habraken, Prof. David Strivay and Prof. Pascal Picart and Dr. Dinh Nguyen, for accepting being my thesis jury and for their careful reading.

Finally, I would thank my family and the Choquer family for their endless love and support. I thank my husband, Didier Choquer, for his company during this *Ph.D. marathon*.

Abstract

This thesis presents the study and development of coherent lensless imaging techniques with THz radiation for potential industrial non-destructive testing and biomedical imaging applications. The detection and generation of different wave ranges in the THz band vary significantly from one to another. The penetration ability of THz radiation also depends on their working wavelength. Therefore, we have studied the appropriate systems and their suitable applications for both the far-infrared side of THz radiation and the sub-THz radiation. Far-infrared has a shorter wavelength. Thus, both the imaging system readiness and the intrinsic resolution are better. However, the penetration ability is limited. On the other hand, sub-THz radiation maintains good penetration ability for a large variety of dielectric materials. It is suitable to carry out non-destructive testing applications with the sub-THz radiation.

Both digital holography and other non-interferometric phase retrieval techniques, including ptychography, have been studied and implemented with THz radiation. Migrating these coherent lensless imaging techniques in the THz needs to tackle the difficulties due to the long working wavelength and the still-developing THz source and detector technologies. We have shown that combining the phase retrieval method with the off-axis digital holography can be beneficial when working with THz radiation. The phase retrieval method helps recover more information that cannot be successfully reconstructed due to the imperfect recording condition of the THz hologram. The validity of the proposed method has been tested both on the far-infrared and the sub-THz digital holographic setups. On the other hand, ptychography allows imaging the sample under investigation over a wide field of view. We have studied the appropriate configuration of THz ptychography in reflection mode and other further improvements. Imaging a dehydrated human breast cancer tissue with our improved THz ptychography setup shows its potential in biomedical imaging applications.

Keywords: Terahertz imaging; Digital holography; Phase retrieval; Ptychography; Non-destructive testing; Biomedical imaging.

Table of contents

List of figures

List of tables

Chapter 1

General Introduction

1.1 Context

Terahertz (THz) waves refer to electromagnetic radiations with frequencies ranged between 0.1 and 10 THz[1], locating between the infrared and microwave frequencies as depicted in Fig. 1.1. Due to its location in the electromagnetic spectrum, the THz band shares properties of both neighboring [1]. Like microwaves, THz waves can penetrate various insulating optically opaque materials such as polymers [2], fabrics [3], biological tissues [4], and semiconductors without ionization damage[2]. The seeing-through ability makes THz imaging an emerging technique of high potential in industrial non-destructive testing (NDT) [5], medical [6], and security applications [7]. THz waves offer a higher spatial resolution for imaging applications thanks to the shorter wavelength compared to the microwave, paving the way for industrial inspection with sub-mm resolution [8–10]. On the other hand, similar to infrared radiation, many molecules have peculiar absorption spectra (i.e. fingerprint spectra) in the THz range. Vibrational absorption frequencies of organic intramolecular chemical bonds are mainly located in the IR band. In contrast, the absorption frequencies of weak intermolecular forces (such as hydrogen bonds and van der Waals' force), molecular structure bending, dipole vibrations, rotational energy transitions, and low-frequency vibrations are mainly located in the THz band [11]. Water, for example, has hundreds of rotational and vibrational absorption lines in the THz region [12]. The rich spectral information makes THz radiations useful for different applications such as pharmaceutical quality assessment [13], illicit drugs detection [14, 15] and agricultural products inspection [16].

[1] Frequency ν =1 THz=10^{12} Hz corresponds to wavelength $\lambda = c / \nu$= 300 µm.

[2] The penetration ability of THz wave is more restrictive than that of microwave radiation.

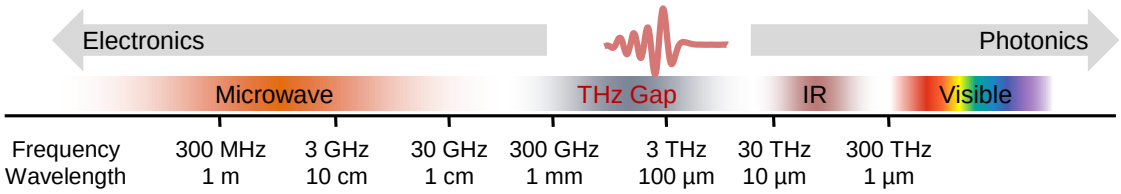

Fig. 1.1 Terahertz gap locates between the millimeter waves and the infrared waves.

The band THz remained the least explored electromagnetic spectrum due to the technological difficulties in THz generation and detection, which is often referred to as the "THz gap" [17, 18]. However, the THz gap has been gradually bridged over the last thirty years. Photonic technologies diminished the limitations from the high-frequency side, while microwave technologies made progress from the low-frequency side. These breakthroughs opened up numerous opportunities for using THz radiation for research purposes and applications mentioned above. A detailed overview of THz techniques will be given later on in this work.

1.2 Objective of the thesis

The ERDF/Wallonia region project TERA4ALL is associated with this Ph.D. thesis. In the first place, the project TERA4ALL aims at promoting THz technologies for industrial application. Various study cases in pharmaceutical, agricultural, biomedical, and NDT domains have been carried out with Terahertz time-domain spectroscopy (THz-TDS) since spectroscopic characterization with THZ-TDS has higher Technology Readiness Level (TRL) [10]. Implementing innovative THz imaging techniques and instrumentation is another essential perspective of the project TERA4ALL. CSL devotes to exploring the possibility of continuous-wave (CW) THz lensless imaging techniques for the NDT of composite materials.

Under this framework, the thesis presents extensive research on CW THz lensless imaging techniques and their potential applications. The first objective is to understand different THz science and technology families to evaluate the feasibility and limitation of inspecting composite materials using different CW THz imaging systems. As explained in Section 1.1, the THz band spans across the photonic and electronic spectrum, the technologies of generating and manipulating THz radiations, as well as their properties, are related to the subdivisions. Both sub-THz and far-infrared (FIR) CW systems are investigated. Experiments are conducted with different systems in both bands. The second objective is to

develop coherent lensless imaging techniques with THz radiation. Coherent lensless imaging techniques allow reconstructing both the amplitude and phase numerically with coherent source and intensity-only detectors. Undoubtedly, the retrieved phase can act as an imaging contrast agent. Moreover, the phase information can reveal additional information such as refractive index fluctuation, thickness, and profile variation [19]. Migration of coherent lensless imaging techniques in THz borrowed their working principles implemented at shorter wavelengths, from the visible to the X-ray range. However, the specific features of THz radiation should be taken into account.

1.3 Outline of the thesis

Figure 1.2 depicts the main contents and their organization of the thesis. The work is conducted as follows:

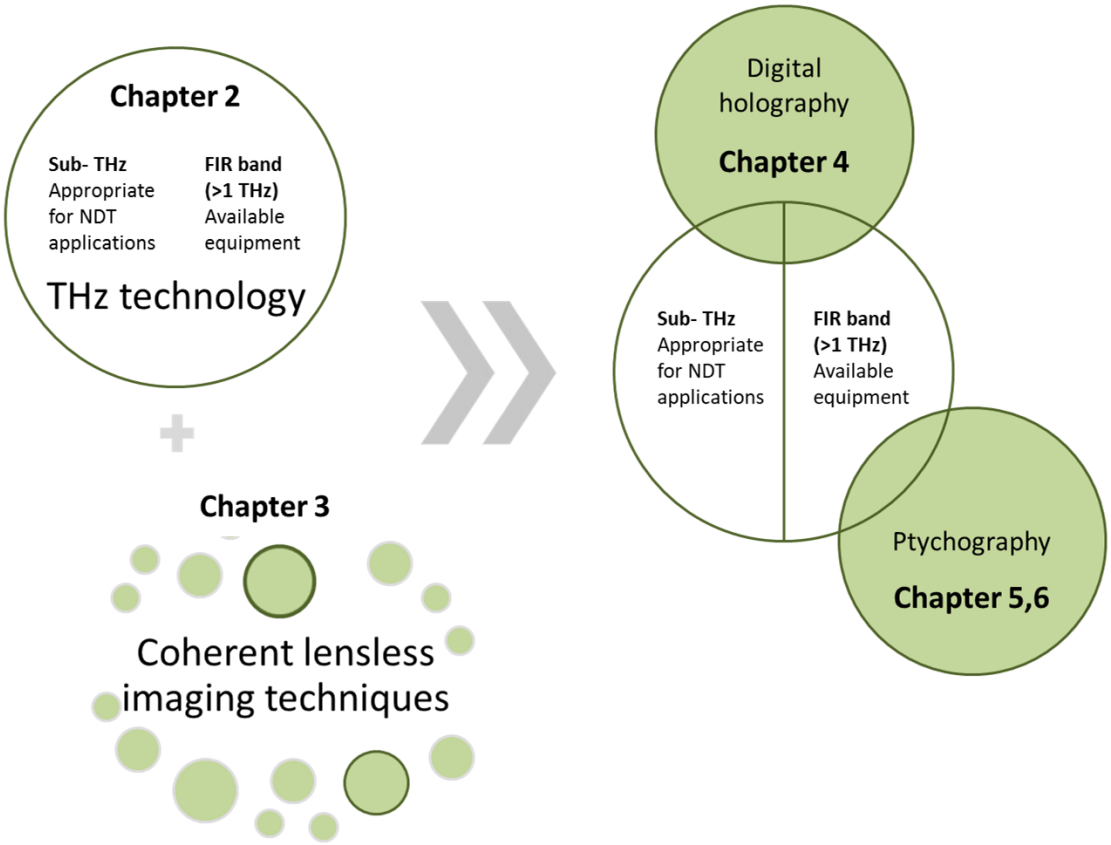

Fig. 1.2 THz technology and the coherent lensless imaging techniques are the two keywords to explore in this thesis. The diagram depicts the main contents with their corresponding chapters.

An overview of THz science and technologies is presented in chapter 2. The representative THz sources, THz detectors, and the properties of different THz subdivisions are reviewed. The chapter also gives a survey of the current THz imaging techniques and applications. Understanding the state-of-the-art in THz technologies helps determine the suitability for specific applications. The appropriateness of inspecting composite materials using CW THz imaging with different technologies will be addressed. The chapter will address the two important conclusions: Our available THz equipment is not suitable for investigating composite materials. However, our THz source and detector are suitable choices for investigating emerging coherent lensless imaging techniques.

Chapter 3 explains the theoretical background of coherent lensless imaging techniques, including digital holography (DH), phase retrieval (PR), and ptychography. The chapter

covers the common free space propagation derived from scalar diffraction theory, the distinctive ways of recovering the phase problem, and their implementation in THz. The benefit of employing lensless coherent imaging techniques in the THz band will be discussed. The contents in Chapter 2 and Chapter 3 are partially published in the review papers [20, 21].

Chapter 4 to Chapter 6 consist of two coherent lensless imaging techniques that have been developed with THz radiation during this thesis, which corresponds to the second main objective. The developed techniques are mainly based on the available FIR THz equipment at CSL. In the meantime, we validated some development at sub-THz, which is the more suitable band for NDT applications, by collaborating with CENTERA (Center for Terahertz Research and Applications), Polish Academy of Sciences.

In Chapter 4, DH is investigated. Due to the large wavelength of THz radiation, some particular concerns for choosing the appropriate DH setup and reconstruction method are addressed at the beginning of this chapter. An iterative PR scheme is developed to enhance the imaging quality of off-axis THz DH. The result is published in the paper [22]. Two distinctive experimental setups at both 2.52 THz and at 280 GHz have been developed. The experimental results have both validated the effectiveness of the proposed iterative PR scheme. The experiments also showed that off-axis THz DH is capable of reconstructing concealed (or optically opaque) objects. The reconstructed phase can be used for retrieving the thickness measurement. The limitation and perspectives of off-axis THz DH are discussed at the end of this chapter.

In Chapter 5, we investigated another coherent lensless imaging technique in THz: ptychography. Ptychography allows full-field, high-resolution imaging with an expended field of view (FOV). THz ptychography in transmission mode was recently demonstrated in [23]. We implemented reflective ptychography by oblique illumination for the first time in collaboration with the Beijing University of Technology (BJUT). The feasibility was demonstrated by measuring the topography of two reflective metal samples. The work is communicated in [24].

Regarding the reconstruction results obtained with reflective ptychography in Chapter 5, as well as the results published in [23] in transmission mode, there is still room for improvement. The reconstruction failed when having complex objects.

In Chapter 6, the optimization of THz ptychography is studied. In transmission mode, the proposed improvements include 1) diffraction pattern post-processing for denoising, 2) enlarging the FOV without more extra scans, and 3) diffuser illumination for resolution enhancement. The experiment demonstrated that the proposed methods produce more satisfying results compared to the earlier development. We successfully reconstructed an image of a paraffin-embedded human breast cancer tissue sample thanks to the improvement mentioned above.

Finally, a conclusion of the THz coherent imaging techniques studied throughout the thesis, as well as their perspectives and hurdles toward real-world applications, are given in Chapter 7.

Chapter 2

Overview of the THz technologies

This chapter provides an overview of THz technologies mainly related to continuous-wave (CW) THz imaging systems and applications. At the beginning of the chapter, the subdivisions of THz radiation is elaborated. THz radiation generation and detection research remain the most challenging yet revolutionary domain. Moreover, it plays a decisive role in THz imaging and other applications. We will firstly review the representative CW THz sources and detectors. The specification of the sources and detectors involved in further experiments will be exhaustively described. We also introduce the THz generation and detection mechanism of two relatively mature THz systems, which can provide practical solutions for NDT applications in the composite material industry: the THz Frequency Modulated Continuous-Wave (FMCW) radars and the THz time-domain spectroscopy (THz-TDS) [10]. Besides the THz wave generation and detection, understanding the optical properties of different materials in THz allows us to choose the appropriate THz optics and understand the specimen's optical behavior under investigation. Different categorizations of THz imaging and their typical applications will be reviewed. The review provided in this chapter is only a glimpse of the promptly developing THz research. It intends to provide the current situation of THz instrumentation and imaging techniques that are relevant to our further development. Other THz imaging techniques and applications which are irrelevant to our equipment are only briefly presented to emphasize the uniqueness and differentiation.

Table of contents

2.1 The subdivisions of THz band

Some basic information of THz radiation has been addressed in the general introduction in Chapter 1. However, the definition of the term "Terahertz" is very broad and ambiguous. It simply refers to the electromagnetic wave that locates between infrared and microwave. The definition of the border is also blurry. In many sources, including the report from the International Telecommunication Union (ITU) [25], THz radiation refers to the range between 0.1 THz to 10 THz. Meanwhile, it is common to see that the definition is narrowed down to 0.3 THz - 3 THz in other papers. Since The THz band does not have a standard definition, instead of broadly discussing the whole THz spectra, it is more appropriate to regard the THz science and technologies as the extension of microwave toward higher frequency (shorter wavelength) and the development of optical/thermal technologies toward lower frequency (longer wavelength). THz wave generation and detection mechanism, the way it interacts with the matter, and their suitable applications on the two sides of THz spectra are distinct from each other. Some THz bands behave similarly to their neighboring spectral band. Therefore they are merged into their neighboring bands as well. The typical subdivisions of the THz bands are as follows [26]:

- **Millimeter wave (MMW)**: 1-10 mm, 30-300 GHz, 0.03-0.3 THz
- **Sub-millimeter wave (SMMW)**: 0.1-1 mm, 0.3-3 THz
- **Far-infrared radiation (FIR)**: 25-350 μm, 0.86-12 THz

In addition, the frequency range of 0.1-1 THz, corresponding to 300-3000 μm is often referred to as sub-THz radiation in many works of literature. Therefore, this term will also be used in the thesis.

2.2 THz generation and detection

2.2.1 Narrowband CW THz sources

CW THz generation can be either based on microwave technologies or optical-based technologies. The subsections introduce typical narrowband CW THz sources.

2.2.1.1 IMPATT diodes, Gunn diodes, and Frequency multiplier chains

Electronic solid-state oscillators emit CW monochromatic sub-THz radiation. **Impact ionization avalanche transit-time (IMPATT) diodes** and **Gunn diodes** belong to this category. A microwave oscillator is created by applying a DC voltage to bias the device into its negative resistance region. Gunn diodes based on gallium arsenide (GaAs) are made for frequencies up to 200 GHz, while those relying on gallium nitride (GaN) can reach up to 3 THz. Most of these devices are compact and low-cost sources. They are easy to use and can be operated at room temperature. Therefore, they are suitable for various imaging applications. Companies such as Terasense provide commercial IMPATT diodes THz sources from 100 GHz up to 300 GHz, as shown in Fig. 2.1(a). The highest output power at 100 GHz is up to hundreds of mW, whereas the 300 GHz sources have an output of 40 mW.

Frequency multiplier chains are often added on the electronic sources such as Gunn and IMPATT diodes to generate even higher frequency radiation at the expense of power loss. Frequency multipliers are Schottky-diode-based or transistor-based electronic circuits, which have a non-linear response to electromagnetic waves. They generate higher harmonic components of the incoming wave. With a suitable filter or waveguide, harmonics are collected. It is also possible to use several frequency multipliers in series to produce even higher frequencies. For instance, Fig. 2.1(b) shows a 90 mW high-power 264 GHz source

developed at Virginia Diodes with the help of three frequency multipliers. Some experiments that we conducted in sub-THz range in Chapter 4 made use of a 35 mW 140 GHz IMPATT diode (Aerfortis) with a multiplier to achieve 280 GHz output frequency (Fig. 2.1(c)), but as a cost, the output power is decreased to 15 mW. Moreover, frequency multiplier modules are often integrated in the transmitter and receiver parts of a millimeter wave vector network analyzer (VNA) as a frequency extender (Fig. 2.1(d)).

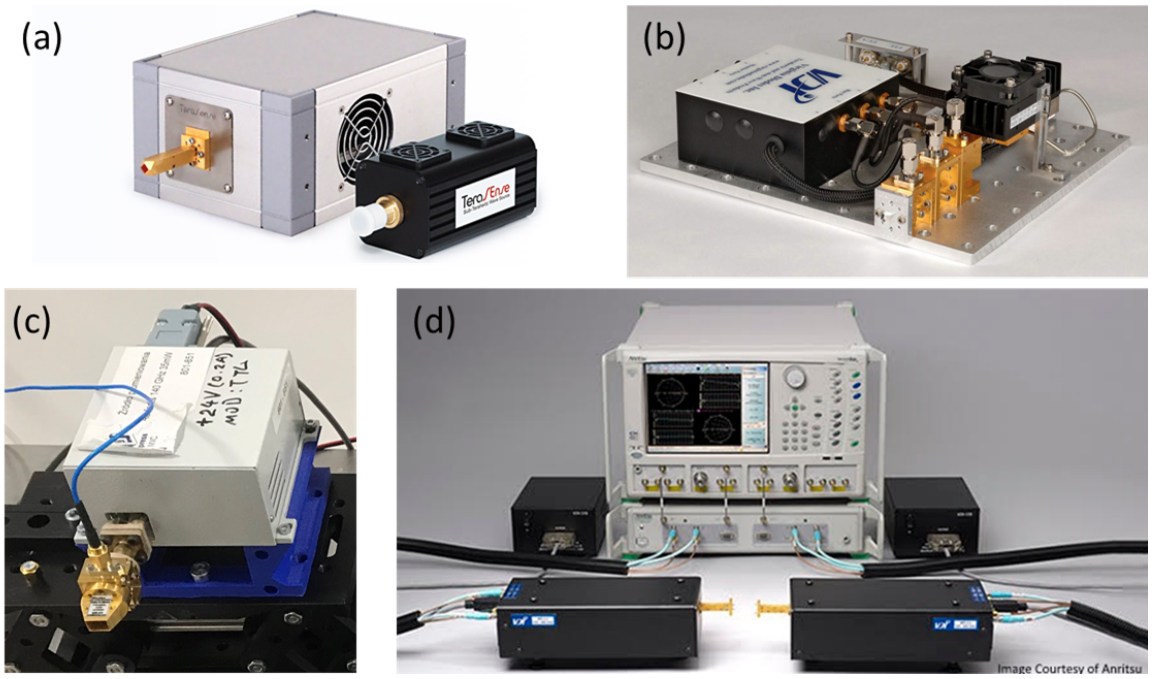

Fig. 2.1 Typical electronic solid-state oscillators for CW THz generation. (a) Commercial IMPATT diode THz sources from Terasense [27]. (b) The high-power 264 GHz source from Virginia Diodes is achieved with the help of three frequency multipliers [28]. (c) The IMPATT diode with a multiplier used in the sub-THz experiment in Chapter 4. (d) A millimetre wave vector network analyzer (VNA) broadband system from Anritsu [29].

.

2.2.1.2 Backward wave oscillators

Back wave oscillators (BWOs) are shoe-box-sized tunable monochromatic THz sources. They produce THz radiation based on the electron movement in the electron vacuum tubes. Figure 2.2(a) shows the working principle of BWO for THz generation. A heated cathode emits electrons that are accelerated by external DC voltage toward the anode side. A metal grating known as a comb slow-wave structure along the vacuum tube induces a periodic spatial modulation of the electron beam and the electrons are driven into bunches. The

bunched electrons excite surface electromagnetic waves on the metal grating. The produced wave, *i.e.*, the THz radiation travels in the opposite direction of the electron beam's direction, justifying the name. The output frequency is determined by the electron velocity. Thus, the frequency is tunable by adjusting the bias voltage. Commercial BWO sources (such as Terasense and Microtech Instruments Inc., as shown in Fig. 2.2(b)) offer high output power up to 100 mW in the sub-THz range and mW-level output at 1 THz. Similar to other electronic sources, the frequency multipliers can be integrated with a BWO source to achieve high frequency. Since the first THz imaging system was demonstrated with BWO in 2004 [30], BWOs are often chosen as ideal sub-THz sources for imaging applications due to their high-power output, compactness and tunability [31–35].

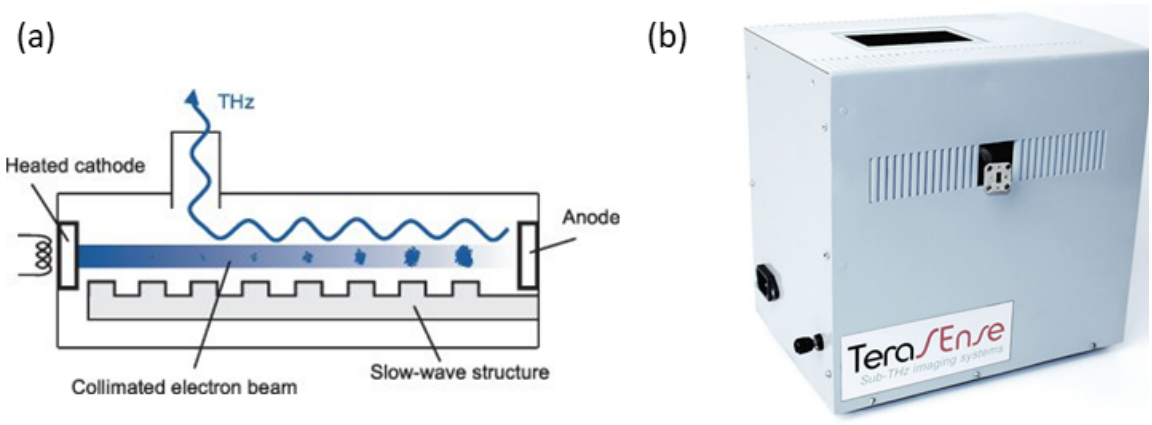

Fig. 2.2 Back wave oscillators for THz generation. (a) Schematic working principle of BWO [36]. (b) Commercial BWO THz sources from Terasense [27].

2.2.1.3 Free electron lasers

Free electron lasers (FELs) are building-sized facilities. They generate high-power (W to kW scale), monochromatic, broadly and continuously tunable THz radiation. Well-known FEL facilities include Novosibirsk FEL (NovoFEL) in Russia, FLASH at DESY in Germany, CAEP THz FEL in China, the FLARE FEL at FELIX Laboratory in the Netherlands, and the SwissFEL in PSI in Switzerland. In FEL, a beam of accelerated free electrons is injected into a wiggler where the magnetic field varies periodically with distance. The electrons move sinusoidally in the wiggler, generating coherent monochromatic electromagnetic radiation. The generated radiation resonates in an optical cavity [37]. The wiggler is analogous to the gain medium of a conventional laser system, whereas the electron beam is the equivalent of the pumping system.

2.2.1.4 Quantum cascade lasers

Quantum cascade Lasers (QCLs) are electrically pumped unipolar lasers. It is the latest way of generating THz radiation. THz sources are mW-level compact sources. Commercialized THz QCL sources exist single-line and multi-line devices operating in pulsed mode, providing a CW equivalent THz power of several mW in the frequency range from 1.2 to 5 THz. Commercialized THz QCL sources can be found from companies such as LongWave Photonics (the US), Alpes Lasers (Switzerland) and Lytid (France).

The working principle of QCL differs from that of conventional semiconductor lasers. In semiconductor lasers, a photon is emitted during the recombination of an electron and a hole. The emission frequency is determined by the discrete difference between the conduction band and the valence band of the used semiconductor. Photon emission in QCL is based on electron transitions (unipolar carrier) in cascaded quantum well structures. For conventional semiconductor lasers, the emission frequency is determined by the energy band of the used material. QCL emission frequency is determined by the engineered band structure: the size and width of the quantum wells. The quantum wells structure is formed by having a semiconductor material (such as GaAs) sandwiched by two layers of material with a wider bandgap (such as $Al_xGa_{1-x}As$). The conduction band offset between these two materials provides the 'wells' and 'barriers'. In a QCL, an electron undergoes an intersubband transition and sequentially emits a photon in one period of the quantum well structure. The same electron is injected into the next period and contributes to another intersubband transition [26].

The difficulty of developing THz QCL can be contributed to two aspects. First, due to the weak energy of emitted THz photon, it is difficult to selectively inject and remove electrons from such close sub-bands. The thermal excitation can easily disturb the electron configuration. The output power of QCLs drops drastically as the temperature increases. Second, the loss due to the absorption of radiation by free carriers increases proportionally to the square of the wavelength. Thus, waveguides are required [38]. The first THz QCL was reported only in 2002. It delivers an output power of 2 mW at 4.4 THz working at 50K operation temperature [39]. Although all the commercially available THz QCLs require Stirling, liquid nitrogen, or cryogenic cooling to reach the claimed output power, progress is being made toward room-temperature high-power sources [40, 41]. Generating sub-THz waves with QCL is another challenge. The latest research demonstrates intracavity generation within THz QCLs over the unprecedented range of 25 GHz to 500 GHz [42].

2.2.1.5 Optically pumped FIR lasers

Optically pumped FIR lasers are considered the oldest technology for THz generation since the FIR generation with optically pumped gas molecules was firstly observed in the 1960s [43]. They play an important role in THz research as a CW high power monochromatic source that operates at room temperature. However, the system can be bulky and expensive. They are based on the stimulated emission from rotational transitions in gas molecules (such as methanol, formic acid, hydrogen fluoride and ammonia) at pressures in the millibar (mbar) range, offering discrete single-line (1MHz and less) emissions from around 60 μm to 500 μm with powers up to hundreds of mW.

Optically pumped FIR lasers consist of a vacuum cavity in which a molecular gas at low pressure is filled and a CO_2 laser that emits IR radiation as the pump. The lasing principle is thoroughly explained in [44]. As shown in Fig. 2.3, an infrared (IR) photon (9.69 μm) is absorbed by Methanol (CH_3OH) vapour, exciting the C-O stretch (vibrational) mode. The molecule then lases between the J (J=16) and J-1 rotational levels, emitting a photon at 118.83 μm. The wavelength of the pump CO_2 laser and the molecule decide the output frequency together. The output power for a given line is determined by the power of the pump CO_2 laser.

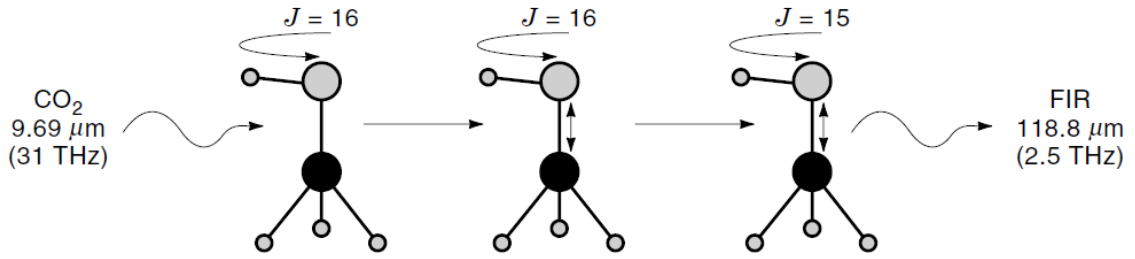

Fig. 2.3 Lasing principle of optically pumped FIR lasers (source: [44])

.

Optically pumped FIR laser at CSL

The optically pumped FIR laser system at CSL is manufactured by Edinburgh Instruments Ltd, shown in Fig. 2.4. The system delivers more than three times as much output power compared to the other two commercialized models FIRL-100 (Edinburgh Instruments Ltd) and SIFIR-50 (Coherent Inc.). The pump CO_2 laser utilized here has a maximum output

power of 180 W (50 W for the other two models). A maximum output power of 500 mW can be obtained at 2.52 THz. The high power comes at the cost of compactness. The pump laser and the FIR cavity are integrated in one box in both FIRL-100 and SIFIR-50. The CO_2 pump laser PL6 works in a flow-through mode with a standard gas mixture composition of 7% CO_2, 18% N_2, and 75% He[1]. A rotating diffraction grating allows selecting the desired IR lines. Two mirrors and a ZnSe lens couple the output IR beam into the FIR-295 cavity. The molecular gas is filled in the cavity and pumped at low pressure. The generated FIR radiation transmits the output coupler, whereas the IR radiation is blocked. The cavity length of FIR-295 is adjustable by changing the position of the output coupler attached to a motorized precision linear translation stage.

Two practical issues exist with our FIR laser system. First, to achieve the optimum output power as indicated on the datasheet, the IR power, the gas pressure and the FIR cavity length should be well-adjusted. Unfortunately, adjusting the FIR cavity length can be tedious and time-consuming since the absolute displacement of the cavity elements cannot be quantitatively readout. Therefore, finding the maximum power with a Gaussian-shaped beam profile is a trial-and-error process. Another issue is power and beam profile stability. The stability of the FIR laser output depends on the stability in frequency and power of the CO_2 pump laser and on the stability of the FIR cavity. Although both cavities are water-cooled, the system is sensitive to ambient thermal fluctuation. The same effect is observed with FIR-100. PL6 + FIR-295 system is more impacted than the other two models mentioned above since the output power of CO_2 laser is higher. The situation is even worse in our case because of the layout of our laboratory. The heat generated by the water-cooling system cannot be evacuated outside of the laboratory. As a result, the FIR output power can drop more than 20% within 10 minutes. To solve this issue, the system should be ideally installed in an air-conditioned laboratory. Moreover, laser stabilizers developed by the same company can be added to actively compensate for the laser output fluctuations and to lock the variation in laser frequency or power to a value close to the passive jitter[2].

[1] It is the same case in FIRL-100, whereas SIFIR-50 utilizes a permanently sealed-off pump laser.

[2] SIFIR-50 has integrated stabilizer, the power can be stable up to one hour according to their specification.

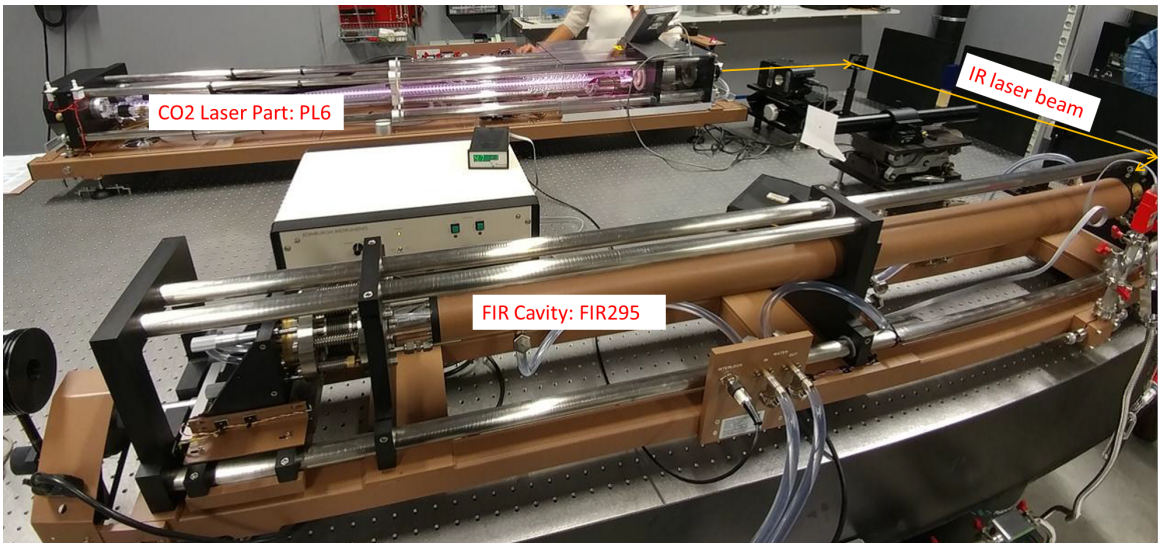

Fig. 2.4 PL6 + FIR-295 laser system in CSL.

2.2.1.6 Summary

Hereby we summarize the output power and the frequency of the CW THz sources mentioned above. FELs are building-sized facilities that provide ultra-high (W-kW scale) output power over a broad frequency range. Microwave technologies such as IMPATT diodes, Gunn diodes and BWOs are compact sources that can generate 100 mW-level output in the deep sub-THz region (<300 GHz). These sources can reach higher frequency output with frequency multiplier blocks at the expense of loss in power. These sources are compact and cost-efficient. Thus, they are suitable for developing applications in the sub-THz range. On the other hand, optical-based sources are mainly used for the FIR radiation generation. Optically pumped FIR lasers are relatively established technologies. They generate discrete single line emissions. The pumped gas molecule and the employed pump line determine together the output power and frequency. The system is QCLs are recently developed THz sources that emit mW-level outputs from 1.1 up to 5 THz.

2.2.2 THz detectors

2.2.2.1 Foreword

There exist different ways for categorizing THz detectors. First, by detecting principle, the THz detectors can be classified into three categories: photon detectors, thermal detectors, and rectification detectors. Second, depending on their working temperature, the detectors can be divided into uncooled and cooled detectors. At last, the detecting system can be divided

into coherent detection and incoherent detection systems. Incoherent detection systems directly provide the signal correlated to the intensity of THz radiation, whereas coherent detection allows detecting both the amplitude and the phase of the THz radiation. Besides the THz-TDS system, which employs a time-gated coherent detection, the heterodyne technique is another coherent detection method. For coherent heterodyne detection, the THz signal at frequency ω_{THz} is down-converted to a few GHz by mixing with the fixed frequency ω_{LO} of the local oscillator. The output signal has an intermediate frequency $\omega_{\mathrm{IF}} = |\omega_{\mathrm{THz}} - \omega_{\mathrm{LO}}|$ and an amplitude proportional to the THz signal. The transceivers in FMCW systems are based on heterodyne detection. The coherent detection offers complete information of the THz signal at the expense of system complexity. Producing 2D arrays with the heterodyne technique is impractical.

In our project, we seek commercially available 2D array THz detectors for room-temperature imaging applications. It narrows down our choice to the following incoherent uncooled thermal detectors and rectification detectors which will be presented in the subsection. A more detailed recent review of available THz detectors can be found in [45].

2.2.2.2 Uncooled thermal detectors

Pyroelectric cameras and **uncooled microbolometers focal plane arrays (FPAs)** are 2D array THz detectors based on thermal detection. Pyroelectric cameras are able to detect broadband spectrum ranging in UV, IR, and up to THz radiation. They are often used as beam profilers for sensitive bands. The detection mechanism is based on the pyroelectric effect in polarized ferroelectric crystals such as lithium tantalate ($LiTaO_3$). The working principle of the pyroelectric camera is depicted in Fig. 2.5(a). The detection crystal is considered as a small capacitor with two conducting electrodes mounted perpendicularly to the direction of spontaneous polarization. With the incident radiation, the temperature variation causes the change of its electric polarization, giving rise to a measurable current across the crystal. Pyrocam III and Pyrocam IV are commercially available pyroelectric cameras from Ophir [46], shown in Fig. 2.5(b). The Pyrocam III has a resolution of 124 $\times$ 124 pixels with a pitch of 100 µm. The latest model Pyrocam IV has a higher resolution of 320 $\times$ 320 pixels with a smaller pitch of 80 µm. An additional radiation chopper is integrated, which allows modulating the irradiance in time. Under chopped CW operation, the Pyrocam has a noise equivalent power (NEP) of 13 $\mathrm{nW}/\sqrt{\mathrm{Hz}}$ per pixel. The lowest measurable signal is 96 nW/pixel. The saturation power is about 4.5 $\mathrm{W/cm^2}$.

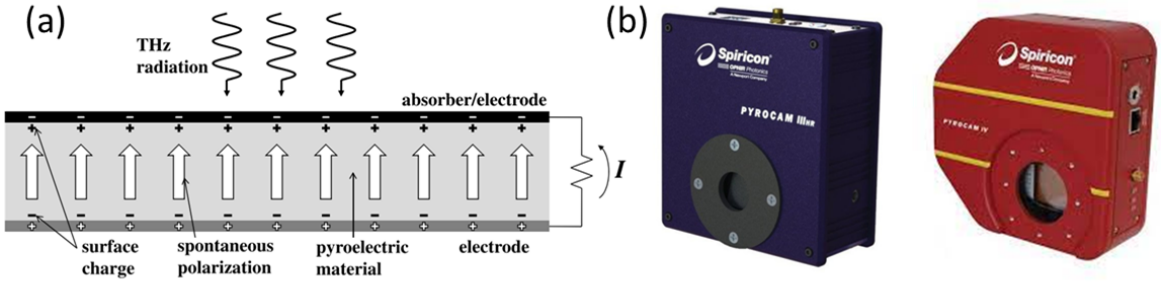

Fig. 2.5 (a) Working principle of pyroelectric cameras [26] and (b) the Pyrocams from Ophir [46].

Uncooled microbolometer FPAs measure the power of electromagnetic radiation indirectly via the temperature-dependent electrical resistance of the detecting materials such as amorphous silicon (a-Si), vanadium oxide (VO_x), and silicon nitride (SiN). Figure 2.6(a) shows an example of the microbolometer structure. A membrane of pixel-sized detecting material is attached to the read out integrated circuit (ROIC) by the metal stud. The membrane is thermally isolated thanks to the micro bridge structure. Therefore it can work under uncooling conditions. Microbolometer arrays were initially developed for long-wave IR (LWIR) band (8-14 μm) imaging. The technology is relatively well-established. Commercial off-the-shelf LWIR cameras with typical resolutions up to 1280 × 1024 pixels with 17 μm pitch can be found. Surprisingly, the LWIR microbolometers remain sensitive to THz radiations. Real-time imaging with LWIR microbolometers at 2.52 THz has been demonstrated since 2005 [47]. Uncooled microbolometer FPAs specifically designed for THz radiation emerged in the market by the time of 2010, including the NEC's IRV-T0831 camera[3] (Japan) [48], the INO's MICROXCAM-384i-THz camera (Canada) [49], the CEA Leti's i2S TZ-CAM THz camera (France) [50], and the recent-developed RIGI THz Camera from the company Swiss Terahertz (Switzerland) [51], shown in Fig. 2.6(b). These microbolometers have optimized their sensitivity in the THz band via different approaches, including the use of metallic absorbers for maximizing THz absorption, coupling designed antennas, and integrating metamaterial-based absorbers [49, 52]. The uncooled microbolometer FPAs are very sensitive at frequencies > 1 THz. For example, the MICROXCAM-384i-THz camera that we possess has a claimed NEP of 35 $\mathrm{pW}/\sqrt{\mathrm{Hz}}$ per pixel at 2.5 THz. The pixel gets saturated around 150 μW/pixel. However, these values are frequency-dependent. Generally,

[3]NEC has already discontinued the production of THz cameras by the year of 2016.

these cameras are less sensitive at < 0.6 THz.

The technical maturity of dedicated THz microbolometers does not reach the same level as LWIR microbolometers. The number and the size of pixels of THz microbolometers are limited compared to the LWIR microbolometers. Hack *et al.* have evaluated the performance of LWIR microbolometers for real-time THz imaging and THz off-digital holography application [53]. The LWIR microbolometer XENICS Gobi 640 showed unexpectedly good sensitivity around 2 THz. Moreover, it is even more suitable to perform THz off-axis digital holography thanks to its small pixel size. Thus XENICS Gobi 640 was also used for our digital holography setup at 2.52 THz in Section 4.5. The high sensitivity of microbolometer FPAs allows working with low power (mW-level) commercial THz sources. However, extra care should be taken when working with microbolometer FPAs (both the LWIR and the THz ones) because their pixels can be permanently damaged when a low-power (μW-level) laser is focused on several pixels. The output of our FIR laser considerably exceeds the damage threshold. Consequently, the laser should be attenuated to the appropriate power level prior to shining on the microbolometer FPAs.

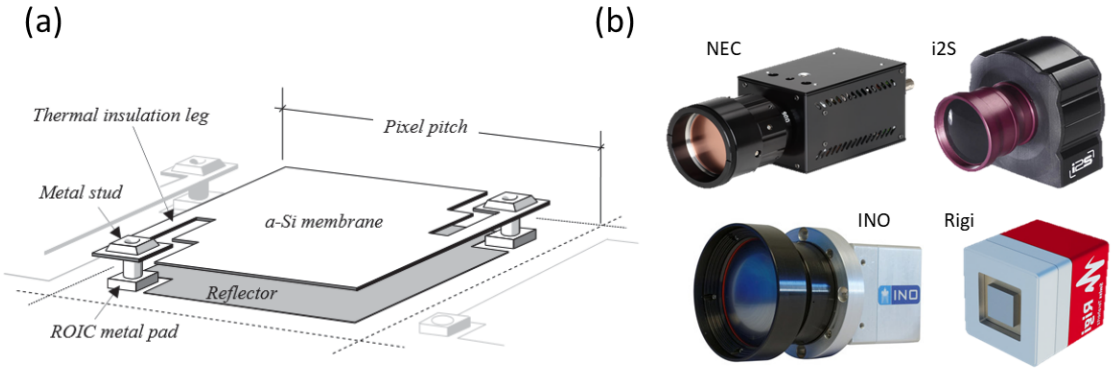

Fig. 2.6 (a) Example of the microbolometer structure and (b) commercially available THz microbolometer cameras.

Detection of sub-THz radiation at room temperature is often realized with uncooled **Rectification THz detectors**, including the **Schottky barrier diodes (SBDs)** and **field effect transistors (FETs) detectors**. Their typical NEP of single-pixel detector is around 1-100 $\mathrm{pW}/\sqrt{\mathrm{Hz}}$ at sub-THz (<0.6 THz) [45]. In Chapter 4, we have employed a single-pixel FET detector with a 2D raster scan for hologram acquisition at the sub-THz (280 GHz) range. The detection mechanism of FET detectors is based on plasma wave's rectification

in the FET channel. When THz radiation is coupled between the gate and the source of the FET, the AC signal is rectified, leading to a DC photoresponse (photovoltaic effect) proportional to the radiation intensity [54]. One advantage of FET THz detectors is that they can be integrated into FPAs based on standard complementary metal–oxide–semiconductor (CMOS) technology. The maturity of the fabrication process guarantees the quality of pixel uniformity and the production cost [55]. Terasense (the USA) has commercialized FET-based THz cameras with NEP of 1 nW/$\sqrt{\text{Hz}}$ in the range of 10 GHz - 1 THz. The increase in NEP compared to that of single-pixel detectors is due to readout procedures and electronics. Terasense camera has a resolution of 64 $\times$ 64 pixels with a pitch of 1.5 mm. Their latest linear imager (256 $\times$ 1 pixels) has reduced the pixel pitch down to 0.5 mm.

2.2.3 THz Frequency Modulated Continuous-Wave (FMCW) radar and THz time-domain spectroscopy (THz-TDS)

In the two previous sections, we have seen different principles and their examples for generating and detecting CW narrowband THz radiation. Different sources and detectors introduced in Sections 2.2.1 and 2.2.2 can be associated with one another for imaging and sensing applications based on incoherent detection as long as the detectivity of the detector matches the source output level. In the meantime, FMCW radar and THz-TDS are two relatively mature THz sensing systems that are based on their unique, coherent detection mechanism. Thanks to the coherent detection, the embedded phase information allows depth-resolving imaging, providing practical solutions for real-world composite material NDT application for the composite material industry. The EU-funded DOTNAC project has investigated their performance in industrial NDT [56]. Since then, the FMCW radars technology has led to different applications for automotive and aviation sectors such as radome inspection, thickness measurement, and acoustic and thermal insulation quality control. THz-TDS is not only capable of performing layer thickness measurement for industrial applications, it is also the standard technology for spectroscopic studies in different domains. The development of application driven FMCW radar and THz-TDS systems has made much progress [57, 58]. In this section, we introduce the generation and detection principles of these two systems.

2.2.3.1 THz Frequency Modulated Continuous-Wave (FMCW) Radar

The principle of the FMCW technique is depicted in Fig. 2.7. FMCW radars are all-electronic based systems. A typical FMCW transceiver unit is described in Fig. 2.7(a). For the signal

generation, a voltage controlled oscillator (VCO) generates a low-frequency saw tooth-like frequency sweep. Then a multiplier chain block, as explained in Section 2.2.1.1 up-converts the low-frequency signal to the THz range, typically centered around 150 GHz up to 600 GHz. The frequency-modulated THz wave (Tx) is transmitted by a horn antenna. The same antenna receives the signal reflected by different reflecting interfaces of the sample under test (Rx). An attached directional coupler sends the received signal Rx to a Schottky diode-based detector. The received signal is mixed with the local reference frequency to get the beating frequency f_{mixer}. Figure. 2.7(b) shows the relation between the transmitted signal (Tx) and the reflected signal (Rx). The beat frequency is correlated with the distance d that the signal propagates during the time delay Δt:

$$d = \frac{c}{2n}\Delta t = \frac{c f_{mixer} T_{sweep}}{2nBW}, \tag{2.1}$$

where c is the speed of light in the vacuum; n is the refractive index of the propagation media at the working frequency; BW is the frequency sweep bandwidth, and T_{sweep} is the sweep period. The depth resolution δd is determined by BW

$$\delta d = \frac{c}{2nBW}. \tag{2.2}$$

The FMCW radar imaging system can be implemented either through the classical focused raster scanning implementation or by the synthetic aperture radar reconstruction. Its lateral resolution is limited by the employed wavelength. Since THz FMCW radars have a smaller wavelength and a wider bandwidth than microwave radars, they can provide a higher resolution.

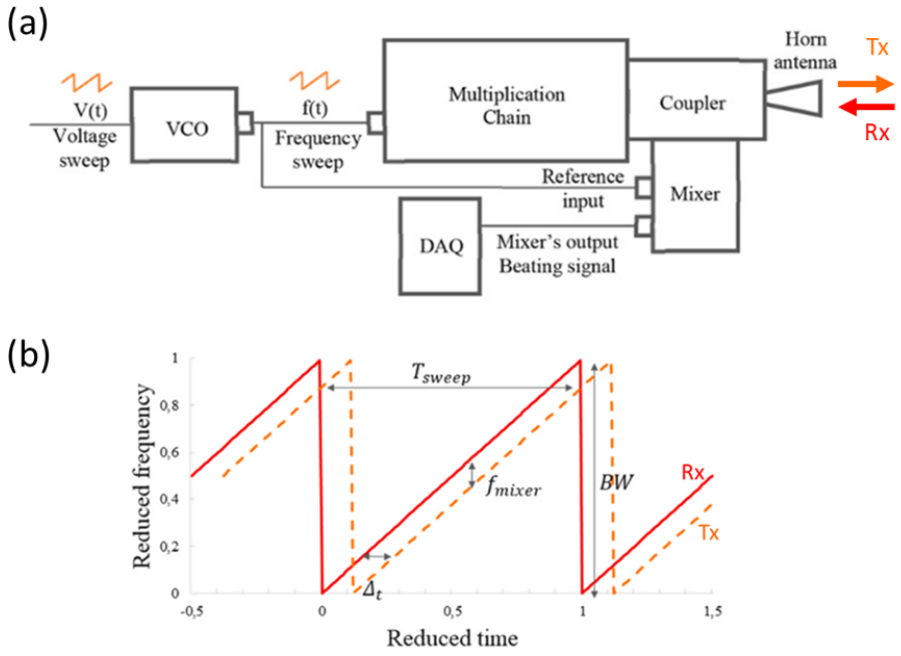

Fig. 2.7 The principle of THz FMCW radar. (a) Typical setup of a FMCW THz transceiver and (b) The frequency sweep sensing scheme during FMCW measurement. The schemes are adopted from [58].

.

2.2.3.2 Terahertz time-domain spectroscopy (THz-TDS)

THz-TDS directly measures the electric field of the generated broadband THz radiation in the time domain. Figure 2.8(a) depicts the generic THz-TDS setup. A pulse generated by a femtosecond laser is divided into two beams: a pump beam that excites the THz emitter to generate broadband THz radiation and a probe beam that passes through a time-delay system and arrives at the THz signal receiver. The detector can only register a signal when both the known probe pulse and the THz field are present. In the time domain, the probe pulse is short (<100 fs) compared to the generated THz field (several ps). Therefore the THz field can be temporally sampled by mechanically varying the distance in the time delay line to achieve a temporal resolution Δt. As indicated in Fig. 2.8(a), varying the position of mirrors determines the sampling time t_1-t_3. Thus, the electric field of the THz pulse as a function of time delay can be obtained (Fig. 2.8(b)). Finally, the spectrum information is obtained by taking the Fourier transform of the real-valued temporal pulse (Fig. 2.8(c)). The result is complex-valued spectrum in the frequency domain with a frequency resolution of $\frac{1}{\Delta t}$ [59]. The amplitude and phase of frequency-dependent complex spectrum allow extracting optical

properties, which will be explained in Section 2.3.

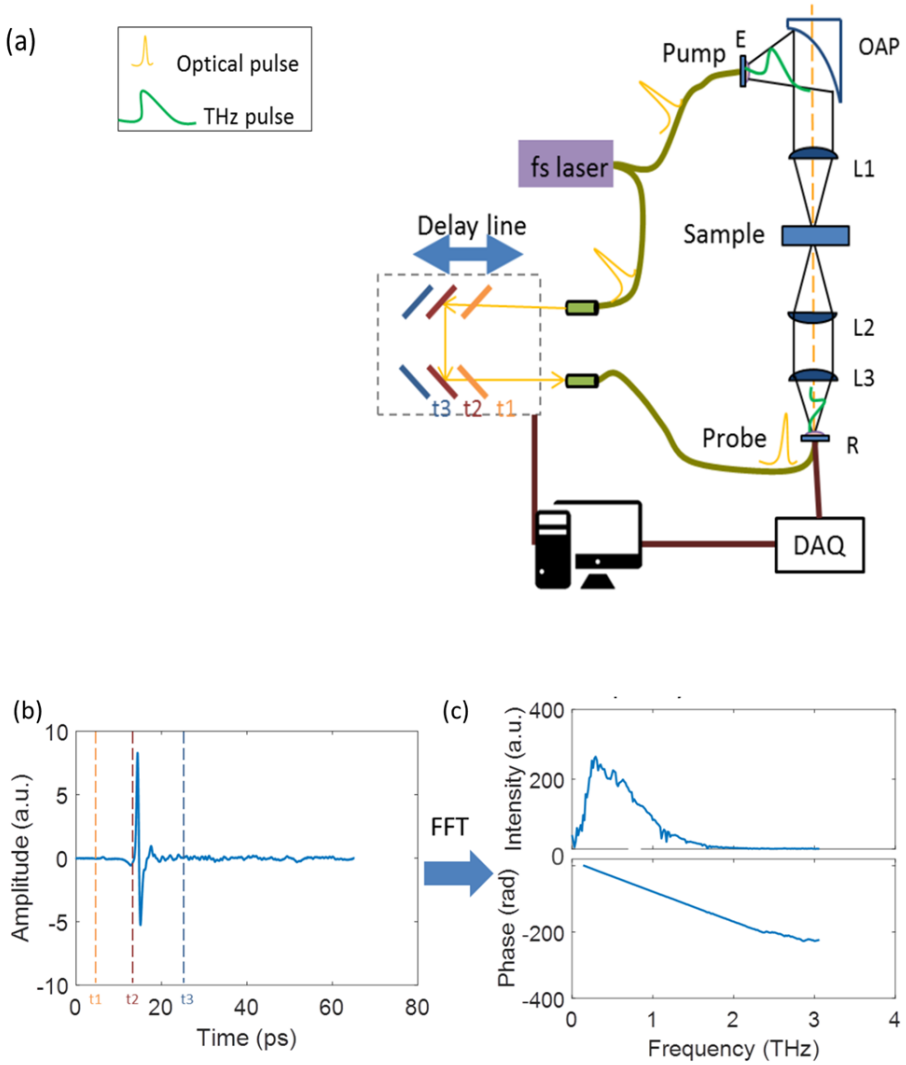

Fig. 2.8 (a) Generic THz time-domain spectroscopy(THz-TDS) setup. (b) measured amplitude of the THz field in the time-domain. Dashed lines correspond to different time-delay position in (a). The Fourier-transform of (b) gives the phase and intensity (c) of the pulse in terms of frequency.

THz emitters and receivers are crucial elements in THz-TDS systems. Photoconductive antennae (PCA), nonlinear crystals or even air/laser-induced plasmas can be utilized for THz generation and detection in THz-TDS. We will hereby describe briefly the working mechanism of PCA since it is widely used in most commercial THz-TDS systems. The Menlo THz-TDS system that we used to measure the optical properties of composite materials is

also based on PCA. Exhaustive review of THZ-TDS with state-of-art emitters and receivers can be found in [37, 59].

Generation of THz pulse with PCA was firstly reported by Auston in 1984 [60]. A PCA consists of two metal electrodes deposited on a semiconductor substrate. Nowadays, the most commonly used semiconductor material in PCA is gallium arsenide (GaAs), such as low-temperature grown gallium arsenide (LT-GaAs), semi-insulating GaAs (SI GaAs). Other possible materials include radiation-damaged silicon-on-sapphire (RD-SOS), indium phosphide (InP), and amorphous silicon [37]. The femtosecond pump pulse, which matches the bandgap of the semiconductor material, is focused into the gap between two electrodes, which creates electron-hole pairs. These charges are accelerated by a DC bias applied between the electrodes, forming a transient photo-current, which is described as a Hertzian dipole. The transient photo-current generates THz electric field, which can be expressed as:

$$E_{\mathrm{THz}}(t) \propto \frac{\partial I_{\mathrm{PC}}(t)}{\partial t}. \tag{2.3}$$

When the probe pulse is focused onto the PCA receiver, electron-hole pairs are again created in the PCA. The arrived THz pulse E_{THz} will accelerate the electron-hole pairs to create a current in the gap. The current value $J_{\mathrm{THz}}(t)$ at instant t_1 is proportional to the convolution between $E_{\mathrm{THz}(t)}$ and the detector response $R(t)$ induced by the femtosecond pulse:

$$J_{\mathrm{THz}}(t_1) = \int_{-\infty}^{t_1} E_{\mathrm{THz}}(t)\, R(t_1 - t)\mathrm{d}t. \tag{2.4}$$

Since the femtosecond pulse is significantly shorter, detector response $R(t)$ can be further approximated as a delta function for sampling. Therefore the produced current $J_{\mathrm{THz}}(t_1)$ is considered directly proportional to $E_{\mathrm{THz}}(t_1)$. The produced current is amplified and converted to a voltage, providing the output signal that is proportional to the time-resolved THz electric field.

2.3 Extracting material optical properties in THz domain

2.3.1 Foreword

Good transparency of the investigated sample should be guaranteed when imaging through the sample. In many works of literature, various non-polar materials, such as glass fiber composites or polycarbonate (PC), are vaguely described as "transparent for THz radiation".

However, in our very first attempt at defect detection in composite materials, no signal was detected when we set a THz detector behind a 2mm-thick glass fiber composites illuminated by the 2.52 THz laser beam at 500 mW. The reason is that the absorption coefficient of a material is frequency-dependent. Therefore, before developing imaging systems, it is essential to investigate the optical behavior of the target material at the working frequency. In this section, we introduce the method of material characterization with THz-TDS to obtain the refractive index and the absorption coefficient. We review the representative material properties in the literature. We also performed a measurement of optical properties of different composite materials experimentally.

2.3.2 Material characterization with THz-TDS

The standard way of characterizing materials in the THz domain is using the THz-TDS system. The two important optical properties parameters: the refractive index and the absorption coefficient, can be retrieved by comparing the electric field modified by the inserted sample E_{Sample} with the reference signal E_{Ref} when the sample is absent. The measurement is often realized in transmission mode with normal incidence. The reference signal $\tilde{E}_{\text{Ref}}(\omega)$ is measured when no sample is presented. The pulse propagates directly through the air. $\tilde{E}_{\text{Sample}}(\omega)$ is measured after the pulse perpendicularly passes through the flat sample surfaces. The ratio between $\tilde{E}_{\text{Sample}}(\omega)$ and $\tilde{E}_{\text{Ref}}(\omega)$ gives the measured complex transmission of the sample:

$$\tilde{T}_{\text{meas}}(\omega) = \frac{\tilde{E}_{\text{Sample}}(\omega)}{\tilde{E}_{\text{Ref}}(\omega)} = A(\omega)\mathrm{e}^{i\Delta\phi(\omega)}. \tag{2.5}$$

If we ignore the possible Fabry-Pérot arising from the multiple reflections that take place in the sample, the transmission after sample's surface is obtained according to the Fresnel equations. Under normal incidence, the theoretical transmission $\tilde{T}_{\text{Theo}}(\omega)$ can be written as:

$$\tilde{T}_{\text{Theo}}(\omega) = \frac{4\tilde{n}_{\text{air}}\tilde{n}_{\text{Sample}}}{(\tilde{n}_{\text{air}}+\tilde{n}_{\text{Sample}})^2}\mathrm{e}^{i\frac{\omega d}{c}(\tilde{n}_{\text{Sample}}-\tilde{n}_{\text{air}})}. \tag{2.6}$$

The $\tilde{n}_{\text{Sample,air}}$ are the complex refractive index defined as

$$\tilde{n(\omega)} = n(\omega) - i\kappa(\omega), \tag{2.7}$$

in which the real part of $n(\tilde{\omega})$ is the refractive index $n(\omega)$. The imaginary part $\kappa(\omega)$ is the extinction coefficient which contains the absorption coefficient $\alpha(\omega)$:

$$\alpha(\omega) = \frac{2\omega\kappa(\omega)}{c}. \tag{2.8}$$

By associating the theoretical transmission $\tilde{T}_{\text{Theo}}(\omega)$ with the measured complex transmission $\tilde{T}_{\text{meas}}(\omega)$, taking $\tilde{n}_{\text{air}}(\omega) = 1$, we can obtain the refractive index $n(\omega)$ and the absorption coefficient $\alpha(\omega)$:

$$n_{\text{sample}}(\omega) = 1 + \frac{c}{d\omega}\Delta\phi(\omega), \tag{2.9}$$

and

$$\alpha_{\text{sample}}(\omega) = \frac{2}{d} \cdot \ln\left(\frac{4n_{\text{sample}}(\omega)}{A(\omega) \cdot (1 + n_{\text{Sample}}(\omega))^2}\right). \tag{2.10}$$

The THz-TDS can also be operated in reflection mode, the comparison between the signal reflected by the sample $\tilde{E}_{\text{Sample}}(\omega)$ and the reference signal $\tilde{E}_{\text{Ref}}(\omega)$ reveals the information of sample's reflection coefficient. However, extracting the absorption coefficient quantitatively and the refractive index solely from the reflection is more challenging. Two factors contribute to this fact. First off, most reflection systems are not under a normal incidence configuration. Consequently, the reflection coefficient is polarization-dependent. Therefore, a precise knowledge of the incident waves' polarization status, as well as the incident angle, should be available to extract the optical parameters [61]. Moreover, unlike the transmission configuration, the reference signal $\tilde{E}_{\text{Ref}}(\omega)$ is measured by placing a metallic mirror (perfect reflector) at the sample's location. Any misalignment of the reference mirror with respect to the sample's location contributes to a phase error in the signal [62]. Therefore reflective THz-TDS requires more rigorous system characterization and data processing to retrieve reliable optical parameters. Despite the difficulties, THz-TDS under reflection configuration is a valuable tool for analyzing highly absorbent samples such as fresh biological tissues since more signals can be captured.

2.3.3 Common material properties in THz range

Table 2.1 summarizes the published optical properties of common material in the THz range. We have concluded that the penetration ability of THz radiation is more selective than X-ray. It depends largely on the materials under investigation and the working wavelength. For various dielectrics materials, the absorption coefficient increases significantly when the frequency exceeds 1 THz. The increase of absorption coefficient along with the frequency in

glasses (Pyrex, BK7) and certain polymers (PMMA, PC, PET) is quantitatively expressed in [63]:

$$\alpha(\omega)n(\omega) = K_0(h\omega)^{\beta}, \tag{2.11}$$

where K_0 is a constant for each amorphous material (independent of temperature and frequency), h is the Plank constant; β depends on material and approaches to 2. The refractive index is relatively stable, whereas the absorption coefficient exhibits a square law increase with respect to the frequency.

Acrylonitrile butadiene styrene (ABS), polylactic acid (PLA), and nylon are standard three-dimensional (3D) printable materials. They have a significant absorption coefficient at frequencies >1 THz range. The absorption coefficient in the sub-THz range is low. Therefore they can be used for fabricating sub-THz optics components. Reported 3D-printed sub-THz components and devices, including lenses and diffractive elements, are made with non-standard low absorption filament such as cyclic olefin copolymer (TOPAS), and HDPE [64]. Polymer composites are often bonded with adhesives. A series of commercially available adhesives are studied in [65]. Although the optical behavior of adhesives depends on chemical bases, the number of components, and the processing procedure, we can still conclude that they are highly absorbent at frequencies >1 THz. It is not surprising that these materials with mm-scale thickness are no longer transparent when observed at 2.52 THz. Seeing through these materials is only possible with sub-THz radiation.

Polymers including polypropylene (PP), polyethylene (PE), polytetrafluoroethylene (PTFE, Teflon), polymethylpentene (TPX), and ZEONEX exhibit low THz absorption up to 5 THz. They are suitable to be used as lenses, substrates, or windows in THz setup, among which TPX and ZEONEX are more favorable for THz optics because of their good mechanical properties, chemical stability, and transparency in the visible range for alignment needs. Quartz, silica, and High Resistivity Float Zone Silicon (HRFZ-Si) are low absorption crystals. They are also important materials for manufacturing THz optics. Moreover, due to the high refractive index, HRFZ-Si provides a transmittance/reflectance ratio of about 54/46 % in the wide wavelength range without any coating [66]. Thus, they can be used as THz beam-splitters and attenuators. For imaging concerns, if one material remains highly transparent along with the whole THz range (including the above-mentioned polymers and crystals, dehydrated biological tissues, and thin textiles), it is preferable to image these samples at a higher frequency (smaller wavelength) for achieving a better resolution.

Table 2.1 Optical properties of common polymer materials in THz range

Material	Refractive index n	α at 1 THz (cm^{-1})	α at 0.5 THz (cm^{-1})	Ref
Polypropylene (PP)	1.49	<1	∼1	[67]
Poly tetrafluoroethylene (PTFE)	1.44	<1	∼1	[67]
High density Polyethylene (HDPE)	1.54	∼2	∼2	[67]
Poly carbonate (PC)	1.651	∼15	<10	[67]
Polymethyl methacrylate (PMMA)	1.569	∼25	<10	[67]
Polyethylene terephthalate (PET)	1.71	∼25	<7	[67]
Polymethylpentene (TPX)	1.46	<1	<1	[68]
ZEONEX	1.53	<1	<1	[68]
Quartz	1.96	∼2	∼1	[2]
Silica	1.96	∼2	∼1	[2]
Pyrex	2.11	∼30	∼10	[2]
BK7	2.5	∼80	∼18	[2]
High Resistivity Float Zone Silicon (HRFZ-Si)	3.41	<0.5	<0.5	[69]
Acrylonitrile butadiene styrene (ABS)	1.57	∼18	∼5	[70]
Polyactic acid (PLA)	1.89	∼20	∼11	[70]
Nylon	1.72	>25	∼7	[70]
Epoxy resins-based adhesives[4]	1.6-2	∼17-32	∼5-7	[65]
Acrylate-based adhesives[5]	1.569	∼6-27	∼2.5-7	[65]

2.3.3.1 Experimental observation

In the scope of investigating NDT for plastic/composite materials, we performed some transmission measurements of typical glass fiber reinforced polymer (GFRP) samples. The GFRP samples in Fig. 2.9(b) turned out to be opaque at 2.52 THz when illuminated with our laser. No signal was detected behind the samples. To evaluate their absorption coefficient, we measured the samples 2.1, 5.1, and 6.1 using the THz-TDS system (Menlo Systems) shown in Fig. 2.9(a). The samples' composition and their thickness are listed in Table. 2.2.

[4]Four two-component adhesives from different companies are tested in this literature.
[5]Five two-component adhesives from different companies are tested in this literature.

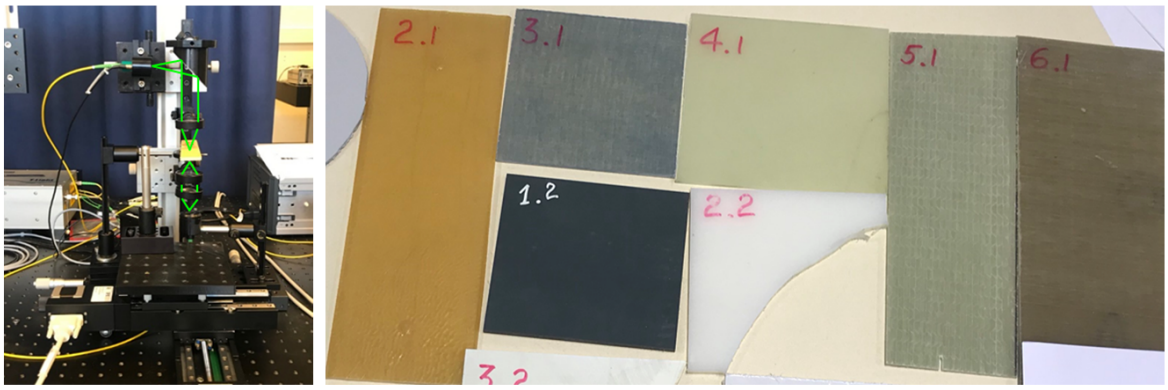

(a) (b)

Fig. 2.9 (a)THz-TDS setup. (b)GFRP samples under investigation.

Table 2.2 Investigated GFRP samples

Sample	Description	Thickness
2.1	30% glass fiber+PMMA +PE	2 mm
5.1	60% glass fiber + epoxy	2 mm
6.1	54% glass fiber + vinylester	5 mm

The measured data and their analysis are presented in Fig. 2.10. Figure 2.10(a) gives the measured time-domain signal. Compared to the reference signal, the pulse after passing through the samples is shrunk and delayed. Figure. 2.10(b) gives the spectra in the frequency domain. The cut-off frequency for the reference signal is around 2 THz. The cut-off frequency for the three samples is brought forward to 1 THz, 0.8 THz, and 0.5 THz, respectively. The signal-to-noise ratio (SNR) after the cut-off frequency is too low for parameter extraction. We extracted the refractive index (Fig. 2.10(c)) and the absorption (Fig. 2.10(d)) using the data before the cut-off frequency using Eq. 2.9 and Eq. 2.10. Even for the least absorbent sample 2.1, the absorption coefficient exceeds 30 cm^{-1} at 1 THz. We applied quadratic regression to the product of the retrieved refractive index and the absorption coefficient according to Eq. 2.11, the fitting results shown in Fig. 2.10(e) are satisfying. If we neglect the refractive index variation, we can roughly estimate the absorption coefficient based on the fitting function. The absorption coefficient of sample 2.1 at 2.52 THz reaches 180 cm^{-1}! Therefore, we conclude that these samples can only be imaged at deep sub-THz.

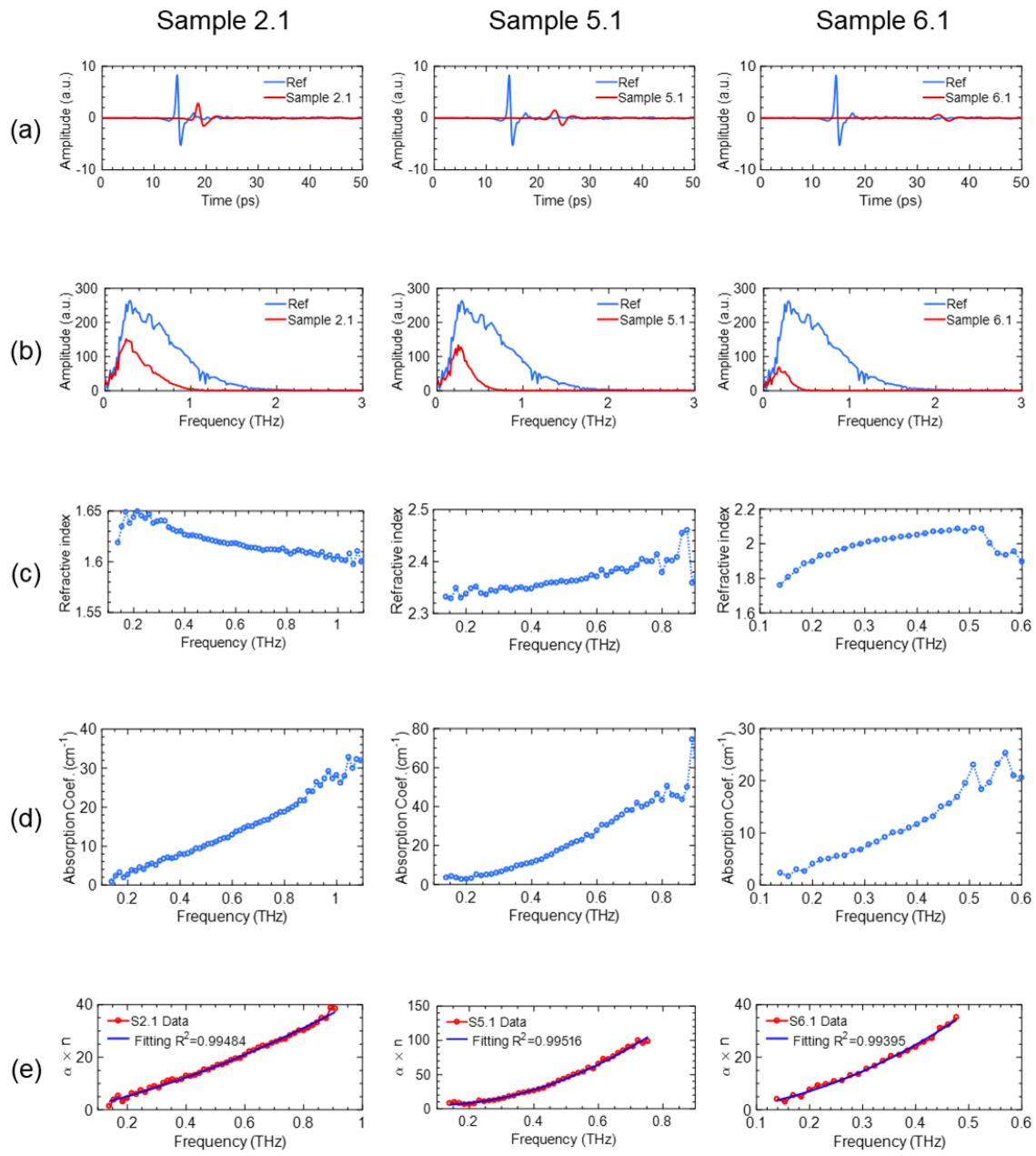

Fig. 2.10 Measured optical properties of three GFRP samples. (a) is the measured time-domain signal. (b) is the spectra in the frequency domain obtained by performing FFT on the datasets in (a). (c) is the refractive index. (d) is the absorption coefficient. (e) is the product of the refractive index and the absorption coefficient.

2.4 Terahertz imaging systems

Hereby we present THz imaging systems and their applications by different common ways of categorization. THz imaging systems can be divided into passive and active imaging depending on whether an external THz source is employed (Fig. 2.11).

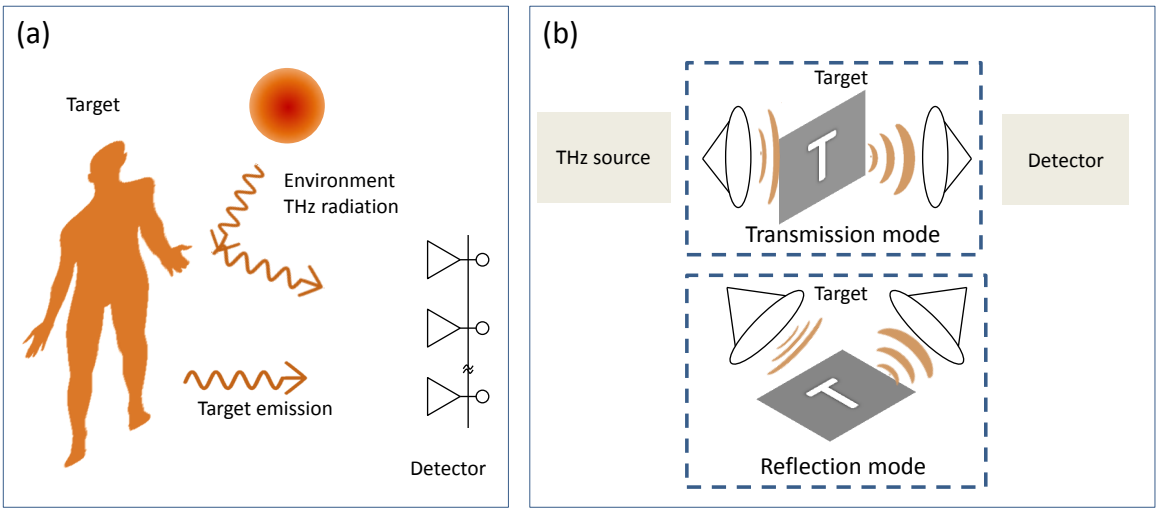

Fig. 2.11 (a) Passive THz imaging. (b) Active THz imaging in reflection and transmission mode, respectively.

A **passive THz imaging system** does not need a source. The detector detects the THz radiation emitted by the target itself as well as the ambient THz radiation (emitted by the sun), as shown in Fig. 2.11(a). It records the slightly differing contrast in radiometric temperature. The difference between ambient temperature (295 K) and human body temperature (310 K) is only around 15 K[6]. Passive imaging system detectors require a very challenging level of sensitivity since the THz signals are extremely weak. It is attainable with cryogenically cooled sensors or with heterodyne receivers [71]. Developing highly sensitive detectors with required optical components and advanced electronics for passive THz radiation detection has been pioneered in the space science community. Herschel and Plank are two famous satellites that carry THz detection instruments [72]. The Herschel Space Observatory specifically targets the far-infrared and has both direct detection imaging bolometers and photometers, as well as seven high-resolution heterodyne spectrometer bands covering 480 to 1910 GHz [72]. Planck was launched in 2009 to study the cosmic microwave background between 27 GHz to 1 THz in even greater detail. The space technology has been gradually transferred to

[6]On the outdoor scene, the sky temperature (60 K) provides higher contrast.

sub-THz/MMW imaging for the detection of concealed weapons for security applications [73]. In 2002, The first THz passive image of a human hand was captured by a 250 GHz/300 GHz with 16-pixel array imager developed by the European Space Agency (ESA)-sponsored StarTiger team and UK Rutherford Appleton Laboratory (Fig. 2.12(a)) [74]. This technology is co-patented by ESA and commercialized by the UK company ThruVision with customers, including airports around the world as well as the US Customs and Border Protection agency, at selected southern border entry ports (Fig. 2.12(b)) [75]. This signature technology transfer benefits from the high ability of sub-THz penetration. The fact that no external radiation is emitted toward the human body eliminates the safety concern. Understandably, passive imaging provides less contrast image compared to active imaging techniques. It becomes an advantage in security applications because it alleviates privacy invasion.

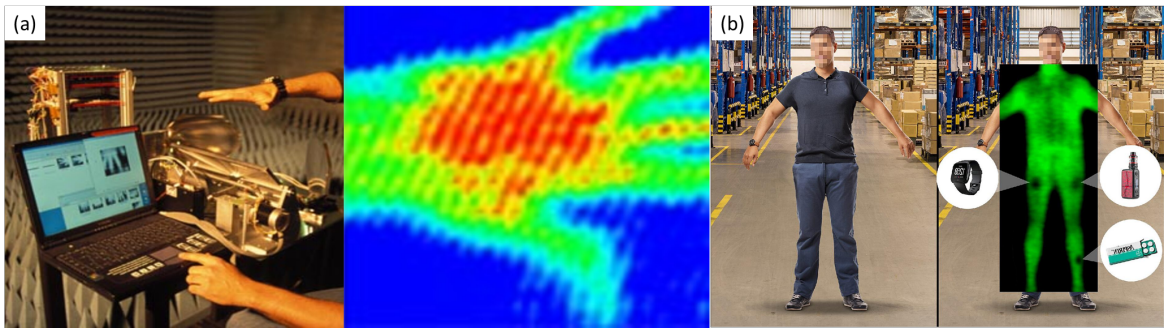

Fig. 2.12 (a) Passive Imaging of human hand [74]. (b) Passive imaging system commercialized by ThruVision [75].

On the other hand, an **active THz imaging system** illuminates the target with a source and collects the transmitted or reflected radiation (Fig. 2.11(b)). The geometrical configuration can be either in **transmission mode** or in **reflection mode**. Besides the THz-TDS, which provides multi-spectral information. THz active imaging systems with other narrowband sources tend to be monochromatic due to the limited choices for THz generation. As reviewed in Section 2.2, THz sources have limited frequencies and power. THz detectors also have different sensitivities and operation frequencies. The THz source should be delicately paired with the appropriate THz detector at the operational frequency to achieve optimum imaging quality.

Active imaging systems can provide high image contrast thanks to the extra source illumination. However, artifacts due to the coherent source illumination deteriorate the imaging quality [76]. First off, the rough surfaces will create the speckle phenomenon, as shown in

Fig. 2.13(a). The image is taken at 650 GHz in reflection geometry by raster-scanning the focused beam over the target. Speckle occurs in the hairy part [77]. Another typical artifact is the interference pattern when the multiple reflections generated by different surfaces interfere with the main beam. It is also known as Fabry-Pérot effect. Figure 2.13(b) shows a typical interference pattern that occurred in the quartz sample (2.5 cm $\times$ 2 cm) holder at 2.52 THz by raster-scanning the sample at the focal plane [78]. A similar observation is discussed in the first demonstration of THz imaging with BWO at 520–710 GHz in [30]. The coherence artifacts have a greater impact on full-field imaging due to the optics for beam expanding and the employed objective. One of the well-known effects of the coherent imaging system is edge ringing due to diffraction. The sharp cutoff of the aperture in the coherent imaging system induces strong oscillations on edge. Figure 2.13(c) from [79] shows a typical image where the strong ring patterns are clearly observable. The illumination beam has strong circular fringes. The image is taken in transmission mode using i2S TZCAM camera with an objective lens at 2.5 THz. The similar phenomenon can be found in [80–83].

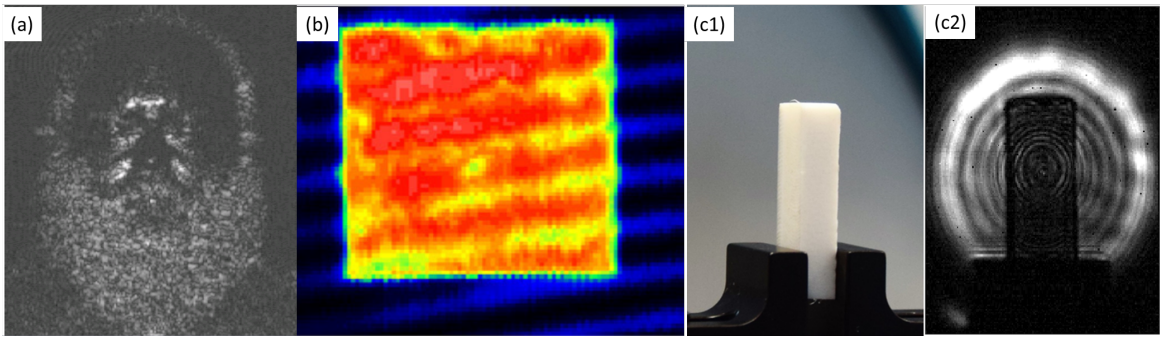

Fig. 2.13 Artifacts due to the coherent source illumination: (a) speckle; (b) spurious interference; (c) Interference patterns in full-field imaging: (c1) is the photograph of the object and (c2) is the THz imaging of (c1).

Naturally, the solution for more homogenized illumination is to break the coherence. Introducing a fast variation of optical path by multi-angle beam steering [79, 77, 84], a rotating diffuser [83] or oscillating axially the optical component [82] will average and blur out the unwanted patterns. Frequency modulation and wavelength modulation are also well-known coherence reduction techniques that can be applied when the THz sources are tunable [30, 85].

It is worth mentioning that although the high coherence of the THz sources is troublesome when employed as illumination in an active imaging system, the coherence property opens up new avenues in coherent lensless imaging. The techniques imple-

mented in this thesis take advantage of the high coherence of employed THz sources.

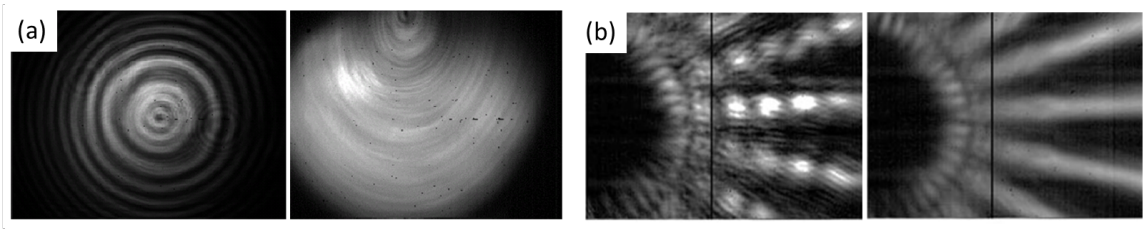

Fig. 2.14 Breaking the coherence for uniform illumination: (a) with a rotating diffuser in [83]; (b) oscillating axially the optical component in [82].

By image acquisition method, the imaging system can categorized as **single-point raster-scanning imaging** and **full-field imaging**. The setup of single-point raster-scanning imaging is depicted in Fig. 2.15(a). The first set of lenses focuses the THz beam to a diffraction-limited spot to illuminate the sample. After transmitting through the sample (or reflected by the sample), the THz beam is collected by the second set of lenses to the detector. Other than THz-TDS, sub-THz imaging is often based on single-point raster-scanning imaging due to the lack of appropriate detector arrays. The time-consuming scan is the main flaw of these imaging systems.

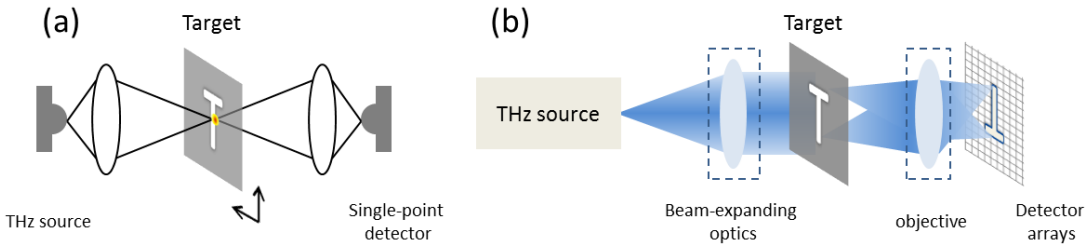

Fig. 2.15 (a) Single-point raster-scanning imaging; (b) Full-field imaging

Full-field imaging captures the image of an illuminated object using detector arrays. An expanded beam illuminates the sample. The image under the FOV is then formed on the detector array by an imaging objective lens. The first real-time THz full-field imaging was demonstrated at 2.52 THz using an uncooled microbolometer in 2005 [47]. Full-field imaging significantly increases the imaging speed because a larger area can be imaged with a single acquisition. The effective imaging area is determined by the optical design of the objective and the illuminated region. However, the image quality of samples using full-field

imaging is less satisfying than that of single-point raster-scanning imaging for three reasons. Primarily, it is challenging to provide a large area of uniformed illumination. The flaws in the illuminating beam, including the coherent artifacts discussed above, will also be imaged. Under a Gaussian beam illumination, the SNR at the border will be lower due to the lower intensity in full-field imaging. Secondly, with the same source power output and detector sensitivity, the SNR at the imaging area is lower when using full-field imaging. Thirdly, the imaging objective can introduce aberration and additional coherent artifacts. Figure 2.16 shows the representative images at a similar frequency that are obtained with single point raster-scanning imaging system [86] and full-field imaging system [80], respectively. The three phenomena discussed above can be clearly observed, although the aim is not to compare the two specific images rigorously.

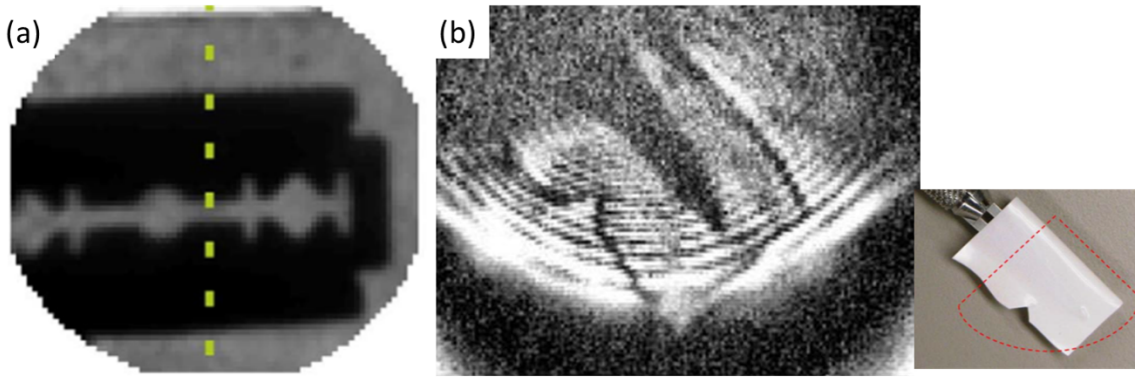

Fig. 2.16 (a) Single-point raster-scanning imaging with QCL at 2.5 THz in [86]; (b) Full-field imaging of the concealed knife (shown in inset) with QCL at 2.8 THz in [80].

The system commercialized by INO company represents the state-of-the-art THz full-field imaging system. Progress has been made in both building large-area uniform illumination and objective design. INO has designed beam homogenizers to break the coherence and polarization while expanding the beam to provide 12 cm $\times$ 15 cm quasi-flat-top illumination [81]. Up to 2021, INO has designed four objectives that are claimed to be diffraction-limited. For large field of view (FOV) objectives, the F-number has been decreased from 0.95 to 0.6. Thus better resolution and higher contrast can be achieved. Figure 2.17(a) shows the imaging system with an F/0.7 objective. Recently, a macro objective that allows imaging a FOV of 13.5 mm $\times$ 10 mm with high resolution has been designed (Fig. 2.17(b)). A resolution of 0.67 λ (0.5 mm at 400 GHz) is obtained with the macro objective. However, a trade-off between large FOV and high resolution exists. Figure 2.17(c) shows the resolution

performance published in [87]. Imaging 75 mm × 56 mm (16.5 mm × 12.4 mm) FOV at 515 GHz ends up with 3.5 λ (6.9 λ) resolution.

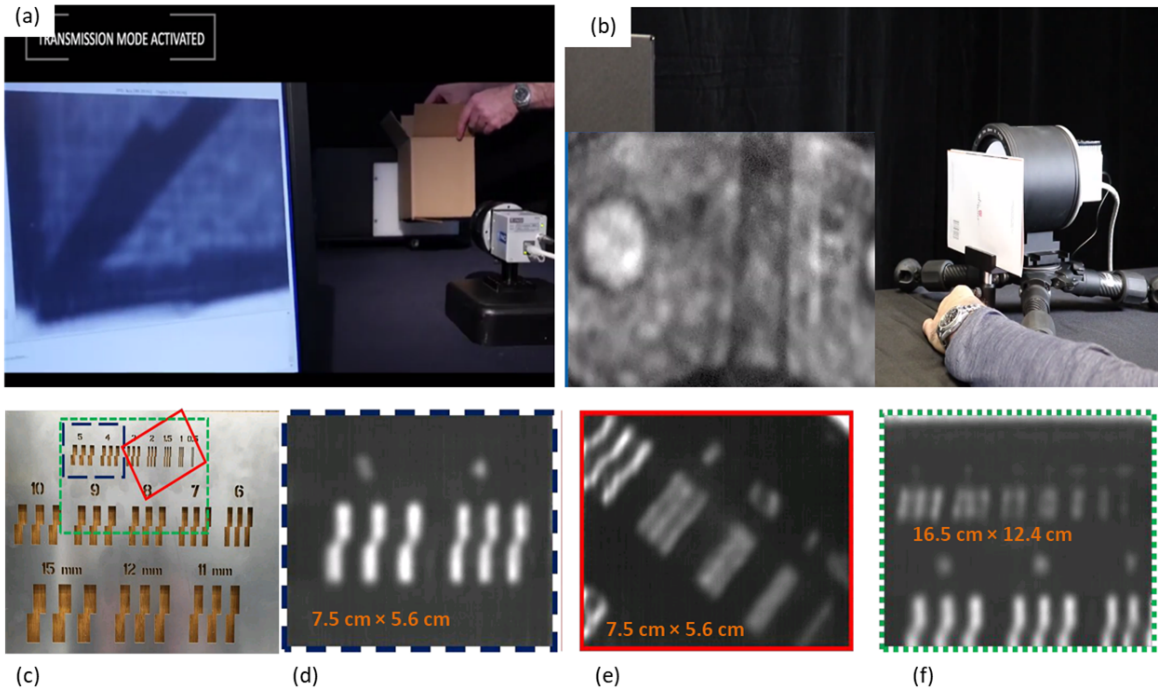

Fig. 2.17 (a) INO THz full-field imaging system with large FOV objective (F/0.7). (b) INO THz full-field imaging system with macro objective (F/0.7) (c-f) Resolution tests performed in [87]. (d-f) are the THz images of the corresponding area in (c).

2.5 Emerging computational imaging techniques in THz

Computational imaging techniques that are well-developed at visible to X-ray range have been adapted in THz imaging. Two forces drive such technical migration. On the one hand, the unique property of THz will offer more application possibilities for the existing computational imaging techniques. On the other hand, these imaging techniques provide an alternative solution to tackle the difficulties encountered in the THz band. As a result, these techniques have remained the focus of attention in recent THz imaging reviews [1, 8, 9, 20, 88, 89].

2.5.1 Computed Tomography

Computed tomography (CT) reconstructs the 3D image of the interior feature of an object based on a series of 2D images taken at multiple scan angles. Each 2D image corresponds to the transmitted light after being attenuated by the object at the projection angle. Thus,

the 3D reconstruction reveals the light absorption inside the sample. CT was originally developed with X-Ray for medical imaging and quality control in NDT applications. Due to THz radiation's penetration ability and the non-ionization feature, developing THz CT for 3D imaging is an active research field. The first THz CT was demonstrated in 2002 with a THz-TDS setup [90], 3D spectral amplitude and phase information are retrieved. THz CT has also been developed with CW THz radiation [91, 33]. Case studies of bones, ancient potteries, porcelain, and polymer products have been carried out in these experiments [9]. Due to the large wavelength of THz radiation, the diffraction effect plays an important role in deteriorating the reconstruction. Effort have been made in both beam-forming [92, 93] and precise reconstruction modeling [94].

2.5.2 Single-pixel imaging

Single-pixel imaging is a computational imaging technique based on compressive sensing. It measures multiple transmitted intensities of the sample illuminated by different modulation masks. Unlike the single-point configuration mentioned in the last section, single-pixel imaging does not require a 2D scan. Instead, the sample's information can be mathematically retrieved using matrix-vector multiplication. The compressive sensing theory proposes that reconstruction can be obtained from a number of measurements lower than that of unknown pixels when the image is sparse under certain representations [95]. Single-pixel imaging is especially pertinent for THz imaging due to the lack of rapid and sensitive 2D THz cameras. However, the single-point measurement is still the standard method in THz-TDS. THz single-pixel imaging was first demonstrated in 2008 [96, 97]. When using THz-TDS, both amplitude and phase were retrieved. Since then, improvements toward real-time imaging with a spinning-disk mask [98], 3D single-pixel tomography [99, 100] and spatial THz modulator (mask) optimization have been realized [101].

2.5.3 CW THz coherent lensless imaging

Retrieving phase information is of interest because the phase distribution of the wavefront provides additional information about the object. Besides measuring the phase via complicated coherent detection, coherent lensless imaging techniques allow extracting phase information from intensity-only measurement based on free-space diffraction of the coherent wavefront. As the name indicates, this family of technology requires a coherent CW source, which is the case for most THz sources as discussed in Section 2.4. No optics for image formation is required. The methods developed in this thesis, digital holography, phase retrieval, and

ptychography, belong to this family. The principle of each method and related work will be elaborated in Chapter 3.

2.6 Chapter summary

In this chapter, we have reviewed the state-of-the-art of THz technology. The review helps us keep a clearer view of the different subdivisions of THz band, generation and detection technologies, and THz imaging systems. Our THz source and detector mainly work in the FIR band. The FIR band offers more facilities for developing full-field emerging imaging techniques. However, their penetration ability is very selective. Once materials remain opaque at the FIR range, imaging with such THz radiation is no longer advantageous over other frequency ranges. Seeing-through applications such as NDT of composite materials should be envisaged at the sub-THz regime. However, the long-wavelength and the lack of a large 2D array detector are the main hurdles to developing high-quality imaging techniques. In the following chapters, we will develop and improve different CW coherent imaging techniques with our equipment in the FIR band. Potential applications will be explored. We will also investigate the migration of developed imaging techniques toward the sub-THz range.

Chapter 3

Overview of coherent lensless imaging techniques

This chapter introduces essential notions of coherent lensless imaging techniques. Contrary to conventional imaging formation by lenses, coherent lensless imaging techniques utilize the diffracted intensities of the object under coherent illumination and retrieve its complex wavefront (both the amplitude and phase) via performing the free-space propagation numerically. Correctly retrieving the lost phase information from the intensity-only acquisitions is the fundamental challenge of coherent lensless imaging techniques. This is often referred to as the "phase problem". The chapter starts with the scalar diffraction theory as explained in many wave optic textbooks to describe free-space light propagation [102]. The angular spectrum method (ASM) for diffraction representation is derived since the method is used throughout the thesis. Afterward, we will introduce digital holography (DH) and phase retrieval (PR), which are two distinctive methods to tackle the "phase problem". DH retrieves the phase by interfering with the diffracted wavefront with a known reference wavefront, while the PR techniques broadly refer to other non-interferometric approaches that solve the phase problem mathematically based on multiple diffraction patterns. The basics of these two techniques are introduced in this chapter. Although the fundamentals of coherent lensless imaging techniques presented in this chapter bear no difference from the cases at shorter wavelengths, the particularity of their implementation in THz due to the tremendous increase of wavelength should be taken care of. Finally, we review the THz coherent lensless imaging techniques.

Table of contents

3.1 Scalar diffraction theory

3.1.1 Scalar wave equation

The electromagnetic wave propagation is based on Maxwell's equations. In absence of free charge, the equations are written as

$$\begin{aligned} \nabla \times \mathbf{E} &= -\mu \frac{\partial \mathbf{H}}{\partial t} \\ \nabla \times \mathbf{H} &= \varepsilon \frac{\partial \mathbf{E}}{\partial t} \\ \nabla \cdot \varepsilon \mathbf{E} &= 0 \\ \nabla \cdot \mu \mathbf{H} &= 0. \end{aligned} \tag{3.1}$$

$\mathbf{E}(x,y,z,t)$ and $\mathbf{H}(x,y,z,t)$ are the electric field and magnetic field, respectively. ε and μ are the permittivity and the permeability of the medium in which the wave propagates. If we assume that the medium is nondispersive (frequency independent), homogeneous (position independent) and isotropic (direction independent), ε and μ are scalar constants. Owing to the relation $\nabla \times (\nabla \times \mathbf{A}) = \nabla(\nabla \cdot \mathbf{A}) - \nabla^2 \mathbf{A}$, if we apply the $\nabla\times$ operation to both sides of

the first and second equations in Eq. 3.1, we get the vector wave equation:

$$\begin{aligned} \nabla^2\mathbf{E} - \frac{n^2}{c^2}\frac{\partial^2\mathbf{E}}{\partial t^2} = 0 \\ \nabla^2\mathbf{H} - \frac{n^2}{c^2}\frac{\partial^2\mathbf{H}}{\partial t^2} = 0, \end{aligned} \tag{3.2}$$

where $n = \sqrt{\varepsilon/\varepsilon_0}$, is the refractive index of medium and $c = 1/\sqrt{\varepsilon_0\mu_0}$ is the velocity of propagation in vacuum; ε_0 and μ_0 are the permittivity and the permeability in vacuum respectively. Since the vector wave equation in Eq. 3.2 is obeyed by both $\mathbf{E}$ and $\mathbf{H}$. Their components $E_{x,y,z}$ and $H_{x,y,z}$ obey the relation, we summarize Eq. 3.2 into one scalar wave equation at location $\mathbf{R}$ and time t:

$$\nabla^2 u(\mathbf{R},t) - \frac{n^2}{c^2}\frac{\partial^2 u(\mathbf{R},t)}{\partial t^2} = 0. \tag{3.3}$$

The scalar wave equation significantly simplifies the problem compared to the full vector theory. However, we emphasize that the assumptions we make to the medium need to be satisfied when using the scalar model. For example, in an inhomogeneous medium, the permittivity depends on the position, Eq. 3.3 is no longer valid since the coupling between different components exists. Light propagation in inhomogeneous or isotropic medium can not be investigated based on the scalar diffraction theory explained hereafter.

In this thesis we employ monochromatic sources. For a purely monochromatic wave with frequency ν, the scalar wavefront can be written as

$$u(\mathbf{R},t) = \Psi(\mathbf{R})\exp(2\pi\nu t). \tag{3.4}$$

The spatial component and the temporal one are separated in this representation. The expression $\Psi(\mathbf{R}) = A(\mathbf{R})\exp[i\phi(\mathbf{R})]$ is the complex amplitude of the wavefront. After injecting Eq. 3.4 in Eq. 3.2, we obtain the Helmholtz equation for the complex amplitude:

$$\left(\nabla^2 + k^2\right)\Psi(\mathbf{R}) = 0, \tag{3.5}$$

with $k = 2\pi n\frac{\nu}{c} = \frac{2\pi}{\lambda}$, the wavenumber. During the propagation, the complex amplitude of a wavefront must satisfy the Helmholtz equation. Hence, the formulation of the diffraction problem is to find the complex distribution $\Psi(\mathbf{R})$ at an arbitrary point $\mathbf{R}(x,y,z)$ which is a solution of Eq. 3.5.

3.1.2 Angular spectrum method for diffraction calculation

The angular spectrum method (ASM) formulates the diffraction problem using the linear-invariant systems theory. The various spatial Fourier components of a complex wavefront across a certain plane can be regarded as plane waves traveling in different directions away from that plane. The field amplitude at other points across other parallel planes can be calculated by summing these plane waves after the propagation.

We suppose that the incident wave $\Psi(x,y,0)$ is located at plane $z=0$. After propagating a distance of z, the wavefront distribution at the observing plane to be calculated is $\Psi(x,y,z)$. The 2D Fourier transform of $\Psi(x,y,0)$ and $\Psi(x,y,z)$ gives their frequency spectrum

$$G(f_x,f_y;0)=\iint_{-\infty}^{\infty}\Psi(x,y,0)\exp\left[-i2\pi\left(f_x x+f_y y\right)\right]\mathrm{dxdy}, \tag{3.6}$$

$$G(f_x,f_y;z)=\iint_{-\infty}^{\infty}\Psi(x,y,z)\exp\left[-i2\pi\left(f_x x+f_y y\right)\right]\mathrm{dxdy}. \tag{3.7}$$

$\Psi(x,y,z)$ is the inverse Fourier of its spectrum $G(f_x,f_y;z)$

$$\Psi(x,y,z)=\iint_{-\infty}^{\infty}G(f_x,f_y;z)\exp\left[i2\pi\left(f_x x+f_y y\right)\right]\mathrm{df_x df_y}. \tag{3.8}$$

The term $\exp\left[i2\pi\left(f_x x+f_y y\right)\right]$ can be regarded as representing a plane wave propagating with direction $\cos\alpha=\lambda f_x, \cos\beta=\lambda f_y$. Therefore, physically, the complex wavefront $\Psi(x,y,z)$ is the sum of the plane wave components. Injecting Eq. 3.8 in the Helmholtz equation Eq. 3.5 gives

$$\frac{\mathrm{d}^2}{\mathrm{d}^2 z}G(f_x,f_y;z)+\left(\frac{2\pi}{\lambda}\sqrt{1-(\lambda f_x)^2-(\lambda f_y)^2}\right)^2 G(f_x,f_y;z)=0. \tag{3.9}$$

One elementary solution of Eq. 3.9 can be written as

$$G(f_x,f_y;z)=G(f_x,f_y;0)\exp\left[i\frac{2\pi}{\lambda}z\sqrt{1-(\lambda f_x)^2-(\lambda f_y)^2}\right]. \tag{3.10}$$

Equation 3.10 shows that the propagation of wavefront on the z direction can be expressed by multiplying a phase factor $\exp\left[i\frac{2\pi}{\lambda}z\sqrt{1-(\lambda f_x)^2-(\lambda f_y)^2}\right]$ to the original frequency spectrum $G(f_x,f_y;0)$, when f_x and f_y satisfy $1-(\lambda f_x)^2-(\lambda f_y)^2\geq 0$. When $1-(\lambda f_x)^2-(\lambda f_y)^2<0$, these evanescent wave components are rapidly attenuated by the propagation. We summarize the ASM representation as

$$\Psi(x,y,z) = \mathscr{F}^{-1}\left\{\mathscr{F}\left\{\Psi(x,y,0)\right\} \times \mathscr{G}\left(k_x,k_y;z\right)\right\}, \tag{3.11}$$

with

$$\mathscr{G}\left(k_x,k_y;z\right) = \begin{cases} \exp\left[i\frac{2\pi}{\lambda}z\sqrt{1-(\lambda f_x)^2-(\lambda f_y)^2}\right], \text{if } 1-(\lambda f_x)^2-(\lambda f_y)^2 \geq 0 \\ 0, \text{if } 1-(\lambda f_x)^2-(\lambda f_y)^2 < 0. \end{cases} \tag{3.12}$$

We mention here that there exists another way of rigorously calculating the diffraction distribution at the observation point $\mathbf{R}(\mathbf{x},\mathbf{y},\mathbf{z})$ using the Green's theorem and alternative Green's function, leading to the Rayleigh-Sommerfeld diffraction formula. The detailed derivation can be found in [102]. The Rayleigh-Sommerfeld formulation can be expressed via the convolution between the original wavefront and the Rayleigh-Sommerfeld kernel:

$$\Psi(x,y,z) = \mathscr{F}^{-1}\left\{\mathscr{F}\left\{\Psi(x,y,0)\right\} \times \mathscr{F}\left\{h(x,y,z)\right\}\right\}, \tag{3.13}$$

with

$$h(x,y,z) = \frac{z}{i\lambda}\frac{\exp\left(ik\sqrt{z^2+x^2+y^2}\right)}{z^2+x^2+y^2}. \tag{3.14}$$

When developing THz coherent imaging techniques, minimizing the object-detector distance is crucial for resolution concerns which will be discussed in the next section. At a short recording distance, both ASM and Rayleigh-Sommerfeld convolution are suitable choices for describing THz propagation. On the contrary, Fresnel and Fraunhofer far-field approximations, which are widely used at shorter wavelengths for their simplicity, are not appropriate for THz propagation. In this thesis, we use ASM to describe the THz wave propagation. Equations 3.11 and 3.12 are used repeatedly in the following chapters.

If we knew the complex distribution of the wavefront at the recording plane, we could obtain the complete information about the object without ambiguity using Eq. 3.11 or Eq. 3.13. Unfortunately, the phase information is lost during the acquisition since the cameras capture only the intensity. The loss of phase information is referred to as "the phase problem". The term originated from the field of X-ray crystallography, and the same problem was encountered in the optics community.

3.2 Some fundamental limits of THz coherent lensless imaging techniques

There is no essential differences between developing coherent lensless imaging techniques using THz radiation and the implementations at shorter wavelength. However, both visible and THz cameras typically have μm-scale pixel pitch and tens of mm-scale imaging area, whereas the working wavelengths differ by 2-3 orders of magnitude. The tremendous increase in working wavelength leads to specific concerns that impact experiment design and future applications. We discuss hereafter two important aspects, the lateral resolution, and the phase measurement range. Other particularities of employing large wavelengths have been studied thoroughly in our paper [21].

3.2.1 Lateral resolution

The intrinsic resolution of coherent lensless imaging techniques is diffraction-limited, *i.e.*, the lateral resolution d_r depends on the wavelength and the numerical aperture (NA) of the imaging system. Under the lensless configuration, the NA is determined by the finite size of imager $Np \times Np$ and the recording distance z between the object plane and the detector plane, as shown in Fig. 3.1:

$$\rho = \frac{\lambda}{2NA} = \frac{\lambda}{2\sin\alpha} = \frac{\lambda}{2}\sqrt{\left(\frac{2z}{Np}\right)^2 + 1} \approx \frac{\lambda z}{Np}. \tag{3.15}$$

The wavefront in front of the detector plane is continuous and infinite, whereas the imager has a finite aperture. Consequently, the high-frequency components of the wavefront are diffracted outside of the imager extent. The information is lost during the recording. The diffraction is severe when using THz wavelength. Yet a sub-mm level resolution is desired in most THz imaging cases. Thus minimizing the object-detector distance is crucial for THz lensless imaging. The recording distance is often squeezed to less than five cm when working with the one cm^2-sized imagers at THz wavelength. The geometrical configuration often sets the lower limit of object-detector distance. Additionally, for the off-axis DH setup, one should leave enough space for reference wave injection; the object-detector distance can be reduced to one cm. For Gabor in-line DH or other reference-free PR setups, the recording distance can be reduced further to several millimeters. The large wavelength of sub-THz radiation implies that a fairly large NA should be employed to achieve an appropriate lateral resolution. An extensive detection area is needed for recording the diffraction patterns due

to the mm-level wavelength. For instance, in [103], when working at 0.495 THz (λ= 606 μm), for a sample located 16.3 cm away from the detector, a detection area of 20× 20 cm is needed to achieve a lateral resolution comparable to the wavelength.

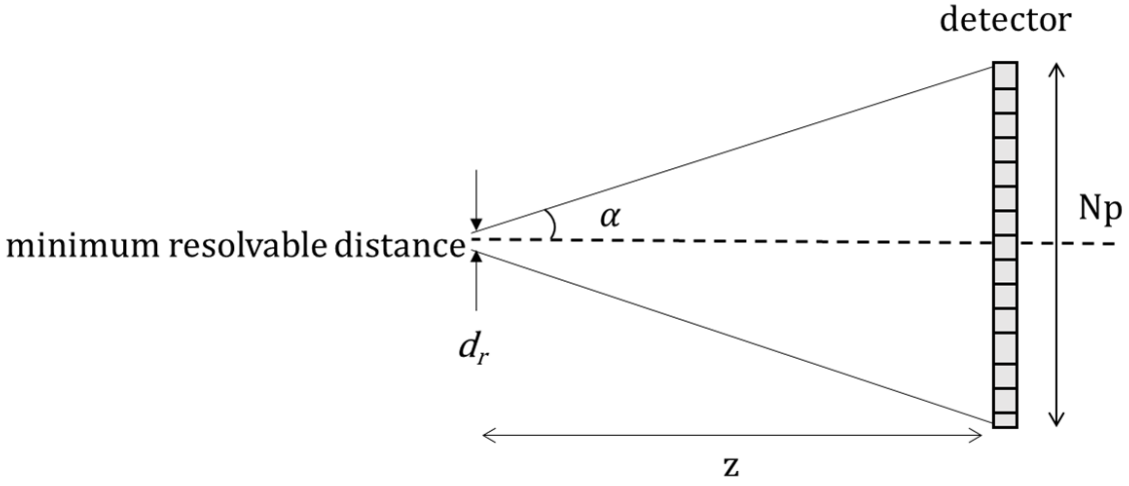

Fig. 3.1 The lateral resolution of a lensless coherent imaging system.

The short recording distance in THz DH translates to a high Fresnel number F

$$F \overset{\text{def}}{=} \frac{a^2}{z\lambda}, \tag{3.16}$$

where a is the radius of the aperture, z is the recording distance. If F is larger than 1, the beam is said to be near-field. It is often the case in the THz configuration for the resolution concern. The paraxial Fresnel approximation or the Fraunhofer far-field approximation are no longer suitable for describing THz propagation in free space in this situation.

3.2.2 Phase measurement range and resolution

The phase distribution obtained from coherent imaging techniques allows us to visualize or even quantify the optical path difference (OPD) between two points. The phase difference $\Delta\phi$ of two points is related to the OPD and the wavelength λ through the relation $\Delta\phi = 2\pi/\lambda \times OPD$.

In transmission mode, the light passes through the transparent object. The OPD between two points relates to the thickness variation Δt or refractive index Δn. For a homogeneous transparent object with refractive index n, the thickness difference between two points is

written as $\Delta t = \Delta\phi\lambda/[2\pi(n-1)]$. For an object with uniform thickness t, the refractive index variation is $\Delta n = \Delta\phi\lambda/[2\pi(t-1)]$. The thickness variation or the refractive index variation is proportional to the phase difference and the working wavelength.

Under reflection configuration, the light is reflected by the surface of the object under investigation. The phase difference reveals the object's 3D profile. The phase difference is proportional to the depth variation Δd of the surface profile.

The measurable range and precision are two aspects should be noticed when relating the phase distribution and the measurand. First off, the obtained phase distribution is wrapped in modulo 2π. A larger measurement range of variation corresponds to 2π phase variation thanks to the large working wavelength. We use a simple case to illustrate this effect. A deformation ranging from 0 to 50 μm shown in Fig. 3.2(a) is observed using reflection configuration with normal incidence illumination. Hence the deformation ΔD and the phase map $\Delta\phi$ obey the relationship:

$$\Delta\phi = \frac{4\pi\Delta D}{\lambda}, \tag{3.17}$$

where the phase map $\Delta\phi$ is wrapped in modulo 2π. The deformation is too large to be observed in visible wavelengths (Fig. 3.2(b)). As shown in Fig. 3.2(b)-(d), the number of wrapped phase fringes reduces with the increase of working wavelength.

However, in the meantime, the measurement resolution decreases when working with large wavelength since the measurand is proportional to the wavelength. This is considered as a shortcoming when working with THz wavelength. If r_ϕ stands for the phase resolution, *i.e.*, the minimum distinguishable phase variation from the phase map, the measurement precision of the deformation r_D is calculated as:

$$r_D = \frac{r_\phi\lambda}{4\pi}. \tag{3.18}$$

The achievable precision of the obtained phase data, *i.e.*, the phase resolution r_ϕ is determined by the SNR of the measured data. If the phase resolution r_ϕ is 0.2 rad for three wavelengths, the minimum measurable deformation r_D will be $\lambda/63$, which corresponds to 0.17 μm in Fig. 3.2(c) whereas 1.9 μm in Fig. 3.2(d). The measurement precision in the latter is less satisfying. Therefore, if prior knowledge of the deformation is known, unwrapping the phase obtained with LWIR in Fig. 3.2(c) will give the optimum result among the three wavelengths in this example.

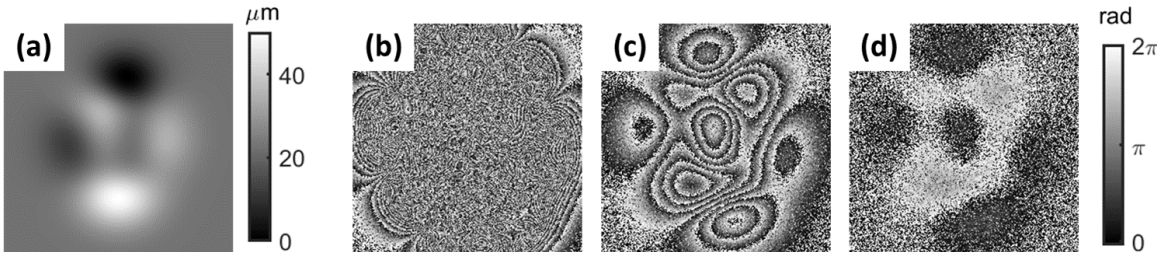

Fig. 3.2 Phase difference mod (2π) of a deformation ranging from 0-50 μm (a) at: (b) 532 nm, (c) 10.6 μm and (d) 118.83 μm.

3.3 Digital holography

Holography was invented by Dennis Gabor in 1948 as a lensless imaging concept when attempting to avoid spherical aberrations in the electron microscope [104]. The discovery of lasers in 1960 subsequently enabled the further development of holography. In 1971, Dennis Gabor was awarded the Nobel Prize in Physics "for his invention and development of the holographic method." As the etymology indicated, the *whole* (*holo*) information of the object's wavefront, both the amplitude and the phase, is recorded by letting the object wavefront $O(x,y)$ interfering with a known reference wave $R(x,y)$ at the recording plane (x,y). The interference pattern, *i.e.*, the hologram $H(x,y)$ is written as:

$$\begin{aligned} H(x,y) &= |R(x,y)+O(x,y)|^2 \\ &= |R(x,y)|^2+|O(x,y)|^2+R^*(x,y)O(x,y)+O^*(x,y)R(x,y). \end{aligned} \tag{3.19}$$

The hologram contains three diffraction orders: the 0 order consists of $|R(x,y)|^2+|O(x,y)|^2$, which is the intensity of two interfering beams; the $+1$ order $R^*(x,y)O(x,y)$ contains the complex amplitude of the object wavefront O; the -1 term $O^*(x,y)R(x,y)$ contains the conjugate of the object wavefront. In analog holography, the hologram is recorded on the photosensitive plates. When illuminating the hologram with the same reference wavefront used during the recording process, our eyes can observe the intensity generated by the original complex field object wavefront $O(x,y)$. With the development of optoelectronic recording devices and progress in computer performance, it became possible to record the holograms with cameras. Using these digital holograms, one can numerically calculate the propagation of the wave based on the scalar diffraction theory explained earlier in the chapter to perform the reconstruction. This process is known as digital holography (DH), which is the most established lensless imaging technique. Owing to the lensless setup and the retrievable phase information, DH is regarded as a versatile tool for applications in contactless metrology of

vibration, displacement, and deformation, as well as for microscopic imaging of biological cells, materials, and particle fields.

3.3.1 In-line digital holography

The holography setup originally conceived by Gabor is the in-line configuration, as depicted in Fig. 3.3(a). A single beam is used to illuminate a small object. The object should be smaller than the lateral extent of the incident wave so that part of the incident wave is not affected by the object serving as the reference wave. Under the in-line configuration, the term $|R(x,y)|^2$ is constant; the relation $|O(x,y)|^2 \ll |R(x,y)|^2$ holds due to the recording requirement. Since the wavefront diffracted by the object and the reference wave travel along the same optical axis, the real image terms $R^*(x,y)O(x,y)$ and $O^*(x,y)R(x,y)$ in Eq. 3.19 overlap. When back-propagating $R(x,y)H(x,y)$ to the object plane using Eqs. 3.11 and 3.12, the real image $O(x,y)$ is in focus with an out-of-focus $O^*(x,y)$. Front propagating the same distance will bring $O^*(x,y)$ in focus and $O(x,y)$ out of focus. Figure 3.3(b) shows the presence of twin image around the in-focus needle when simply back-propagating the 2.52 THz hologram in the inset of Fig. 3.3.

There exist different solutions for twin image elimination in in-line configuration. One widely used method is based on iterative PR techniques. *A priori* knowledge of the object such as support constraints or positive absorption will be applied on the object plane to solve the twin image problem [105]. Figure 3.3(c) shows the effectiveness of twin image elimination by employing the iterative PR method and the positive absorption constraint proposed in [106].

Compact and straightforward setup is the main merit of in-line DH. The single-beam configuration relaxes the coherence requirement for hologram recording. In visible wavelengths, in-line DH using partially-coherence light sources is often implemented in digital holographic microscopy (DHM) to avoid coherent noises. However, in-line DH is restrictive to the choice of samples. The sample under investigation is limited to a small dimension variation with a highly transparent background to guarantee the presence of the reference wave. Large objects or diffusely reflecting objects are not suitable for in-line DH. Due to these specific features, in-line DH is particularly useful for microscopic imaging such as particle field, droplet distribution, blood cells, or other microscopic organisms.

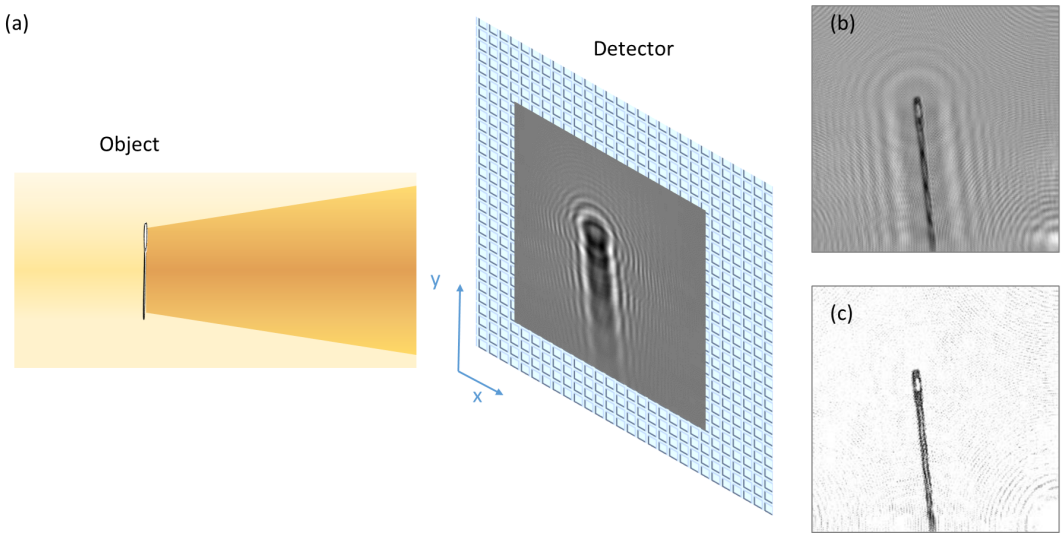

Fig. 3.3 (a) Recording geometry of Gabor in-line holography: the unscattered reference wave interferes with the object wave. (b) The amplitude after back-propagating the hologram to the object plane. Both the in focus real image and the out-of-focus twin image present. (c) The amplitude after removing the twin image by iterative phase retrieval.

3.3.2 Off-axis digital holography

The setup of off-axis DH is depicted in Fig. 3.4(a). A laser beam is separated into two individual beams: the reference beam and the object beam, traveling in different directions. Historically, the first optical off-axis hologram was recorded and reconstructed with a He-Ne laser by Leith and Upatnieks in 1963 [107]. The authors showed that, unlike the in-line configuration, the off-axis configuration is suitable for any type of object. Moreover, the off-axis DH separates the different diffracted terms thanks to the off-axis angle. Assuming that the object wave $O(x,y) = A_{\mathrm{O}}(x,y)\exp(i\phi_{\mathrm{O}}(x,y))$ travels along the optics axis, a tilted plane wave with off-axis angle θ_x with respect to the optical axis on x direction, is injected as the reference wave $R(x,y) = A_{\mathrm{R}}(x,y)\exp(i\frac{2\pi}{\lambda}x\sin\theta_x)$. Equation 3.19 can be expressed as

$$H(x,y) = A_{\mathrm{O}}^2(x,y) + A_{\mathrm{R}}^2(x,y) + 2A_{\mathrm{O}}A_{\mathrm{R}}\cos(2\pi\Delta f_x x - \phi_{\mathrm{O}}(x,y)), \tag{3.20}$$

the off-axis angle θ_y on y direction is 0 in this example. The spatial carrier frequency $\Delta f_x = \sin\theta_x/\lambda$ modulates the object phase information into sinusoidal bright and dark intensity patterns, as shown in Fig. 3.4(b). If we take the Fourier transform of the hologram,

the distribution of three orders in the Fourier domain can be written as

$$\begin{aligned}\mathscr{F}\{H\} = \mathscr{F}\left\{R^2+O^2\right\} + \mathscr{F}\{R^*O\} + \mathscr{F}\{O^*R\} = \mathscr{F}\left\{A_{\mathrm{O}}^2 + A_{\mathrm{R}}^2\right\} \\ + A_{\mathrm{R}}\mathscr{F}\{O\} \circledast \delta(f_{\mathrm{x}} - \Delta f_{\mathrm{x}}) + A_{\mathrm{R}}\mathscr{F}\{O^*\} \circledast \delta(f_x + \Delta f_x),\end{aligned} \tag{3.21}$$

with $\circledast$ as the convolution symbol and $\delta(x)$ as the Dirac delta function. The three orders are separated in the Fourier domain thanks to the carrier frequency as shown in Fig. 3.4(c). Applying a band-pass filter on $\mathscr{F}\{H\}$ allows eliminating the -1 and 0 orders. Centering the $+1$ order by shifting Δf_x towards the origin, then performing the inverse Fourier transform reconstructs the complex object wavefront $O(x,y)$ at the recording plane. The reconstructed object at the object plane is then obtained by back-propagation using Eqs. 3.11 and 3.12, as shown in Figs. 3.4(d2) and (e2).

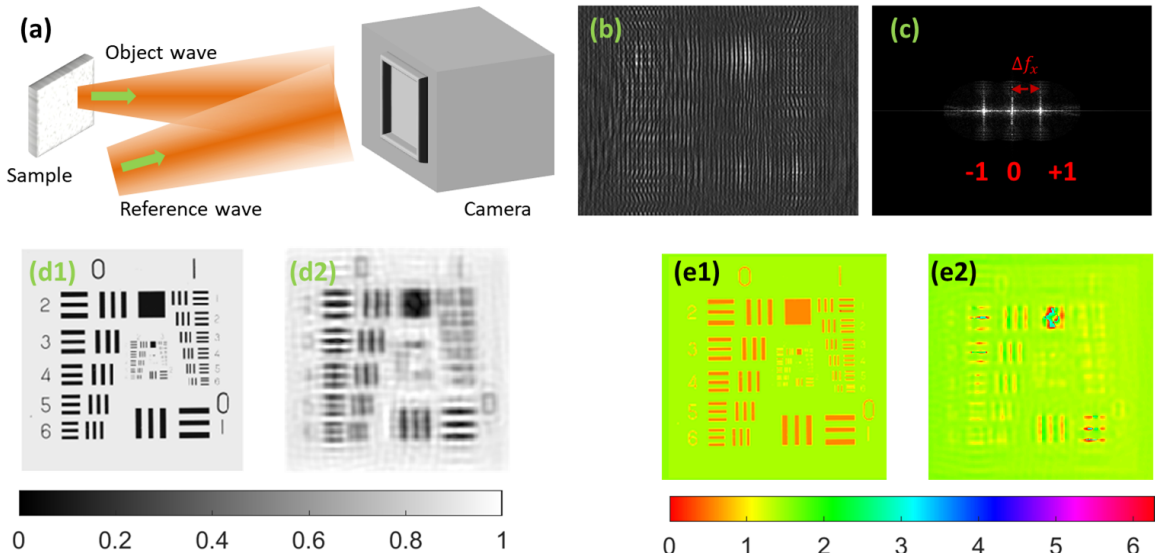

Fig. 3.4 (a) Recording setup of the off-axis digital holography. The three orders are separated in the Fourier spectrum (c) of the hologram (b). The reconstructed amplitude (d2) and phase (e2) are obtained by filtering and back-propagating the $+1$ order. (d1) and (e1) are the original amplitude and phase of simulated object wavefront.

The choice of off-axis angle is crucial for off-axis DH recording and reconstruction. Larger off-axis angle will naturally better separate the three diffraction orders. However, the upper limit of the off-axis angle should also be respected. If we consider the general case as depicted in Fig. 3.5, the angles θ_{Ref} and θ_{Obj} are the incident angle of the object wave and the reference wave, respectively. The overall off-axis angle is denoted as θ. The fringe space

Λ can be calculated as:

$$\Lambda = \frac{\lambda}{\sin\theta_{\mathrm{Ref}}\sin\theta_{\mathrm{Obj}}} = \frac{\lambda}{2\sin\frac{\theta_{\mathrm{Ref}}+\theta_{\mathrm{Obj}}}{2}\cos\frac{\theta_{\mathrm{Ref}}-\theta_{\mathrm{Obj}}}{2}}. \tag{3.22}$$

Taking the approximation $\cos\frac{\theta_{\mathrm{Ref}}-\theta_{\mathrm{Obj}}}{2} = 1$ and the relation $\theta = \theta_{\mathrm{Ref}} + \theta_{\mathrm{Obj}}$, then Eq. 3.22 can be written as:

$$\Lambda = \frac{\lambda}{2\sin\frac{\theta}{2}}. \tag{3.23}$$

In order to fulfill the spatial sampling condition, according to the Shannon sampling theorem, the minimum required sampling frequency must be twice the signal bandwidth in order to avoid the loss of information. One period of fringe Λ should be sampled at least by two detector pixels with a size of Δ: $2\Delta \leq \Lambda$. This restricts the maximum off-axis angle:

$$\theta \leq \theta_{\mathrm{max}} = 2\sin^{-1}(\frac{\lambda}{4\Delta}). \tag{3.24}$$

The maximum off-axis angle θ_{max} is determined by the working wavelength and the pixel size of the detector. In the visible range, the pixel size is usually dozens of times the wavelength. Consequently, θ_{max} is limited to several degrees. Therefore, the Mach–Zehnder configuration with a beam combiner is often employed in visible off-axis DH setups to achieve a small off-axis angle. Moreover, extended objects should be located at a minimum recording distance to minimize θ_{Obj}. The increase of wavelength when working with THz radiation relaxes this requirement. In most cases, $\lambda/(4\Delta) > 1$ holds. Therefore, there is no restriction on the off-axis angle or the recording distance.

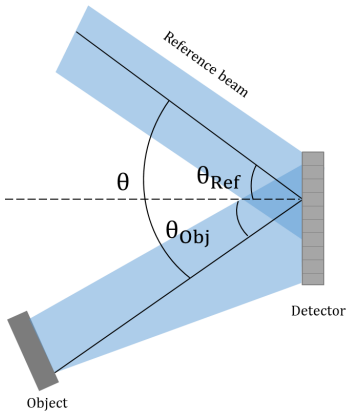

Fig. 3.5 The schema of off-axis angle θ.

Unlike in-line DH, the off-axis DH configuration can be used to image both microscopic and macroscopic objects, either under transmission mode or under reflection mode. Moreover, off-axis DH allows retrieving the complex wavefront of the sample with a single-shot hologram, making it suitable for observing dynamic scenarios. Therefore, off-axis DH has extensive applications in both scientific and industrial fields, such as microscopic biomedical imaging and surface morphology measurement.

3.4 Non-interferometric phase retrieval

3.4.1 General principle of iterative phase retrieval (PR)

In contrast to DH, which is considered as an interferometric method to retrieve the phase information, many non-interferometric methods have been developed over the past decades, especially for the cases where it is impractical to build up an interferometer (such as X-ray diffraction imaging and astronomical imaging). The term "phase retrieval" refers to techniques that recover the phase information mathematically as a solution that matches the diverse diffraction patterns' intensity measurements and the pre-knowledge or constraints, if available. The problem can be solved deterministically or iteratively. The most prominent deterministic method is the transport-of-intensity equation (TIE) introduced by Teague in 1983 that proposed an analytic solution [108]. The PR methods investigated in this thesis are subject to iterative PR, specifically projection-based iterative PR.

The family of projection-based iterative PR was initially introduced by Gerchberg and Saxton in 1972 [109] and generalized by Fienup, namely error reduction (ER) and hybrid input-output (HIO) algorithms in the 1980s [110]. The original Gerchberg-Saxton approach is based on the propagation between two planes with recorded intensities, whereas Fienup's methods are associated with one intensity measurement at the detector plane and the pre-knowledge of the object plane. Miao *et al.* gives a theoretical analysis of the uniqueness of the phase problem in [111]. If each measured intensity has N^2 pixels and the object plane has M^2 unknown pixels to solve, leading to $2M^2$ unknowns in total since they are complex values, the oversampling ratio σ,

$$\sigma \equiv \frac{\text{total number of measured pixels}}{\text{numbers of unknown pixels to solve}} = \frac{N^2}{M^2}, \tag{3.25}$$

should be at least superior to two so that the phase can be correctly retrieved. More data redundancy that leads to $\sigma \gg 2$ is desired to recover the phase robustly in the presence of noise. Besides the fact that *a priori* knowledge on the object plane reduces the number of unknown pixels, another way to increase σ is to take multiple intensity measurements, known as single-beam multiple-intensity reconstruction (SBMIR). The diverse diffraction intensity patterns can be taken at different distances [112] or using multiple wavelengths [113].

Figure 3.6 sketches the recording schema (Fig. 3.6(a)) as well as a typical iterative PR routine (Fig. 3.6(b)). The PR procedure contains the following steps:

1. Initialization of the complex distribution at the object plane $O(x,y,0)$. For example, one can use the square root of the measured intensity to initialize its amplitude and a random distribution for the phase, as shown outside of the iterative loop in Fig. 3.6.

2. Propagation to the detector plane located at d away from the object plane. We propagate the current estimation of the object wavefront $O(x,y,0)$ to the detector plane using, for example, the ASM representation in Eqs. 3.11 and 3.12 or other diffraction propagators such as the Fresnel propagation kernel, to obtain the complex-valued field at the detector plane $O(x,y,\mathrm{d})$.

3. Application of intensity constraints on the detector plane. We replace the computed amplitude of the wavefront $O(x,y,\mathrm{d})$ by the square root of the measured intensity while keeping the phase unchanged. The updated wavefront is denoted as $O'(x,y,\mathrm{d}) = \sqrt{I(x,y,\mathrm{d})}O(x,y,\mathrm{d})/\left|O(x,y,\mathrm{d})\right|$. If multiple intensity measurements are available, we apply these intensity constraints at their corresponding condition. As the example shown here, $O'(x,y,\mathrm{d})$ will be propagated to the other two recording planes and get updated by the recorded intensity accordingly.

4. Back-propagation to the object plane. We back-propagate the updated wavefront $O'(x,y,\mathrm{d})$ to the object plane.

5. Update the object wavefront on the object plane. After the back-propagation, we apply the constraints of the obtained object wavefront, such as the support mask, the positive adsorption, or the sparsity on the object plane to obtain the updated object wavefront $O'(x,y,0)$ on the object plane. The updated object wavefront is ready to be used in the next iteration.

6. iterate steps 2-5 contained in the iterative loops box in Fig. 3.6 until convergence is achieved.

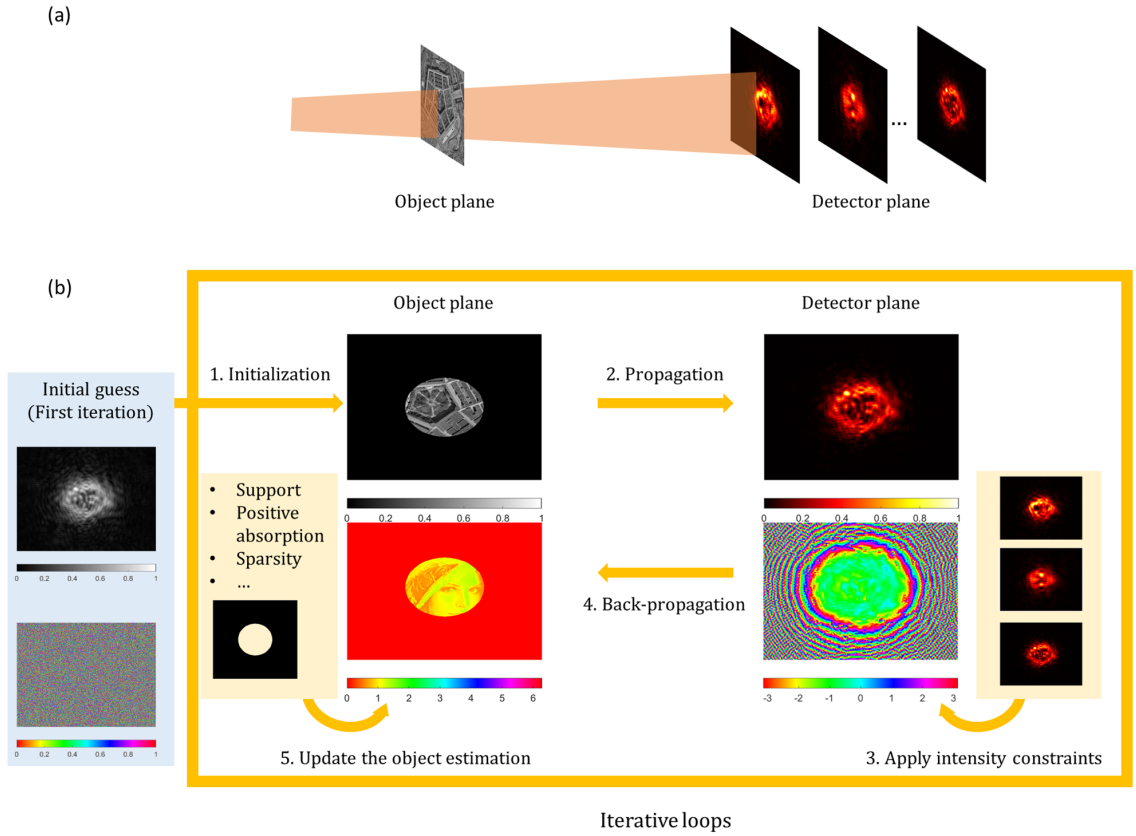

Fig. 3.6 The principle of iterative phase retrieval technique. The recording setup (a) and the reconstruction procedure (b) are given. The different steps during phase retrieval are indicated in the schema. The example illustrated here has three intensity measurements at different recording distances.

3.4.2 Ptychography: a particular type of phase retrieval

3.4.2.1 General description

Ptychography derives from the Greek word *ptycho*, signifying *to fold*. The original concept of ptychography was introduced by Hoppe in 1969 to compute the phase of the Bragg reflections from a periodic crystalline structure [114]. Later works suggested that overlapped coherent illumination spots made it even possible to estimate the phase variation of the non-periodic object. As Hoppe's prediction, nowadays, modern ptychography has been successfully implemented in visible light, x-ray, electron, and extreme ultraviolet (EUV), capable of imaging various types of samples.

Figure 3.7 shows the setup of a basic ptychographic experiment. A coherent beam passes through a pinhole with a radius of r, forming the "probe" $P(x,y,0)$ at the object plane to illuminate a zone of the object $O(x,y,0)$. The wave emerging from the object plane is referred to as the "exit wave". The exit wave can be modeled as $\Psi = O(x,y,0) \cdot P(x,y,0)$ if the object is considered as a thin object, the multiplication approximation holds for this case [115]. The exit wave propagates to the detector plane. A collection of K diffraction patterns $I_k(x,y,\mathrm{d})$, $k = 1...K$ is recorded by scanning the object with a constant step s at K positions. Figure 3.7(b) shows an example of the illumination area of 5×3 scan positions on the object plane. The illumination spots at two consecutive positions are partially overlapped with a linear distance offset o, as depicted in Fig. 3.7(c). We use the definition of normalized overlap ratio given in [116]:

$$\text{overlap ratio} \equiv \frac{\mathrm{o}}{2\mathrm{r}} \times 100\% = (1 - \frac{s}{2r}) \times 100\%. \tag{3.26}$$

The optimum value of the overlap ratio is between 60% to 80% according to [116]. Ptychography can solve the phase problem thanks to the powerful overlap constraint on the object plane, which fold together all the diffraction patterns. Ptychography is a particular scheme of PR methods. Compared to conventional PR techniques, ptychography provides two significant advantages. First off, the scanning recording approach removes the limit on the total dimension of the sample under investigation. The final imaging FOV can be larger than the extent of the detector area. Moreover, the illumination overlap constraints offer strong data redundancy. The phase problem can be more rapidly and robustly solved. Ptychography is even capable of recovering the object function and the illumination function simultaneously. Decoupling the contribution of illumination waves is highly beneficial for the cases where uniform illumination is hard to achieve, just as when imaging with coherent THz radiation.

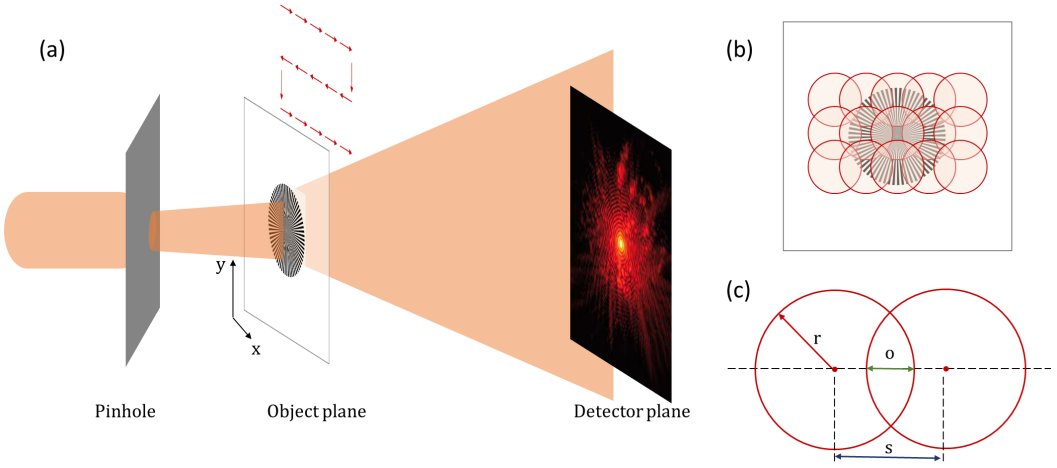

Fig. 3.7 (a) depicts the setup of ptychography. The object is moved on the x and y direction that perpendicular to the propagation direction, illuminated by the probe beam. The diffraction patterns $I_k(x, y, \mathrm{d})$ are captured on the detector plane. (b) shows the overlapped illuminated area. (c) illustrates the notion of overlap rate at two scanning positions.

Although a few proof-of-concept examples of ptychography reconstruction have been demonstrated in the 1990s, they primarily relied on the direct inversion such as Wigner Distribution Deconvolution (WDD) [117], which requires a large quantity of data. It is expected that these methods did not get promoted widely due to the computation capacities at that time. The widespread adoption of ptychography occurred only after the first iterative algorithm, ptychographic iterative engine (PIE), was proposed in 2004 by Faulkner and Rodenburg [118, 119]. PIE requires a well-characterized and coherent probe distribution and knowledge of translation steps. In 2008, Thibault *et al.* demonstrated the possibility of reconstructing the object and probe simultaneously from the ptychographic data with a difference map (DM) algorithm [115]. The probe recovery alleviated the reconstruction artifacts due to inaccurate probe information. In 2009, Maiden and Rodenburg published the extended ptychographic iterative engine (ePIE), which extended the PIE method to find the solution for probe simultaneously [120]. DM projects the whole data of all positions at once to update the object and probe functions, whereas the PIE family algorithms update the two functions gradually, one position after another. DM and ePIE remain the most widely used reconstruction methods. Since their discovery, different ptychography algorithms have been developed to better accommodate the recording condition, including mixed-state ptychography for partial coherent illumination [121–123], correction of translation errors [124–126], and multi-slice model 3PIE for thick sample reconstruction [127]. An exhaustive survey about ptychography, covering the principle, common algorithms,

and the state-of-art implementations, can be found in the recent-published book chapter [128].

3.4.2.2 Extended ptychographic iterative engine (ePIE) algorithm

Hereby we describe the ePIE algorithm that will be used in this thesis. The flowchart of the ePIE algorithm is given in Fig. 3.8.

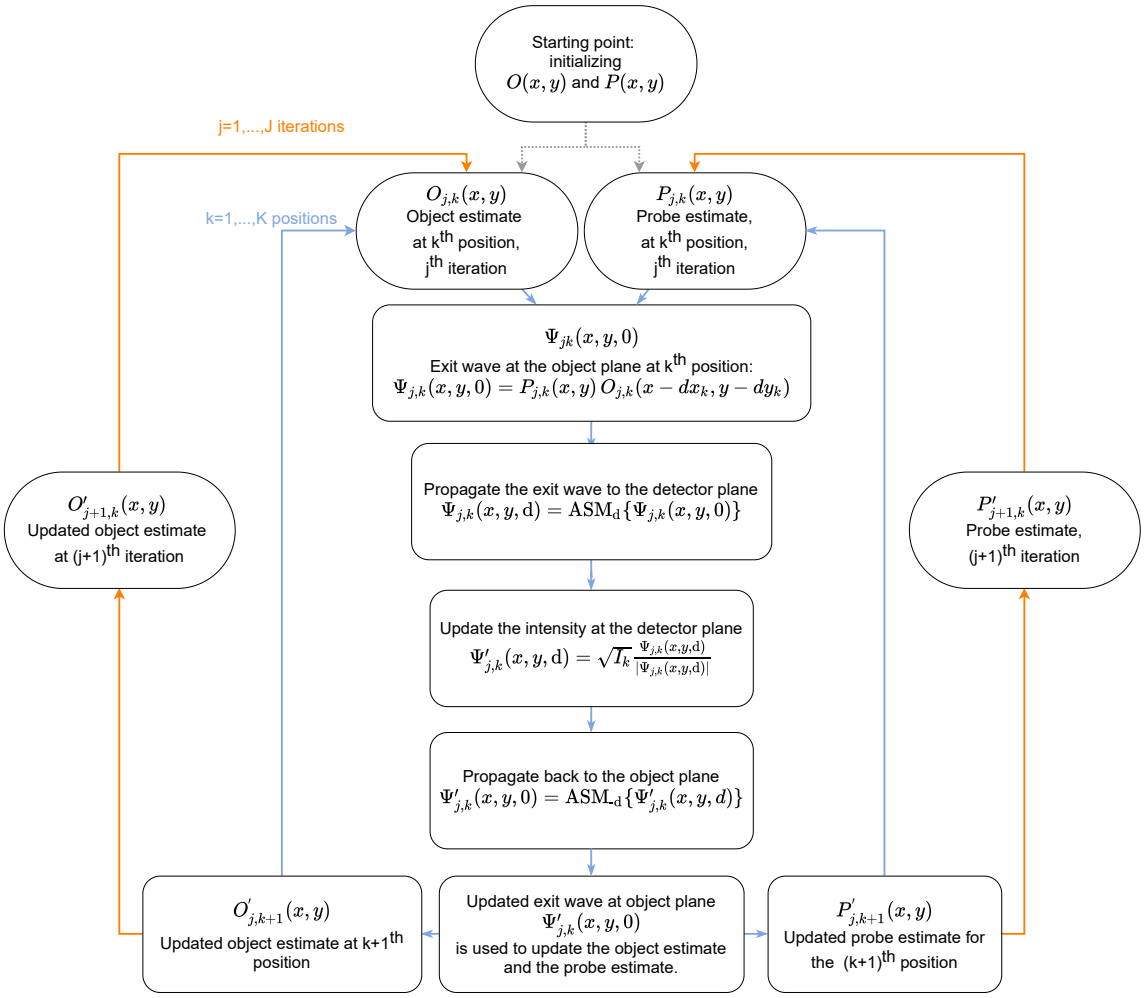

Fig. 3.8 The flowchart of ePIE algorithm. The inner loop (marked with blue arrows) represents the update at each scan location. The outer loop (marked with orange arrows) is the iterative loop.

We initialize the complex-valued object transmission function $O(x,y,0)$ and the probe $P(x,y,0)$ prior to the first iteration. The first step of ePIE is to model the exit wave at the k^{th}

position at the object plane $O_{j,k}(x,y,0)$ is obtained by multiplying the probe and the shifted object:

$$\Psi_{j,k}(x,y) = P_{j,k}(x,y)O_{j,k}\left(x-dx_k, y-dy_k\right), \tag{3.27}$$

where (dx_k, dy_k) with $k = 1,\cdots,K$ refer to the scanning displacement of the object during the recording. The z component, which represents the propagation, is omitted in Eq. 3.27. The validity of Eq. 3.27 is guaranteed by the thin object approximation. Similar to the iterative PR scheme, we propagate the exit wave to the detector plane located d away from the object plane using ASM representation in Eqs. 3.11 and 3.12 (denoted as operator $\mathrm{ASM_d}$), obtaining its complex distribution at the detector plane:

$$\Psi_{j,k}(x,y,\mathrm{d}) = \mathrm{ASM_d}\left\{\Psi_{j,k}(x,y,0)\right\}. \tag{3.28}$$

We apply intensity constraint on $\Psi_{j,k}(x,y,\mathrm{d})$ to update its amplitude by the measured intensity $\sqrt{I_k}$:

$$\Psi'_{j,k}(x,y,\mathrm{d}) = \sqrt{I_k}\frac{\Psi_{j,k}(x,y,\mathrm{d})}{\left|\Psi_{j,k}(x,y,\mathrm{d})\right|}. \tag{3.29}$$

The updated wavefront at the detector plane $\Psi'_{j,k}(x,y,\mathrm{d})$ is then back propagated to the object plane, yielding the updated exit wave function $\Psi'_{j,k}(x,y,0)$:

$$\Psi'_{j,k}(x,y,0) = \mathrm{ASM_{-d}}\left\{\Psi'_{j,k}(x,y,d)\right\}. \tag{3.30}$$

The object and probe function estimates to be used for the next position $k+1$ are updated using the difference between the original and updated exit functions at the object plane $\Psi'_{j,k}(x,y) - \Psi_{j,k}(x,y)$, the component z is omitted. An update of the object function at the illuminated area can be written as:

$$\begin{aligned} O'_{j,k+1}\left(x-dx_k, y-dy_k\right) &= O_{j,k}\left(x-dx_k, y-dy_k\right) \\ &+\alpha\frac{P^*_{j,k}(x,y)}{\left|P_{j,k}(x,y)\right|^2_{\max}}\left[\Psi'_{j,k}(x,y) - \Psi_{j,k}(x,y)\right], \end{aligned} \tag{3.31}$$

where $\alpha \in [0,1]$ tunes the step-size of the update. In [129], the authors gave three ways of proofing the update mechanism. Since the roles of the object function and the probe function in forming the exit wave are equal, the exit wave would remain the same if we reversed the probe function and the object function. Therefore we update the probe function in the same way by swapping the roles of probe and object functions in Eq. 3.31 with $\beta \in [0,1]$ as the

weight parameter:

$$P'_{j,k+1}(x,y) = P_{j,k}(x,y) + \beta \frac{O^*_{j,k}(x-dx_k, y-dy_k)}{\left|O_{j,k}(x-dx_k, y-dy_k)\right|^2_{\max}} \left[\Psi'_{j,k}(x,y) - \Psi_{j,k}(x,y)\right]. \quad (3.32)$$

The updated object function $O'_{j,k+1}(x,y)$ and the probe function $P'_{j,k+1}(x,y)$ are ready to be used for the next position $k+1$. We repeat the procedure for all the K positions to accomplish one iteration, as shown in the inner loop in Fig. 3.8. The algorithm terminates when J iterations are executed, or the convergence is achieved.

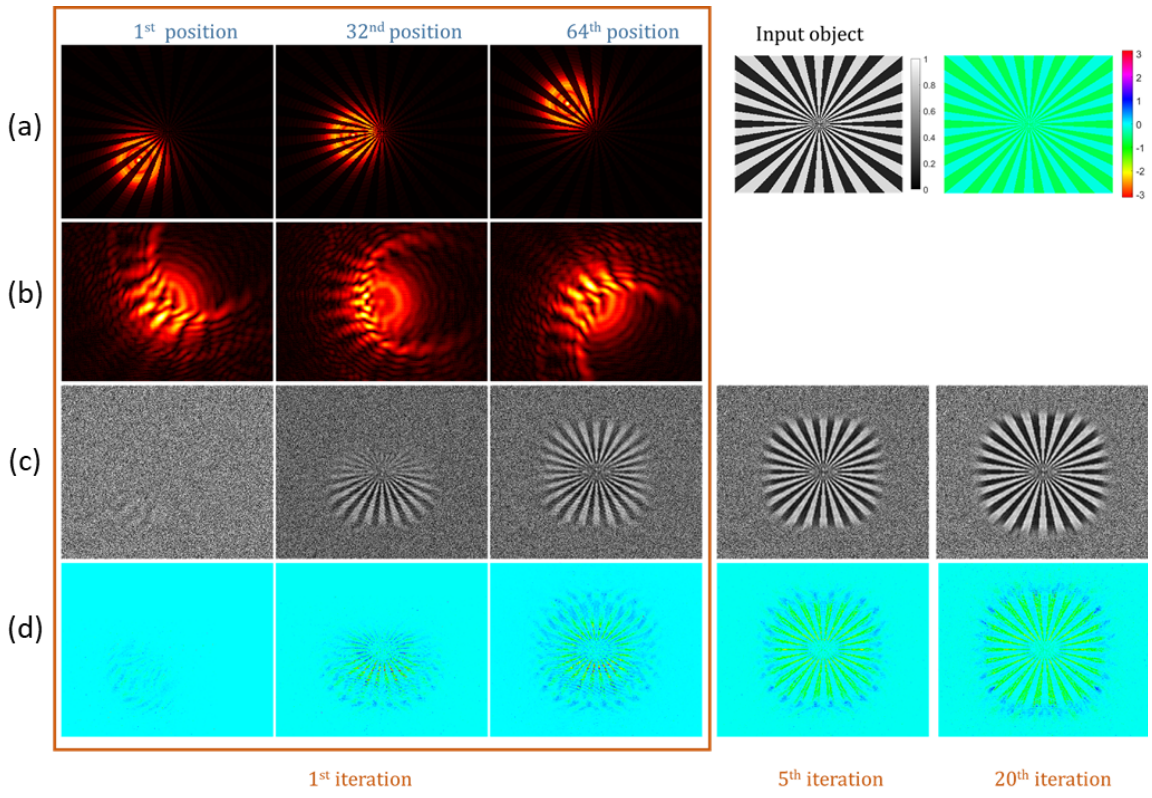

Fig. 3.9 The evolution of ePIE reconstruction is shown via simulation. The reconstruction at three different positions during the first iteration is exhibited. In the box that illustrates the first iteration, row (a) is the simulated exit wave at each position. Row (b) gives the recorded diffraction patterns at the corresponding positions. Rows (c) and (d) are the reconstructed amplitude and phase. The reconstructed amplitude and phase after the 5th and the 20th iterations are given.

Figure 3.9 illustrates the evolution of the ePIE reconstruction via simulating the process with a known input image scanned at 8×8 positions with an overlap of 86%. We observe

that the information of the object wavefront is gradually completed one position after another in the first iteration. The reconstruction is further improved after iterations until convergence is achieved. After 20 iterations, decent imaging quality is already achieved for both the amplitude and the phase. The efficient recovery rate confirms the benefit of the high data redundancy in ptychography.

3.5 THz coherent lensless imaging: state-of-the-art

The coherent lensless imaging techniques, from the well-established DH to versatile PR strategies, have been migrated progressively towards the THz range in the last two decades. The first development of coherent lensless imaging techniques with THz radiation originated from sub-THz. Dated back to 2004, an off-axis THz digital hologram was recorded with a 100 GHz Gunn diode oscillator, and a single-point SBD detector [130]. In 2008, Tamminen *et al.* proposed a THz reflective off-axis DH setup using a vector network analyzer as transmitter and receiver at 310 GHz to image a metallic target placed 1.5 m away from the detector [131]. In 2010, Cull *et al.* built a Gabor in-line DH system at 100 GHz [132]. The reconstruction algorithm for twin-image elimination was based on compressive sensing. In 2011, Heimbeck *et al.* realized THz off-axis DH with a tunable frequency-multiplied microwave synthesizer and an SBD single-point detector in the range 0.66-0.76 THz [133]. The frequency tunability of the THz source allowed them to apply the well-known dual-wavelength approach to eliminate the 2π phase ambiguity problem.

Full-field imaging was the inevitable trend for THz DH and other possible coherent lensless imaging techniques. However, in the sub-THz range, the long-wavelength requires very large 2D arrays with adequate sensitivity for sub-THz radiation [134]. Although the company Terasense has recently released a 1D linear camera with a pitch of 0.5 mm working at 300 GHz, making it a promising candidate, its sensitivity and performance for DH recording have not been studied. Sub-THz DH is still realized with a single-pixel detector until now. On the other hand, despite the selective penetration ability in the FIR range, which limits the further application, the band is more suitable for investigating emerging coherent lensless imaging techniques with commercially available 2D thermal FPA arrays in single-shot without tedious raster-scanning using a single-point detector. In 2011, Ding *et al.* reported the first full-field THz coherent lensless imaging: an off-axis THz DH setup with a FIRL laser and a pyroelectric camera at 2.52 THz with a lateral resolution of 3.4λ [135]. The first THz

in-line DH was performed in 2012 by the same research group [136]. The compactness of the in-line DH (shorter recording distance) configuration increased the resolution (1.7λ) by a factor of 2 compared to the off-axis configuration. Since this first successful demonstration, the THz coherent lensless imaging has become an active research area. Thermal FPAs paired with FIR CW sources (pyroelectric cameras or uncooled microbolometers paired with QCLs or FIRL lasers)[1] became the mainstream equipment for investigating full-field THz coherent lensless imaging techniques.

After the above proof-of-concept demonstrations, THz DH's development devoted itself to further improving the imaging performance. In terms of DH recording, besides minimizing recording distance for resolution enhancement, the synthetic aperture (SA) technique was successfully implemented with both off-axis [137, 138] and in-line configuration [139, 140], making up for the insufficient size of THz detectors. Phase-shifting DH, a well-known strategy in the DH community, has been implemented with THz off-axis DH [137, 141, 142]. Since the FOV of THz DH reconstruction is limited to the detector size, moving the reflective object during recording and stitching the reconstructed results together, have been proposed for observing objects larger than the size of a detector [143, 144]. For in-line THz DH, efforts have been mainly made on reconstruction algorithms towards better reconstruction quality. For twin-image suppression, besides the widely-used iterative PR method based on the absorption constraint [145], L1-sparsity constraint has been added to the object plane to enforce the *a priori* knowledge [146]. Moreover, in [146], the working wavelength was at 57.25 μm. The recording distance was minimized to 3 mm, yielding a NA up to 0.87. A sub-wavelength resolution of 40 μm (0.7λ) was achieved. It was the best resolution of THz DH to date. As a post-processing method, self-extrapolation estimates numerically the high-frequency information that was not measured due to the finite size of the detector. Support constraint on the object plane is used to guarantee the fidelity of the estimation. It is an effective tool in many in-line THz DH cases. Finer details can be resolved [145, 147]. However, distinguished from the SA method for resolution enhancing, self-extrapolation's estimation remains a guessed solution, depending to a significant extent on the applied constraint deduced from the nature of the object under investigation. In addition, denoising [148] and auto-focusing algorithms were investigated in the context of THz in-line DH [149]. The concept of data redundancy originated from PR contributes to THz DH. Two-intensity in-line DH was demonstrated in [150]. In our development published in [22], PR is a tool to

[1]The output of QCL and various FIRL lines are at mW level, pyroelectric cameras are not sensible enough, uncooled microbolometers are needed.

enhance the performance of off-axis DH reconstruction results.

As the imaging ability is maturing, THz DH has been gradually carried out towards application. Similar to visible wavelengths, due to the specificity of the setup, in-line THz DH was solely implemented in digital holographic microscopy (DHM) fashion for biomedical applications, seeing through sparse samples. The testing samples have transitioned from dehydrated insect specimens to cancerous tissue. In [151], the reconstruction of a human hepatocellular carcinoma tissue slice (Fig. 3.10(a)) proved that early signs of liver cancer and diseases could be traced using THz in-line DH. The reconstructed phase after resolution enhancement revealed a sign of tissue fibrosis, *i.e.*, , the blue arrow in the phase map in Fig. 3.10(c), making THz in-line DH a promising tool for cancer diagnosis. Off-axis THz DH offers a wider choice of samples, thus more application scenarios, thanks to the independent reference wave. The samples can be measured in both transmission and reflection modes. In transmission mode, the thickness measurement of optically opaque materials at FIR range was carried out in [141] and [22]. In the sub-THz range, visualizing the void in a 3D-printed sample has been demonstrated at 0.495 THz in [103, 152]. A depth of 45 μm was clearly distinguished from the phase image shown in Fig. 3.11. On the other hand, imaging concealed objects using off-axis DH under reflection mode paves the way for applications in non-destructive inspections. In [153, 143], real-time imaging of moving metallic objects hidden by a thin yet rigid plate made of optically opaque yet highly transparent polymers (PE or PP) has been successfully demonstrated, as shown in Fig. 3.12(c)-(d). However, despite the encouraging results, the perturbation caused by the interaction between complex cover materials and the samples still needs to be tackled before meeting the challenge of real-world industrial inspection applications. Moreover, the reflectivity and the transmittance of both the imaging targets, as well as the cover materials, are important concerns that have a significant impact on imaging results [154].

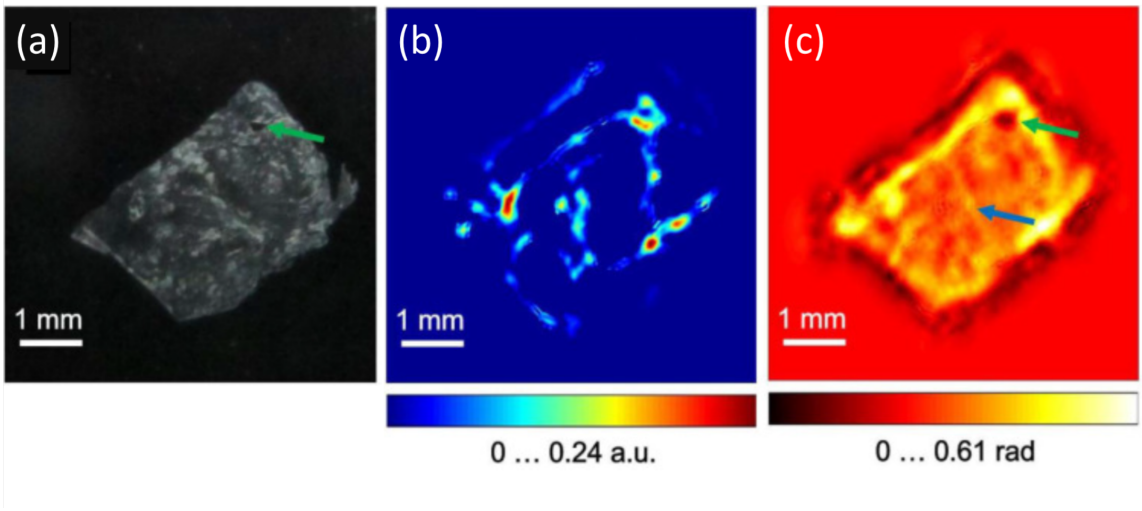

Fig. 3.10 THz in-line digital holographic reconstructions from [151]. (a) Photograph of the object, a human hepatocellular carcinoma tissue; (b) reconstructed absorption and (c) phase shift after numerically extrapolating the holograms recorded via sub-pixel registration method. The green arrow indicates a cut across a vessel or a region damaged after freezing the tissue. The blue arrow indicates a vertical line which is a sign of tissue fibrosis.

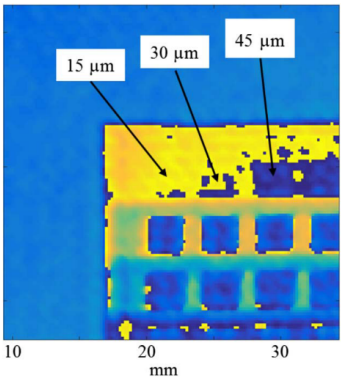

Fig. 3.11 The reconstructed phase of 0.495 THz DH adapted from [152]. The voids are identified.

The first THz ptychography in transmission mode was successfully implemented in 2018 [23]. A lateral resolution of about 2λ and a depth resolution of $\lambda/30$ were obtained. By virtue of its compact geometry, large FOV, and the ability to separate the incident wavefront and the object contribution, THz ptychography has the potential to conquer certain limitations in THz DH. In the meantime, topics that improve THz ptychography, such as probe-position correction, multi-layered ptychography via 3PIE, reflective THz ptychography, and resolution enhancement, have been studied [24, 155–157]. Recently, THz ptychography

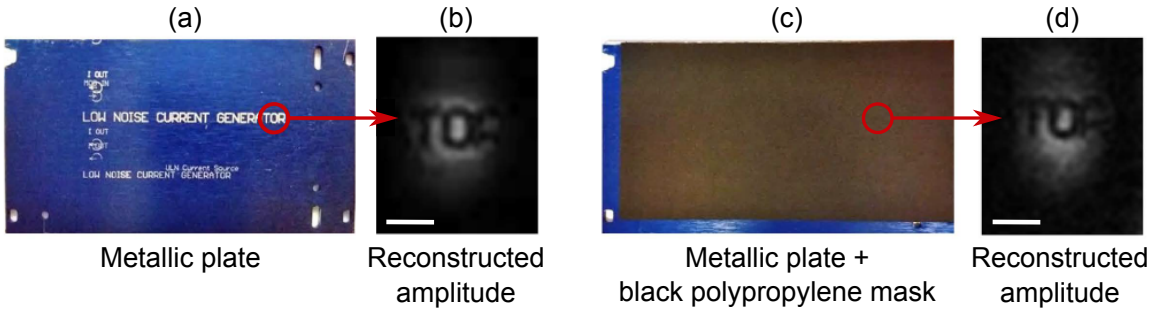

Fig. 3.12 Real-time imaging concealed object using reflective off-axis THz DH from [153]. (a) Photograph of the object, a metallic plate with inscription; (b) reconstructed amplitude of the object at one position during its movement; (c) photograph of the plate covered by polypropylene mask; (d) reconstructed amplitude of the hidden object at the same position as in (b). Scale bar: 4 mm.

has been implemented in the sub-THz range at 0.1 THz with a single-point detector. A long-distance diffraction-free beam generated by multiple cascaded lens–axicon doublets was used as the probe beam [158].

3.6 Chapter summary

Free-space propagation of THz radiation and retrieving the lost phase information are the two key elements of THz coherent lensless imaging. In this chapter, we have revisited the fundamental of scalar diffraction theory, deducing the appropriate formula for THz wave propagation: the ASM representation. We have analyzed some specific features when implementing THz lensless imaging techniques. The impact of large wavelengths on lateral resolution remains valid for all the lensless imaging techniques. It was taken into consideration in the later implementations. We have detailed the interferometric DH and non-interferometric PR approaches. Finally, we have reviewed the imaging techniques that have been implemented with THz radiations. We have witnessed the progress of THz coherent lensless imaging techniques and their attempt toward applications. We will study THz DH combined with the PR techniques and THz ptychography in the following chapters.

Chapter 4

Investigating Terahertz digital holography

Digital holography is the first lensless imaging technique we investigate with the THz radiation. This chapter introduces an iterative PR scheme inspired by the in-line DH, which makes full use of a recorded object intensity to further improve the off-axis DH reconstruction results. We carry out some numerical simulations to demonstrate the benefit of the proposed method. Experimentally, we start by developing THz DH in the FIR range (at 2.52 THz) using the available equipment at CSL. As indicated in Chapter 2, FIR radiation has limited penetration ability for many materials; hence it is advantageous to develop imaging systems in the sub-THz range for NDT applications. Thus we investigate THz DH in the sub-THz range. There are fewer 2D detector arrays that are suitable for sub-THz imaging. The THz FET detectors based on plasma wave's reification show fast response and high sensitivity at room temperature. Moreover, they can be easily and cost-efficiently integrated into arrays, making them good candidates. Finally, we build a proof-of-concept THz DH setup at 280 GHz by raster-scanning a single-point THz FET detector developed by the laboratory CENTERA in Warsaw, Poland. Both setups validate the effectiveness of the proposed iterative PR method.

Table of contents

4.1 Particular concerns about off-axis THz DH recording

We have introduced the principle of Gabor in-line DH and off-axis DH, respectively, in Chapter 3. Both techniques have been demonstrated with THz radiation. The published works showed that the compactness of in-line configuration offers higher lateral resolution thanks to the short recording distance, according to Eq. 3.15. However, the in-line configuration is restrictive to the choice of samples. The sample should be much smaller than the incident beam to allow passing through the reference wave. Furthermore, the PR method for twin image elimination in in-line DH can be challenging for objects with strong phase variation, although it can efficiently suppress the twin image when a sparse object is located in the free space. Therefore, the in-line DH is only suitable for investigating microscopic samples. On the other hand, the off-axis DH configuration is more flexible that can be applied in various study cases since a separated tilted reference wave is employed. Both transmission and reflection mode DH can be developed under the off-axis configuration. The off-axis DH offers a more reliable reconstruction despite the nature of the sample under investigation. For

these reasons, the off-axis DH configuration is our preferred choice.

We discussed the choice of the off-axis angle in Section 3.3.2. The limitation of the maximum off-axis angle determined by Eq. 3.24 is very loose in THz DH setups since the relationship $\lambda/(4\Delta) > 1$ holds. Therefore the reference wave can be injected with a large incident angle. Moreover, the recording distance should be minimized to achieve better lateral resolution according to Section 3.2.1. Injecting the reference wave with a large incident angle instead of using a beam combiner is a more appropriate choice. On the other hand, the off-axis angle should be large enough to well separate different orders in Eq. 3.21 in the spectrum plane. As depicted in Fig. 4.1, if the bandwidth of the object wave is $B = 2/\delta$ with δ as the smallest smallest resolvable object detail, the autocorrelation term $\mathscr{F}\left\{O^2\right\}$ has a bandwidth of 2B. With a given off-axis angle θ, the separable bandwidth is limited to

$$B \leq \frac{2\sin\theta}{3\lambda}, \tag{4.1}$$

which limits the attainable resolution for the given object size. If we can get ride of the autocorrelation term $\mathscr{F}\left\{O^2\right\}$, the limitation is relaxed to

$$B \leq \frac{2\sin\theta}{\lambda}. \tag{4.2}$$

We conclude that subtracting the object wave intensity I_O from the hologram I_H will avoid the spectral overlap caused by the autocorrelation term, achieving better imaging quality.

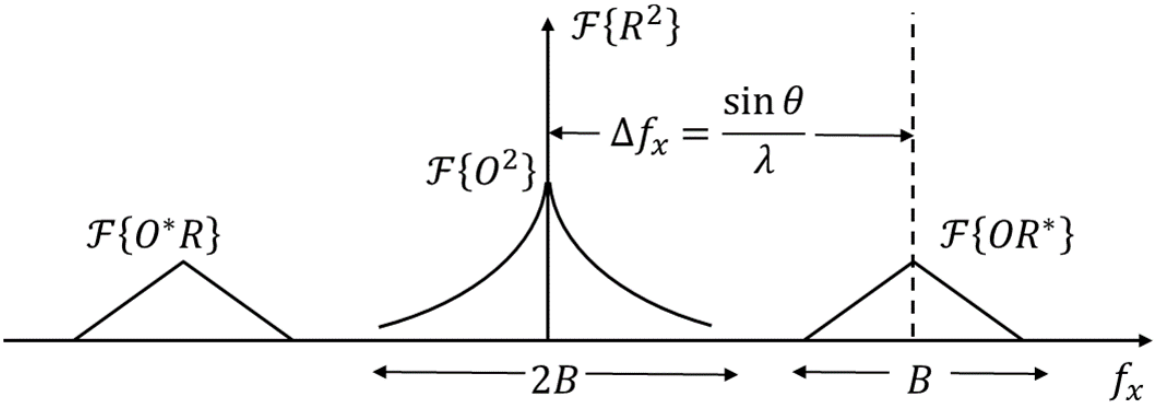

Fig. 4.1 1D spectrum of the off-axis hologram.

Another concern is the thermal background. When the THz holograms are recorded with thermal THz detectors, both the recorded hologram and the object intensity also contain the incoherent infrared emission $I_{thermal}$ originated from the environment, the detector, and the object placed just in front of the detector. The subtraction allows to eliminate the recorded thermal background:

$$I_H - I_O = (H + I_{\text{thermal}}) - \left(|O|^2 + I_{\text{thermal}}\right) = |R|^2 + OR^* + O^*R. \tag{4.3}$$

4.2 Phase retrieval assisted off-axis DH reconstruction

Attempts to combine off-axis and in-line configurations have been carried out at X-ray [159] and visible wavelengths [160]. These works have shown that the off-axis DH offers a more reliable reconstruction, especially for the low-frequency components, while the in-line DH improves the resolution. Hence the overall image quality is improved thanks to the hybrid approach. In our implementation, we attempt to improve the off-axis THz DH reconstruction with the iterative PR routine. The object diffraction intensity I_O recorded without the reference beam serves as the intensity constraint at the recording plane.

We propose an iterative PR routine based on the back and forth projection as explained in Section 3.4. On the object plane, we assume that the object is illuminated by unitary intensity. The algorithm proceeds as follows:

Step 1 We compute the wavefront distribution using the processed off-axis hologram $I_H - I_O$ to retrieve the normalized wavefront distribution in the object plane: $O_{\text{o,off}} = a_{\text{o,off}} \exp(i\phi_{\text{o,off}})$. $O_{\text{o,off}}$ serves as the initial guess in the object plane.

Step 2 Propagate O_{o} to the detector plane using ASM representation in Eqs. 3.11 and 3.12, forming the complex wavefront distribution $O_{\text{d}} = a_{\text{d}} \exp(i\phi_{\text{d}})$.

Step 3 Update the wavefront in the detector plane. The square root of the normalized object intensity $\sqrt{I_O}$ is used to replace a_{d} while the phase ϕ_{d} is kept: $O_{\text{d,update}} = \sqrt{I_O} \exp(i\phi_{\text{d}})$.

Step 4 Propagate $O_{\text{d,update}}$ back to the object plane, forming the updated object wavefront O_{o}. Positive absorption and non-negativities constraints can be applied on the obtained amplitude a_{o} if the object is small to further constrain the PR process [106]: $a_{\text{o}}(a_{\text{o}} > 1) = 1$ and $a_{\text{o}}(a_{\text{o}} < 0) = 0$. The phase remains unchanged.

Step 5 Repeat steps 2-4 until convergence is achieved.

4.3 Apodization for aperture diffraction effect elimination

In coherent imaging systems, the edge of the aperture induces the ringing effects on the edge. The ringing effect also occurs during DH. Digital holographic reconstruction performs the propagation numerically with the 2D discrete Fourier transformations. Due to the finite size of the detector aperture, the border points on the recorded hologram cause the ringing oscillation artifact on the reconstructed image after the numerical propagation [161]. The horizontal and vertical lines shown in Fig. 4.2(a) and Fig. 4.2(b) represent this effect at both visible wavelength and THz wavelength. The effect becomes more important with the increase of wavelength.

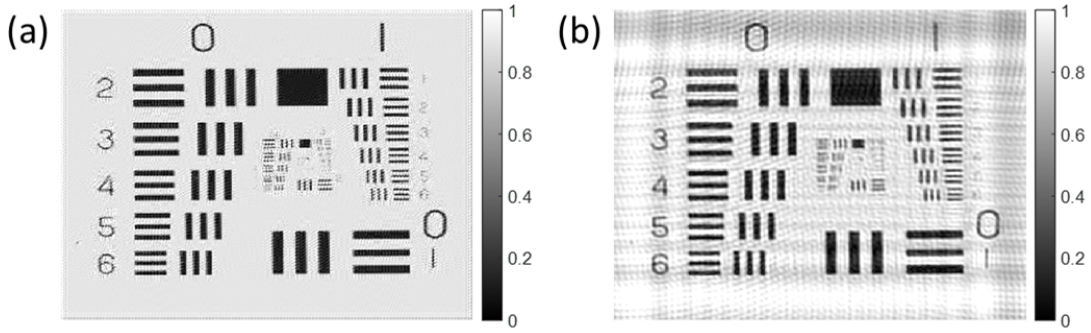

Fig. 4.2 Illustration of the osculation artifacts due to the aperture truncation at (a) 653 nm and (b) 118.83 μm.

An apodization processing can efficiently suppress the unwanted artifact [162]. To perform the apodization, a 2D window that smoothly vanishes towards the border is multiplied to the recorded intensity. In this thesis, we applied the apodization processing with a 2D Tukey window: $W(x,y) = W(x)W(y)$. The 1D Tukey window $W(m)$ is written as:

$$W(m) = \begin{cases} \frac{1}{2}\left\{1+\cos\left(\frac{2\pi}{r}\left[\frac{m-1}{M-1}-r/2\right]\right)\right\}, 0 \le m < \frac{r}{2}(M-1) \\ 1, \frac{r}{2}(M-1) \le m < (M-1)\left(1-\frac{r}{2}\right) \\ \frac{1}{2}\left\{1+\cos\left(\frac{2\pi}{r}\left[1-\frac{m-1}{M-1}-r/2\right]\right)\right\}, (M-1)\left(1-\frac{r}{2}\right) \le m < M \end{cases} \tag{4.4}$$

The parameter r controls the size of the vignetting area. In our work, we set r to 0.5 after a trail and error selection.

4.4 Simulation analysis

4.4.1 General description of the simulation analysis and performance matrix

We carried out a series of simulations to demonstrate the benefit of the proposed scheme: the combination of off-axis reconstruction with the iterative PR method. We simulated different off-axis holograms with an off-axis angle of 45° in both the x and y directions. Other parameters used in the simulation (wavelength, camera parameters, and recording distance) respect the 2.52 THz experimental configuration described in Section 4.5.1. To evaluate the performance, we compare the reconstructed results with the input image used for simulation. We define the root-mean-squared-error (RMSE) between the reconstructed value at k^{th} iteration $O_{rec}^{k}(m,n)$ and the input value $O_{simu}(m,n)$ to quantitatively monitor the reconstruction error. We have

$$RMSE_A{}^k = \left\{ \frac{1}{M \times N} \sum_{\substack{m=1\cdots M \\ m=1\cdots N}} \left| |O_{rec}^{k}(m,n)| - |O_{simu}(m,n)| \right|^2 \right\}^{0.5} \tag{4.5}$$

for amplitude comparison and

$$RMSE_P{}^k = \left\{ \frac{1}{M \times N} \sum_{\substack{m=1\cdots M \\ m=1\cdots N}} \left| \arg(O_{rec}^{k}(m,n)) - \arg\left(O_{simu}(m,n)\right) \right|^2 \right\}^{0.5} \tag{4.6}$$

for phase comparison. A lower RMSE value indicates a higher similarity. In the mean time, we employ the structural similarity index (SSIM) to evaluate the perceptual similarity between the reconstructed images and the original ones [44,45]. The SSIM between image x and y is written as:

$$\mathrm{SSIM}(x,y) = \frac{(2\mu_x\mu_y + C_1)(2\sigma_{xy} + C_2)}{\left(\mu_x^2 + \mu_y^2 + C_1\right)\left(\sigma_x^2 + \sigma_y^2 + C_2\right)}, \tag{4.7}$$

where μ_x, μ_y, σ_x, σ_y and σ_{xy} are the local means, standard deviations, and cross-covariance of images x and y. $C_1 = (0.01 \times L)^2$ and $C_2 = (0.03 \times L)^2$ are two parameters that are related to L, the dynamic range of investigated images. SSIM ranges between [0,1]. A higher SSIM value represents a better similarity between the reconstructed image and the original data.

4.4.2 Simulation of cases where in-line DH reconstruction struggles

As indicated in Chapter 3, one needs a sufficiently small object to record a Gabor in-line DH. We simulated some cases where the requirement for Gabor in-line DH configuration is not met. The first example is a pure amplitude object, as shown in Fig. 4.3. The amplitude distribution of the simulated object is a negative USAF resolution target (Fig. 4.3(a)). Its value is between [0,1] after normalization with the arbitrary unit. The phase is set to zero. The recorded object wave intensity and off-axis hologram are shown in Fig. 4.3(b) and Fig. 4.3(c), respectively. The recorded object wave intensity is not a Gabor in-line hologram because there is not enough reference wave from the background that passes through to interfere with the object. Consequently, reconstructing Fig. 4.3(b) with iterative PR without additional information fails. Fig. 4.3(d) shows the reconstruction result after 50 iterations. It gives RMSE=0.18 and SSIM=0.35. Figure 4.3(e) gives the off-axis reconstruction with RMSE=0.09 and SSIM=0.61. The object wave intensity has been subtracted from the hologram before reconstruction. Periodic patterns remain in Fig. 4.3(e). Filtering the spectrum with a smaller filter will eliminate this phenomenon at the price of lowering the resolution of the reconstructed image. The reconstruction using the proposed method is shown in Fig. 4.3(f) with RMSE=0.06 and SSIM=0.73 at the 50th iteration. The image quality is improved.

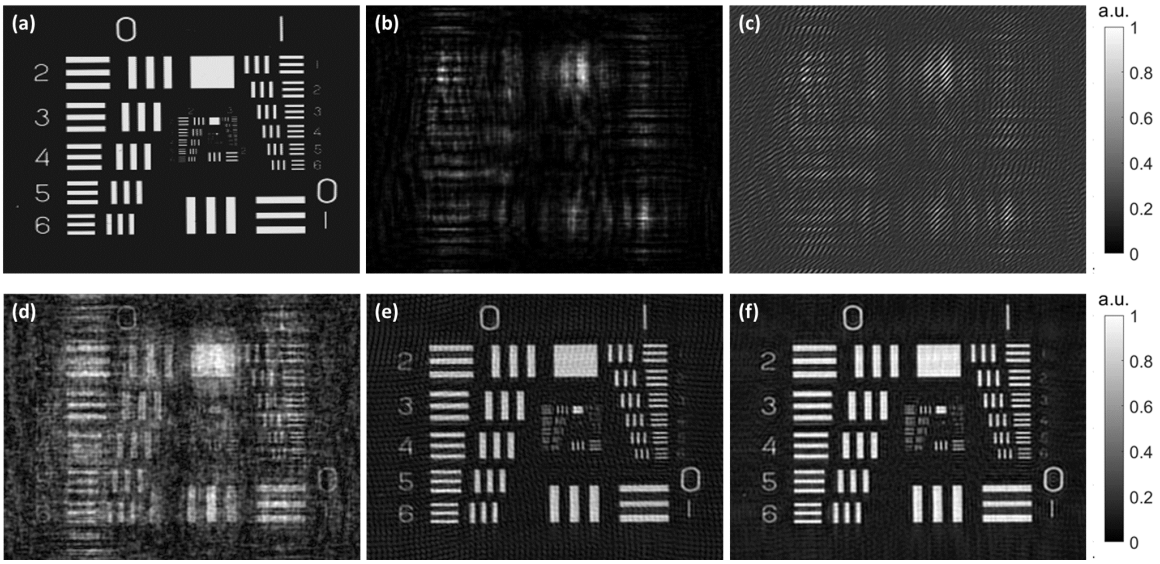

Fig. 4.3 Simulation of a pure amplitude object. (a) is the amplitude distribution of the simulated object. (b) and (a) are the object intensity and off-axis hologram, respectively. (d) shows the conventional in-line reconstruction after 50 iterations. (e) shows the off-axis reconstruction and (f) shows the reconstruction using the proposed method after 50 iterations.

The spectra of the object intensity and the hologram are given in Fig. 4.4(a) and Fig. 4.4(b). The overlap of different orders exists despite the fact that large off-axis angles are employed. Therefore, subtracting the object intensity from the hologram is necessary. The spectra of off-axis only reconstruction and the proposed method are given in Fig. 4.4(c) and Fig. 4.4(d). The elimination of artifacts and the completion of the spectrum can be observed by comparing Fig. 4.4(c) and Fig. 4.4(d). Figure. 4.5 plots the RSME to observe the convergence behavior. The RMSE decreases quickly. The difference of RMSE between the seventh and the eighth iteration in Fig. 4.5 is less than 0.001, indicating the convergence has already been achieved. The convergence rate is faster compared to conventional PR approaches reconstruction thanks to the initial guess that is close to the actual distribution offered by off-axis DH reconstruction.

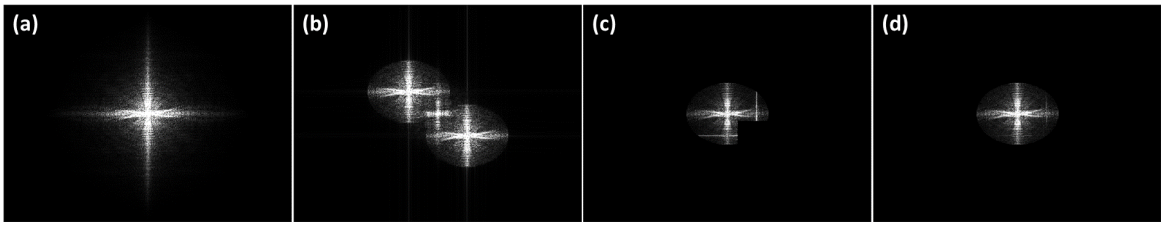

Fig. 4.4 (a) Spectrum of the object wave intensity. (b) spectrum of the off-axis hologram. (c) spectrum of the reconstructed object using off-axis spectrum filtering. (d) spectrum of the reconstructed object using the proposed method.

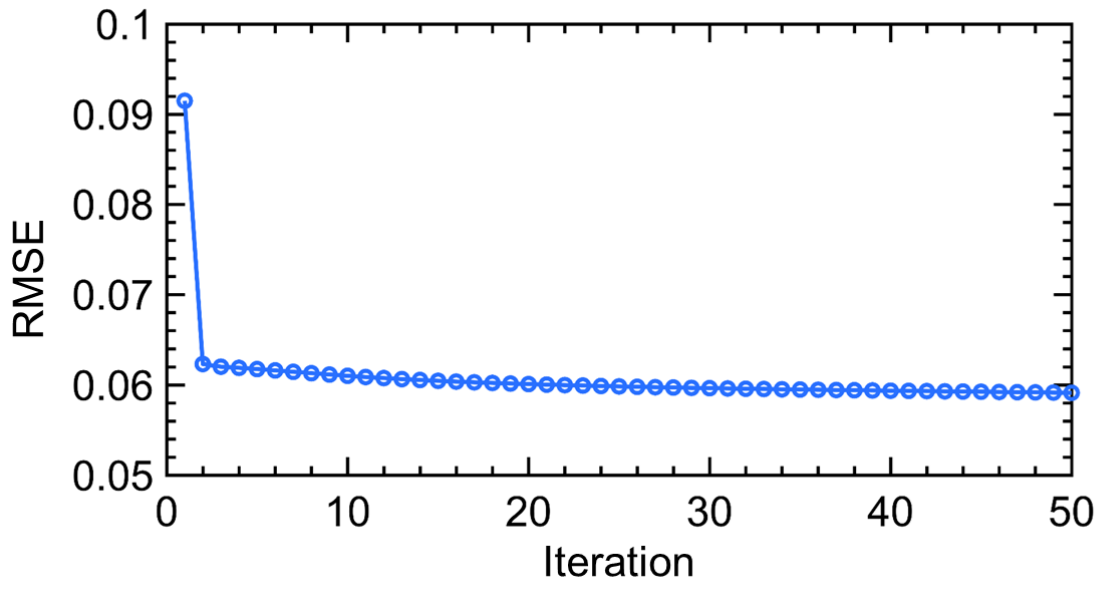

Fig. 4.5 RMSE evolution of the iterative PR with the simulated data.

The simulation of a pure phase object is performed in a similar way as shown in Fig. 4.6. The amplitude distribution of the simulated object is set to 1. The phase distribution is a *Pentagon* picture normalized to $[0, \pi]$, shown in Fig. 4.6(a). The recorded object intensity and the hologram are shown in Fig. 4.6(b) and Fig. 4.6(c).

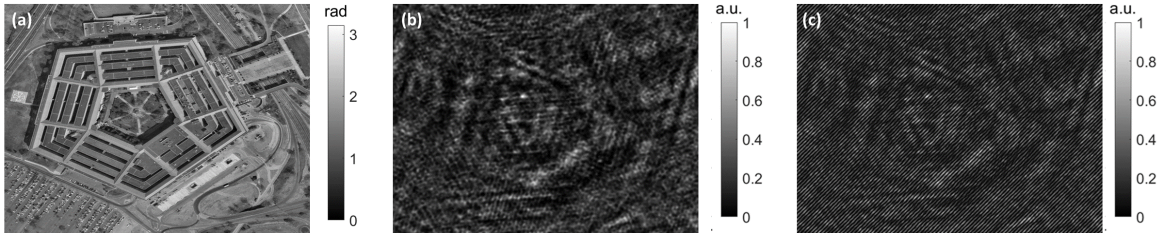

Fig. 4.6 Simulation of the pure phase object: (a) the phase distribution of the simulated object (b) the object intensity and (c) the off-axis hologram.

The reconstruction results, *i.e.*, the phase distribution obtained from the in-line PR, the off-axis reconstruction, and the proposed method, are shown in Fig. 4.7. The in-line PR method has difficulties in the reconstruction of the pure phase object. The retrieved phase value is not reliable, with RMSE=1.35 and SSIM=0.11. The mismatch between the reconstructed phase and the original data can be easily observed in Fig. 4.7(a). Compared to the off-axis reconstruction in Fig. 4.7(b) with RMSE=0.33 and SSIM=0.41, the proposed method shown in Fig. 4.7(c) gives a better-resolved result with RMSE=0.24 and SSIM=0.52.

Fig. 4.7 Results of the pure phase object reconstruction: (a) conventional in-line reconstruction; (b) conventional off-axis reconstruction and (c) reconstruction using the proposed method.

4.4.3 Effect of apodization operation: simulation of highly transparent object

To demonstrate the effect of apodization operation on the border diffraction effect, we simulated a highly transparent USAF pattern with the following properties: the amplitude distribution is between 0.8 and 1.0, as shown in Fig. 4.8(a). The phase shift is between 0.5 and 1.5 rad, as shown in Fig. 4.8(b). This case is similar to the actual samples that will be investigated experimentally later in the chapter. The border effect can be observed in both amplitude (Fig. 4.8(c)) and phase (Fig. 4.8(d)) distribution after off-axis reconstruction. It is due to the bulk intensity change caused by camera truncation. Fig. 4.8(e) and Fig. 4.8(f) give the reconstruction result with apodization operation applied on the off-axis hologram; no iterative PR is applied. On the other hand, Fig. 4.8(g) and Fig. 4.8(f) used the proposed method; apodization is only applied to object intensity during the iterative PR step. The border effect vanishes in Fig. 4.8(e) and Fig. 4.8(h), indicating that apodization efficiently tackles the border effect. However, the apodization operation decreases the effective recording area (the values on the border vanish to zero), thus lowering the lateral resolution. Compared to apodizing the off-axis hologram (Fig. 4.8(e) and Fig. 4.8(f)), the proposed routine (Fig. 4.8(g) and Fig. 4.8(h)) yields better image quality. The details are better preserved. In both cases, however, the apodization operation inevitably causes intensity vignetting disturbances in the border area. Thus, we calculated RSME and SSIM values based on the central area of 400×400 pixels for each reconstructed amplitude and phase regarding the original data. The results are summarized in Table 4.1. The obtained values confirm the effectiveness of apodization. The proposed method is proven to be the optimum solution.

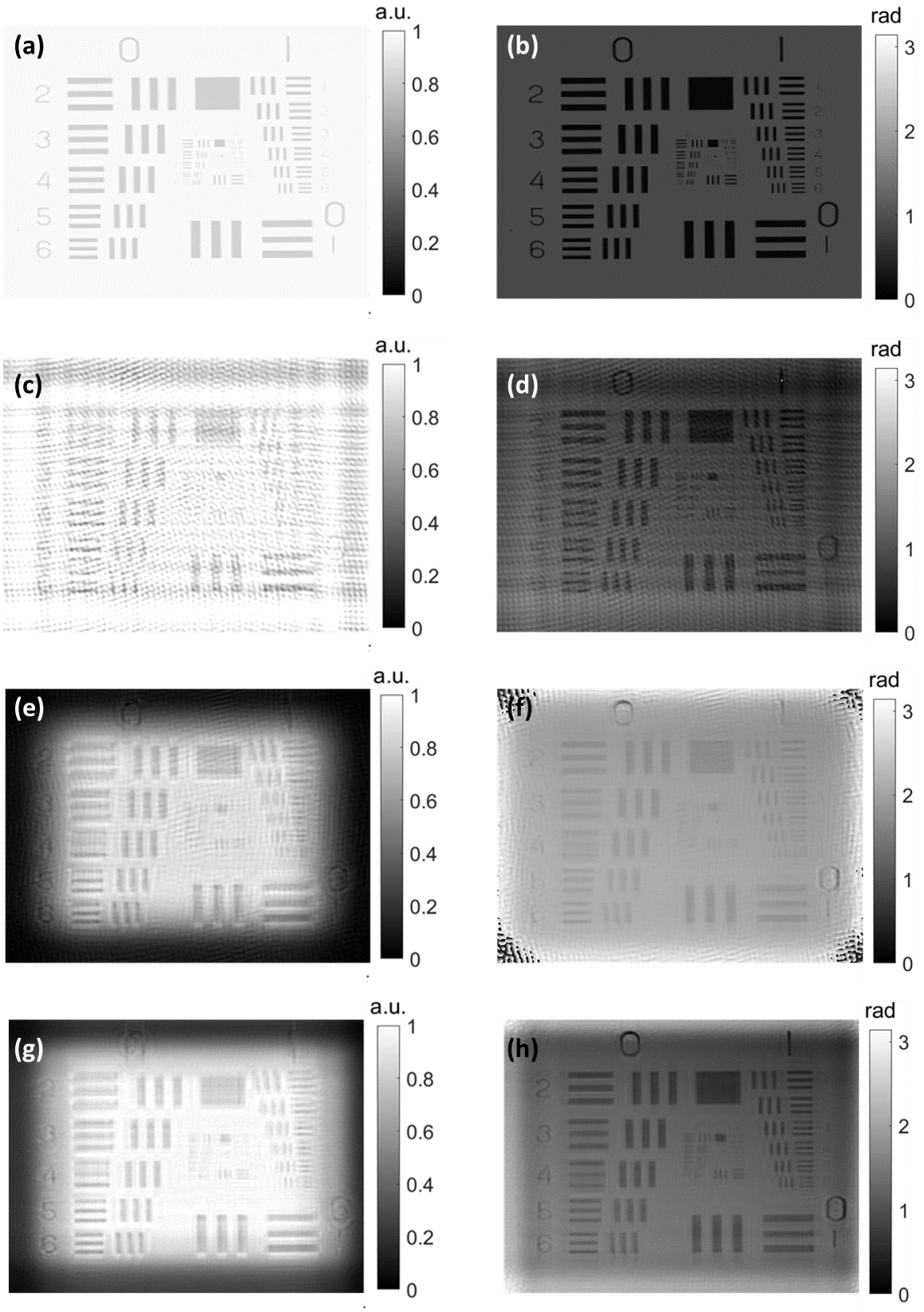

Fig. 4.8 Effect of apodization processing. Amplitude (a) and phase (b) distribution of simulated object; amplitude (c) and phase (d) of off-axis reconstruction without apodization; amplitude (e) and phase (f) of off-axis reconstruction with apodization applied on off-axis hologram; Amplitude (g) and phase (h) of reconstruction using the proposed method with apodization applied on object intensity during iterative PR.

Table 4.1 Quantitative comparison of reconstruction results in Fig. 4.8

	off-axis DH reconstruction		Apodizing the off-axis hologram reconstruction		Phase retrieval using apodized object intensity reconstruction	
	RMSE	SSIM	RMSE	SSIM	RMSE	SSIM
Amplitude	0.33	0.36	0.33	0.49	0.16	0.70
Phase	0.23	0.39	0.23	0.51	0.21	0.72

4.4.4 Effect of the uniformity of the reference wave

We already knew that the best contrast of the recorded hologram is achieved when the object wave and the reference wave have the same level of intensity. Therefore, the reference wave should have a uniform intensity distribution that matches the intensity level of the object wave to optimize the fringe modulation. Unfortunately, the uniformity of the reference wave in the THz configuration is not easy to be guaranteed. The THz beam is often Gaussian shaped. Moreover, the excessive diffraction caused by the optic mounts or the camera housing contributes to bright and dark fringes. The uneven intensity of the reference wave degrades the reconstruction quality. We expect the proposed PR technique to help recover cases where the off-axis hologram has poor contrast.

We simulated the effect of the uniformity of the reference wave, as shown in Fig. 4.9. We used two patterns to simulate the amplitude (Fig. 4.9(a)) and the phase (Fig. 4.9(c)) of the object wave. The amplitude of the reference wave (Fig. 4.9(b)) has four distinct values in the four quadrants: 0.1, 0.2, 0.5 and 1. The generated off-axis hologram is shown in Fig. 4.9(d). The best contrast is observed in the quadrant where the amplitude of the reference wave is close to 1, *i.e.*, the value of the object wavefront. The fringe modulation is very poor in the zones where the amplitude of the reference wave is weak.

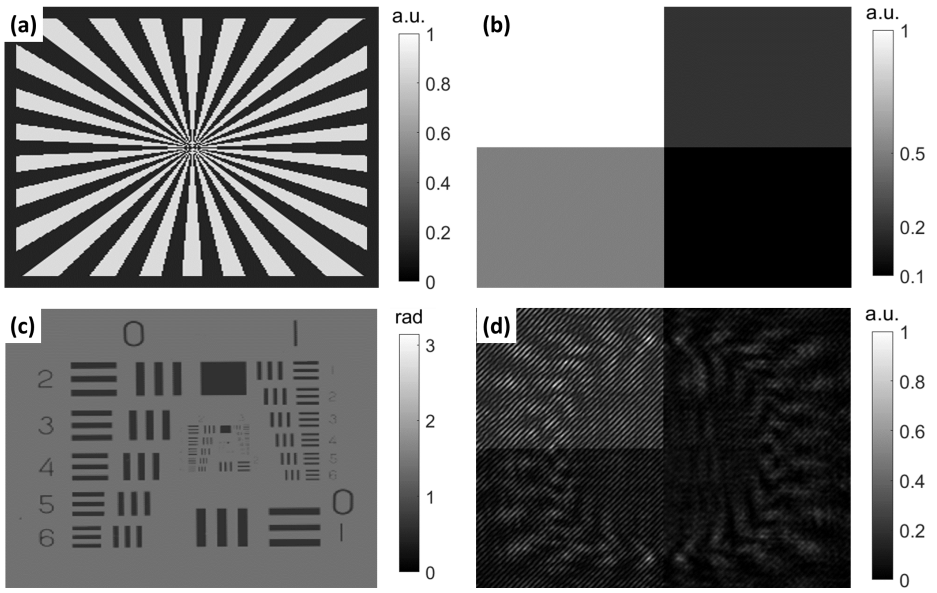

Fig. 4.9 Effect of the uniformity of the reference wave. (a) and (c) are the amplitude and the phase of the simulated object. (b) shows the simulated reference wave's amplitude with four different light levels. (d) gives the simulated off-axis hologram.

The reconstruction results of the off-axis hologram in Fig. 4.9(d) are given in Fig. 4.10. The conventional reconstruction struggles in the regions where the reference wave intensity is weak. In the regions where the reference wave is weak, the reconstructed amplitude vanishes (Fig. 4.10(a)). The phase in these regions cannot be retrieved because the fringe modulation in the hologram is degraded (Fig. 4.10(c)). More information has been recovered after having applied the proposed PR scheme to the off-axis reconstruction results, as shown in Fig. 4.10(b) and Fig. 4.10(d). Both the phase and the amplitude are retrieved all over the imaging area. Thus the proposed method can improve the unfavorable reconstruction results caused by the uneven reference wave intensity. The conclusion also holds when the object wavefront has drastic intensity variation.

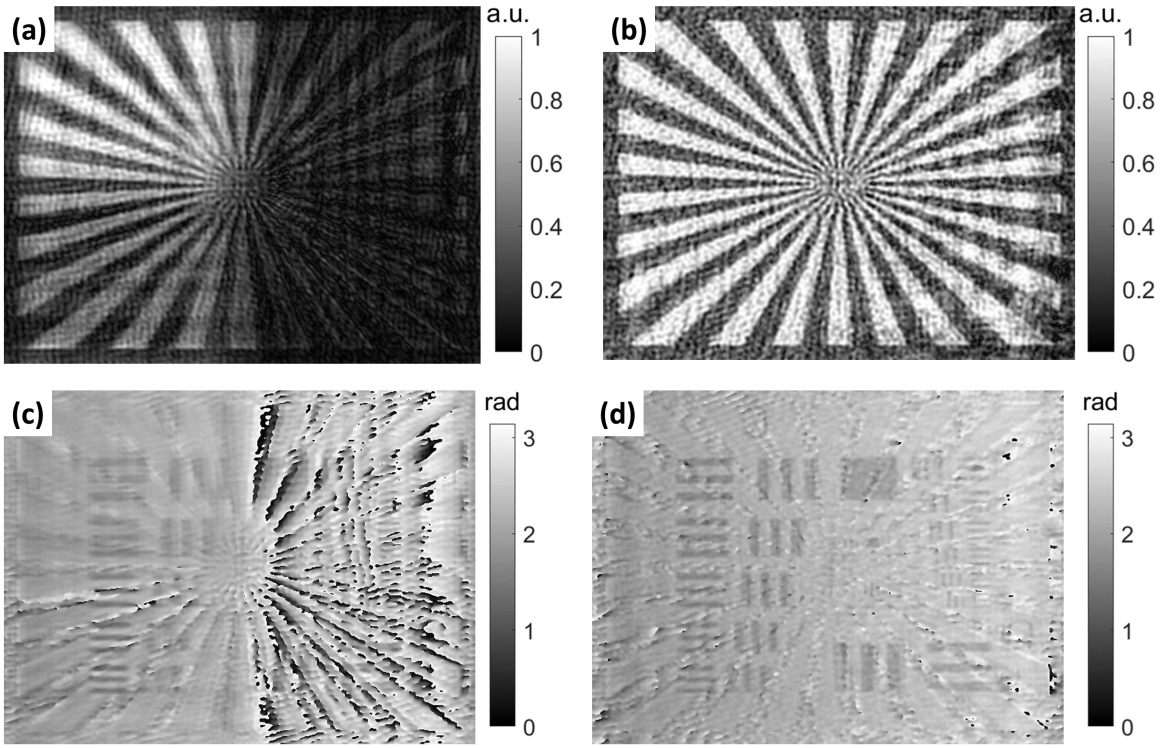

Fig. 4.10 Reconstruction results of the off-axis hologram simulated with uneven reference wave intensity. (a) and (c) are the amplitude and the phase obtained from the conventional off-axis reconstruction. (b) and (d) are reconstructed with the proposed method.

4.5 Experiments of off-axis DH at 2.52 THz

4.5.1 Setup and sample description

The employed experimental setup is illustrated in Fig. 4.11(a). The CH_3OH vapor in the THz FIR-295 laser is pumped by the line 9P36 of the CO2 laser PL6, emitting 2.52 THz (wavelength: 118.83 μm) radiation with a maximum output power of 500 mW. After being attenuated to an appropriate level (tens of mW), the laser beam is split into two beams with approximately equivalent power by a High Resistivity Float Zone Silicon (HRFZ-Si) THz beam splitter from Tydex. The transmitted beam passes through the investigated object. The object is placed at 9.5 mm in front of the recording plane. The reflected beam directed by a mirror serves as the reference beam. The off-axis angle between the object beam and the reference beam is around 45°. A shutter is inserted in the reference beam. When the shutter is open, the reference beam interferes with the object beam; a hologram is captured. When the shutter is closed; the reference beam is blocked; only the diffraction pattern of the object

beam is captured. The uncooled microbolometer camera Gobi-640-GigE from Xenics is used to capture the intensity pattern. The detector has 480×640 pixels on a pitch of 17 μm. At the given recording condition, the theoretical intrinsic resolution of the system is 138.3 μm according to Eq. 3.15.

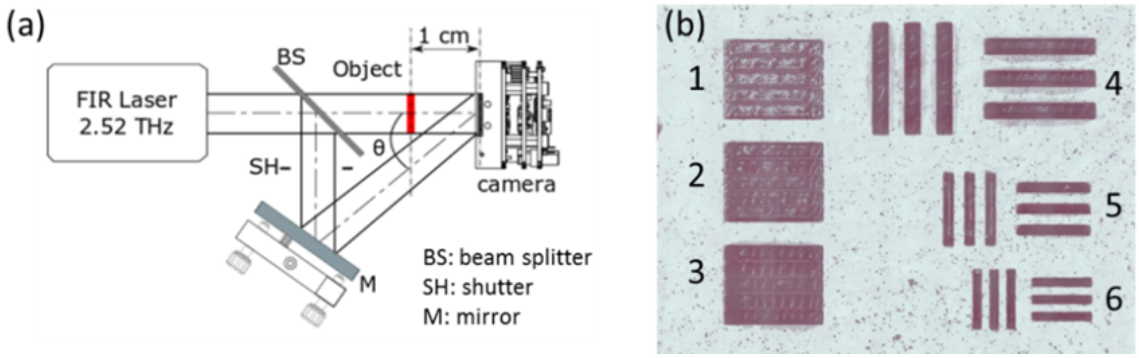

Fig. 4.11 Experimental setup and sample description at 2.52 THz. (a): Schematic of the experimental setup; (b): the white light image of the sample.

The investigated sample is a piece of visibly opaque 550 μm-thick PP slab. PP is highly transparent at 2.52 THz with an absorption coefficient of around 1.5 cm^{-1} and refractive index $n_{pp} = 1.49$ [67]. The backside of the sample surface (the side facing the laser) is engraved using excimer laser ablation. As shown in Fig. 4.11(b), the square patterns 1-3 are three squares of $1 \times 1mm^2$ with a depth of 44 μm, 72 μm, and 105 μm, respectively. The line width of patterns 4-6 are 245 um, 155 μm, and 140 μm to evaluate lateral resolution performance. The depth of these line patterns is 150 μm. Figure 4.12 shows the profile of the sample under the optical microscopy.

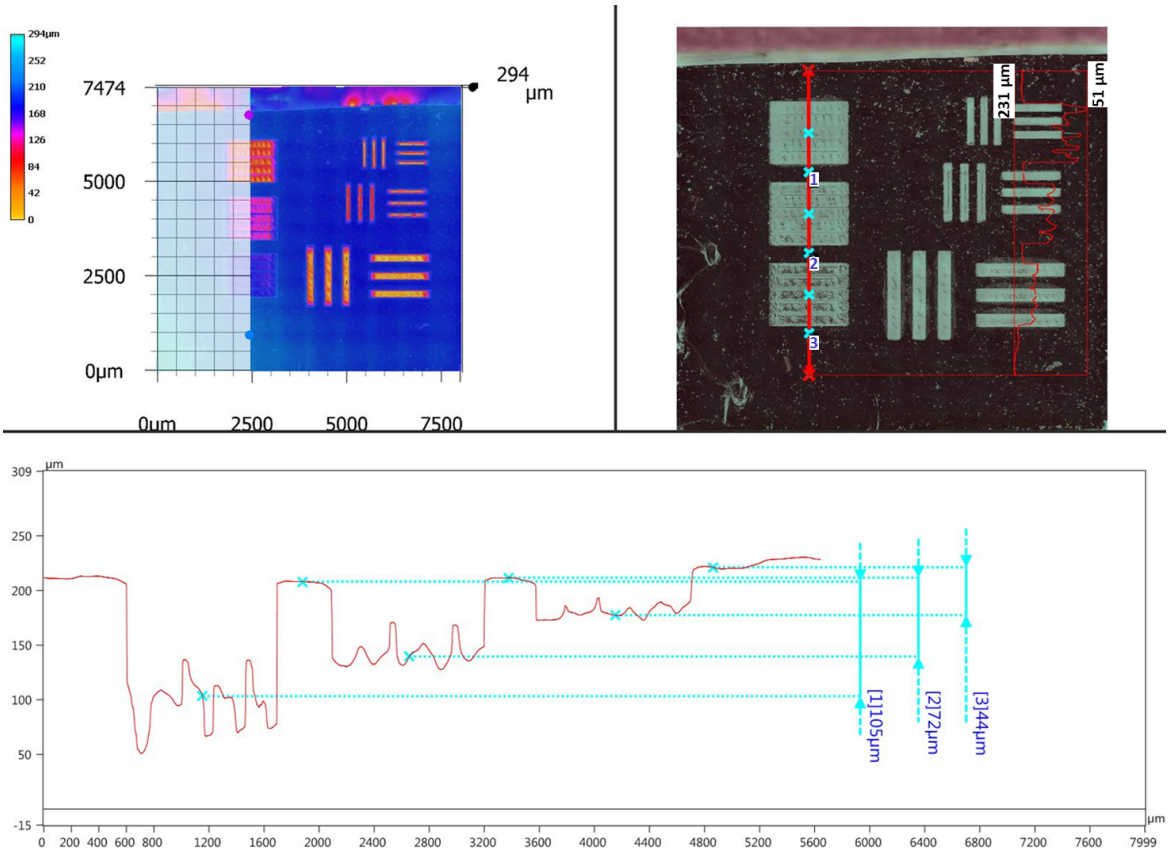

Fig. 4.12 Profile of the patterns on the PP slab observed under an optical microscopy.

4.5.2 Results and discussions

Figure 4.13 shows the intensities recorded with the setup and their Fourier spectra. The thermal background (Fig. 4.13(a)) was recorded when blocking the FIR laser output. The thermal background image (Fig. 4.13(e)) does not contain high frequency details. Its Fourier spectra is located near the origin. The recorded hologram (Fig. 4.13(b)) and the object wave intensity (Fig. 4.13(c)) are shown along with the amplitude of their Fourier spectra (Fig. 4.13(f) and Fig. 4.13(g)). We observed that the autocorrelation term shown in Fig. 4.13(g) is overlapped with the +1 order of the hologram in Fig. 4.13(f). Figure 4.13(d) shows the result after subtracting the object wave intensity from the hologram. The effectiveness can be observed from its spectrum in Fig. 4.13(h). We used the the intensity in Fig. 4.13(d) to perform the off-axis reconstruction. The actual off-axis angles of the reference beam extracted from Fig. 4.13(h) are 44.8° and -0.83° in the horizontal and vertical direction, respectively. We observed two spurious components caused by multiple reflections in the Fourier spectra in Fig. 4.13(f-h) at the 45° direction. They can be removed in the spectra by replacing the

value with zero during the spectrum filtering. In the four spectra images, the horizontal and vertical lines originating from the border diffraction can be observed. We applied apodization processing using Eq. 4.4 on recorded intensities (Fig. 4.13(b-d)). The processed intensities as well as their spectra are given in Fig. 4.14. The apodization produced a vignetting effect in Fig. 4.14(a-c). The horizontal and vertical lines vanished in their spectra in Fig. 4.14(d-f) after the apodization operation.

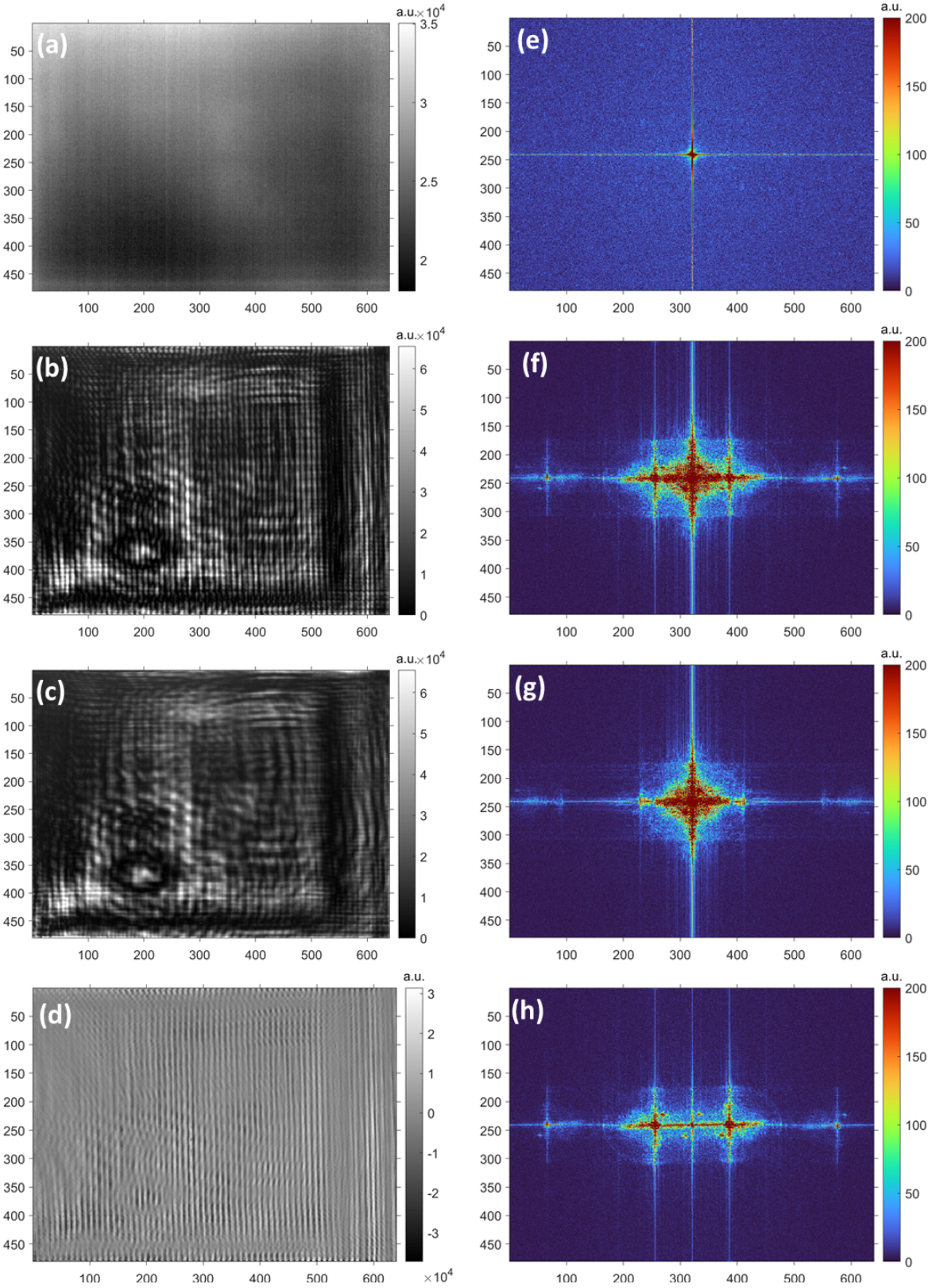

Fig. 4.13 Recorded intensities at 2.52 THz and their spectra. (a) Thermal background; (b) off-axis hologram; (c) object wave intensity; (d) the subtraction between (b) and (c). (e)-(h) are their corresponding spectra.

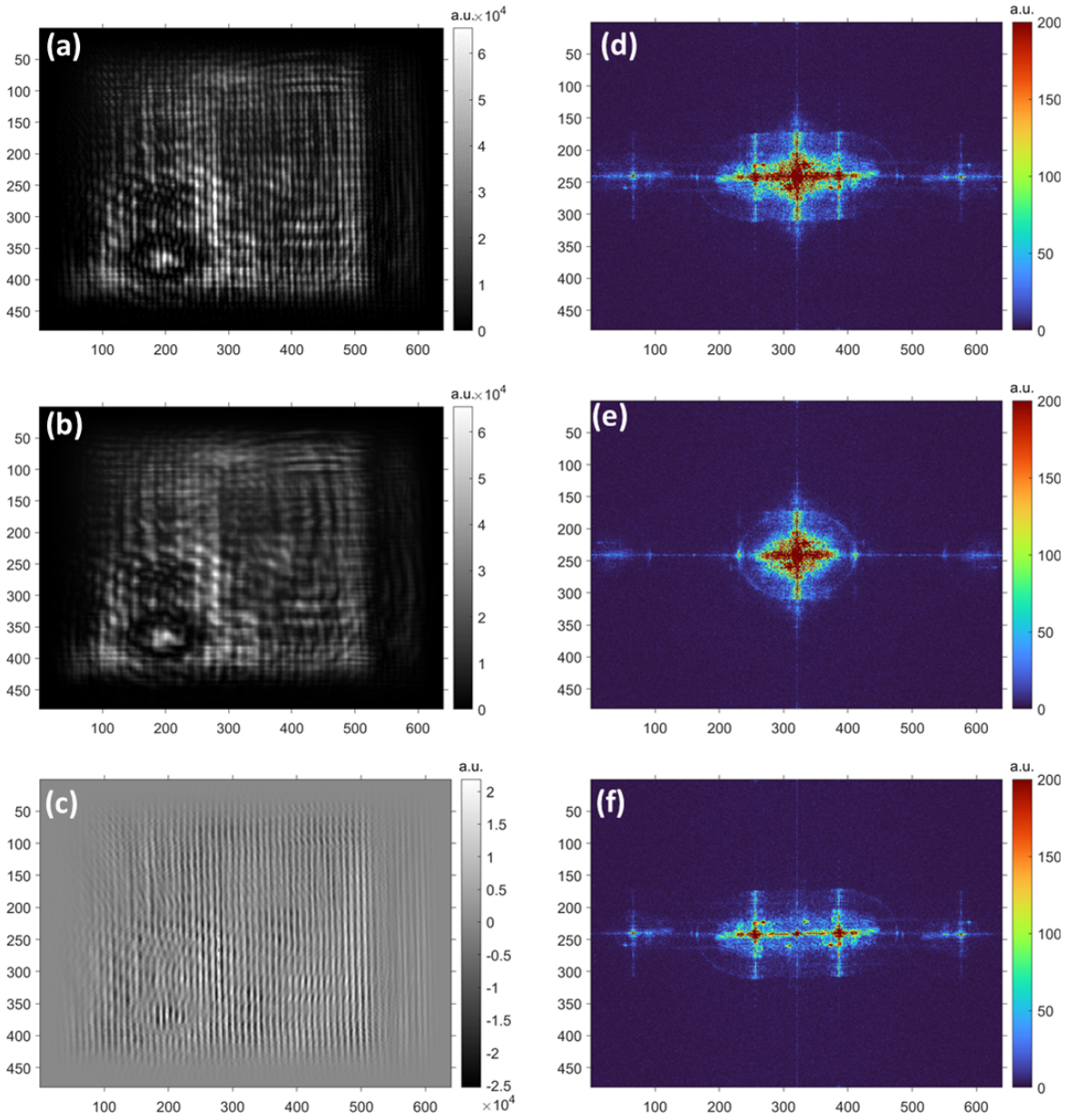

Fig. 4.14 Intensities and spectra after the apodization processing. (a)-(c) are the results after apodizing Fig. 4.13(b)-(d). (d)-(f) are their corresponding spectra.

The comparison of different reconstruction results is shown in Fig. 4.15. The amplitude and wrapped phase in Fig. 4.15(a) and Fig. 4.15(b) are obtained from reconstructing the off-axis hologram after subtracting the object intensity, *i.e.*, the intensity shown in Fig. 4.13(d). We observed severe border diffraction artifact. Moreover, line pair 6 on the right bottom, whose width is 140 μm, approaching the intrinsic resolution, cannot be resolved. Figures. 4.15(c)-(d) show the reconstruction results with the apodized off-axis hologram,

i.e., the intensity shown in Fig. 4.14(c). The border diffraction artifact is significantly alleviated. However, the resolution of line pair 6 is still not satisfactory. Then, we applied the PR-assisted method. We used the reconstruction results in Fig. 4.15(a) and Fig. 4.15(b) as the initial guess of the object wave. The apodized object intensity (Fig. 4.14(b)) is used as the intensity constraint on the detector plane. We performed 50 iterations of back and forth propagation PR as explained in Section 4.2.

A considerable improvement is achieved using the proposed method after 50 iterations of PR with apodized object intensity. Line pair 6 is recognizable in both amplitude (Fig. 4.15(e)) and phase (Fig. 4.15(f)) reconstruction, implying an improvement of resolution. The background is more uniform than the results without applying PR. The visible differences between Figs. 4.15(e-f) and Figs. 4.15(a-b) validate the method. It should be noted that the noise and vertical fringes at the left border in Figs. 4.15(a-f) are caused by the metallic sample holder when the object beam impinged the sample. Those artifacts are part of the object beam; therefore, it cannot be removed using the proposed method.

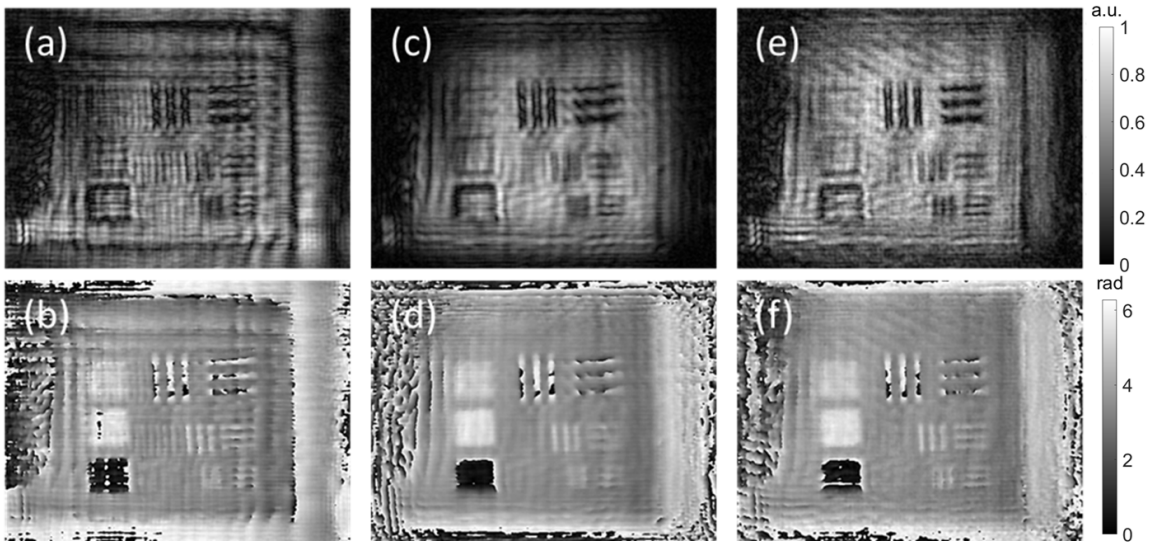

Fig. 4.15 Experimental reconstruction results of the engraved PP slab at 2.52 THz. (a) and (b) are the reconstructed amplitude and phase, respectively, using the off-axis hologram in Fig. 4.13(d) without apodization. (c) and (d) are reconstruction using the apodized off-axis hologram in Fig. 4.14(c). (e) and (f) are reconstruction using the proposed method with apodized object intensity in Fig. 4.14(b).

The relation between the unwrapped phase $\varphi(x,y)$ and the sample thickness $d(x,y)$ is given as

$$\varphi(x,y) = \frac{2\pi\,(n_{pp}-1)\,d(x,y)}{\lambda}. \tag{4.8}$$

After unwrapping the phase distributions in Fig. 4.15(b)-(f), the phase differences between different patterns and flat areas are summarized in Table 2. Mean values, as well as their standard deviations (std, given in the parenthesis) of the region of interest (ROI), are calculated. We observed that the std values decrease to 0.14 rad in Fig. 4.15(f) after having applied the proposed method. According to the std values, a phase resolution of 0.2 rad is achieved in this experiment.

Table 4.2 Phase differences calculated from different DH reconstruction methods.

Zone	Depth [μm]	Calculated phase [rad]	Unwrapped Fig. 4.15(b) [rad]	Unwrapped Fig. 4.15(d) [rad]	Unwrapped Fig. 4.15(f) [rad]
Pattern 1	44	1.14	1.13 (0.32)	1.18 (0.22)	1.13 (0.21)
Pattern 2	72	1.87	1.88 (0.39)	1.82 (0.19)	1.88 (0.14)
Pattern 3	105	2.72	2.96 (0.33)	2.98 (0.23)	2.95 (0.14)

4.6 Experiments of off-axis Sub-THz DH at 280 GHz

4.6.1 Introduction

As analyzed in Section 2.3, most NDT applications should be carried out with sub-THz radiation, thanks to the high transparency in this frequency regime. On the other hand, from the THz imaging techniques' aspect, the undesirable diffraction and interference effects due to the high coherence of the narrowband sources are more challenging to be tackled concerning the large working wavelength. Therefore developing lensless imaging techniques in the sub-THz range is of great interest. After developing the off-axis DH and PR techniques in the FIR range, we investigate sub-THz DH at 280 GHz in collaboration with CENTERA. CENTERA is devoted to the study of FET-based THz detectors in the form of an integrated circuit. THz FET detectors exhibit a fast response time and high sensitivity at room temperature operation for sub-THz detection. Moreover, the THz FET detectors present the advantage of easy integration, making it more straightforward for array detector fabrication.

Thus this detector technology is a good candidate for THz imaging in industrial applications.

Before building the THz DH setup, we performed two THz imaging tests based on the existing confocal imaging systems in CENTERA. The single-pixel raster scanning imaging system at 140 GHz, shown in Fig. 4.16(a1), provides high-quality image results (Fig. 4.16(a2)) at the expense of long scanning duration. In our test, a GFRP composite honeycomb sandwich panel is imaged in transmission mode with a scanning pitch of 0.5 mm. The sample exhibits high transparency. Both the cross-shaped metal sticker on the backside and the L-shaped one on the front side are visible in the recorded image. Although some defective cells are visible in the image, the honeycomb structure can not be well resolved due to the large wavelength (2 mm). Figure. 4.16(b1) shows a 300 GHz fast postal scanner prototype developed by CENTERA and a Polish company Orteh for high-speed imaging [163]. The postal scanner contains three lines of 48 FET detector arrays. The system allows imaging of an A4-size envelope within one second. The linear scanner combined with the transportation belt solution is particularly suitable for industrial NDT applications. Figure. 4.16(b3) shows the real-time imaging result of the samples listed in Figure. 4.16(b2), hidden in an envelope. The scanning results showed that the PCB substrate made in glass epoxy, the PC, and the yellow GFRP composite pieces are transparent at 300 GHz, whereas they remain opaque at the FIR range. Despite the poor imaging quality of the prototype scanner, the system allows identifying different concealed objects efficiently. These preliminary tests showed the potential of developing sub-THz DH with THz FET detectors. We could imagine a THz holographic imager prototype similar to Fig. 4.16(b1), but with additional phase measurement, which helps reveal more information about the testing samples. Assembling high-performance linear detector arrays which meet the requirement for hologram recording would require a significant volume of engineering work. Therefore in this thesis, we demonstrated the feasibility sub-THz DH by raster-scanning a single THz FET detector.

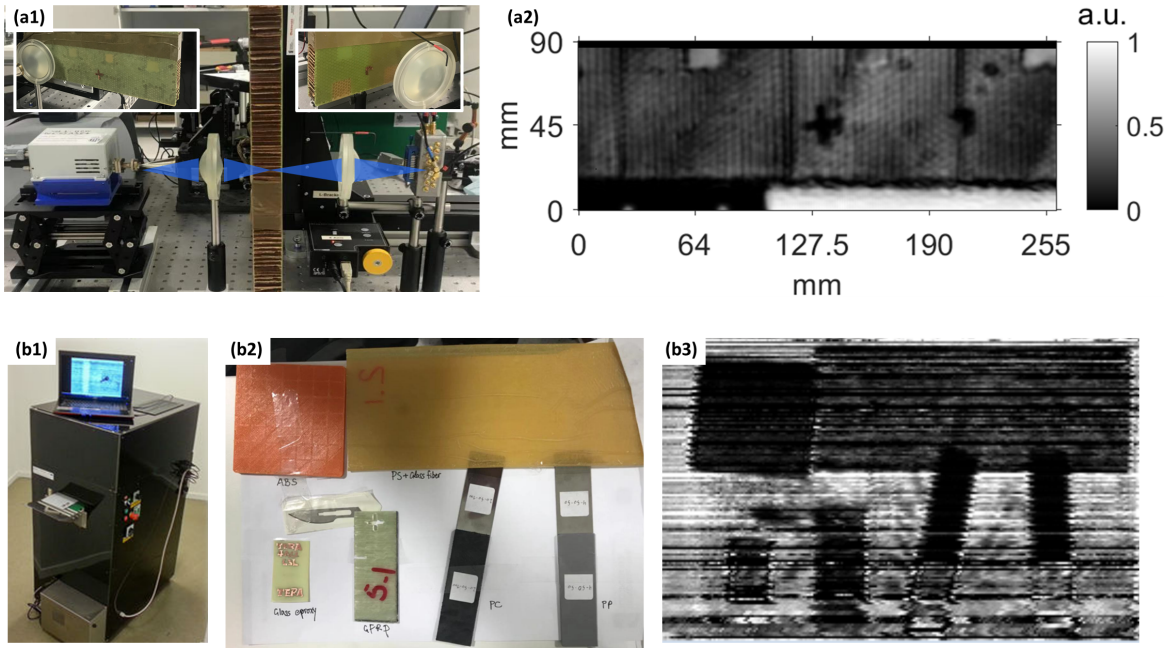

Fig. 4.16 Sub-THz confocal imaging with FET detectors. (a1) is a single-pixel imaging system at 140 GHz. (a2) shows the imaging result of a GFRP composite honeycomb sandwich panel. (b2) is a 300 GHz postal scanner developed by CENTERA for fast imaging. The scanner contains three lines of 48-pixel FET THz detector arrays soldered on the PCB supports. The samples in (b2) are kept in an A4-sized envelope, moving on the transportation belt. (b3) is an example of image recorded by the fast poster scanner system.

4.6.2 Experimental setup

We built an off-axis DH experimental setup with the available materials in CENTERA. Figures. 4.17(a) and (b) are the schematic and the photograph of the experimental setup at 280 GHz for hologram recording, respectively. The principle bears no difference from that at 2.52 THz in Fig. 4.11(a). An IMPATT diode emits radiation at 140 GHz with an output power of 30 mW. We assembled a frequency multiplier to the IMPATT diode, which generates the radiation at 280 GHz with an output of 14 mW (Fig. 4.17(c)). The comparatively shorter wavelength after frequency multiplication offers better imaging resolution. The source is collimated by a three-inch 90° off-axis parabolic mirror (focal length: 152.4 mm) located 15 cm away from the source output. A three-inch wire grid beam splitter separates the beam into the object wave and the reference wave. A piece of 15×15 cm^2 glass is used as a mirror to redirect the reference wave toward the detector. The off-axis angle is around 35 ° along the x direction. The object wave illuminates the sample located d in front of the detector plane. A packaged single-pixel THz FET detector is mounted on a three-axis translation

stage, as shown in Fig. 4.17(d). The raster scan is performed in the x-y plane. The THz FET detector employed here is based on GaAs HEMT (high electron mobility transistor). A broadband bow-tie antenna structure is designed for optimizing the THz absorption. A silicon-substrate lens with a diameter of 4 mm is mounted in front of the FET detector by the 3D-printed holder to couple the input THz radiation on the detector [164]. The output voltage of the FET detector is integrated into a lock-in amplifier. Due to the high coherence of the input THz radiation, the interference problem caused by the multiple reflections between the optics and the detector occurred during our trial. We slightly tilted the detector to reduce this undesirable effect. The recording distance, the scanning area, and the scanning pitch are the three decisive factors for long-wavelength DH recording. According to the discussion in Section 3.2.1, the long-wavelength would benefit from a large scanning area at the expense of recording time. The recording distance should be minimized as long as the sample does not obstruct the reference wave for a better resolution. In the experiment, the imaging area is set to 10×10 cm^2. The recording distance is restricted to less than 10 cm. Such configuration guarantees an intrinsic resolution on the order of wavelength (1.07 mm). The scanning pitch should be small enough to well sample the interference fringes on the hologram. The employed wavelength and the off-axis angle require that the scanning pitch should be larger than 0.83 mm, as suggested by Eq. 3.24. In our experiment, we set the scanning step to 0.25 mm. It takes around four hours for one hologram acquisition of 400×400 pixels.

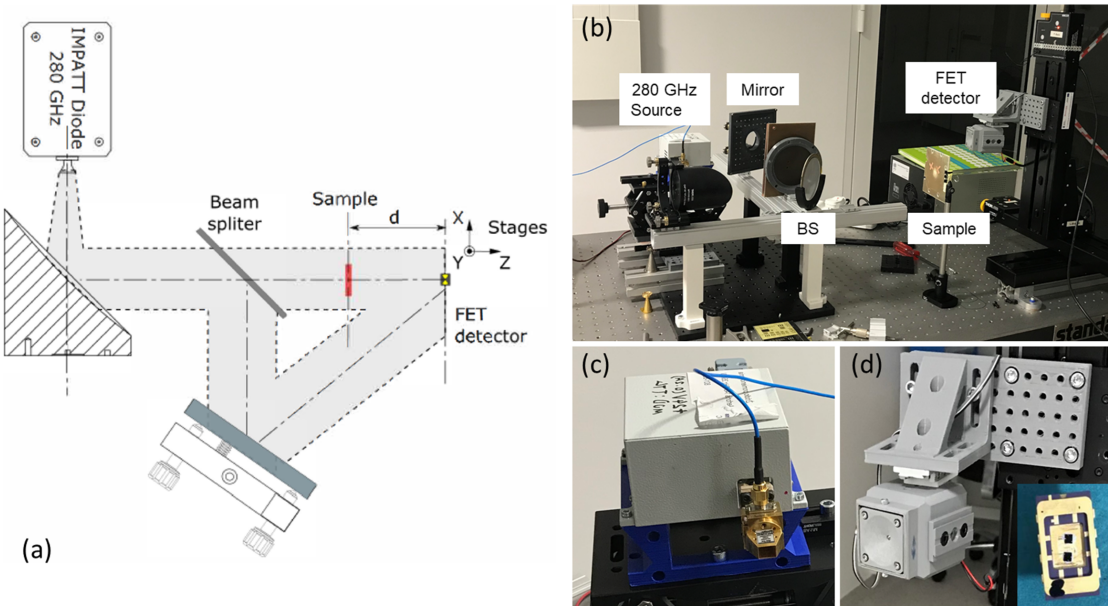

Fig. 4.17 Experimental setup of the off-axis sub-THz DH at 280 GHz. (a) and (b) show the schematic and the photograph of the experimental setup, respectively. (c) and (d) are the employed 280 GHz source and the packaged THz FET detector. The inset photo in (d) is a photo of the THz FET device.

4.6.3 Results

4.6.3.1 Amplitude contrast object: metallic optical chopper wheel

The first case of study is a metallic optical chopper wheel, shown in Fig. 4.18. This sample is regarded as a pure amplitude contrast object since the metallic structure blocks the THz radiation entirely. On the edge, every two metallic stripes are separated with a period of 3.6°. Three holes with a diameter of 3 mm are equally spaced on the wheel. These mm-scaled structures are suitable for testing the imaging performance of DH at 280 GHz.

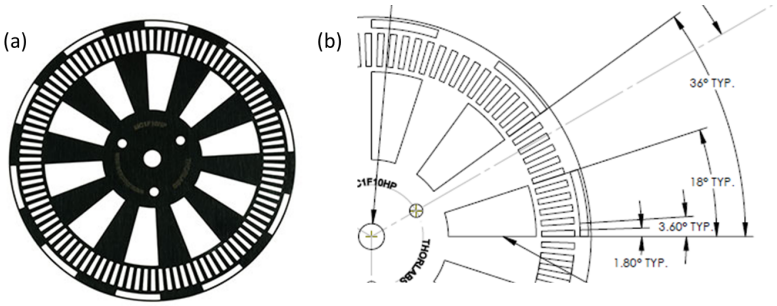

Fig. 4.18 The photograph and the drawing of the metallic optical chopper blade used for sub-THz DH imaging [165].

Before recording the hologram, we recorded an image of the object beam intensity without the reference beam, as shown in Fig. 4.19(a). The beam diameter is around 5 cm. Some inhomogeneities are observed. This is mainly due to the interference that we mentioned earlier. Then we placed the wheel around 8 cm in front of the detector. The exact recording distance is found to be 7.9 cm after comparing the reconstruction results using different distances. Figure. 4.19(b) shows an image of the diffraction pattern of the object wave. This pattern will be used for iterative PR. We observed that the diffraction pattern of the object wave exhibits some extra dark zones. The dynamic range of the recorded diffraction pattern is low. Finally, we removed the baffle that blocks the reference beam to record the off-axis hologram, shown in Fig. 4.19(c).

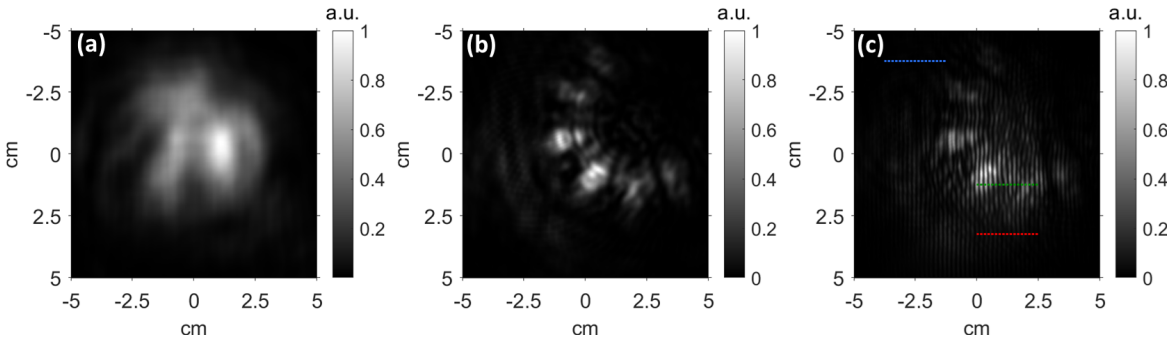

Fig. 4.19 Hologram recording of the chopper wheel: (a) the object beam without sample; (b) the diffraction pattern induced by the chopper wheel; (c) the off-axis hologram.

Due to the inhomogeneous intensity distribution of the object wave, the contrast of the interference fringe in Fig. 4.19(c) varies. We extracted the intensities at three different locations to evaluate the fringe contrast. The intensity profiles of the three cut lines are

plotted in Fig. 4.20. The formula for fringe visibility is written as

$$V = \frac{I_{\max} - I_{\min}}{I_{\max} + I_{\min}}. \tag{4.9}$$

The fringe visibility quantitatively describes the quality of the recorded interference pattern. In Fig. 4.20, the maximum fringe visibility of the green curve is around 0.7. The value is around 0.5 for the red curve. The blue curve is located in the zone where there is barely any THz radiation. The fringe visibility of the blue curve is close to zero. The poor modulation, in this case, is similar to the effect of an inhomogeneous reference wave discussed previously, which degrades the reconstruction quality. Hence we believe that the proposed PR method will improve the reconstruction quality in this case.

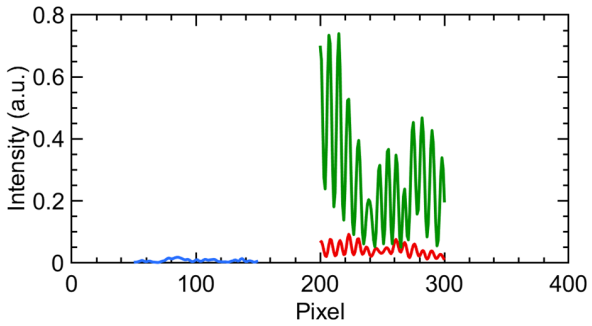

Fig. 4.20 The three intensity profiles of the recorded hologram extracted from Fig. 4.19(c).

The reconstruction results are presented in Fig. 4.21. It is not surprising that inline reconstruction is unable to reconstruct Fig. 4.19(b), as shown in Fig. 4.21(a1)-(a2). The off-axis reconstruction in Fig. 4.21(b1)-(b2) allows retrieving the overall morphology of the optical chopper wheel. We performed the proposed iterative PR method using Figs. 4.21(b1)-(b2) and 4.19(c). The results after 20 iterations are shown in Figs. 4.21(c1)-(c2). Comparing Fig. 4.21(c1) with Fig. 4.21(b1), first off, we observed an increase of imaging area. The top right corner is not visible in Fig. 4.21(b1). Only one of the three holes is visible in Fig. 4.21(b1). All the three holes are visible in Fig. 4.21(c1). Especially the top one is clearly reconstructed. The metal stripes on the edge are visible in Fig. 4.21(c1).

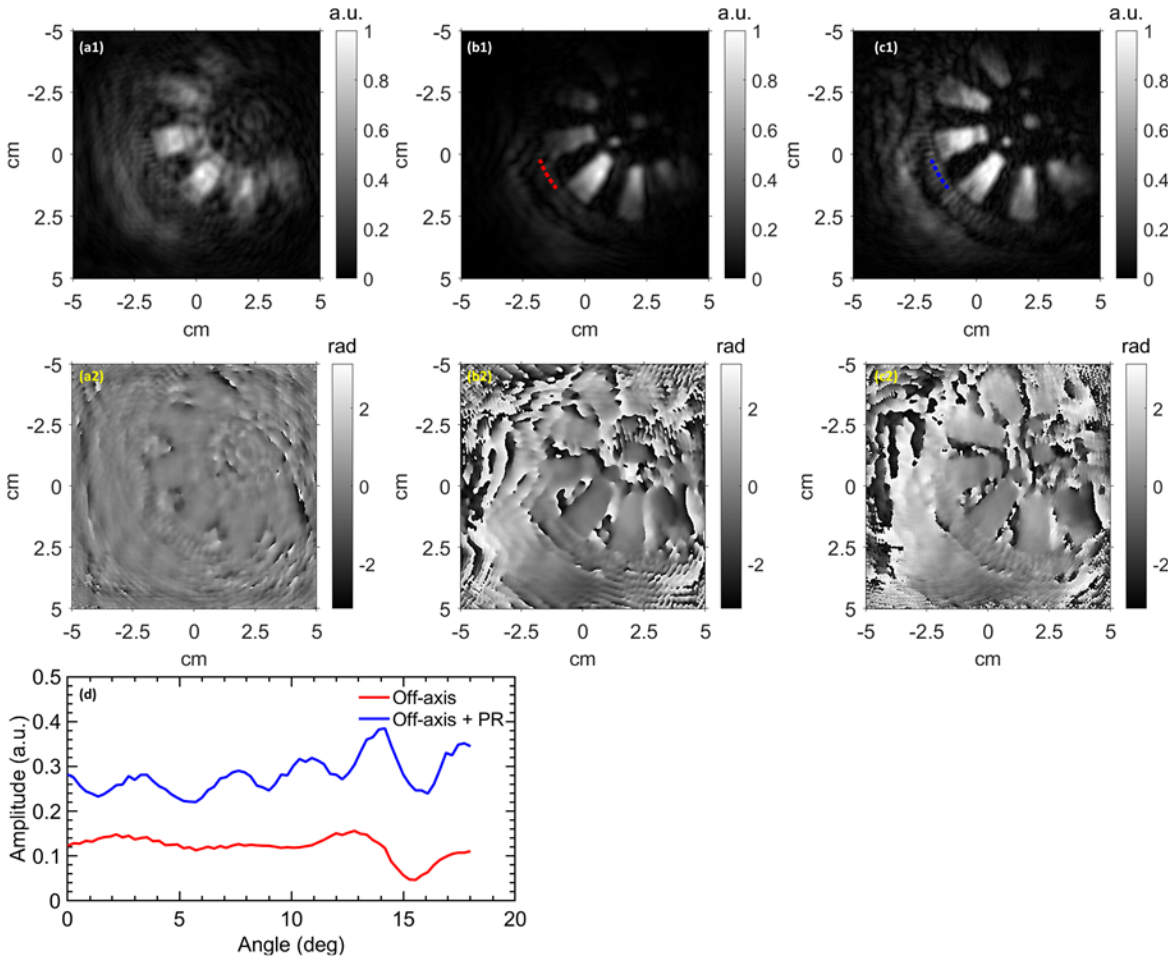

Fig. 4.21 DH reconstruction results of the optical chopper wheel at 280 GHz. (a1)-(a2) are obtained using conventional in-line reconstruction with Fig. 4.19(b). (b1)-(b2) are obtained with the conventional off-axis reconstruction using Fig. 4.19(b). (c1)-(c2) are reconstructed using the proposed iterative PR method. (d) plots the profiles extracted from (b1) and (c1).

We identified the centroid of the central hole in Fig. 4.21(c1), which is also the centroid of the optical chopper wheel. We plotted the intensity of the periodic edge located 4 mm away from the centroid for 18 °, as the red and the blue dotted lines in Fig. 4.21(b1) and Fig. 4.21(c1). It can be observed that the five periods of stripes are distinguishable in Fig. 4.21(c1) when the iterative PR method is applied. They are clearly separated on the blue curve in Fig. 4.21(d). However, they are not visible in Fig. 4.21(b1) since the red curve in Fig. 4.21(d) is mostly flat.

We repeated the experiment with a concealed object. The same optical chopper wheel was hidden into an envelope (Fig. 4.22(a)) while other parameters remained the same as in the previous experiment. The diffraction pattern of the object wave and the off-axis hologram

are recorded, shown in Figs. 4.22(b) and (c). The reconstruction results are given in Fig. 4.23. The performance of the three different reconstruction methods is similar to the conclusion obtained in the case where the object is uncovered. The proposed PR-assisted off-axis reconstruction gives the best results. Although the concealed object is distinguishable, the reconstruction quality is degraded when compared with Fig. 4.21. The reason is that the two sides of the envelope can cause both attenuation and random reflection of the object wave, inducing artifacts to the object wave diffraction and the off-axis hologram.

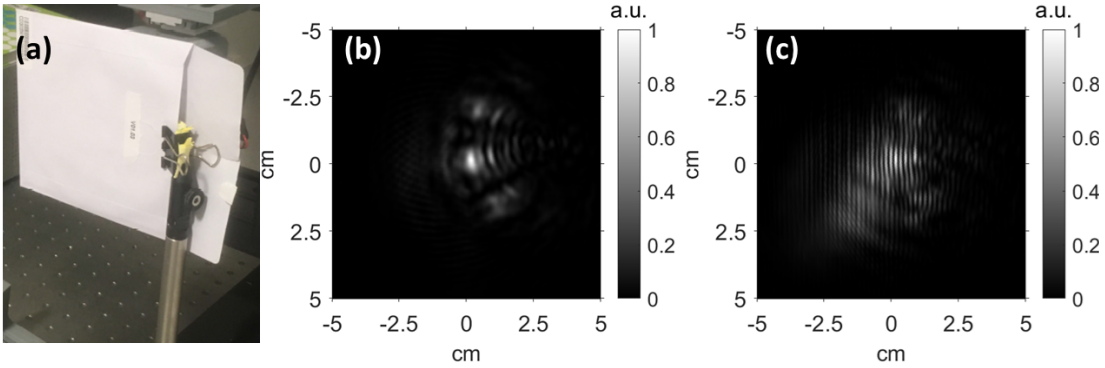

Fig. 4.22 DH recording of the concealed optical chopper wheel at 280 GHz. (a) the optical chopper concealed by a envelope. The diffraction pattern of the object wave (b) and the off-axis hologram (c) are recorded.

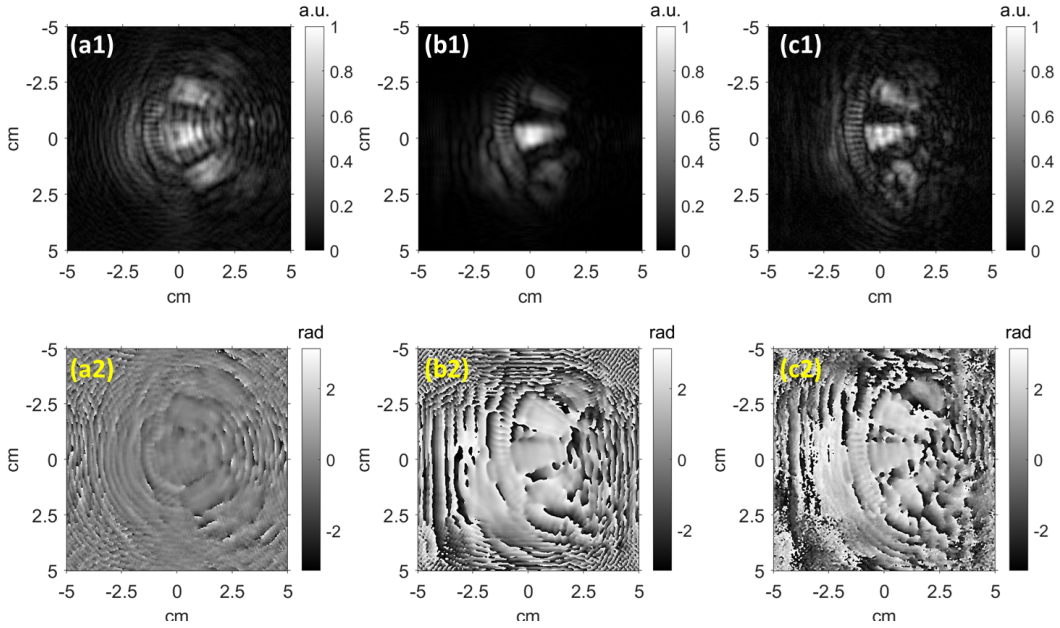

Fig. 4.23 DH reconstruction results of the concealed optical chopper wheel at 280 GHz. (a1-a2) are obtained using conventional in-line reconstruction with Fig. 4.19(b). (b1-b2) are conventional off-axis reconstruction using Fig. 4.19(b). (c1-c2) are reconstructed using the proposed method.

4.6.3.2 Pure phase object: TPX lens

Next, we investigated a pure phase object, a TPX lens, to estimate its optical thickness. The TPX lens is made of two plano-convex aspheric lenses. It has an effective focal length of 50 mm and a diameter of 38 mm (Fig. 4.24(a)). The refractive index of TPX is around 1.465 and relatively independent of wavelength [166]. According to the technical drawing, the thickness of the lens at the center is 6.7$\pm$ 0.1 mm. We employed the digital holographic interferometry technique to observe the phase variation induced by the phase. We first recorded a free space hologram without the object, shown in Fig. 4.24(b). Then we recorded the hologram with the presence of the lens (Fig. 4.24(c)). The lens is located 77 mm in front of the detector. We obtained the phase reconstructions of both holograms, ϕ_{obj} and ϕ_{ref}, at the object plane. The phase difference, $\Delta\varphi = \phi_{\text{obj}} - \phi_{\text{ref}}$, is the phase variation induced by the lens. The unwrapped phase difference $\Delta\varphi_{\text{unwrap}}$ and thickness t follow the relation: $\Delta\varphi_{\text{unwrap}} = (2\pi t/\lambda)(n_{\text{TPX}} - 1)$. The thickness can be extracted.

The reconstruction results are presented in Fig. 4.25. Figure. 4.25(a) shows the reconstructed amplitude. The metallic lens mount blocked the THz radiation, appearing as dark zones. Figure. 4.25(b) shows the phase difference $\Delta\varphi$ after subtraction. We used a robust

phase unwrapping algorithm based on the least-squares method [167] to unwrap the phase in Fig. 4.25(c). To estimate the central thickness, we identified the red-circled zone with a diameter of 38 mm as the clear aperture of the lens, based on Fig. 4.25(a) and (b). The phase difference between the border and the center of the ROI in Fig. 4.25(c) gives the central thickness. Using this method, we estimated that the central thickness of the selected region is around 6.1 mm, as shown in Fig. 4.25(d) and (e). Despite the uncertainty caused by the selection of the ROI region, the obtained result is in agreement with the value indicated on the technical drawing.

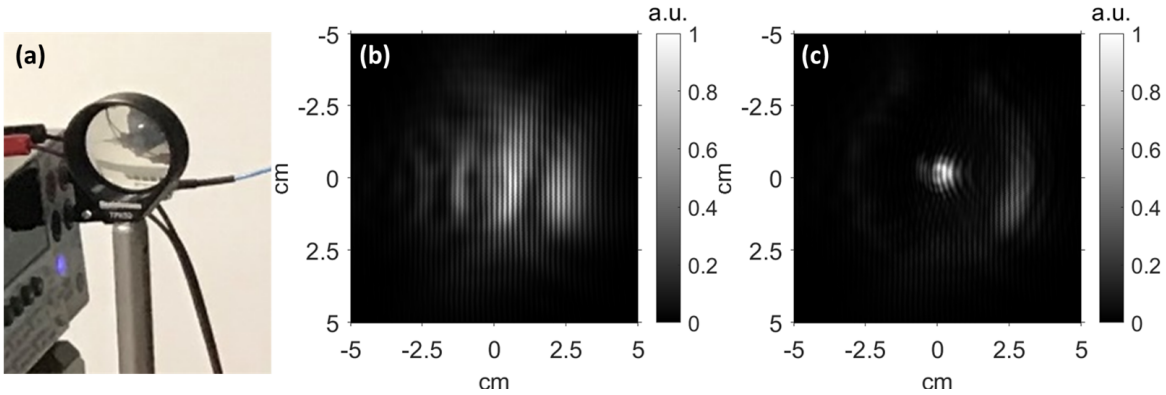

Fig. 4.24 DH recording of a TPX lens as a pure phase object at 280 GHz. (a) is the photograph of the TPX lens. (b) is a free space hologram without inserting the object. (c) is the hologram with the lens inserted in the object beam.

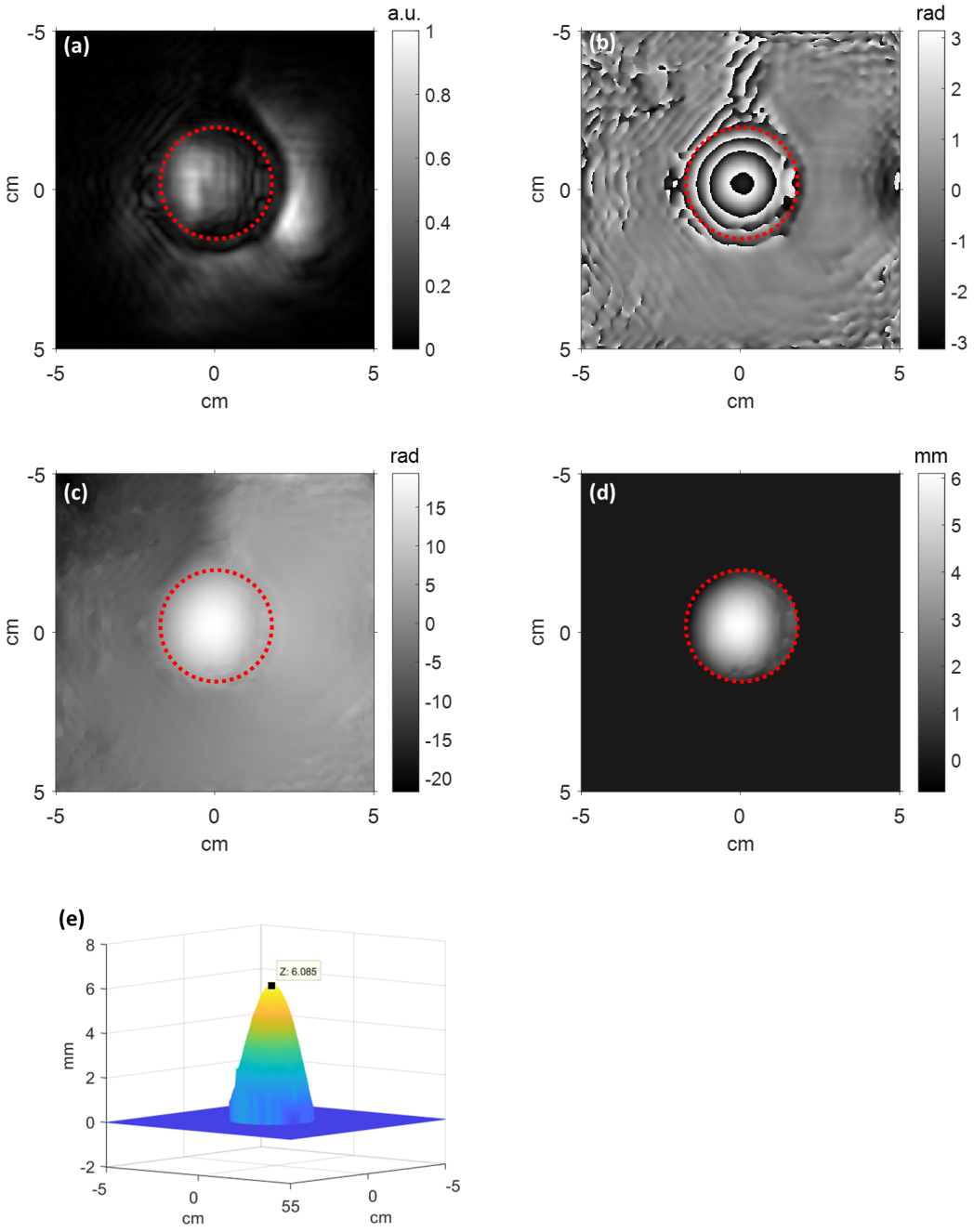

Fig. 4.25 DH reconstruction results of the TPX lens at 280 GHz. (a) is amplitude reconstructed using Fig. 4.24(c). (b) is the wrapped phase difference induced by the object. (c) is the unwrapped phase obtained from (c). (d) and (e) give the thickness distribution obtained from (c).

4.6.3.3 Towards complex samples: observation of a 3D-printed plate with cross patterns

Lastly, we imaged an inhomogeneous dielectric sample which is more relevant to the actual situations of NDT application. The sample under investigation is a 3D-printed plate with cross patterns using PLA filament. Nine crosses with thicknesses ranging from 0.2 mm to 1.8 mm are printed on a 2 mm-thick plate, as shown in Fig. 4.26(a) and (b). Besides the off-axis hologram, we also recorded the free space hologram and the diffraction pattern of the object wave. In Fig. 4.26, (c) and (d) are reconstructed from the off-axis hologram. (e) and (f) are reconstructed using the PR-assisted technique. In both cases in (d) and (f), the phase distribution of the free space has been subtracted from the obtained object phase. We can barely extract any information from the amplitude reconstruction in Fig. 4.26(c) and (e). However, the cross patterns are distinguishable from the phase reconstruction in Fig. 4.26(d) and (f). The PR technique is shown to be effective again in this case. The amplitude distribution in Fig. 4.26(e) shows a sharper outline of the plate as well as the foldback clip on the right. More importantly, in the phase difference map, the nine crosses are visible in Fig. 4.26(f) after the PR processing, whereas only the crosses on the middle line are visible in Fig. 4.26(d).

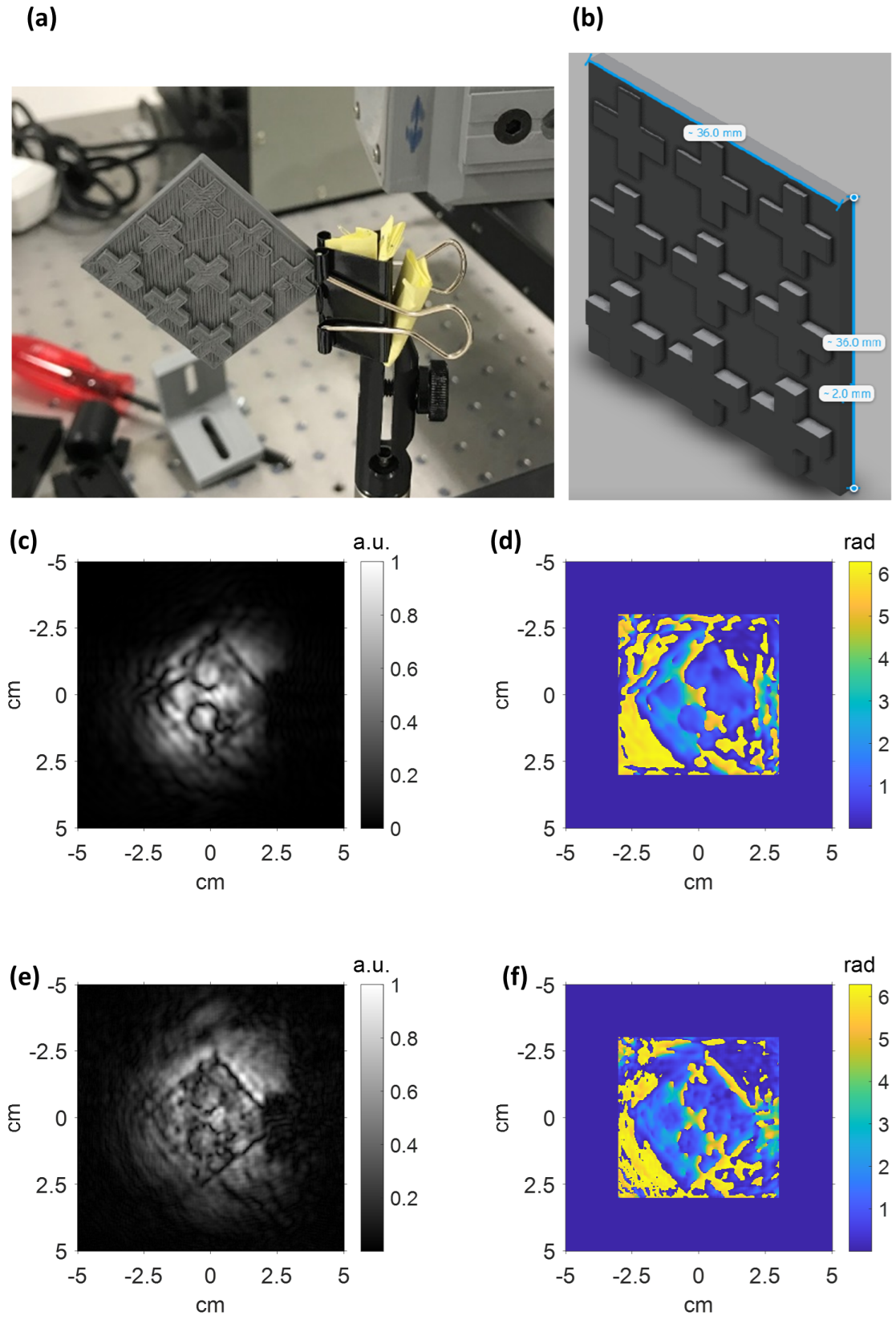

Fig. 4.26 DH reconstruction results of a 3D-printed plate with cross patterns at 280 GHz. A square plate with nine crosses patterns is 3D-printed using PLA filament. (a) and (b) are the photo and the schema of the sample, respectively. (c) and (d) are reconstructed from the off-axis hologram. (e) and (f) are reconstructed using the PR assisted technique.

We were expecting a phase shift that is proportional to the cross thickness. However, it is difficult to extract such correlation from the result in Fig. 4.26(f). This can be attributed to two possible reasons. First off, unwrapping the phase map in Fig. 4.26(f) is a difficult task, especially in the presence of various artifacts and noises. Dual-wavelength DH technique would tackle the phase wrapping ambiguity. Moreover, unlike an engraved dielectric slab, the effective refractive index of a 3D-printed object has significant variations depending on the printing parameters during the fabrication process, such as the layer height, the printing orientation, and the total thickness [168]. Thus the phase map in this experiment only allows qualitatively identifying the inhomogeneity of dielectrics.

4.7 Chapter summary

In this chapter, we implemented the off-axis digital holography with THz radiation. We studied the particular concerns of the off-axis DH setup in the THz range, including the choice of the off-axis angle and the presence of the incoherent thermal background. We developed a PR-based method to improve the off-axis DH reconstruction further. The off-axis hologram reconstruction plays the lead role in retrieving the complex wavefront of the object wave. It provides a reliable initial guess to a subsequent iterative PR process. The PR process further refines the reconstruction result at the cost of only one additional acquisition of the object wave intensity. The convergence can be rapidly achieved after only several iterations, thanks to the credible initial guess. The PR is particularly useful for tackling the imperfect hologram recording condition. The PR would contribute even more to the result if some *a priori* constraints, such as the sparsity and the support region, are applicable to the sample under investigation or multiple intensities can be acquired. This method is proven to be effective with both an off-axis DH setup at 2.52 THz using uncooled microbolometer arrays and a sub-THz setup with a THz FET detector at 280 GHz. Among these two setups, the sub-THz DH has significant potential in various NDT applications since many materials are transparent in this regime. Our experiment at this range showed that sub-THz DH is capable of imaging concealed metallic structures and indicating the inhomogeneities of the dielectrics. Additional information can be retrieved from the phase using the DH reconstruction than the conventional imaging techniques. The single-pixel scanning detector is the current limitation of the employed sub-THz DH setup. The hologram acquisition is time-consuming. Although assembling the THz FET detector array is technically feasible, we did not have a suitable array detector for hologram recording. The recently-released high resolution (1×256 pixel with 0.5 mm pitch) linear scanner developed by Terasense will be a game-changer for sub-

THz DH recording if the sensitivity is satisfying [169, 134]. Limited FOV (less or equal to the size of the detector) is the limitation of both the off-axis DH and the conventional PR methods. Developing imaging plane DH to increase the FOV is not always feasible since inserted optics would cause severe coherent artifacts, as shown in Section 2.4. Ptychography that will be developed in the further chapters will break this limitation.

Chapter 5

Development of Terahertz reflective ptychography

Developing THz imaging under reflective geometry would broaden the application scenarios such as imaging the concealed reflective objects, imaging wound healing, and inspecting packaged integrated circuits, to name a few.

In this chapter, we extend the THz ptychography from transmission geometry to reflection geometry for the first time. Although it seems to be straightforward for this extension, both the experimental setup and the reconstruction deserve careful consideration. Even in the EUV, x-ray, and optical wavelengths where ptychography has become a relatively mature and robust imaging technique, the reflection geometry has performed less than the in transmission mode. The first reflective ptychography setups using optical and EUV radiation were only demonstrated in 2013 [170] and 2014 [171], respectively. We tailored a compact oblique illumination layout for THz reflective ptychography recording. The tilt of the object plane with respect to the recording plane is then numerically corrected. We investigated two metal samples to illustrate the feasibility.

Table of contents

5.1 The choice of configuration for reflection mode THz ptychography

Figure 5.1 shows the schematic of THz ptychography in transmission mode and two possible configurations in reflection mode. As discussed in Section 3.2.1, shortening the recording distance d to the range of 1-2 cm is mandatory when building a THz ptychographic system with currently limited size THz FPAs to achieve a wavelength-scale lateral resolution. It can be easily adapted in practice in the case of transmission configuration, as shown in Fig. 5.1(a). However, such a strict compactness requirement is undoubtedly more challenging to realize in reflection mode.

The normal incidence illumination mode in Fig. 5.1(b) is not suitable in this case. The use of a beam splitter (BS) between the object and the camera restricts the minimum recording distance. For example, with a two-inch BS, the recording distance will be much larger than 3.5 cm (corresponding to $\sqrt{2}/2$ times the diameter). Moreover, the presence of an optical mount for the BS might lead to obstruction and spurious reflection. We should not forget to mention the limited output power of several THz sources due to the THz Gap. In the case where the output power of the THz radiation is not sufficient, the normal incidence illumination configuration is even more inappropriate since the BS will attenuate twice the THz power. On the other hand, the configuration using oblique illumination in Fig. 5.1(c) allows for further reducing the recording distance. The minimum recording distance is restricted by the physical extent of the object and the camera housing. However, the oblique illumination will require tilt plane correction, which will be introduced in the next section. There are many optical configurations to form the probe beam [172]. The single aperture configuration, as shown in the transmission mode, is the simplest configuration. Alternatively,

lens systems can be employed to form the confined probe beam as depicted in the figure, offering more flexibility to the narrowed setup.

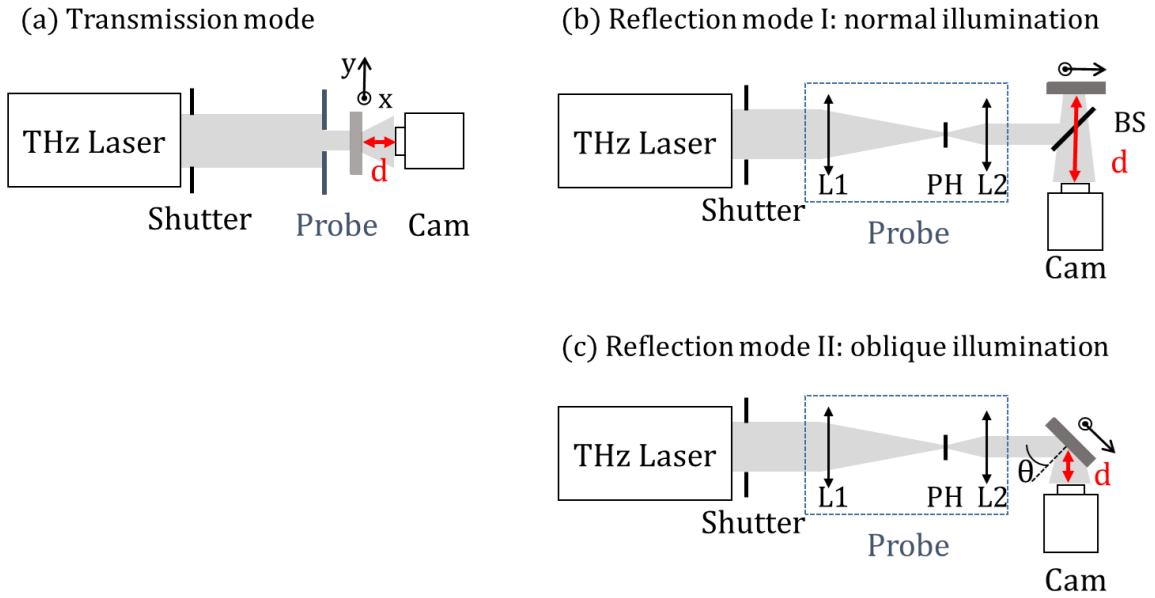

Fig. 5.1 Schematic of ptychography in transmission mode and two possible configurations in reflection mode.

5.2 Tilt plane correction for oblique illumination reflective ptychography

Under oblique illumination, the object is no longer parallel to the recording plane. Therefore, we apply a correction on the recorded diffraction patterns to compensate for the tilt. We employ the notations as depicted in Fig. 5.2. The sample is located in the object plane $(x, y, 0)$. It is illuminated by the incident wave with an angle of incidence θ. The detector is placed in the recording plane (ξ, η, d) which is perpendicular to the specular reflection direction. Therefore, the detection plane is tilted to θ with respect to the object plane. We aim to perform a rotation transformation to relocate the diffraction patterns into the corrected recording plane (ξ', η', d) which is parallel to the object plane. We will denote the original recording plane and the corrected recording plane as (ξ, η) and (ξ', η') for simplicity.

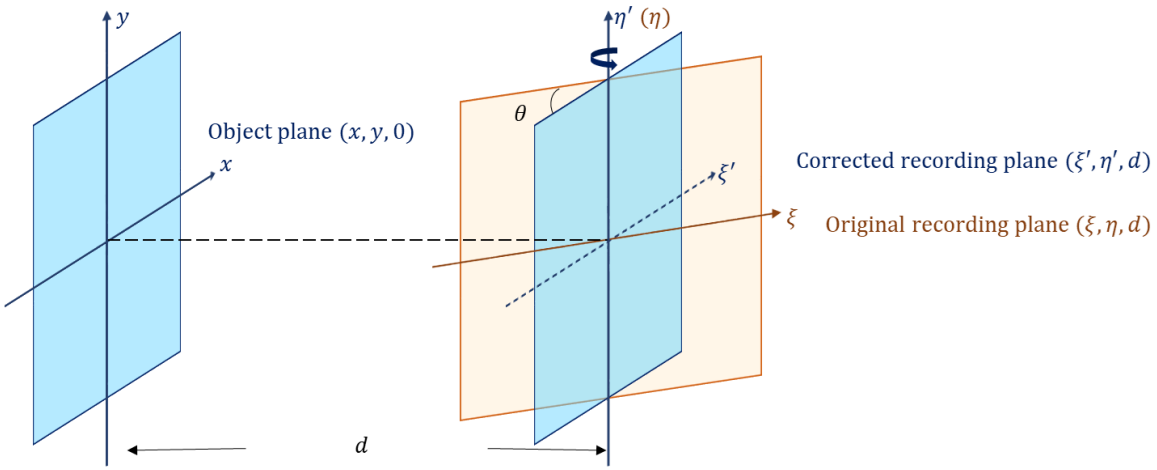

Fig. 5.2 The schematic of the coordinate of the object plane, the tilted recording plane and the recording plane after compensating for the tilt.

The spectrum A_k of each acquired diffraction patterns I_k $(k = 1, \cdots, K)$ is obtained after performing the two-dimensional Fourier transform:

$$A_k\left(f_\xi, f_\eta\right) = \mathfrak{F}\left[I_k(\xi,\eta)\right] = \iint I(\xi,\eta) \times \exp\left[-j2\pi\left(f_\xi \xi + f_\eta \eta\right)\right] \mathrm{d}\xi \mathrm{d}\eta, \tag{5.1}$$

where f_ξ and f_η are the coordinates of the spatial frequency. Assuming that ω and ω' are the directions perpendicular to the original plane and the corrected plane, respectively. The spatial frequency along these directions can be written as $f_{\omega,\omega'} = \sqrt{\lambda^{-2} - f_{\xi,\xi'}^2 - f_{\eta,\eta'}^2}$. In our configuration, the rotation is performed along the η axis. The spatial frequency coordinates of these two planes satisfy the following relation:

$$\begin{pmatrix} f_\xi \\ f_\eta \\ f_\omega \end{pmatrix} = \begin{pmatrix} \cos\theta & 0 & \sin\theta \\ 0 & 1 & 0 \\ -\sin\theta & 0 & \cos\theta \end{pmatrix} \begin{pmatrix} f_{\xi'} \\ f_{\eta'} \\ f_{\omega'} \end{pmatrix}. \tag{5.2}$$

We obtain

$$\begin{cases} f_\xi = \alpha\left(f_{\xi'}, f_{\eta'}\right) = f_{\xi'}\cos\theta + f_{\omega'}\sin\theta \\ f_\eta = \beta\left(f_{\xi'}, f_{\eta'}\right) = f_{\eta'} \end{cases}. \tag{5.3}$$

Moreover, the Jacobian determinant need to be involved when the change of variables takes place in an integral:

$$\mathrm{d}f_\xi \mathrm{d}f_\eta = \left|J\left(f_{\xi'}, f_{\eta'}\right)\right| \mathrm{d}f_{\xi'} \mathrm{d}f_{\eta'} \tag{5.4}$$

with

$$\left|J\left(f_{\xi'},f_{\eta'}\right)\right| = \left|\cos\theta + \sin\theta\frac{f_{\xi'}}{f_{\omega'}}\right|. \tag{5.5}$$

Finally, the diffraction pattern in the corrected coordinate system can be written as

$$\begin{aligned} I'_k(\xi',\eta') = \mathfrak{F}^{-1}\left[A'_k\left(f_{\xi'},f_{\eta'}\right)\right] = \iint A_k\left(\alpha\left(f_{\xi'},f_{\eta'}\right),\beta\left(f_{\xi'},f_{\eta'}\right)\right) \\ \times\exp\left[j2\pi\left(f_{\xi'}\xi'+f_{\eta'}\eta'\right)\right]\left|\cos\theta+\sin\theta\frac{f_{\xi'}}{f_{\omega'}}\right|\mathrm{d}f_{\xi'}\mathrm{d}f_{\eta'}. \end{aligned} \tag{5.6}$$

In practical numerical implementation, the recorded diffract patterns are discrete the complex value of the spectrum $A'_k\left(f_{\xi'},f_{\eta'}\right)$ is then obtained using bi-cubic interpolation method. The corrected diffraction patterns I'_k are then ready to be used as the input for ptychographic reconstruction algorithms. Similar correction method has been performed for oblique-illumination DH [173]. The impact of the correction will be discussed with the obtained results.

5.3 Experimental setup

Figure 5.3 shows a photograph of our built reflective ptychography setup. We wished to work with a relatively small wavelength for the resolution concern. By pumping the methanol vapor with the 9P32 line of the CO2 laser, we obtained an approximate output of 100 mW at 96.5 μm (3.1 THz) with our FIR-295 laser system. We used two TPX lenses L1 and L2, with a focal length of 152.4 mm and 50.8 mm, respectively, to collimate and condense the output laser beam. A pinhole was placed near the focal plane to shelter the spurious reflection. The beam's power was attenuated to an appropriate level (several mW) by a series of attenuators to avoid saturation and microbolometer damage. The diameter of this collimated beam was around 3 mm. The beam impinged the reflective samples with an incidence angle of approximately 45 degrees. Due to the oblique illumination, the probe beam on the object plane should exhibit an elliptical shape. The major axis on the x axis direction was stretched to 4.24 mm, while the minor axis on the y axis direction remained 3 mm. The samples were mounted on an assembled two-axis translation stage. The on-axis accuracy of the translation stages is $\pm$ 5 μm. The sample under investigation was raster-scanned over 8×8 positions with a step of 0.7 mm. The scanning scheme ensured an overlap ratio of 84% and 78% on the x and y directions according to Eq. 3.26. The uncooled microbolometer (MICROXCAM-384i-THz by company INO) with a pixel pitch of 35 μm and 388×284 pixels was located on the plane perpendicular to the specular reflection direction to record

the diffraction patterns. The theoretical observable area of the built system is 18.34 mm × 14.98 mm. The recording distance between the center of the illuminated area of the object plane and the detector was squeezed to 18 mm, expecting an intrinsic resolution of 1.34λ according to Eq. 3.15. The uncooled microbolometer is quite sensitive to the incoherent thermal background. Therefore, we inserted a shutter in the optical path. At each position, ten frames of dark acquisitions were obtained by turning off the shutter prior to recording ten diffraction patterns at the same position but switching on the shutter. The averaged dark offset was subtracted from the corresponding averaged diffraction pattern. The total acquisition procedure took up to five minutes.

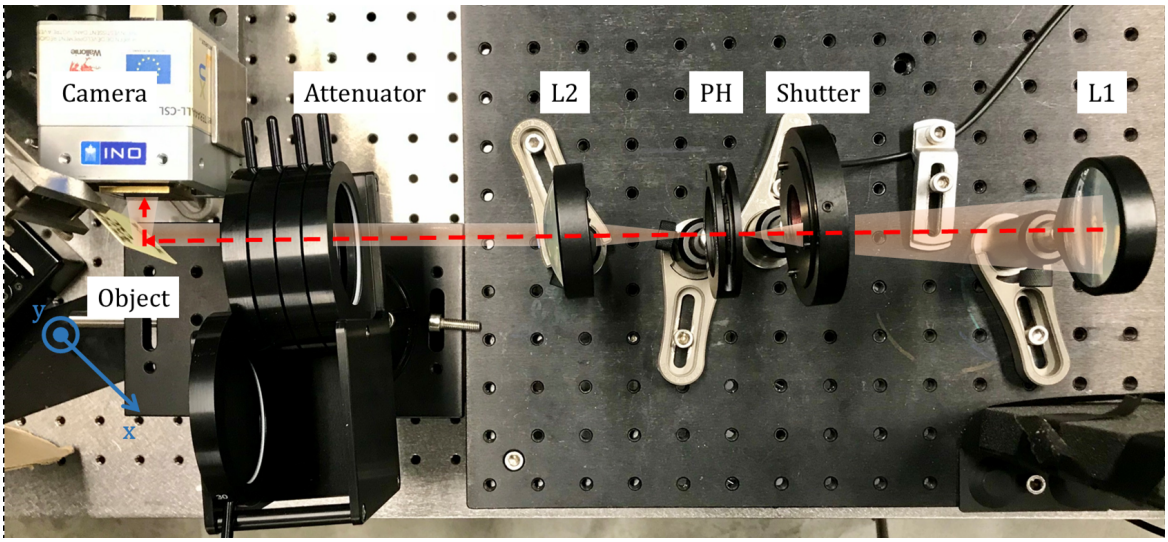

Fig. 5.3 The photograph of Terahertz reflective ptychography setup.

5.4 Results

5.4.1 Embossed object: Polish one-Grosz coin

We firstly investigated the reverse side of a Polish one-Grosz coin with the proposed reflective ptychography setup. As shown in Fig. 5.4(a), the coin is composed of steel bronze with a diameter of 15.5 mm. Its reverse side has the embossed pattern of its value "1 Grosz" as well as one leaf. Figures 5.4(b)-(c) show the profile of the cutting line measured using a digital microscope (VHX-5000, KEYENCE). The height of the embossed number "1" above the surface is 60 ± 1 μm. The width in the middle of the number "1" is 1280 μm.

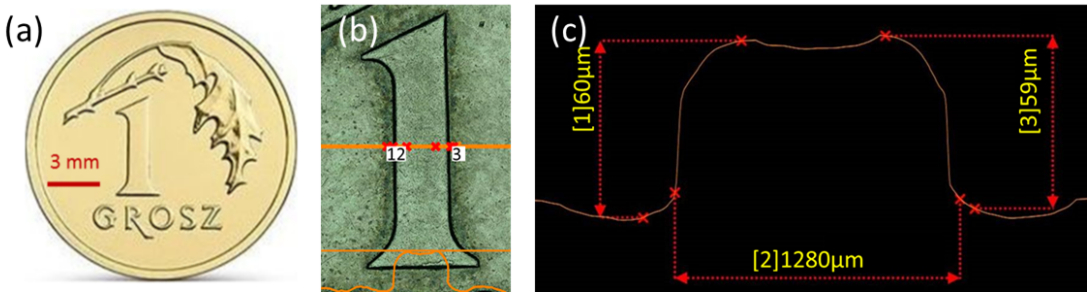

Fig. 5.4 A polish coin one Grosz with embossed patterns is measured using THz reflective ptychography. (a) is he photograph of the sample, (b-c) the profile measured by optical microscopy.

The data acquisition is realized with the proposed method. Figure 5.5 shows an example of different pre-processing steps of the diffraction patterns at one scanning position. Figure 5.5(a) and (b) show the diffraction pattern and the dark offset at the 33rd scanning position. Figure 5.5(c) shows the diffraction pattern after dark removal. Applying the tilted plane correction on Fig. 5.5(c) yields Fig. 5.5(d). The two patterns are displayed under the normalized scale. The latter is parallel to the object plane. Thus the diffraction pattern is stretched to an oval shape along the x axis, which is in line with the expectation. All the diffraction patterns at 64 positions were processed in the same way.

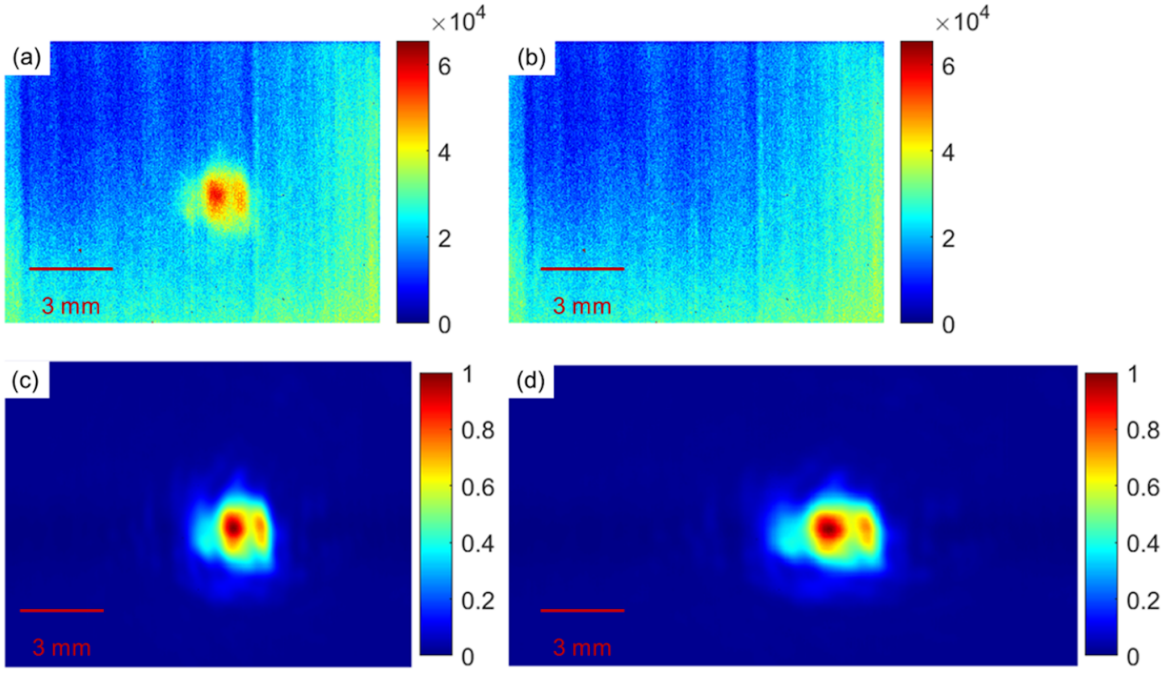

Fig. 5.5 (a) The diffraction pattern at the 33rd scanning position. (b) is the dark offset at the same position. (c) is the diffraction pattern after dark removal. (d) is the diffraction pattern after tilt plane correction.

We used the ePIE algorithm to reconstruct both the uncorrected and the corrected dataset. The weight coefficients α and β defined in Eqs. 3.31 and 3.32 are set to 1. The algorithm converged to consistent results with both datasets after 15 iterations. The retrieved recording magnitudes, the object function, and the probe function no longer vary when increasing the number of iterations. The reconstruction distance of 18 mm gives the optimum in-focus image.

The reconstruction results are shown in Figs. 5.6(a)-(b). When using the uncorrected patterns for the reconstruction, the reconstructed image is out of focus and blurry (Figs. 5.6(a1) and (a2)). A significant improvement had been remarked when using corrected diffracted patterns, shown in Figs. 5.6(b1)-(b2). The reconstructed images show more distinct borderlines. There are also initial signs of reconstructing the letters "GROSZ" at the bottom of the FOV in Fig. 5.6(b1), whereas it was not the case in Fig. 5.6(a1). The width of the number "1" is 41 pixels in Fig. 5.6(a1), corresponding to 1435 µm, while the value is of 37 pixels in Fig. 5.6(b1), corresponding to 1295 µm. The latter is apparently closer to reality. The effectiveness of the tilted plane correction can also be observed from the reconstructed probe distribution in Figs. 5.6(a3)-(a4) and Figs. 5.6(b3)-(b4). The reconstructed probe's shape

changed from a circular to an elliptical form after the tilted plane correction, which is in accordance with the fact that the object is illuminated by an elliptical probe beam under the oblique illumination configuration. The major and minor axes of the main lobe in Fig. 5.6(b3) are around 3.0 and 2.1 mm, respectively. A ratio of 1.4 is due to the 45-degree configuration. There is no phase ramp in the probe's phase distribution in Fig. 5.6(b4), indicating that the tilt plane correction has successfully transformed the oblique illumination configuration into a normal incidence equivalent configuration. As discussed in Section 3.2.2, the height of the object's surface profile $d(x,y)$ and the unwrapped phase variation $\varphi(x,y)$ under the oblique configuration satisfy the following relationship:

$$d(x,y) = \frac{\varphi(x,y)\lambda}{4\pi\cos\theta}. \tag{5.7}$$

We retrieved the topography of the measured object from the reconstructed phase in Fig. 5.6(b2), shown in Fig. 5.6(c). We calculated the height difference between a 21×36 pixels region on the embossed area and two rectangular regions on the adjacent flat areas of the same size. The height of the embossed feature is $59 \pm 1\mu$m.

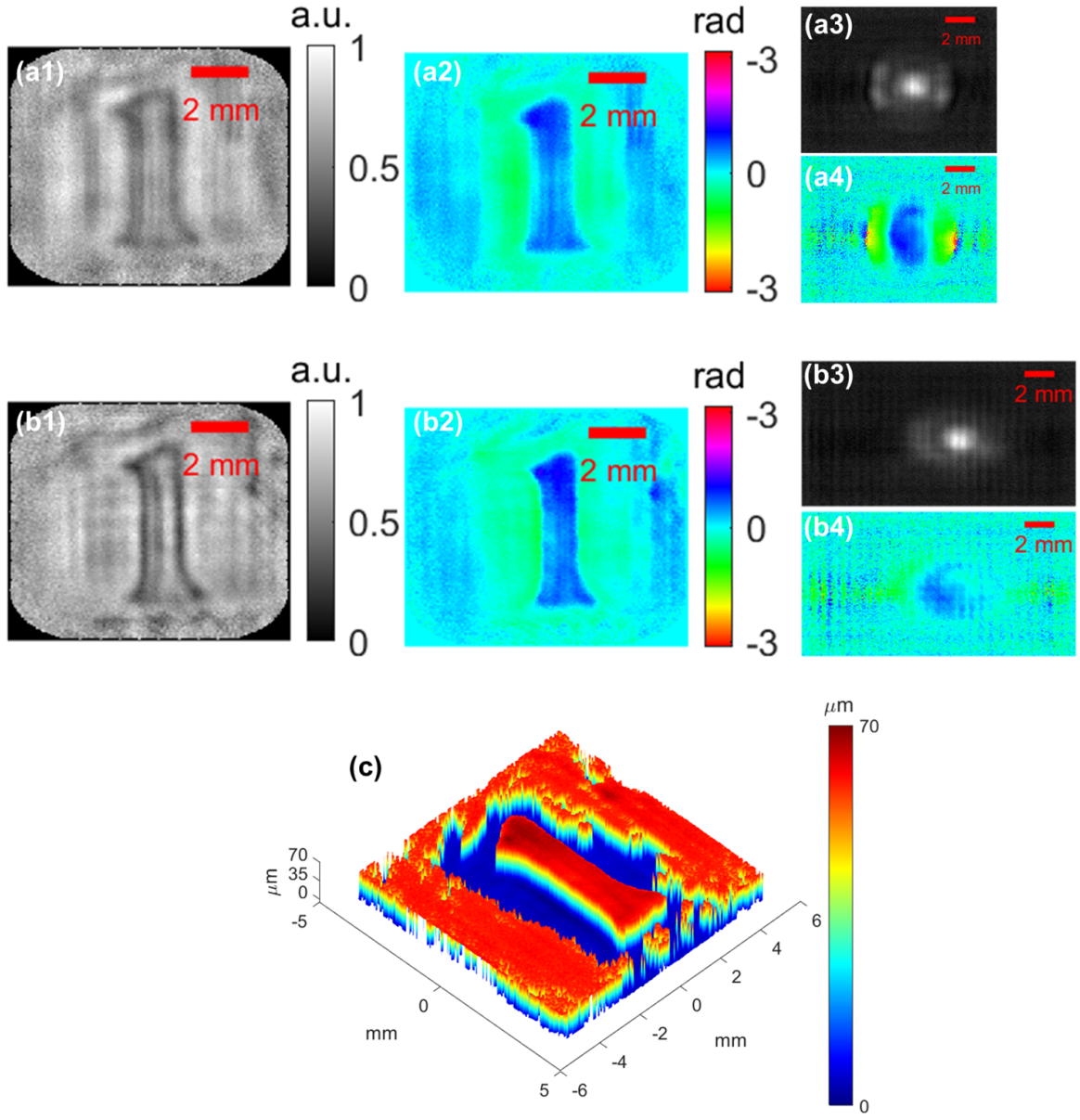

Fig. 5.6 Reconstruction results of the Polish one-Grosz coin. Images in set (a) are the reconstruction obtained without applying the tilted plane correction, whereas the ones in set (b) are reconstructed with corrected diffraction patterns. The numbers 1 to 4 correspond to the reconstructed object amplitude, the object phase, the retrieved probe amplitude, and the retrieved probe phase, respectively. The probe figures share the same colorbar as the reconstructed objects. (c) is the topography of the surface extracted from (b2).

5.4.2 Engraved object: Stainless steel ruler

We also applied the proposed setup to image the engraved profiles on a stainless steel ruler, as shown in Fig. 5.7. Under digital microscopy, the average depth of the engraved pattern is $15 \pm 1\mu$m. The width of each scale mark is 180 μm. The aspect ratio of the number "2" is 1.17.

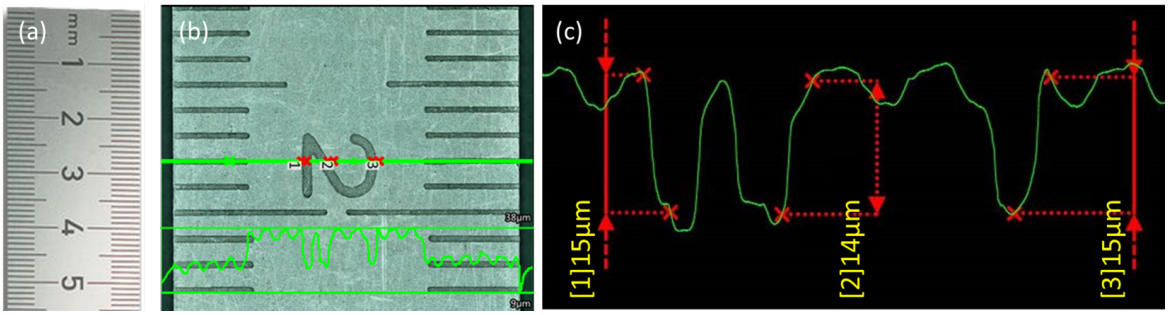

Fig. 5.7 A stainless steel ruler with engraved patterns is measured using THz reflective ptychography. (a) is photograph of the sample, (b-c) shows the profile measured by 250 × microscopy.

The reconstruction parameters are identical to the previous experiment. The results are given in Fig. 5.8. Similar behaviors have been remarked. The reconstruction without the tilt plane correction gives blurry images (Fig. 5.8(a1)-(a2)) compared to the results with the correction applied (Fig. 5.8(b1)-(b2)). The aspect ratio of the number "2" is 1.57 in the former case and 1.26 in the latter case. Thus, the latter is closer to the actual value. The depth of the measured profile is calculated from Fig. 5.8(b2), plotted in three-dimension in Fig. 5.8(c). The depth of the engraved features on the stainless steel ruler is around 11 ± 1 μm.

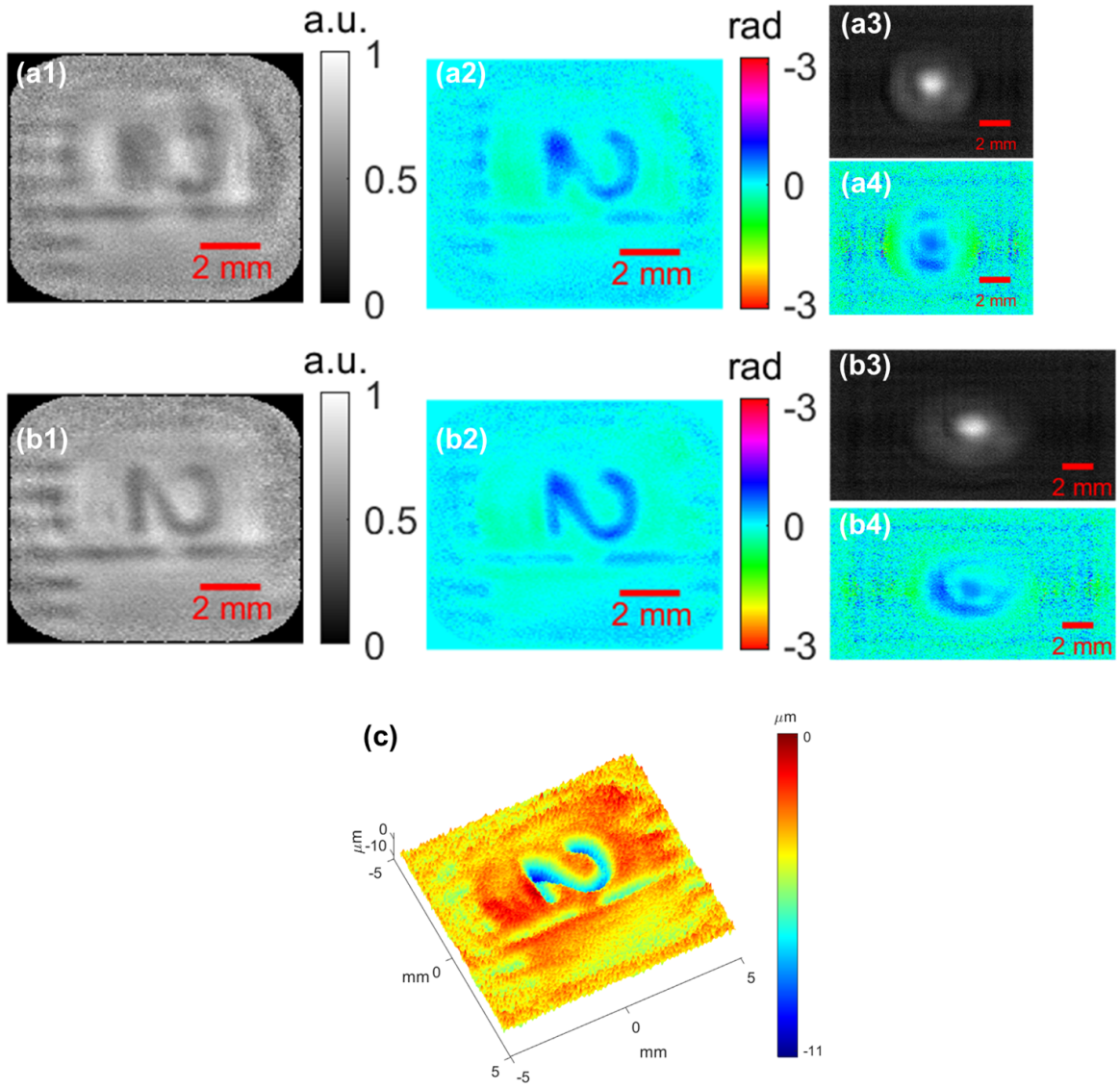

Fig. 5.8 Reconstruction results of the engraved profile on a stainless steel ruler. Images in set (a) are the reconstruction obtained without applying the tilted plane correction whereas the ones in set (b) are reconstructed with corrected diffraction patterns. The numbers 1 to 4 correspond to the reconstructed object amplitude, the object phase, the retrieved probe amplitude, and the retrieved probe phase, respectively. The probe figures share the same colorbar as the reconstructed objects. (c) is the topography of the surface extracted from (b2).

5.5 Discussion

In the above two experiments, the tilt plane correction significantly improved the reconstruction quality. The reason is that the stretching of the probe under the oblique illumination

modified the overlapped region shared by two adjacent positions. This modification is an important nuisance for ptychography since ptychography relies on the pre-knowledge of the displacement to find the object function that is consistent with all the measured diffraction patterns. We summarized the two phase measurement results in Table 5.1. We used the actual height measured by the optical microscopy to compute their theoretical phase variations at 96.5 μm. The measured phase variation obtained from Fig. 5.6(b2) and Fig. 5.8(b2) as well as the calculated height are listed. The standard deviation of the phase map is given in the parentheses. A phase resolution of 0.1 rad is estimated during our experiment, which corresponds to a depth variation of 1.1 μm ($\lambda/88$).

Table 5.1 Summary of depth measurements using THz reflective ptychography

	Polish 1 Grosz coin	Stainless Steel ruler
Actual height [μm]	60 (1.0)	-15 (1.0)
Theoretical phase value [rad]	5.5 (0.1)	-1.4 (0.1)
Measured phase value [rad]	5.5 (0.1)	-1.1 (0.1)
Calculated height [μm]	59 (1.1)	-11 (1.1)

The result obtained hereby is comparable to that in transmission mode reported in [23]. Despite this, currently, the algorithm stagnated after 15 iterations to the best solution, while better reconstruction quality should be expected. We analyze the possible factors that contribute to the limited quality of recorded diffraction patterns. The flawed recorded dataset limits the current reconstruction quality. First off, the noise, such as dark noise residual and spurious reflection, especially the multiple reflections that travel back and forth between the camera window and the reflective sample presented in each acquisition, degrades the dataset consistency [174]. The microbolometer manufacturer INO provides anti-reflective coating options for a given working wavelength, which would benefit the experiment. However, these coatings would lead to a decrease in transmission when working at different THz spectral ranges. The limited dynamic range is another issue. The intensity distribution diffracted by a pinhole has an extended dynamic range. The zero-order component has orders of magnitude more intense than the scattered signal [175]. The microbolometer of the INO camera is incapable of faithfully recording the diffraction patterns with the full dynamic range. In [176], the authors have also reported the unsatisfactory sensitivity and stability during diffraction pattern recording when working with the INO camera during their preliminary experiment.

In the next chapter, we will further investigate and propose solutions to circumvent these limitations.

5.6 Chapter summary

In this chapter, we proposed a THz reflective ptychographic imaging system for the first time. The large working wavelength makes the compactness of the system more demanding. We picked the oblique illumination configuration after having investigated different options for recording geometries. The tilt plane correction was proposed to ensure a better reconstruction. We demonstrated the feasibility by imaging the surfaces of two metal samples. It is worth noting that there is limited research in THz ptychography. Many experimental parameters, such as the overlap rate, or the probe size, were empirically inherited from the X-ray or optical ptychography. We pointed out some possible improvements that will be further investigated in the next chapter. More challenging cases such as imaging concealed reflective objects or complex samples with low reflectivity could be envisaged once better reconstruction quality is achieved.

Chapter 6

Further improvements of Terahertz ptychography towards biomedical sample imaging

Investigating biological tissue with THz radiation has always been of great interest. In the TERA4ALL project consortium, the INTELSIG research unit of te University of Liège investigates the human breast cancer margins assessment via THz-TDS imaging technique in order to accurately remove the cancerous part with a minimal layer of healthy tissue during the breast-conserving surgery. During the first phase, the dehydrated paraffin-embedded samples are studied. These dehydrated biomedical samples exhibit good transparency at the FIR range. We attempt to image these samples with THz ptychography. These samples have complex structures and unknown refractive index distributions, whereas the imaging quality and stability of our first THz ptychographic development need to be further improved. Another concern is imaging efficiency when the samples have a larger size. Although ptychography is a full-field imaging technique with the possibility to image extended objects, ptychography still requires collecting and processing multiple diffraction patterns. Therefore, optimizing the scanning scheme is necessary to image a large FOV more efficiently. This chapter explores the solutions to further improve our ptychographic experimental setup to meet these requirements.

Table of contents

6.1 First attempt: Imaging a reduced-size sample

6.1.1 Experimental setup and sample description

As the first attempt, we simply modified the THz reflective ptychography setup in Fig. 5.3 back to in transmission mode. The sample mounted on the translation stage is impinged by the probe beam. The THz camera is placed 11 mm away from the sample to record the diffraction patterns. We set the working wavelength back to the strongest emission line, at 118.83 μm (2.52 THz) because the laser was less stable at the moment when we performed the experiment. As in the reflective ptychography presented in Chapter 5, the scan was performed over an 8×8 grid with a step of 0.7 mm, leading to a overlap ratio of 78% and a theoretical observable region of 18.34×14.98 mm^2. However, as remarked during the reflective experiment, only the central area around 5×5 mm^2 was well reconstructed.

The paraffin-embedded human breast tissue samples to be tested are provided by the biobank of Liège University Hospital (CHU). Such samples were sliced into 50 μm from a formalin-fixed, paraffin-embedded breast tissue block obtained from one patient. The sliced tissue is mounted on a 2 mm-thick Teflon plate. These steps followed a standard protocol for histology slide preparation [177]. The actual sample, as shown in Fig. 6.20 in Section 6.3.3 has a typical size of 20 mm $\times$ 20 mm. The actual sample contains both healthy and

cancerous regions. When preparing these samples, an additional pair of 4 µm-thick slices (the slice before and after the 50 µm-thick sample under investigation) are mounted on glass slides for a classic histopathological assessment.

Measuring the full-sized sample will require about 4 times more of the scanning positions on each direction, which will consume 16 times more acquisition time using the current setup. However, the stability of the FIR laser cannot guarantee the long-time acquisition. Therefore, due to the limited FOV of the current setup, we first used a reduced-size (5 mm $\times$ 5 mm) paraffin-embedded human breast cancer tissue sample to verify the imaging quality for the preliminary test as shown in Fig. 6.1(a). Then, we observed the sample under optical microscopy, shown in Figs. 6.1(b) and (c), to verify if the ptychographic reconstruction can recover the same morphology of the sample under investigation.

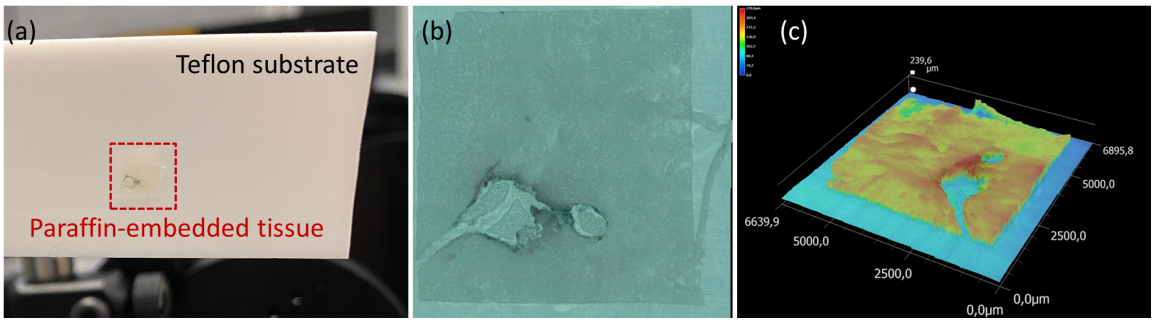

Fig. 6.1 A 5 mm $\times$ 5 mm paraffin-embedded human breast cancer tissue sample (a) is used for our preliminary test. (b) and (c) are the photograph and the morphology of the sample under optical microscopy.

6.1.2 Impact of the background noise residual

We performed the data acquisition, dark removal pre-processing, and the ePIE reconstruction as introduced in Chapter 5. The tissue is Figure 6.2(a1) shows the 30th diffraction pattern after the dark removal pre-processing. Unfortunately, the reconstruction result after 100 iterations based on the dataset could not correctly recover the sample's information. Just like the reflective ptychography experiment, the algorithm stagnated after 15 iterations. Grid-shaped artifacts are visible on the reconstructed object (Figs. 6.2(a2) and (a4)) and probe function (Figs. 6.2(a3) and (a5)), even in the region where the probe function was supposed to be zero.

After reviewing relevant literature[174, 178, 179], we learned that the success of ptychography reconstruction is highly dependent on the SNR of the recorded dataset. Different sources of noise that contaminate the dataset lead to data inconsistencies. We identified the presence of background noise residual in the pre-processed diffraction pattern, as shown in Fig. 6.2(a1). The intensity in the red rectangle area should have been zero. However, the pixels in these region has a mean value of 0.17 (std: 0.084). As suggested in [174], we estimated the mean value and the standard deviation of the red rectangle area. The mean value is subtracted from the entire image. After the subtraction, all the values below three times the standard deviation were considered as pixels that contain only the noise. Their values are set to zero. Figure 6.2(b1) shows the same diffraction pattern after denoising. The reconstruction based on the denoised dataset gave satisfying results, shown in Figs. 6.2(b2)-(b5). Details such as the broken hole and the excessive tissue stripe are visible in Fig. 6.2(b2) and Fig. 6.2(b4). The reconstructed probe function is also closer to reality.

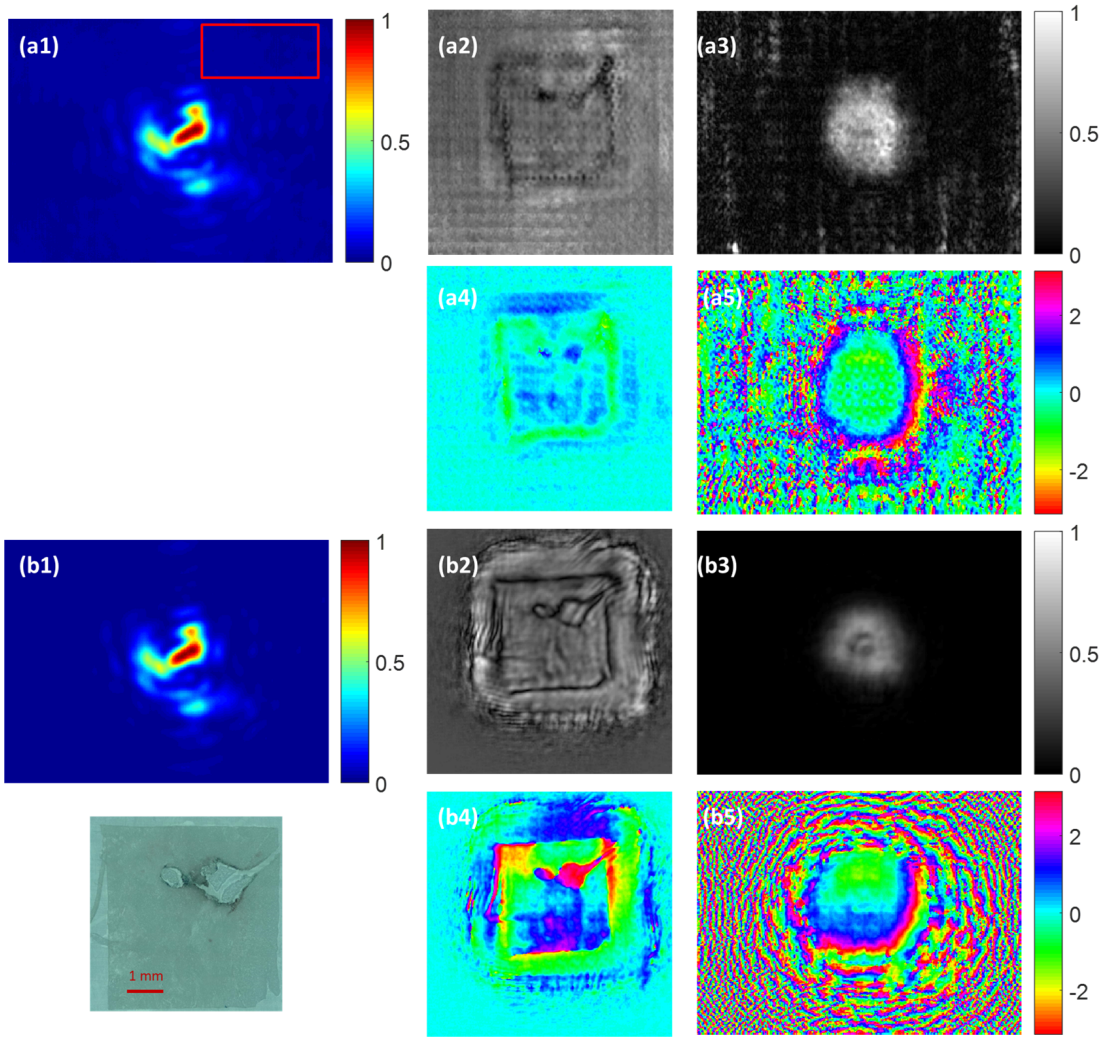

Fig. 6.2 Impact of the background noise residual in ptychographic reconstruction of the reduced-size tissue sample. Images in set (a) correspond to the originally recorded diffraction patterns (a1) and their reconstruction results (a2-a4). Images in set (b) correspond to the denoised diffraction patterns (b1) and their reconstruction results (b2-b4). The background noise is estimated in the red rectangle area in (a1).

In ptychography, the performance of the reconstruction at each iteration j can be assessed with the error metric E_j, defined as

$$E_j \equiv \frac{\sum_{k=1}^{K}\sum_{x,y}\left(\sqrt{I_k(x,y)} - \left|\Psi_{j,k}(x,y,d)\right|\right)^2}{\sum_{k=1}^{K}\sum_{x,y} I_k(x,y)}. \tag{6.1}$$

The evolution of the error metric using original dataset and the denoised dataset are plotted in Fig. 6.3. The reconstruction using denoised dataset converged to a lower error value whereas

the reconstruction using original dataset stagnated.

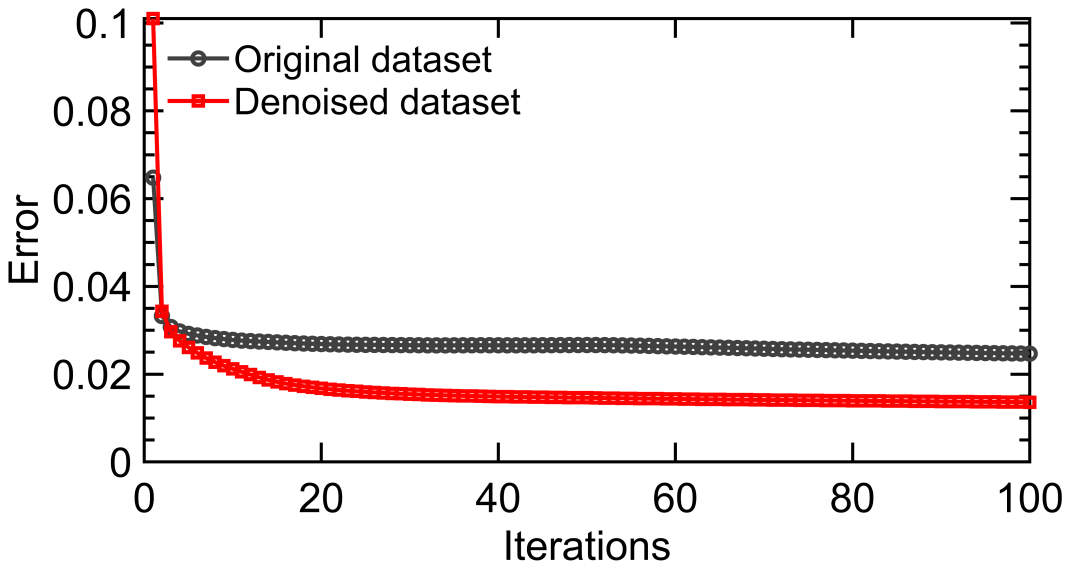

Fig. 6.3 Evolution of the error metric using original dataset and the denoised dataset over 100 iterations.

We also applied the denoising method to the one-Grosz coin (in Section 5.4.1) dataset acquired under the reflective configuration. The comparison between the original dataset and the denoised dataset is presented in an analogous way in Fig. 6.4. The denoising operation removed the grid-like artifact. Moreover, the effective reconstructed area is enlarged on Figs. 6.4(b2) and (b4), and the letters "GROSZ" are recognizable.

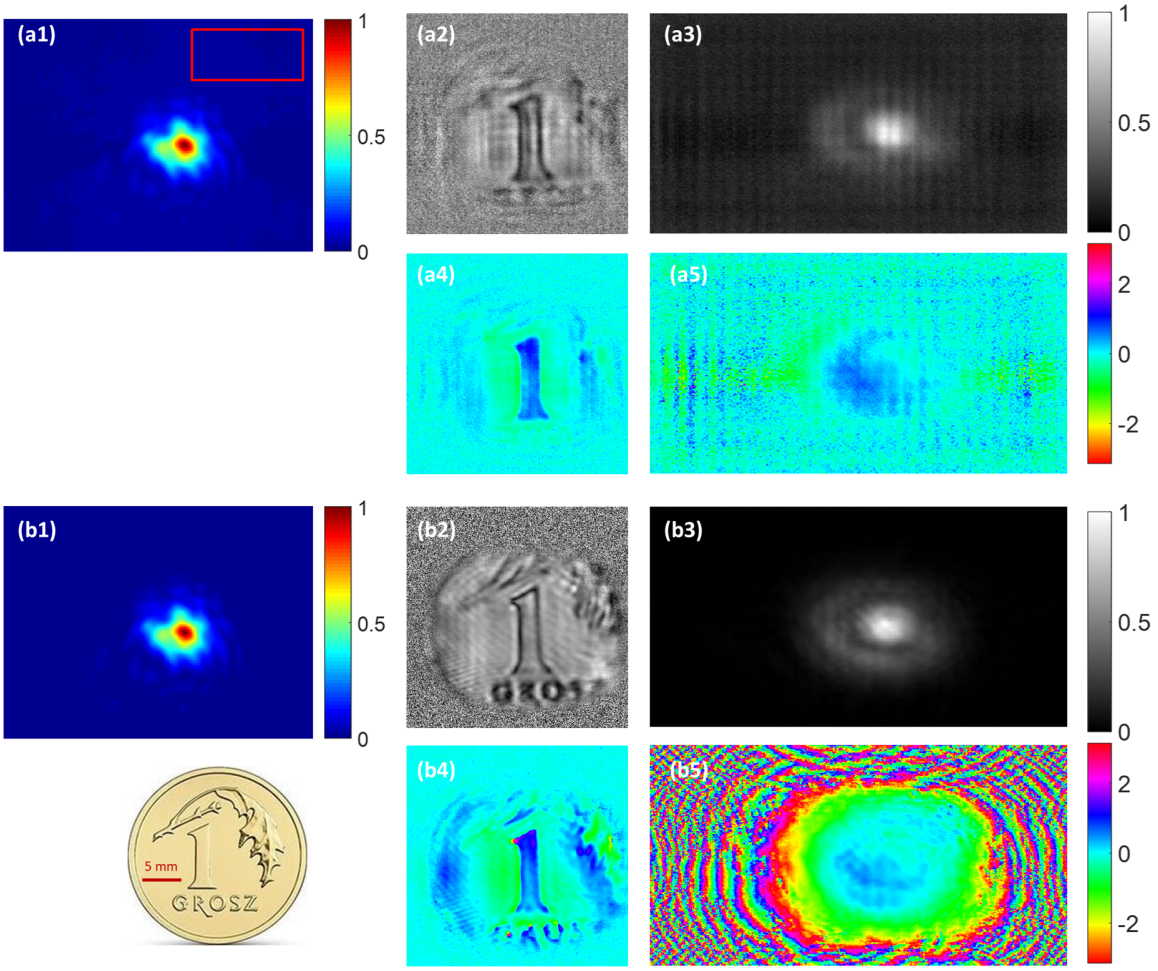

Fig. 6.4 Impact of the background noise residual in ptychographic reconstruction of the dataset recorded in reflection mode. Images in set (a) correspond to the original recorded diffraction patterns (a1) and their reconstruction results (a2-a4). Images in set (b) correspond to the denoised diffraction patterns (b1) and their reconstruction results (b2-b4). The background noise is estimated in the red rectangle area in (a1).

We successfully reproduced the impact of the background noise residual via simulation, shown in Fig. 6.5. With the presence of 1% background noise residual, the reconstruction result in Fig. 6.5(c) exhibits similar grid-like artifacts. The reconstruction based on the denoised dataset in Fig. 6.5(d) recovered from such artifacts. The very slight degradation of reconstruction quality in Fig. 6.5(d) compared to the noise-free case in Fig. 6.5(b) is due to the loss of weak signals. Therefore, we validate the denoising procedure as a simple yet powerful way to improve the ptychography reconstruction. This procedure will be applied to the further experimental dataset.

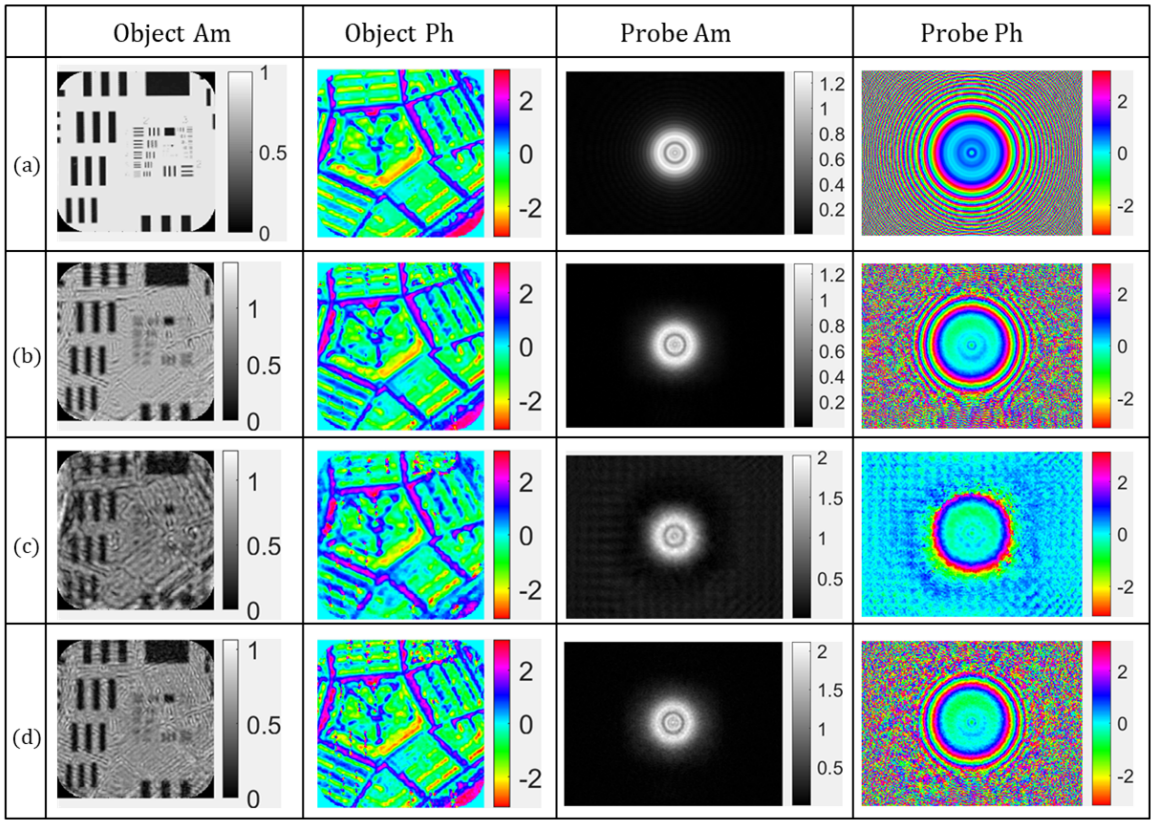

Fig. 6.5 Simulation of the impact of thermal background noise residual. Images in (a) are the input data for simulating the diffraction patterns in the ptychographic dataset. (b) are the reconstruction results after 50 iterations without the presence of thermal background noise. (c) are the reconstructed with the ptychographic dataset used in (b) with additional 1% thermal background noise residual. (d) are reconstructed with the noisy ptychographic dataset but with the denoising method applied on the diffraction patterns before the reconstruction.

6.2 Further improvement of THz ptychographic data acquisition

6.2.1 Enlarging the FOV: choice of the probe beam size

Using the original setup for imaging the actual sample would require much more scanning positions, leading to more time-consuming data acquisition and processing. Consequently, reducing the data acquisition time could be especially advantageous in our case since the FIR laser is not stable. Therefore we seek for a solution to efficiently enlarge the FOV. A reduced-sized illumination beam needs to be employed to meet the oversampling condition

in a conventional phase retrieval experiment where only one diffraction pattern is measured. However, the multiple overlap acquisitions provide the oversampling condition in ptychography. Therefore, the restriction of illumination size is not applicable in ptychography. According to the definition of overlap ratio expressed in Eq. 3.26, employing a larger probe beam size allows enlarging the scanning step proportionally while maintaining the same overlap ratio. Since the effective FOV of ptychography is determined by the scanning step and the number of acquisitions. A Larger scanning step results in recording the same FOV efficiently with fewer acquisitions.

We simulated four cases to understand the impact of the probe beam size. In the simulation, we kept the overlap ratio as a constant, *i.e.*, 78.8%, as the original experimental configuration. The simulated probe beams with four pinholes with a diameter of 3.3 mm, 6.6 mm, 9.9 mm, and 13.2 mm, respectively. The scanning steps are adjusted to 0.7 mm, 1.4 mm, 2.1 mm, and 2.8 mm, according to Eq. 3.26. The simulated object is scanned at 8×8 positions to record 64 diffraction patterns. Other parameters remain the same as the original experimental configuration described in Section 6.1.1. We launched the ePIE algorithm for the four datasets with 50 iterations.

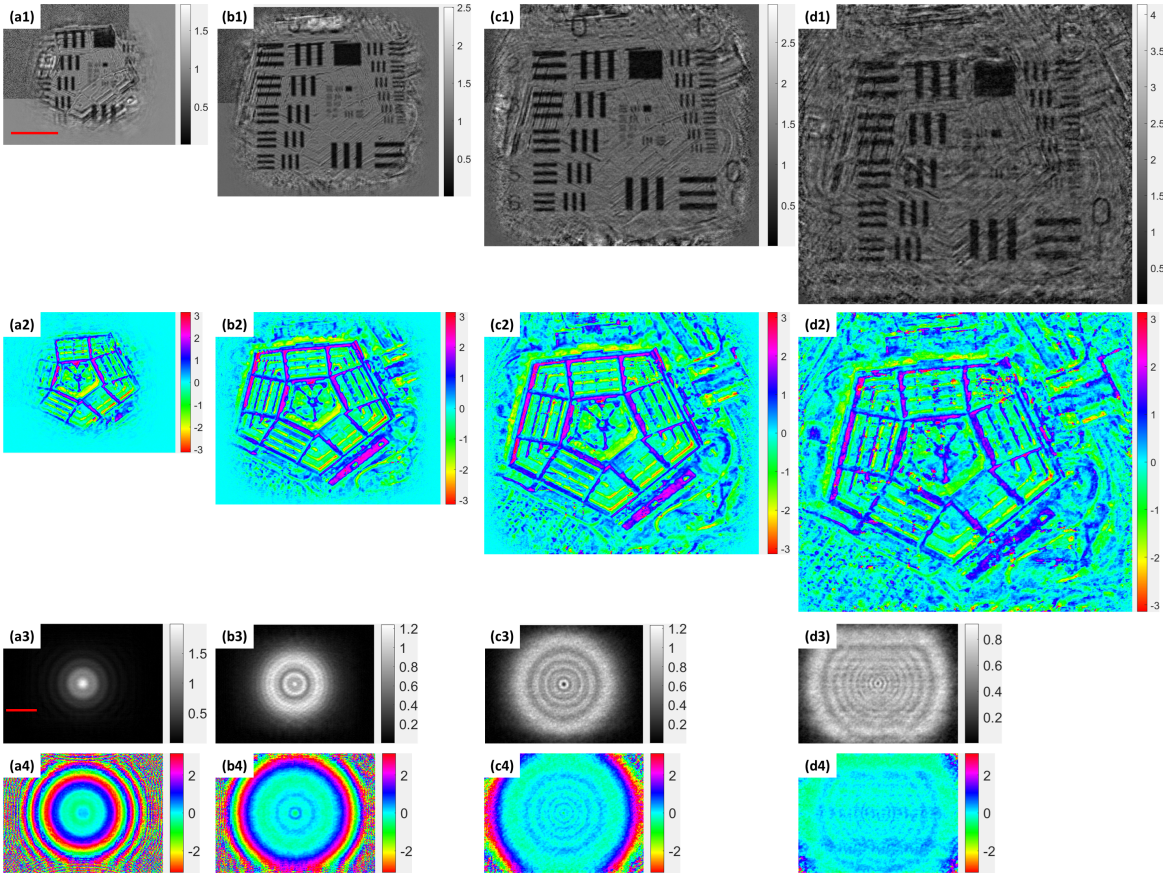

Fig. 6.6 The impact of the probe beam size in ptychography. (a-d) are the reconstruction results after 50 iterations with simulated ptychographic dataset of 8×8 scanning positions. The overlap ratio is fixed to 78.8% in the four cases. The employed pinholes for probe beam creation have a diameter of (a) 3.3 mm, (b) 6.6 mm, (c) 9.9 mm and (d) 13.2 mm. Scale bar: 3 mm.

The reconstructed results are given in Fig. 6.6. The increase in FOV is significant. Moreover, we observed that the border region is better reconstructed in the cases where a larger probe beam is employed. To quantitatively evaluate the results, we computed the SSIM (Eq. 4.7) and the correlation coefficient (CC) between the reconstruction results and the input image on the central 400×400 pixels. The definition of CC is expressed as

$$\mathrm{CC}(x,y) = \frac{\sum (x-\mu_x)(y-\mu_y)}{\sqrt{\sum\sum (x-\mu_x)^2 \times \sum\sum (y-\mu_y)^2}}, \tag{6.2}$$

where μ_x, μ_y, σ_x, σ_y and σ_{xy} are the local means, standard deviations, and cross-covariance of images x and y. Similar to SSIM, CC ranges between [0,1]. Higher CC indicates a better

reconstruction.

The comparison is summarized in the Table. 6.1. The probe formed by the 6.6 mm aperture gives optimum reconstruction quality. From the four phase maps in Fig. 6.6, we observed that the cross-talk is more severe in (c) and (d) than in (b). One explanation is that in cases (c) and (d), the probe beams are close to or even superior to the size of the detector array. Consequently, the diffraction pattern at the border of the probe cannot be recorded. Data redundancy is not guaranteed. Moreover, the drastic intensity change on the border causes artifacts as in the DH cases explained in Section 4.4.3. Such artifacts already appear in the reconstructed probe maps in Figs. 6.6(d3) and (d4).

Table 6.1 Quantitative comparison of reconstruction results in Fig. 6.6

Pinhole diameter [mm]	3.3	6.6	9.9	13.2
Scanning step [mm]	0.7	1.4	2.1	2.8
Scanning position	64	64	64	64
Overlap ratio [%]	78.8	78.8	78.8	78.8
Theoretical FOV [mm^2]	14.98×18.34	19.88×23.24	24.75×28.14	29.68×33.04
Amplitude CC	0.51	0.94	0.92	0.74
Phase CC	0.66	0.94	0.93	0.81
Amplitude SSIM	0.33	0.48	0.34	0.15
Phase SSIM	0.25	0.60	0.47	0.24

To ensure that such a probe can be generated experimentally, we drilled three holes with a diameter of 3.3 mm, 6.6 mm, and 9.9 mm on a metal plate and measured their diffraction pattern. These hole apertures are placed 5 cm in front of the THz camera. The measured diffraction patterns are in excellent accordance with the simulated results, shown in Fig. 6.7. Since the simulation suggested that the probe beam formed with the 6.6 mm aperture gives the optimum solution, it is picked to generate the probe beam in the further experimental setup.

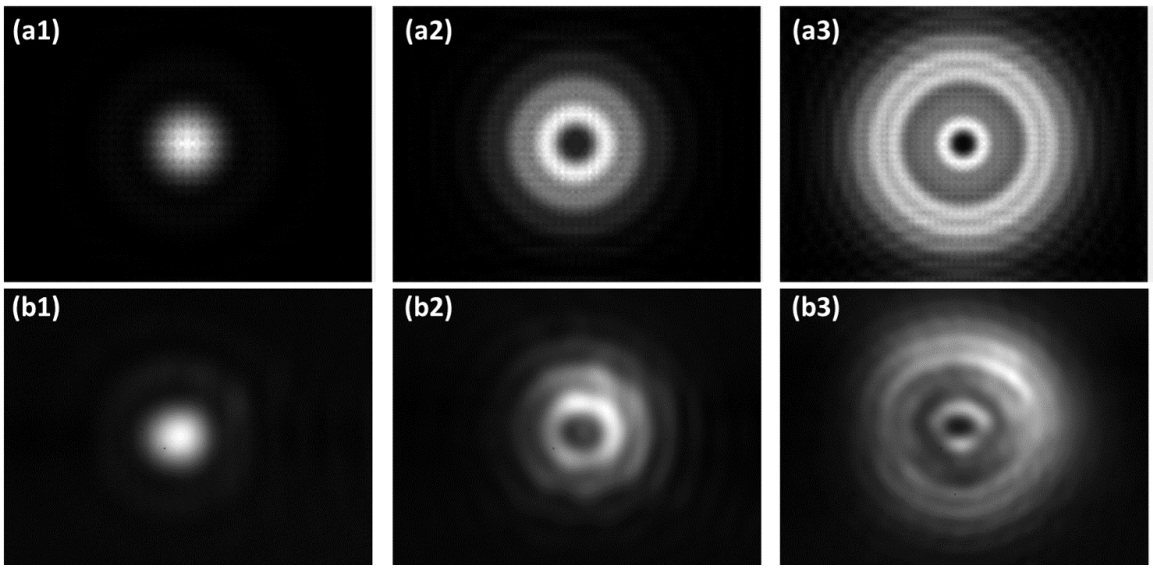

Fig. 6.7 Comparison of measured diffraction patterns (b1-b3) and the simulation results (a1-a3) of different pinholes with a diameter of 3.3 mm, 6.6 mm and 9.9 mm.

6.2.2 The benefit of speckle illumination

The implementation of optical [172, 180], X-ray [175, 181], and electron [182] ptychography has reached a consensus that speckle illumination created by inserting a diffuser is appreciable for blind ptychography reconstruction which allows recovering the probe function and the object wave function simultaneously. Hereby we illustrate the benefit of employing a diffuser for speckle illumination in our THz ptychography configuration.

The randomized phase created by the diffuser introduces higher incident angles in the probe beam. As a result, the incident beam is spread to a broader area on the detector. The dynamic range of the diffraction pattern using the speckle illumination is reduced compared to a plane wavefront since the pixels on the border area of the detector receive more flux. These pixels have higher SNR. Therefore, they can be recorded more reliably with low dynamic range detectors in the ptychographic dataset. Figure 6.8 demonstrates the benefit of dynamic range decrease using speckle illumination. We simulated the ptychographic recording with a plane wavefront probe and a randomized probe, respectively. The diffraction patterns are cropped by the THz camera aperture. To simulate a camera with a limited dynamic range, we set the weak signal (1% of the maximum value) to zero and then quantized the diffraction patterns to 16 levels. In reality, the dynamic range limitation can be more restrictive. A pure amplitude object, the USAF target is used as the original input. Figures 6.8(a1) and (b1)

are the diffraction patterns at the same scan position recorded with a plane wavefront probe and a randomized probe, respectively. We observe that more high-frequency signal on the border area is preserved in Fig. 6.8(b1). Consequently, its reconstruction result in Fig. 6.8(b2) exhibits higher resolution than the plane wavefront illumination case in Fig. 6.8(a2) when comparing zoom-in image of the central region inside the red square. We also observe that the background in Fig. 6.8(b2) is more homogeneous than in Fig. 6.8(b1).

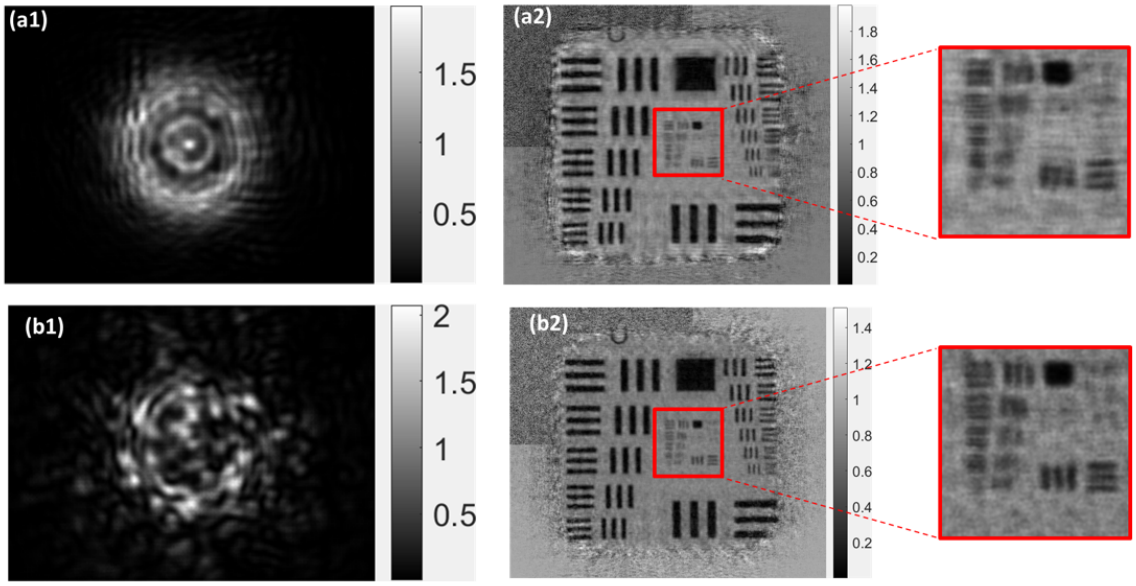

Fig. 6.8 Simulation results of ptychographic recording with speckle illumination. (a1) is the diffraction pattern with a plane wavefront probe whereas (b1) is recorded with a randomized wavefront probe generated by a diffuser. (a2) and (b2) are the reconstructed amplitude after 50 iterations using the plane wavefront dataset and the diffuser illuminated dataset, respectively.

We simulated another case where the object is considered difficult to be reconstructed, shown in Fig. 6.9. The object is a highly transparent slab with little structures. Its phase is in the range of $[0,2\pi]$. All the other parameters are the same except for the presence of the diffuser. In this case, we did not degrade the dataset with quantization or saturation. After 50 iterations, the reconstruction failed in Fig. 6.9(b), whereas the object is successfully reconstructed in Fig. 6.9(d) thanks to the diffuser. Without the presence of the diffuser, we need to increase the overlap ratio to higher than 90% to get the similar results in Fig. 6.9(d). Comparing the probe beam in (a) and (c), the probe generated with the diffuser covers a larger extent with adequate intensity. Therefore, the effective overlap ratio is higher thanks to the

diffuser illumination. A larger data redundancy guaranteed the success of the reconstruction.

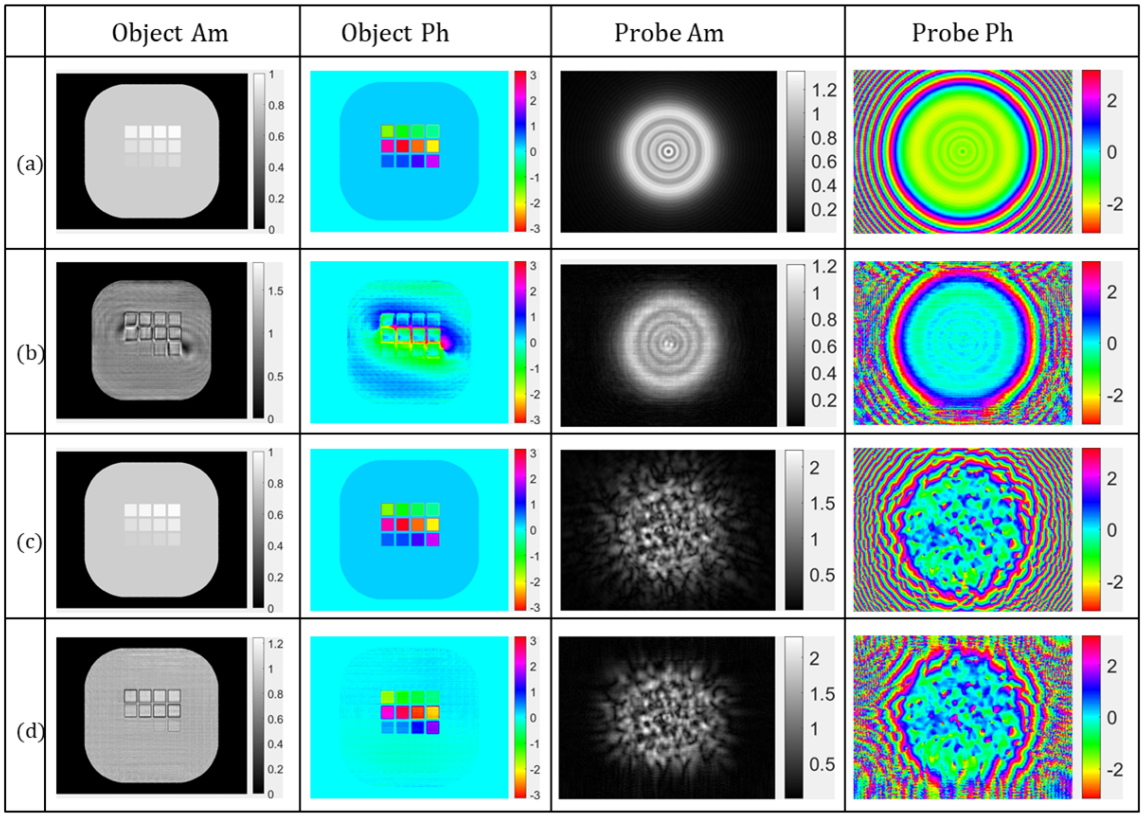

Fig. 6.9 Simulation result of ptychographic reconstruction of an object that is difficult to be reconstructed. (a) and (c) are the input for the simulation with plane-wave illumination and speckle illumination, respectively. (b) and (d) are the reconstructed results after 50 iterations in these two cases.

Since THz diffusers are not commercially available, we found an inexpensive way to fabricate our own piece of diffuser. We knew that wavelength-scale structure will help scatter the coherent light and create speckle patterns. We adhered several pieces of porous PE foam to a PP substrate, as shown in Fig. 6.10. Figure 6.10 shows the optimized experimental setup for THz ptychography. The self-made diffuser is mounted in front of the 6.6 mm-diameter aperture to generate the probe beam with randomized phase. The sample is placed 3 cm away from the aperture. The distance between the sample and the camera is about 11 mm.

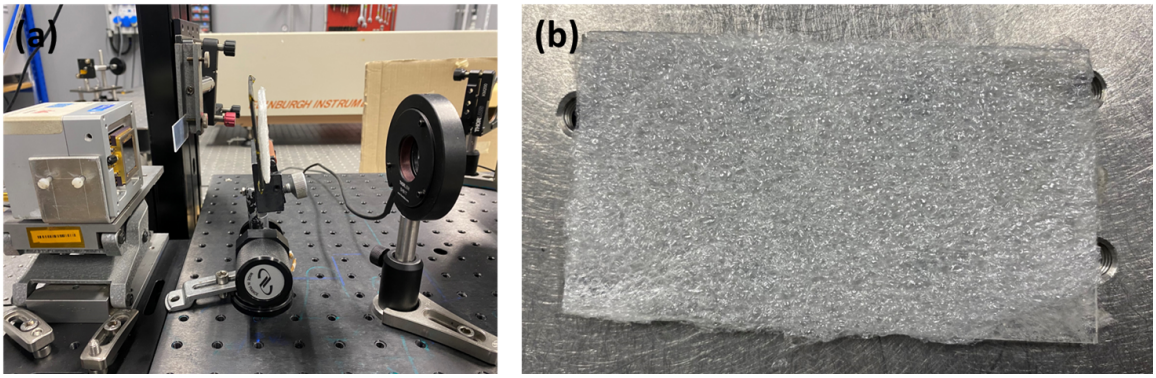

Fig. 6.10 (a) Photograph of the final optimized experimental setup for THz ptychography. A 6.6 mm aperture combined with a self-made diffuser, as shown in (b), is used to generate the probe beam. The distance between the aperture and the sample on the photo was modified for the sake of visibility.

6.3 Experimental results

6.3.1 Amplitude contrast object: A USAF target for lateral resolution characterization

We first measured an amplitude contrast USAF target to characterize the lateral resolution of the proposed THz ptychographic imaging system. We utilized a clear optical path USAF target from Edmund (Fig. 6.11(b)) as a master for sample fabrication. The pattern was transferred to a PP slab by depositing 200 nm silver coating, as shown in Fig. 6.11(a). This operation was performed at the surface laboratory of the CSL. The sample was mounted on the translation stage and scanned over 13×13 positions with a step of 1.4 mm. The scanning scheme allows a theoretical imaging area of 26.88×30.24 mm^2.

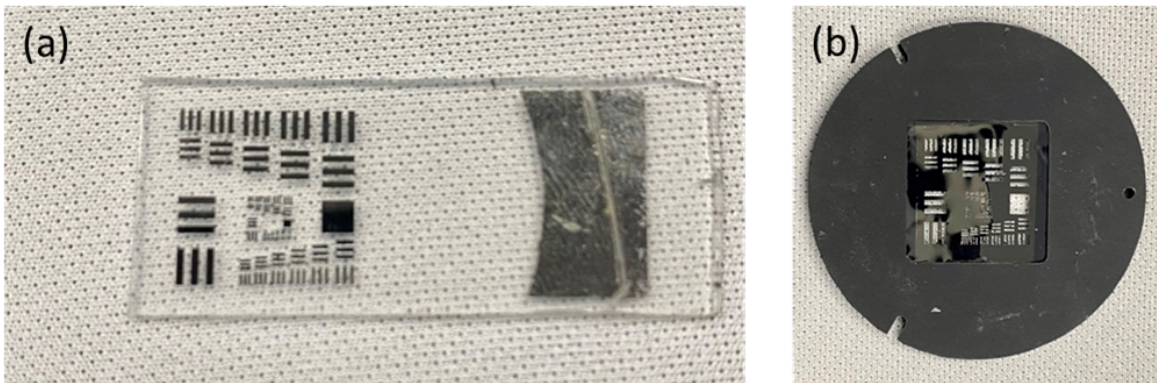

Fig. 6.11 (a) The photograph of the PP sample with the silver USAF target pattern and (b) the hollow USAF target pattern master.

To prove that the diffuser is beneficial, we performed the acquisition both under the plane-wave illumination (without diffuser) and with the inserted diffuser, as depicted in Fig. 6.12(a1) and (b1). We observed the diffraction patterns of the two cases when the probe beam passes through a clear sample zone, shown in Fig. 6.12(a2) and (b2). The diffraction pattern under the diffuser illumination covers a larger area on the detector. We plotted the intensity profiles of the two cut-lines under the log scale in Fig. 6.12(c). The blue profile is obtained with the collimated beam, the green one with the diffuser. The border area in Fig. 6.12(b2) has higher SNR than in Fig. 6.12(b1).

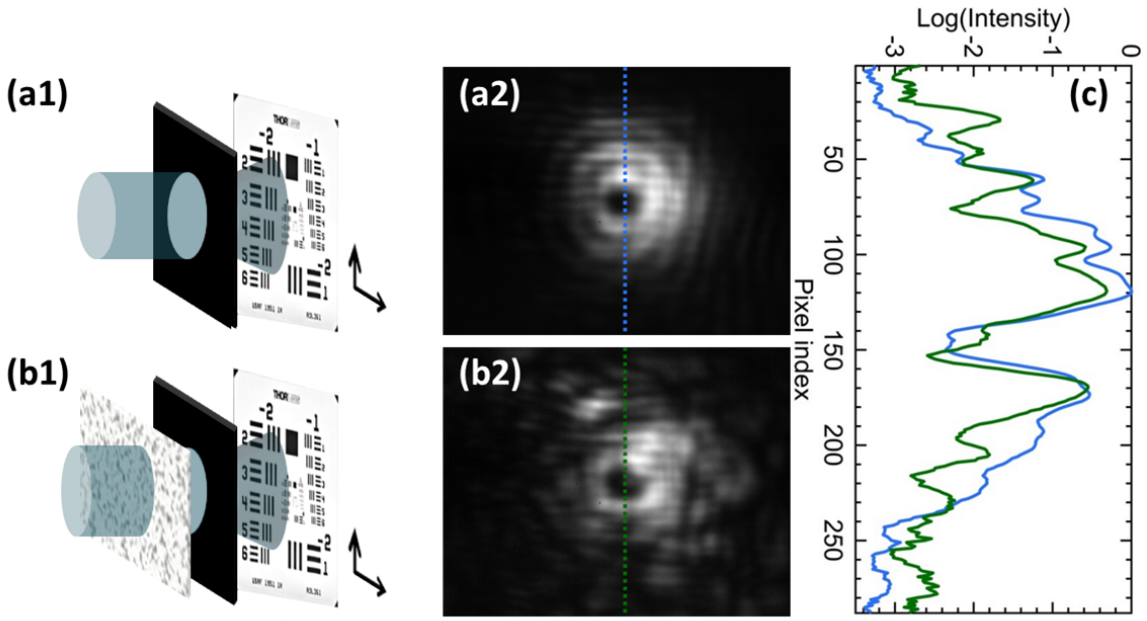

Fig. 6.12 Comparison of the dynamic range of the recorded diffraction patterns. The diffraction pattern in (a2) is recorded without the diffuser as depicted in a(1); the diffraction pattern in (b2) is recorded with the diffuser. The intensity profiles of the cut-lines in (a2) and (b2) are plotted in (c) under the log scale.

We executed the ePIE algorithm for 50 iterations at several different reconstruction distances. We observe that the lower part of the sample is best in focus at 10.8 mm while the upper part is in focus at 12 mm. Figures 6.13(a) and (b) give the central area of the reconstruction results of the USAF target at 10.8 mm with the dataset recorded without the diffuser and with the diffuser, respectively. The reconstruction result in Fig. 6.13(b) has a more uniform background with less artifact than that in Fig. 6.13(a). The elements in the dark green dashed line area are used to estimate the lateral resolution of the system. In Fig. 6.13(b), all the six elements are distinguishable in the horizontal direction, corresponding to a lateral resolution of 140.4 μm (1.18λ). The third smallest line pair is distinguishable on the vertical direction, corresponding to a lateral resolution of 177.3 μm (1.49λ). In Fig. 6.13(a), however, the first two line pairs in the horizontal direction are not well separated. According to Eq. 3.15, the intrinsic resolution of the setup is 0.95λ in the horizontal direction and 1.18λ in the vertical direction. Our result is only 25% higher than the intrinsic resolution. Moreover, the images in dark red rectangles give the reconstruction results of the line pairs on the upper part of the sample at 12 mm when they are in focus. The reconstruction obtained with the diffuser illumination dataset in Fig. 6.13(b) remains a better result.

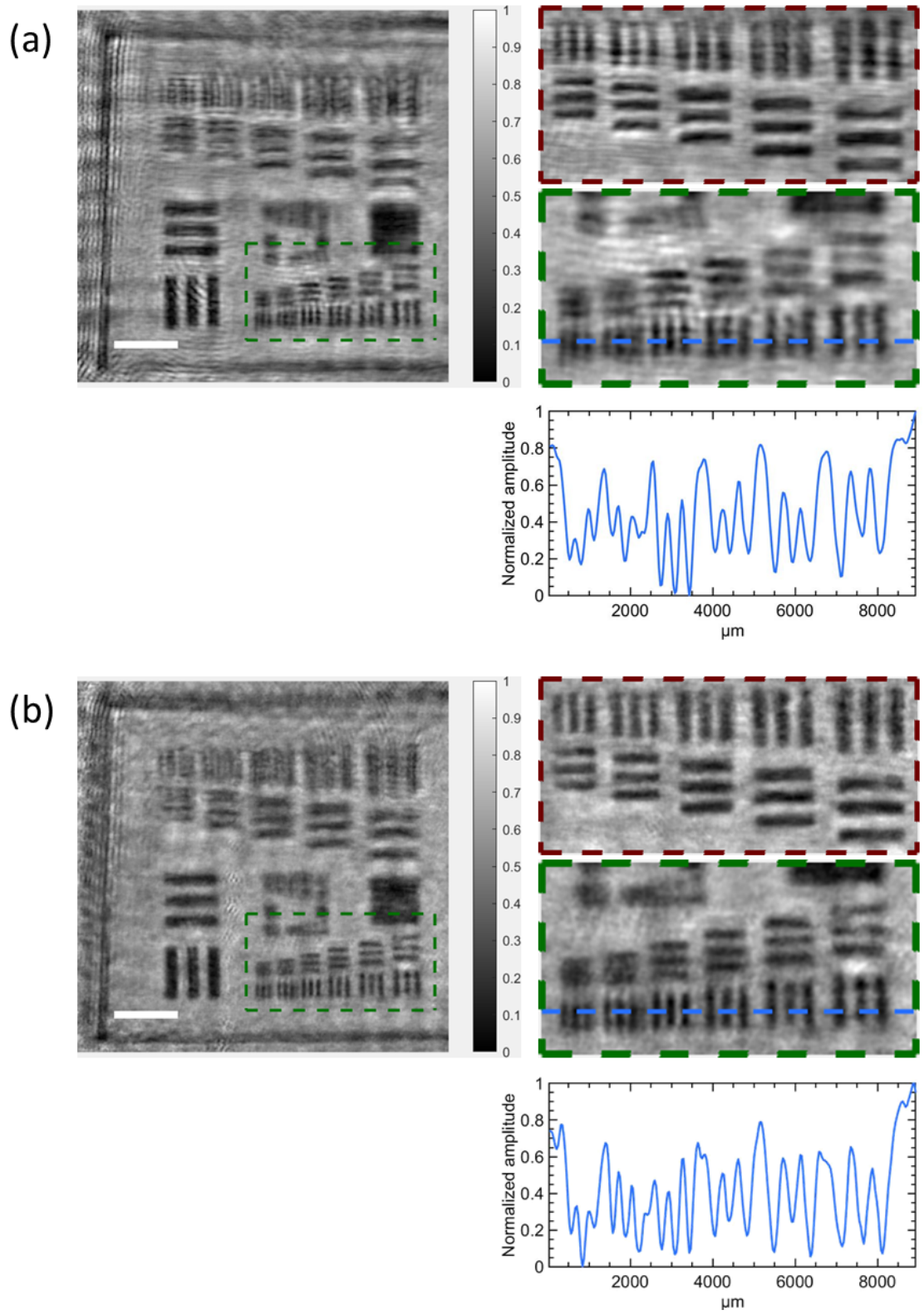

Fig. 6.13 Comparison of the reconstruction results of the USAF target using different probe illumination. (a) is reconstructed amplitude with the dataset recorded without a diffuser, whereas (b) is reconstructed with the dataset with diffuser illumination. Scale bar: 3 mm. The sample is tilted; the upper side of the sample is in focus at 12 mm, whereas the lower side is best in focus at 10.8 mm. The full-scale image and the zoomed-in part in the dark green dashed line are reconstructed at 10.8 mm. The dark red rectangle gives the reconstruction results of the upper line pairs at 12 mm.

6.3.2 Pure phase object: An engraved HDPE slab for phase measurement characterization

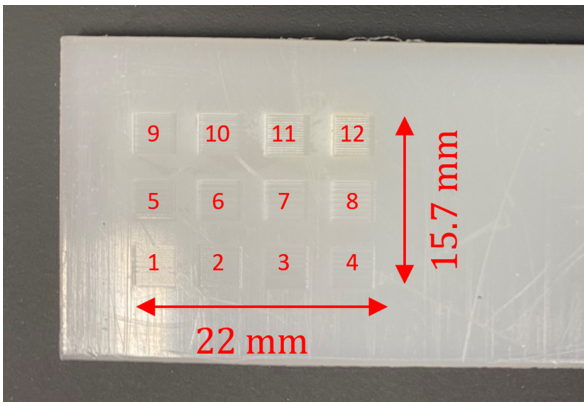

Fig. 6.14 The HDPE slab sample engraved with twelve squares for phase resolution characterization.

The second sample under investigation is a 2 mm-thick HDPE ($n_{\mathrm{HDPE}} = 1.54$ at 2.52 THz) slab engraved with 12 squares with different depths using excimer laser ablation, shown in Fig. 6.14. The depth of each square is summarized in Table 6.2. The HDPE sample has low absorption in the THz range. Thus it is regarded as a pure phase object. We recorded the diffraction patterns both under the plane-wave illumination (without diffuser) and with the inserted diffuser to evaluate its performance. The sample is placed 14 mm in front of the detector. We scanned 20×20 positions to gather a collection of the diffraction patterns, corresponding to a theoretical imaging area of 36.68×40.04 mm^2.

Table 6.2 Depth of each square shown in Fig. 6.14

Square number	1	2	3	4	5	6	7	8	9	10	11	12
Depth [μm]	9.2	22	32.5	41	61.8	68.5	76	77	106	113	227	328

The reconstructed results of the two datasets after 100 iterations are given in Fig. 6.15. The central area of the reconstructed object, as well as the retrieved probe function, are given for the comparison. The experimental result obtained here is consistent with the simulation analysis shown in Fig. 6.9. The reconstruction was unsuccessful with the dataset acquired

under plane-wave illumination (Fig. 6.15(a)-(c)) while the diffuser illuminated dataset gave distinct and sharp reconstruction results (Fig. 6.15(d)-(e)). The comparison of the error metric plotted in Fig. 6.16 validates that the reconstruction result of the diffuser illuminated dataset converged to a lower error, yet it was stagnated with the dataset under plane-wave illumination. The tilted fringes appeared in the background of Fig. 6.15(d) and (e) are originated from the Fabry–Pérot effect occurring between the two surfaces of the sample.

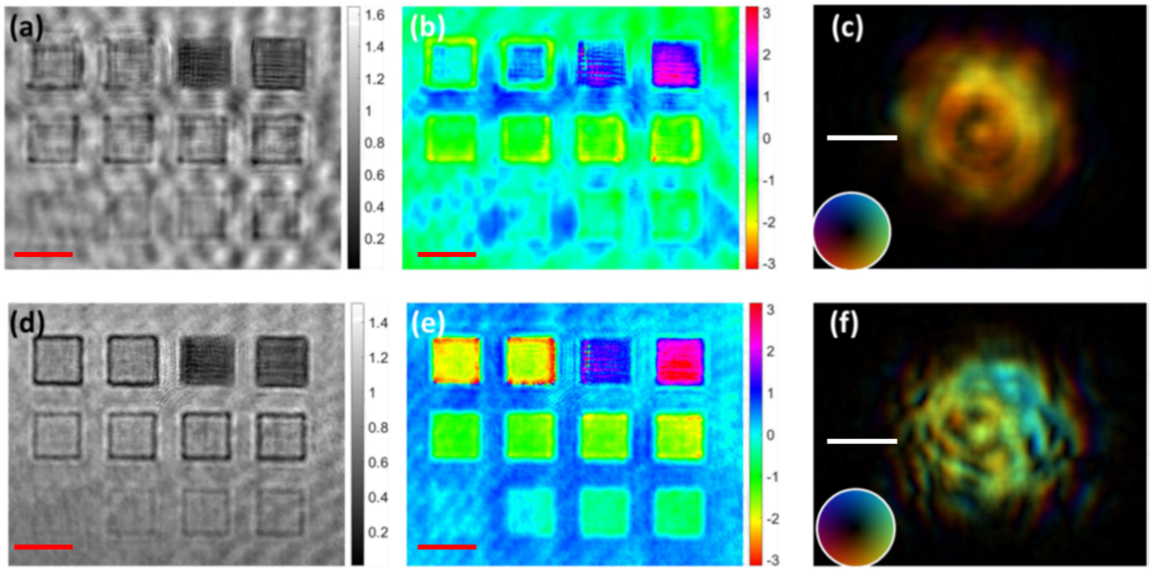

Fig. 6.15 Comparison of the reconstruction results of the HDPE slab using different probe illumination after 100 iterations. (a)-(c) are reconstructed object amplitude, object phase and the complex probe function, respectively, using plane-wave illumination. (d)-(f) are the reconstruction results of the dataset recorded with diffuser illumination. The color wheel in (c) and (f) displays the complex distribution of the probe function. The hue color represents the $[0,2\pi]$ phase range and the brightness gives the normalized amplitude ranging from 0 to 1. Scale bar: 5 mm.

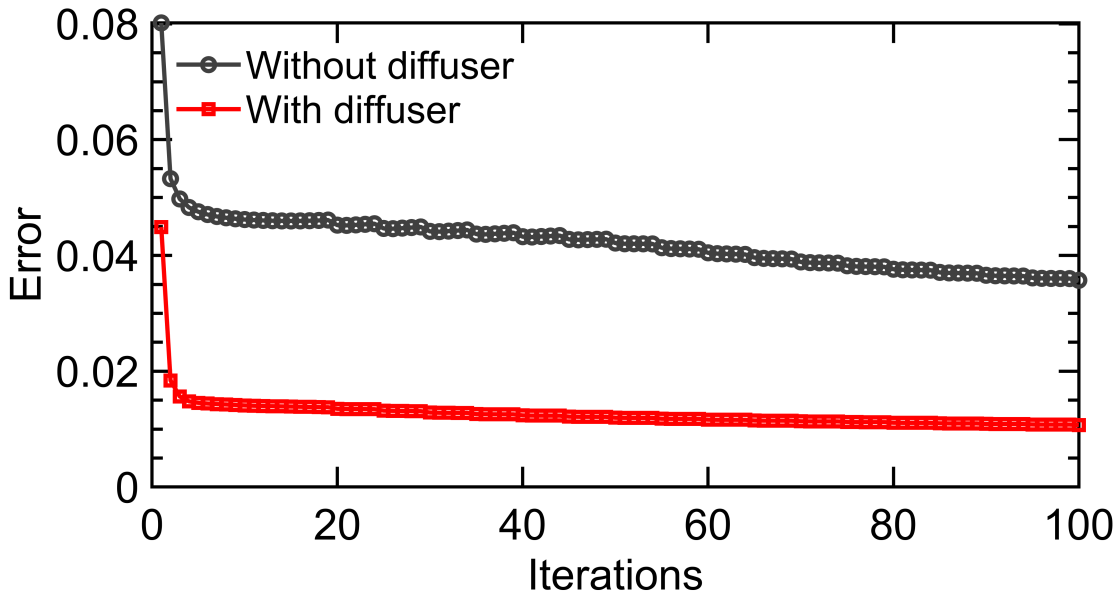

Fig. 6.16 Evolution of the error metric of the HDPE slab sample reconstruction after 100 iterations.

Unwrapping the phase map in Fig. 6.15(e) allows retrieving the thickness variation in the same way as Eq. 4.8, except that the refractive index of the material should be replaced by n_{HDPE}. However, the phase unwrapping process requires pre-knowledge of the sample, and it could introduce additional errors. Alternatively, we generated a theoretical wrapped phase map ranging between $[-\pi, \pi]$ based on the known thickness and compared it with Fig. 6.15(e) to quantitatively evaluate the phase resolution of the reconstructed result. On the reconstruction map, we took the central 50×50 pixels to compute its mean phase value and standard deviation. The generated theoretical phase map is given in Fig. 6.17(a). The wrapped phase values of each square are plotted in Fig. 6.17(b). The values are also summarized in Table 6.3. The retrieved phase values of squares 1 to 8, and the flat area denoted as 0, are in accordance with the simulated value. The standard variation is around 0.1 rad. A depth variation of 10 µm ($\approx \lambda/11.8$) is distinguishable from the measurement from the experimental result in Fig. 6.15(e). The retrieved phase values for the squares 9 to 12 exhibit higher systematic error. We remark that the cross-talk between the phase and amplitude values occurred for these cases since the amplitude shows lower amplitude distribution, which would a significant increase of the absorption coefficient. As analyzed in [183], this type of cross-talk could happen when reconstructing a strong phase-shift object with a noise-contaminated dataset. This type of cross-talk has also appeared in simulations in Figs. 6.5 and 6.6. The phase residues can be found on the reconstructed amplitude. The high standard

deviation values of squares 11 and 12 are mainly due to the wrapped 2π shift. Therefore, a fair estimation of the phase resolution of the THz ptychographic setup is around 0.1 rad. The thickness variation as low as $\lambda/11.8$, corresponding to 0.3 rad, is distinguishable.

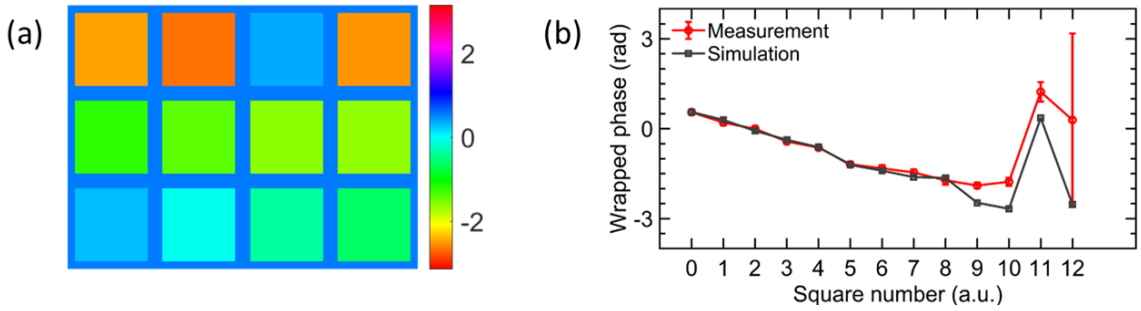

Fig. 6.17 Comparison of the reconstructed phase and the theoretical value. (a) is the theoretical wrapped phase variation introduced by the HDPE sample. The measured results are plotted with the theoretical value in (b).

Table 6.3 Comparison of the reconstructed phase and the theoretical value

Square number	Thickness [μm]	Theoretical wrapped phase value [rad]	Measured wrapped phase value [rad]
0	2000 (1.0)	0.56 (0.03)	0.55 (0.08)
1	1990.8 (1.0)	0.29 (0.03)	0.21 (0.09)
2	1978 (1.0)	-0.07 (0.03)	-0.01 (0.11)
3	1967.5 (1.0)	-0.37 (0.03)	-0.43 (0.08)
4	1959 (1.0)	-0.61 (0.03)	-0.63 (0.09)
5	1938.2 (1.0)	-1.21 (0.03)	-1.19 (0.11)
6	1931.5 (1.0)	-1.40 (0.03)	-1.32 (0.11)
7	1924 (1.0)	-1.61 (0.03)	-1.46 (0.11)
8	1923 (1.0)	-1.64 (0.03)	-1.72 (0.15)
9	1894 (1.0)	-2.47 (0.03)	-1.89 (0.09)
10	1887 (1.0)	-2.67 (0.03)	-1.77 (0.13)
11	1773 (1.0)	0.36 (0.03)	1.23 (0.32)
12	1672 (1.0)	-2.52 (0.03)	0.29 (2.88)

6.3.3 Imaging the full-sized breast cancer tissue sample

Finally, the full-sized dehydrated breast cancer tissue sample, shown in Fig. 6.18, is measured with the proposed THz ptychography setup in transmission mode using speckle illumination. Likewise, the sample was scanned at a grid of 20×20 positions with a step of 1.4 mm. The sample was placed 14.8 mm in front of the detector plane. The reconstruction results after 200 iterations are given in Fig. 6.19. The morphology of the tissue, as well as the excessive paraffin drops on the side, are clearly reconstructed. The reconstructed amplitude in Fig. 6.19(a) is related to the absorption distribution of the sample. Since the sample is dehydrated, the absorption is relatively low. The phase variation in Fig. 6.19(b) reveals more information. The central area of the sample exhibits lower phase shift than both ends.

Fig. 6.18 Photograph of a full-sized paraffin-embedded human breast cancer tissue sample on the Teflon substrate.

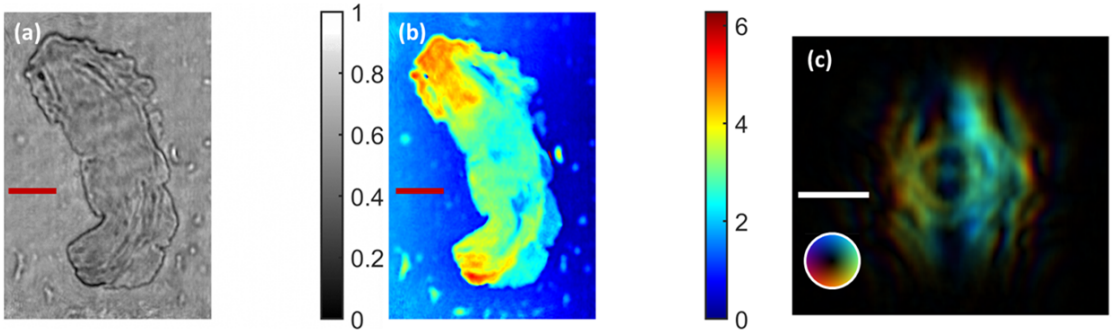

Fig. 6.19 Ptychographic reconstruction results of a full-sized dehydrated breast cancer tissue sample after 200 iterations. (a) and (b) are the reconstructed amplitude and the phase images, respectively. (c) is the reconstructed probe function.The hue color represents the $[0,2\pi]$ phase range and the brightness gives the normalized amplitude ranging from 0 to 1. Scale bar: 5 mm.

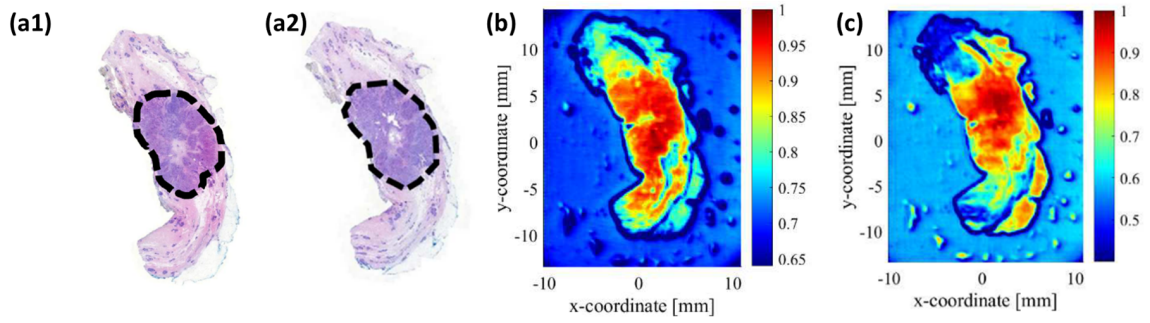

Fig. 6.20 THz-TDS measurement of the full-sized breast cancer sample provided in [184]. (a1) and (a2) are the images of the two neighbour slides used for histopathological analysis. In each image, the margin of cancerous region is circled by the dashed line. (b) and (c) are measured with THz-TDS spectrometer under reflection mode (TeraPulse 4000, TeraView). (b) is the normalized amplitude of the sample impulse response in the time domain. (c) is the normalized amplitude of the frequency response at 1.12 THz in the frequency domain.

To better understand our results, we compared our reconstruction with the histopathology analysis as well as the THz-TDS measurement of the same sample provided in [184]. The conventional histopathology analysis applied on the neighboring slides has identified the central area of the sample as cancerous, as shown in Fig. 6.20(a1) and (a2). More interestingly, the highly-contrasted area observed using the THz-TDS spectrometer, (b) the impulse response in the time-domain and (c) the amplitude at 1.12 THz in the frequency-domain are highly correlated to the phase-shift distribution in Fig. 6.19(b). Such encouraging results show that the optimized THz ptychographic setup is capable of imaging large, complex biological samples efficiently. Further quantitative analysis could be carried on with the phase-contrast imaging result provided by THz ptychography. It is worth mentioning that the data acquisition time of 400 diffraction patterns using our ptychography setup only took less than 30 minutes. However, the TDS results were obtained with a spatial scan step of 200 μm in each direction. It took several hours to perform the data acquisition. In terms of acquisition time, the proposed ptychography technique has a distinct advantage over TDS measurement. It is more suitable for fast screening biomedical samples. Performing 200 iterations of ePIE reconstructions with a laptop PC with the current CPU based code took up to 1680 seconds. Developing GPU-based acceleration ptychography could significantly reduce the reconstruction time.

6.4 Chapter summary

In this chapter, we explored avenues to improve further the imaging capability of our THz ptychographic system for biomedical imaging applications. Many bottlenecks are originated from the limited THz detector technologies. We showed that correctly denoising the measured diffraction pattern is crucial for successful reconstruction. Moreover, we relaxed the dynamic range requirement by introducing a diffuser illumination. The scattered probe illumination not only decreased the dynamic range of the diffraction pattern but also illuminated a larger area of the sample, leading to a more significant overlap rate. The diffuser illumination provides more reliable reconstruction results. We also accelerated the acquisition process of a large FOV sample by enlarging the probe size. The proposed improvement vanishes both via simulation and experiment. After the improvement, a lateral resolution of 1.18λ is achieved. A phase variation of 0.3 rad on the depth direction, corresponding to a depth of 10 μm ($\lambda/11.8$) is distinguishable. We used a self-made diffuser in the current experimental setup. If we engineered the scattering angle of the diffuser, it would bring more benefit. A large scattering angle allows us to extrapolate the diffraction patterns that fall outside of the detector, further enhancing the lateral resolution. The diffuser can also be combined with a divergent beam to achieve this goal [157, 172].

We successfully imaged a paraffin-embedded human breast cancer tissue sample using THz ptychography. Undoubtedly, more quantitative analysis is still needed to perform cancer detection via THz imaging techniques. The ptychographic reconstruction provided an encouragingly highly correlated phase-contrast image. The result showed the potential of THz ptychography for further biomedical applications.

Chapter 7

Conclusions and Perspectives

Through this work, we have developed different coherent lensless imaging techniques with THz radiation, namely the DH (Chapter 4) and iterative phase retrieval techniques, including ptychography (Chapter 5 and Chapter 6), after having conducted a systematic literature review of the THz technology (Chapter 2) and the coherent lensless imaging (Chapter 3). The main discoveries have been concluded in the corresponding chapter summary section. Hereby we discuss the lessons learned during this journey as well as the further work directions.

The first lesson learned in this thesis is a better understanding of THz radiation and the state-of-the-art of THz technology. One big attraction of the THz radiation to the NDT community is its seeing-through ability without causing ionization, as a less harmful alternative to x-rays. However, is it worth the hype? In reality, the penetration ability of THz is more selective than x-ray. THz radiation cannot penetrate metal or water. Even for dielectric materials, only a few exhibit low absorption in the FIR range, whereas most are transparent in the sub-THz regime. The technologies for generating and detecting the THz radiation and their corresponding imaging systems differ a lot depending on the regime. Furthermore, in terms of imaging application, an increase of 10^7 times in wavelength compared with x-ray leads to a very limited lateral resolution. Therefore, a fair conclusion is that THz imaging will only act as an advantageous alternative when the sample of interest remains transparent at the given wavelength while the achievable resolution meets the application needs.

Another reflection is the technical readiness of current THz imaging techniques for real-world applications after the successful development of THz science and technology for two decades. We have learned the mainstream THz sources and detectors for various THz imaging systems. Imaging with THz-TDS systems for material characterization and the

thickness measurement based on the time-of-flight contributes to numerous successful applications [185], spanning from identifying the polymorph compounds, inspecting pill's coating thickness in the pharmaceutical industry to the detection of internal defects in different types of specimens. On the one hand, THz-TDS measurement contains rich spectral information about the sample. On the other hand, a map of the layer of interest can be extracted from the time-domain measurement. Nowadays, many integrated THz-TDS systems with diverse performance specifications are commercially available. The remaining challenge of THz-TDS imaging toward real-world applications can be summarized into the following three aspects: First off, the sensitivity or the imaging resolution of the THz-TDS system cannot meet the application requirement. It is often the case for food contamination inspection and biomedical sample imaging applications. Second, biomedical applications such as cancer detection and dental caries studies remain in the early stage due to the limited understanding of the interaction between the sample and the THz radiation. Finally, the application of fast quality inspection in different industries is turned down due to the limited imaging acquisition speed of THz-TDS, which contains both the optical delay line scan and the 2D spatial raster scan. CW THz imaging systems are favorable for fast-imaging applications. The speed was also a problem in the earlier single-pixel CW imaging systems. The current THz 2D cameras based on uncooled microbolometer and field-effect transistor technologies allow full-field imaging of tens of cm^2 imaging area in one single shot. Techniques that eliminate undesirable interference effects caused by the coherent THz sources are adopted, offering a better imaging quality. However, these CW THz imaging systems with fixed wavelength only provide intensity distribution. Thus, limited information can be interpreted from the imaging result. Consequently, fewer application scenarios are foreseen compared to the THz-TDS imaging systems.

Exploring lensless coherent imaging provided an alternative to the THz CW imaging systems. The coherence of the CW narrowband THz sources allows retrieving both the sample's amplitude and phase information. Our developments showed that the phase distribution obtained using DH and ptychography revealed the variation of the optical thickness in the sample. Our development in the FIR range has benefited from the convenience offered by the uncooled microbolometer 2D FPA. Due to the lack of sufficiently large FPAs with adequate sensitivity at the sub-THz range, the single-pixel detector was employed, leading to a very time-consuming acquisition. It was the most significant constraint for further optimizing the sub-THz holographic system. Under the single-pixel detector system, developing other phase retrieval techniques that require multiple intensity acquisitions, including ptychography, does

not seem like a good idea due to the low acquisition efficiency, although it is feasible. The state-of-art sub-THz linear scanner with higher sensitivity and higher resolution offers a gleam of hope.

The main drawback of our FIR system is the FIR optically pumped laser source itself. Its bulky size and complicated installation, unfortunately, turn down all the out-of-the-laboratory applications. The stability becomes a serious flaw when continuous acquisitions are needed, such as recording the ptychographic datasets, applying the synthetic aperture approach, or imaging a larger area via scanning. Using one of the latest compact, high-power QCLs with relaxed cooling conditions will make up for these flaws. Moreover, the tunable frequency of the QCL source will offer more possibilities for lensless imaging techniques such as dual-wavelength DH and multi-wavelength phase retrieval. There is still much room for THz detector arrays. A larger array size will offer a higher system NA, leading to a higher lateral resolution. Detectors with a wider dynamic range and lower NEP will be very beneficial for holograms and diffraction patterns recording. The imaging quality of PR techniques, including ptychography, highly depends on the reliability of diffraction pattern recording.

Comparing the performance of the two THz lensless imaging techniques, the off-axis DH allows retrieving a relatively credible object wavefront with only one hologram. However, the usage of a reference wave prevents shortening the recording distance since the object should not obscure the reference wave, thus decreasing the resolution. Ptychography breaks this limitation. Moreover, ptychography allows high-resolution imaging with large FOVs without additional optics. It is an indispensable solution since it is challenging to perform image-plane DH in THz with an object image with sufficient resolution and minimize unwanted coherent artifacts. However, the cost is that ptychography requires more data acquisition and heavier data processing to solve the phase problem. The strict restriction on recording distance to remain a high NA holds for both techniques when using THz radiation. Developing these techniques under reflection mode becomes very challenging, particularly for reflective ptychography due to the need to move the object. For reflective DH, the synthetic aperture can be carried out to relax the distance requirement. For THz reflective ptychography, our current setup is only capable of imaging small, highly reflecting samples for their surface profile measurement as a proof-of-concept experiment. In reality, using THz radiation for surface profile measurement is not advantageous unless its seeing-through ability can be exploited. Continuous efforts still need to be paid in both the above-mentioned improvement in THz detectors and the ptychographic data processing methods to enable appealing applications

such as imaging concealed structures or *in vivo* measurement of biological tissues. Another important feature of ptychography is its ability to recover the illuminating beam. This is particularly advantageous over DH in THz since the illumination is not always homogeneous. On the other hand, ptychography can be used for characterizing the illuminating beam.

Ptychography itself is still an active area of research. In this work, we only explored the classic ePIE reconstruction algorithm. Many advanced algorithms are based on a more elaborated physical model that matches the actual experimental conditions, such as the multi-slice approach, the decomposition of the mixed probe states, and the modelization of the noise. These algorithms will lead to more credible reconstruction results. Besides that, GPU-based implementation will accelerate the speed of ptychography reconstruction.

Looking to the future, developing ptychography at 280 GHz with the linear scanner after the validation of its sensitivity will allow inspecting the large-sized composite panels, like the sample shown in Fig. 4.16(a). Applying multi-slice reconstruction methods will allow locating the defects at their corresponding layers. A prototype of an imaging scanner with both amplitude and phase information can be foreseen for NDT applications. Both DH and ptychography in the FIR range have shown satisfying imaging results with wavelength-level (<150 μm) lateral resolution and μm-level depth resolution when imaging polymer samples that are highly transparent in this range. Some study cases towards real-world applications in plastic industries can be tested using our FIR setup, such as identifying the inclusions and voids in plastic parts. Both techniques can be further implemented for 3D tomographic reconstructions.

Nomenclature

Acronyms / Abbreviations

ABS Acrylontrile butadiene styrene

ASM Angular spectrum method

BJUT Beijing University of Technology

BS Beam splitter

BWO Backward wave oscillator

CC Correlation coefficient

CENTERA Center for Terahertz research and applications

CMOS Complementary metal-oxide-semiconductor

CSL Centre Spatial de Liège

CT Computed tomography

CW Continuous-wave

DH Digital holography

ePIE Extended ptychographic iterative engine

ER Error reduction

HIO Hybrid input-output

ESA European Space Agency

EUV Extreme ultraviolet

FEL Free electron laser

FET Field effect transistor

FFT Fast Fourier transform

FFT Fast Fourier Transform

FIR Far-infrared

FMCW Frequency Modulated Continuous-Wave

FOV Field of view

FPAs Focal plane arrays

GFRP Glass fiber reinforced polymer

HDPE High density Polyethylene

HEMT High electron mobility transistor

HRFZ-Si High Resistivity Float Zone Silicon

IMPATT Impact ionization avalanche transit-time

IR Infrared

ITU International Telecommunication Union

LWIR Long-wave infrared

MMW Millimeter wave

NA Numerical aperture

NDT Non-destructive testing

NEP Noise equivalent power

OPD Optical path difference

PCA Photoconductive antenna

PC Poly carbonate

PET Poly terephthalate

PIE Ptychographic iterative engine

PLA Polyactic acid

PMMA Polymethyl methacrylate

PP Polypropylene

PR Phase retrieval

PTFE Poly tetrafluoroethylene, Teflon

QCL Quantum cascade laser

RMSE Root-mean-squared-error

ROIC Read out integrated circuit

ROI Region of interest

SBD Schottky barrier diode

SBMIR Single-beam multiple-intensity reconstruction

SMMW Sub-millimeter wave

SNR Signal-to-noise ratio

SSIM Structural similarity index

THz-TDS Terahertz time-domain spectroscopy

THz Terahertz

TOPAS Cyclic olefin copolymer

TPX Polymethylpentene

TRL Technology readiness level

VCO Voltage controlled oscillator

VNA Vector network analyzer

WDD Wigner Distrinution Deconvolution

References

[1] SS Dhillon, MS Vitiello, EH Linfield, AG Davies, Matthias C Hoffmann, John Booske, Claudio Paoloni, M Gensch, Peter Weightman, GP Williams, et al. The 2017 terahertz science and technology roadmap. *Journal of Physics D: Applied Physics*, 50(4):043001, 2017.

[2] Mira Naftaly and Robert E Miles. Terahertz time-domain spectroscopy for material characterization. *Proceedings of the IEEE*, 95(8):1658–1665, 2007.

[3] M Naftaly, JF Molloy, GV Lanskii, KA Kokh, and Yu M Andreev. Terahertz time-domain spectroscopy for textile identification. *Applied optics*, 52(19):4433–4437, 2013.

[4] Peter H Siegel. Terahertz technology in biology and medicine. *IEEE transactions on microwave theory and techniques*, 52(10):2438–2447, 2004.

[5] Albert Redo-Sanchez, Nicholas Karpowicz, Jingzhou Xu, and Xi-Cheng Zhang. Damage and defect inspection with terahertz waves. In *The 4th International Workshop on Ultrasonic and Advanced Methods for Nondestructive Testing and Material Characterization*, pages 67–78, 2006.

[6] Emma Pickwell-MacPherson and Vincent P Wallace. Terahertz pulsed imaging—a potential medical imaging modality? *Photodiagnosis and Photodynamic Therapy*, 6(2):128–134, 2009.

[7] Hai-Bo Liu, Hua Zhong, Nicholas Karpowicz, Yunqing Chen, and Xi-Cheng Zhang. Terahertz spectroscopy and imaging for defense and security applications. *Proceedings of the IEEE*, 95(8):1514–1527, 2007.

[8] Daniel M Mittleman. Twenty years of terahertz imaging. *Optics express*, 26(8):9417–9431, 2018.

[9] Hichem Guerboukha, Kathirvel Nallappan, and Maksim Skorobogatiy. Toward real-time terahertz imaging. *Advances in Optics and Photonics*, 10(4):843–938, Dec 2018.

[10] Albert Redo-Sanchez, Norman Laman, Brian Schulkin, and Thomas Tongue. Review of terahertz technology readiness assessment and applications. *Journal of Infrared, Millimeter, and Terahertz Waves*, 34(9):500–518, 2013.

[11] Chao Song, Wen-Hui Fan, Ling Ding, Xu Chen, Ze-You Chen, and Kai Wang. Terahertz and infrared characteristic absorption spectra of aqueous glucose and fructose solutions. *Scientific Reports*, 8(1):8964, 2018.

[12] David M. Slocum, Elizabeth J. Slingerland, Robert H. Giles, and Thomas M. Goyette. Atmospheric absorption of terahertz radiation and water vapor continuum effects. *Journal of Quantitative Spectroscopy and Radiative Transfer*, 127:49–63, 2013.

[13] Philip F Taday. Applications of terahertz spectroscopy to pharmaceutical sciences. *Philosophical Transactions of the Royal Society of London. Series A: Mathematical, Physical and Engineering Sciences*, 362(1815):351–364, 2004.

[14] Kodo Kawase, Yuichi Ogawa, Yuuki Watanabe, and Hiroyuki Inoue. Non-destructive terahertz imaging of illicit drugs using spectral fingerprints. *Optics express*, 11(20):2549–2554, 2003.

[15] John F Federici, Brian Schulkin, Feng Huang, Dale Gary, Robert Barat, Filipe Oliveira, and David Zimdars. THz imaging and sensing for security applications—explosives, weapons and drugs. *Semiconductor Science and Technology*, 20(7):S266, 2005.

[16] Jianyuan Qin, Yibin Ying, and Lijuan Xie. The detection of agricultural products and food using terahertz spectroscopy: a review. *Applied Spectroscopy Reviews*, 48(6):439–457, 2013.

[17] Masayoshi Tonouchi. Cutting-edge terahertz technology. *Nature Photonics*, 1:97, feb 2007.

[18] Yun-Shik Lee. *Principles of terahertz science and technology*, volume 170. Springer Science & Business Media, 2009.

[19] YongKeun Park, Christian Depeursinge, and Gabriel Popescu. Quantitative phase imaging in biomedicine. *Nature Photonics*, 12(10):578–589, 2018.

[20] Lorenzo Valzania, Yuchen Zhao, Lu Rong, Dayong Wang, Marc Georges, Erwin Hack, and Peter Zolliker. THz coherent lensless imaging. *Applied optics*, 58(34):G256–G275, 2019.

[21] Marc Georges, Yuchen Zhao, and Jean-François Vandenrijt. Holography in the invisible. from the thermal infrared to the terahertz waves: outstanding applications and fundamental limits. *Light: Advanced Manufacturing*, 2:1–14, 2022.

[22] Yuchen Zhao, Jean-François Vandenrijt, Murielle Kirkove, and Marc Georges. Iterative phase-retrieval-assisted off-axis terahertz digital holography. *Applied Optics*, 58(33):9208, nov 2019.

[23] Lorenzo Valzania, Thomas Feurer, Peter Zolliker, and Erwin Hack. Terahertz ptychography. *Optics Letters*, 43(3):543–546, 2018.

[24] Lu Rong, Chao Tang, Yuchen Zhao, Fangrui Tan, Yunxin Wang, Jie Zhao, Dayong Wang, and Marc Georges. Continuous-wave terahertz reflective ptychography by oblique illumination. *Optics Letters*, 45(16):4412–4415, 2020.

[25] Donald Knuth. Technology trends of active services in the frequency range 275-3 000 GHz. https://www.itu.int/pub/R-REP-SM.2352-2015, accessed: 30.05.2021.

[26] Yun-Shik Lee. *Principles of terahertz science and technology*. Lecture Notes in Physics. Springer, 1st ed edition, 2008.

[27] Terahertz sources. https://terasense.com/products/terahertz-sources/, accessed: 30.06.2021.

[28] Jeffrey Hesler and Thomas Crowe. High-power solid-state terahertz sources. *SPIE Newsroom*, 07 2015.

[29] Anritsu introduces broadband VNA system with single-sweep coverage broadband VNA system: VectorStar ME7838AX/EX series. https://www.microwavejournal.com/articles/36658-anritsu-introduces-broadband-vna-system-with-single-sweep-coverage, accessed: 30.05.2021.

[30] Adrian Dobroiu, Masatsugu Yamashita, Yuichi N Ohshima, Yasuyuki Morita, Chiko Otani, and Kodo Kawase. Terahertz imaging system based on a backward-wave oscillator. *Applied optics*, 43(30):5637–5646, 2004.

[31] John H Booske, Richard J Dobbs, Colin D Joye, Carol L Kory, George R Neil, Gun-Sik Park, Jaehun Park, and Richard J Temkin. Vacuum electronic high power terahertz sources. *IEEE Transactions on Terahertz Science and Technology*, 1(1):54–75, 2011.

[32] Nikita V Chernomyrdin, AS Kucheryavenko, GS Kolontaeva, GM Katyba, IN Dolganova, PA Karalkin, DS Ponomarev, VN Kurlov, IV Reshetov, M Skorobogatiy, et al. Reflection-mode continuous-wave 0.15λ-resolution terahertz solid immersion microscopy of soft biological tissues. *Applied Physics Letters*, 113(11):111102, 2018.

[33] Bin Li, Dayong Wang, Lu Rong, Changchao Zhai, Yunxin Wang, and Jie Zhao. Application of continuous-wave terahertz computed tomography for the analysis of chicken bone structure. *Optical Engineering*, 57(2):023105, 2018.

[34] Yesenia A García-Jomaso, Dahí L Hernández-Roa, Jesús Garduño-Mejía, Carlos G Treviño-Palacios, Oleg V Kolokoltsev, and Naser Qureshi. Sub-wavelength continuous THz imaging system based on interferometric detection. *Optics Express*, 29(12):19120–19125, 2021.

[35] Greg Hislop, Li Li, and Andrew Hellicar. Phase retrieval for millimeter-and submillimeter-wave imaging. *IEEE transactions on antennas and propagation*, 57(1):286–290, 2009.

[36] Créidhe M. O'Sullivan and J. Anthony Murphy. *Field Guide to Terahertz Sources, Detectors, and Optics - Backward Wave Oscillators*, pages 25–25. SPIE, 2012.

[37] Joshua R Freeman, Harvey E Beere, and David A Ritchie. Generation and detection of terahertz radiation. In Kai-Erik Peiponen, Axel Zeitler, and Makoto Kuwata-Gonokami, editors, *Terahertz Spectroscopy and Imaging*, pages 1–28. Springer Berlin Heidelberg, 2012.

[38] Benjamin S Williams. Terahertz quantum-cascade lasers. *Nature photonics*, 1(9):517–525, 2007.

[39] Rüdeger Köhler, Alessandro Tredicucci, Fabio Beltram, Harvey E Beere, Edmund H Linfield, A Giles Davies, David A Ritchie, Rita C Iotti, and Fausto Rossi. Terahertz semiconductor-heterostructure laser. *Nature*, 417(6885):156–159, 2002.

[40] Mikhail A Belkin and Federico Capasso. New frontiers in quantum cascade lasers: high performance room temperature terahertz sources. *Physica Scripta*, 90(11):118002, 2015.

[41] Ali Khalatpour, Andrew K Paulsen, Chris Deimert, Zbig R Wasilewski, and Qing Hu. High-power portable terahertz laser systems. *Nature Photonics*, 15(1):16–20, 2021.

[42] Valentino Pistore, Hanond Nong, Pierre-Baptiste Vigneron, Katia Garrasi, Sarah Houver, Lianhe Li, A Giles Davies, Edmund H Linfield, Jerome Tignon, Juliette Mangeney, et al. Millimeter wave photonics with terahertz semiconductor lasers. *Nature communications*, 12(1):1–7, 2021.

[43] A Crocker, HA Gebbie, MF Kimmitt, and LES Mathias. Stimulated emission in the far infra-red. *Nature*, 201(4916):250–251, 1964.

[44] Eric R. Mueller. *Optically Pumped Terahertz (THz) Lasers*. John Wiley & Sons, Ltd, 2016.

[45] F Sizov. Terahertz radiation detectors: the state-of-the-art. *Semiconductor Science and Technology*, 33(12):123001, 2018.

[46] Terahertz measurement. https://www.ophiropt.com/laser--measurement/laser-power-energy-meters/products/Terahertz-Laser-Measurement, accessed: 30.05.2021.

[47] Alan WeiMin Lee and Qing Hu. Real-time, continuous-wave terahertz imaging by use of a microbolometer focal-plane array. *Optics letters*, 30(19):2563–2565, 2005.

[48] Naoki Oda, Seiji Kurashina, Masaru Miyoshi, Kohei Doi, Tsutomu Ishi, Takayuki Sudou, Takao Morimoto, Hideki Goto, and Tokuhito Sasaki. Microbolometer terahertz focal plane array and camera with improved sensitivity at 0.5–0.6 THz. In *2014 39th International Conference on Infrared, Millimeter, and Terahertz waves (IRMMW-THz)*, pages 1–2, 2014.

[49] Denis Dufour, Linda Marchese, Marc Terroux, Hassane Oulachgar, Francis Généreux, Michel Doucet, Luc Mercier, Bruno Tremblay, Christine Alain, Patrick Beaupré, et al. Review of terahertz technology development at INO. *Journal of Infrared, Millimeter, and Terahertz Waves*, 36(10):922–946, 2015.

[50] François Simoens, Jérôme Meilhan, and Jean-Alain Nicolas. Terahertz real-time imaging uncooled arrays based on antenna-coupled bolometers or FET developed at CEA-Leti. *Journal of Infrared, Millimeter, and Terahertz Waves*, 36(10):961–985, 2015.

[51] G. Steinfeld, C. Brodeur, M. Shalaby, and G. Santiso. RIGI camera for real time ultrasensitive terahertz imaging. In *2019 44th International Conference on Infrared, Millimeter, and Terahertz Waves (IRMMW-THz)*, pages 1–1, 2019.

[52] François Simoens. Buyer's guide for a terahertz (THz) camera. https://www.photoniques.com/articles/photon/pdf/2018/02/photon2018S3p58.pdf, accessed: 30.06.2021.

[53] Erwin Hack, Lorenzo Valzania, Gregory Gäumann, Mostafa Shalaby, Christoph P Hauri, and Peter Zolliker. Comparison of thermal detector arrays for off-axis THz holography and real-time THz imaging. *Sensors*, 16(2):221, 2016.

[54] Wojciech Knap, Mikhail Dyakonov, Dominique Coquillat, Frederic Teppe, Nina Dyakonova, Jerzy Łusakowski, Krzysztof Karpierz, Maciej Sakowicz, Gintaras Valusis, Dalius Seliuta, et al. Field effect transistors for terahertz detection: Physics and first imaging applications. *Journal of Infrared, Millimeter, and Terahertz Waves*, 30(12):1319–1337, 2009.

[55] Justinas Zdanevičius, Maris Bauer, Sebastian Boppel, Vilius Palenskis, Alvydas Lisauskas, Viktor Krozer, and Hartmut G Roskos. Camera for high-speed THz imaging. *Journal of Infrared, Millimeter, and Terahertz Waves*, 36(10):986–997, 2015.

[56] Development and optimization of THz NDT on aeronautics composite multi-layered structure, public EU project DOTNAC, grant ID: 266320. https://cordis.europa.eu/project/rcn/96573/factsheet/en, accessed: 30.05.2021.

[57] F Ellrich, M Bauer, N Schreiner, A Keil, T Pfeiffer, J Klier, S Weber, J Jonuscheit, F Friederich, and D Molter. Terahertz quality inspection for automotive and aviation industries. *Journal of Infrared, Millimeter, and Terahertz Waves*, 41(4):470–489, 2020.

[58] A Chopard, Q Cassar, J Bou-Sleiman, Jean-Paul Guillet, M Pan, JB Perraud, A Susset, and Patrick Mounaix. Terahertz waves for contactless control and imaging in aeronautics industry. *NDT & E International*, 122:102473, 2021.

[59] Jens Neu and Charles A Schmuttenmaer. Tutorial: An introduction to terahertz time domain spectroscopy (THz-TDS). *Journal of Applied Physics*, 124(23):231101, 2018.

[60] David H Auston, Kin P Cheung, and Peter R Smith. Picosecond photoconducting hertzian dipoles. *Applied physics letters*, 45(3):284–286, 1984.

[61] SY Huang, YXJ Wang, DKW Yeung, AT Ahuja, YT Zhang, and Emma Pickwell-MacPherson. Tissue characterization using terahertz pulsed imaging in reflection geometry. *Physics in Medicine & Biology*, 54(1):149, 2008.

[62] Maxime Bernier, Frédéric Garet, and Jean-Louis Coutaz. Precise determination of the refractive index of samples showing low transmission bands by THz time-domain spectroscopy. *IEEE Transactions on Terahertz Science and Technology*, 3(3):295–301, 2013.

[63] U. Strom and P. C. Taylor. Temperature and frequency dependences of the far-infrared and microwave optical absorption in amorphous materials. *Phys. Rev. B*, 16:5512–5522, Dec 1977.

[64] Jingye Sun and Fangjing Hu. Three-dimensional printing technologies for terahertz applications: a review. *International Journal of RF and Microwave Computer-Aided Engineering*, 30(1):e21983, 2020.

[65] E. Stübling, L. Gomell, S. Sommer, A. Winkel, M. Kahlmeyer, S. Böhm, and M. Koch. THz Properties of Adhesives. *Journal of Infrared, Millimeter, and Terahertz Waves*, 39(6):586–593, 2018.

[66] VE Rogalin, IA Kaplunov, and GI Kropotov. Optical materials for the thz range. *Optics and Spectroscopy*, 125(6):1053–1064, 2018.

[67] Yun-Sik Jin, Geun-Ju Kim, and Seok-Gy Jeon. Terahertz dielectric properties of polymers. *Journal of the Korean Physical Society*, 49(2):513–517, 2006.

[68] Alexander Podzorov and Guilhem Gallot. Low-loss polymers for terahertz applications. *Applied optics*, 47(18):3254–3257, 2008.

[69] EV Fedulova, Maxim M Nazarov, AA Angeluts, MS Kitai, VI Sokolov, and AP Shkurinov. Studying of dielectric properties of polymers in the terahertz frequency range. In *Saratov Fall Meeting 2011: Optical Technologies in Biophysics and Medicine XIII*, volume 8337, page 83370I. International Society for Optics and Photonics, 2012.

[70] SF Busch, M Weidenbach, M Fey, F Schäfer, T Probst, and M Koch. Optical properties of 3D printable plastics in the THz regime and their application for 3D printed THz optics. *Journal of Infrared, Millimeter, and Terahertz Waves*, 35(12):993–997, 2014.

[71] Erich N Grossman, Joshua Gordon, David Novotny, and Richard Chamberlin. Terahertz active and passive imaging. In *The 8th European Conference on Antennas and Propagation (EuCAP 2014)*, pages 2221–2225. IEEE, 2014.

[72] Peter H Siegel. THz instruments for space. *IEEE Transactions on Antennas and Propagation*, 55(11):2957–2965, 2007.

[73] R Appleby. Passive millimetre-wave imaging and how it differs from terahertz imaging. *Philosophical Transactions of the Royal Society of London. Series A: Mathematical, Physical and Engineering Sciences*, 362(1815):379–393, 2004.

[74] Space camera blazes new terahertz trails. https://www.esa.int/Applications/Technology_Transfer/Space_camera_blazes_new_terahertz_trails, accessed: 30.03.2021.

[75] Herbert J. Kramer. Covid-19: Passive thz technology for security applications. https://eoportal.org/web/eoportal/satellite-missions/content/-/article/covid-19-passive-thz-technology-for-security-applications, accessed: 30.05.2021.

[76] Philip S Considine. Effects of coherence on imaging systems∗. *J. Opt. Soc. Am.*, 56(8):1001–1009, Aug 1966.

[77] Douglas T Petkie, Corey Casto, Frank C De Lucia, Steven R Murrill, Brian Redman, Richard L Espinola, Charmaine C Franck, Eddie L Jacobs, Steven T Griffin, Carl E Halford, et al. Active and passive imaging in the thz spectral region: phenomenology, dynamic range, modes, and illumination. *JOSA B*, 25(9):1523–1531, 2008.

[78] Yuye Wang, Linyu Chen, Tunan Chen, Degang Xu, Jia Shi, Yuchen Ren, Changzhao Li, Chao Zhang, Hongxiang Liu, Limin Wu, et al. Interference elimination in terahertz imaging based on inverse image processing. *Journal of Physics D: Applied Physics*, 51(32):325101, 2018.

[79] Jean-Baptiste Perraud, Adrien Chopard, Jean-Paul Guillet, Pierre Gellie, Antoine Vuillot, and Patrick Mounaix. A versatile illumination system for real-time terahertz imaging. *Sensors*, 20(14):3993, 2020.

[80] Barry N Behnken, Gamani Karunasiri, Danielle R Chamberlin, Peter R Robrish, and Jérôme Faist. Real-time imaging using a 2.8 thz quantum cascade laser and uncooled infrared microbolometer camera. *Optics letters*, 33(5):440–442, 2008.

[81] Alain Bergeron, Marc Terroux, Linda Marchese, Ovidiu Pancrati, Martin Bolduc, and Hubert Jerominek. Components, concepts, and technologies for useful video rate THz imaging. In Neil Anthony Salmon and Eddie L. Jacobs, editors, *Millimetre Wave and Terahertz Sensors and Technology V*, volume 8544, pages 60 – 67. International Society for Optics and Photonics, SPIE, 2012.

[82] François Simoens and Jérôme Meilhan. Terahertz real-time imaging uncooled array based on antenna-and cavity-coupled bolometers. *Philosophical Transactions of the Royal Society A: Mathematical, Physical and Engineering Sciences*, 372(2012):20130111, 2014.

[83] François Simoens, Laurent Dussopt, Jérôme Meilhan, Jean-Alain Nicolas, Nicolas Monnier, Alexandre Siligaris, Bruno Hiberty, Jean-Baptiste Perraud, Patrick Mounaix, Jérémy Lalanne-Dera, et al. Towards industrial applications of terahertz real-time imaging. In *Terahertz, RF, Millimeter, and Submillimeter-Wave Technology and Applications XI*, volume 10531, page 105310T. International Society for Optics and Photonics, 2018.

[84] Kiwon Moon, Il-Min Lee, Eui Su Lee, and Kyung Hyun Park. Thz reflective imaging system utilizing broadband homodyne amplification for artifact-free see-through imaging. *Applied Sciences*, 10(20):7228, 2020.

[85] Douglas T Petkie, Jennifer A Holt, Mark A Patrick, and Frank C De Lucia. Multimode illumination in the terahertz for elimination of target orientation requirements and minimization of coherent effects in active imaging systems. *Optical Engineering*, 51(9):091604, 2012.

[86] Nick Rothbart, Heiko Richter, Martin Wienold, Lutz Schrottke, M Giehler, R Hey, HT Grahn, and H-W Hübers. Fast terahertz imaging with a quantum-cascade laser and a scanning mirror. In *2012 37th International Conference on Infrared, Millimeter, and Terahertz Waves*, pages 1–2. IEEE, 2012.

[87] Linda Marchese, Michel Doucet, Nathalie Blanchard, Melanie Leclerc, Marc Terroux, Martin Briand, Martin Otis, Michel Jacob, Cleophace Akitegetse, Helene Spisser, et al. Overcoming the challenges of active THz/MM-wave imaging: an optics perspective. In *Micro-and Nanotechnology Sensors, Systems, and Applications X*, volume 10639, page 106392B. International Society for Optics and Photonics, 2018.

[88] Gintaras Valušis, Alvydas Lisauskas, Hui Yuan, Wojciech Knap, and Hartmut G Roskos. Roadmap of terahertz imaging 2021. *Sensors*, 21(12):4092, 2021.

[89] Yaya Zhang, Chuting Wang, Bingxin Huai, Shiyu Wang, Yating Zhang, Dayong Wang, Lu Rong, and Yongchang Zheng. Continuous-wave THz imaging for biomedical samples. *Applied Sciences*, 11(1):71, 2020.

[90] Bradley Ferguson, Shaohong Wang, Doug Gray, Derek Abbot, and X-C Zhang. T-ray computed tomography. *Optics Letters*, 27(15):1312–1314, 2002.

[91] Qi Li, Yun-Da Li, Sheng-Hui Ding, and Qi Wang. Terahertz computed tomography using a continuous-wave gas laser. *Journal of Infrared, Millimeter, and Terahertz Waves*, 33(5):548–558, 2012.

[92] Suman Mukherjee, John Federici, Paulo Lopes, and Miguel Cabral. Elimination of fresnel reflection boundary effects and beam steering in pulsed terahertz computed tomography. *Journal of Infrared, Millimeter, and Terahertz Waves*, 34(9):539–555, 2013.

[93] Dayong Wang, Bin Li, Lu Rong, Zhihao Xu, Yanlin Zhao, Jie Zhao, Yunxin Wang, and Changchao Zhai. Extended depth of field in continuous-wave terahertz computed tomography based on Bessel beam. *Optics Communications*, 432:20–26, 2019.

[94] Jean Paul Guillet, Benoît Recur, Louis Frederique, Bruno Bousquet, Lionel Canioni, Inka Manek-Hönninger, Pascal Desbarats, and Patrick Mounaix. Review of terahertz tomography techniques. *Journal of Infrared, Millimeter, and Terahertz Waves*, 35(4):382–411, 2014.

[95] Marco F Duarte, Mark A Davenport, Dharmpal Takhar, Jason N Laska, Ting Sun, Kevin F Kelly, and Richard G Baraniuk. Single-pixel imaging via compressive sampling. *IEEE signal processing magazine*, 25(2):83–91, 2008.

[96] Wai Lam Chan, Matthew L Moravec, Richard G Baraniuk, and Daniel M Mittleman. Terahertz imaging with compressed sensing and phase retrieval. *Optics letters*, 33(9):974–976, 2008.

[97] Wai Lam Chan, Kriti Charan, Dharmpal Takhar, Kevin F Kelly, Richard G Baraniuk, and Daniel M Mittleman. A single-pixel terahertz imaging system based on compressed sensing. *Applied Physics Letters*, 93(12):121105, 2008.

[98] H Shen, L Gan, N Newman, Y Dong, C Li, Y Huang, and YC Shen. Spinning disk for compressive imaging. *Optics letters*, 37(1):46–48, 2012.

[99] Kyung Hwan Jin, Youngchan Kim, Dae-Su Yee, Ok Kyun Lee, and Jong Chul Ye. Compressed sensing pulse-echo mode terahertz reflectance tomography. *Optics letters*, 34(24):3863–3865, 2009.

[100] Till Mohr, Andreas Herdt, and Wolfgang Elsässer. 2D tomographic terahertz imaging using a single pixel detector. *Optics express*, 26(3):3353–3367, 2018.

[101] Rayko Ivanov Stantchev, Xiao Yu, Thierry Blu, and Emma Pickwell-MacPherson. Real-time terahertz imaging with a single-pixel detector. *Nature communications*, 11(1):1–8, 2020.

[102] J.W. Goodman. *Introduction to Fourier Optics*. McGraw-Hill physical and quantum electronics series. W. H. Freeman, 2005.

[103] Martin S Heimbeck, Wei-Ren Ng, Dathon R Golish, Michael E Gehm, and Henry O Everitt. Terahertz digital holographic imaging of voids within visibly opaque dielectrics. *IEEE Transactions on Terahertz Science and Technology*, 5(1):110–116, 2014.

[104] Dennis GABOR. A New Microscopic Principle. *Nature*, 161(4098):777–778, 1948.

[105] Tatiana Latychevskaia. Iterative phase retrieval for digital holography: tutorial. *J. Opt. Soc. Am. A*, 36(12):D31–D40, Dec 2019.

[106] Tatiana Latychevskaia and Hans-Werner Fink. Solution to the twin image problem in holography. *Physical review letters*, 98(23):233901, 2007.

[107] Emmett N Leith and Juris Upatnieks. Wavefront reconstruction with continuous-tone objects∗. *J. Opt. Soc. Am.*, 53(12):1377–1381, Dec 1963.

[108] Michael Reed Teague. Deterministic phase retrieval: a green's function solution. *J. Opt. Soc. Am. A*, 73(11):1434–1441, 1983.

[109] Ralph W Gerchberg. A practical algorithm for the determination of phase from image and diffraction plane pictures. *Optik*, 35:237–246, 1972.

[110] James R Fienup. Phase retrieval algorithms: a comparison. *Applied optics*, 21(15):2758–2769, 1982.

[111] Jianwei Miao, David Sayre, and HN Chapman. Phase retrieval from the magnitude of the fourier transforms of nonperiodic objects. *J. Opt. Soc. Am. A*, 15(6):1662–1669, Jun 1998.

[112] Giancarlo Pedrini, Wolfgang Osten, and Yan Zhang. Wave-front reconstruction from a sequence of interferograms recorded at different planes. *Optics letters*, 30(8):833–835, 2005.

[113] Peng Bao, Fucai Zhang, Giancarlo Pedrini, and Wolfgang Osten. Phase retrieval using multiple illumination wavelengths. *Optics letters*, 33(4):309–311, 2008.

[114] W Hoppe. Diffraction in inhomogeneous primary wave fields. 1. principle of phase determination from electron diffraction interference. *Acta Crystallographica Section a-Crystal Physics Diffraction Theoretical and General Crystallography*, page 495, 1969.

[115] Pierre Thibault, Martin Dierolf, Andreas Menzel, Oliver Bunk, Christian David, and Franz Pfeiffer. High-resolution scanning x-ray diffraction microscopy. *Science*, 321(5887):379–382, 2008.

[116] Oliver Bunk, Martin Dierolf, Søren Kynde, Ian Johnson, Othmar Marti, and Franz Pfeiffer. Influence of the overlap parameter on the convergence of the ptychographical iterative engine. *Ultramicroscopy*, 108(5):481–487, 2008.

[117] JM Rodenburg and RHT Bates. The theory of super-resolution electron microscopy via Wigner-distribution deconvolution. *Philosophical Transactions of the Royal Society of London. Series A: Physical and Engineering Sciences*, 339(1655):521–553, 1992.

[118] Helen Mary Louise Faulkner and JM Rodenburg. Movable aperture lensless transmission microscopy: a novel phase retrieval algorithm. *Physical review letters*, 93(2):023903, 2004.

[119] John M Rodenburg and Helen ML Faulkner. A phase retrieval algorithm for shifting illumination. *Applied physics letters*, 85(20):4795–4797, 2004.

[120] Andrew M Maiden and John M Rodenburg. An improved ptychographical phase retrieval algorithm for diffractive imaging. *Ultramicroscopy*, 109(10):1256–1262, 2009.

[121] Pierre Thibault and Andreas Menzel. Reconstructing state mixtures from diffraction measurements. *Nature*, 494(7435):68–71, 2013.

[122] Peng Li, Tega Edo, Darren Batey, John Rodenburg, and Andrew Maiden. Breaking ambiguities in mixed state ptychography. *Optics express*, 24(8):9038–9052, 2016.

[123] Zhen Chen, Michal Odstrcil, Yi Jiang, Yimo Han, Ming-Hui Chiu, Lain-Jong Li, and David A Muller. Mixed-state electron ptychography enables sub-angstrom resolution imaging with picometer precision at low dose. *Nature communications*, 11(1):1–10, 2020.

[124] AM Maiden, MJ Humphry, MC Sarahan, B Kraus, and JM Rodenburg. An annealing algorithm to correct positioning errors in ptychography. *Ultramicroscopy*, 120:64–72, 2012.

[125] Fucai Zhang, Isaac Peterson, Joan Vila-Comamala, Ana Diaz, Felisa Berenguer, Richard Bean, Bo Chen, Andreas Menzel, Ian K Robinson, and John M Rodenburg. Translation position determination in ptychographic coherent diffraction imaging. *Optics express*, 21(11):13592–13606, 2013.

[126] Priya Dwivedi, AP Konijnenberg, SF Pereira, and HP Urbach. Lateral position correction in ptychography using the gradient of intensity patterns. *Ultramicroscopy*, 192:29–36, 2018.

[127] Andrew M Maiden, Martin J Humphry, and John M Rodenburg. Ptychographic transmission microscopy in three dimensions using a multi-slice approach. *JOSA A*, 29(8):1606–1614, 2012.

[128] John Rodenburg and Andrew Maiden. Ptychography. *Springer Handbook of Microscopy*, pages 819–904, 2019.

[129] Andrew Maiden, Daniel Johnson, and Peng Li. Further improvements to the ptychographical iterative engine. *Optica*, 4(7):736–745, 2017.

[130] Ronan Mahon, Anthony Murphy, and William Lanigan. Terahertz holographic image reconstruction and analysis. In *Infrared and Millimeter Waves, Conference Digest of the 2004 Joint 29th International Conference on 2004 and 12th International Conference on Terahertz Electronics, 2004.*, pages 749–750. IEEE, 2004.

[131] A. Tamminen, J. Ala-Laurinaho, and A. V. Raisanen. Indirect holographic imaging at 310 GHz. In *2008 European Radar Conference*, pages 168–171, Oct 2008.

[132] Christy Fernandez Cull, David A Wikner, Joseph N Mait, Michael Mattheiss, and David J Brady. Millimeter-wave compressive holography. *Applied optics*, 49(19):E67–E82, 2010.

[133] Martin S Heimbeck, Myung K Kim, Don A Gregory, and Henry O Everitt. Terahertz digital holography using angular spectrum and dual wavelength reconstruction methods. *Optics Express*, 19(10):9192–9200, 2011.

[134] Andrei Gorodetsky, Suzanna Freer, and Miguel Navarro-Cía. Assessment of cameras for continuous wave sub-terahertz imaging. In Manijeh Razeghi and Alexei N. Baranov, editors, *Terahertz Emitters, Receivers, and Applications XI*, volume 11499, pages 73 – 81. International Society for Optics and Photonics, SPIE, 2020.

[135] Sheng-Hui Ding, Qi Li, Yun-Da Li, and Qi Wang. Continuous-wave terahertz digital holography by use of a pyroelectric array camera. *Optics letters*, 36(11):1993–1995, 2011.

[136] Kai Xue, Qi Li, Yun-Da Li, and Qi Wang. Continuous-wave terahertz in-line digital holography. *Optics Letters*, 37(15):3228–3230, 2012.

[137] Peter Zolliker and Erwin Hack. THz holography in reflection using a high resolution microbolometer array. *Optics express*, 23(9):10957–10967, 2015.

[138] Lorenzo Valzania, Erwin Hack, Peter Zolliker, Rolf Brönnimann, and Thomas Feurer. Resolution limits of terahertz ptychography. In *Unconventional Optical Imaging*, volume 10677, page 1067720. International Society for Optics and Photonics, 2018.

[139] Haochong Huang, Lu Rong, Dayong Wang, Weihua Li, Qinghua Deng, Bin Li, Yunxin Wang, Zhiqiang Zhan, Xuemin Wang, and Weidong Wu. Synthetic aperture in terahertz in-line digital holography for resolution enhancement. *Applied Optics*, 55(3):A43–A48, 2016.

[140] Qinghua Deng, Weihua Li, Xuemin Wang, Zeyu Li, Haochong Huang, Changle Shen, Zhiqiang Zhan, Ruijiao Zou, Tao Jiang, and Weidong Wu. High-resolution terahertz inline digital holography based on quantum cascade laser. *Optical Engineering*, 56(11):113102, 2017.

[141] Masatomo Yamagiwa, Takayuki Ogawa, Takeo Minamikawa, Dahi Ghareab Abdelsalam, Kyosuke Okabe, Noriaki Tsurumachi, Yasuhiro Mizutani, Testuo Iwata, Hirotsugu Yamamoto, and Takeshi Yasui. Real-time amplitude and phase imaging of optically opaque objects by combining full-field off-axis terahertz digital holography with angular spectrum reconstruction. *Journal of Infrared, Millimeter, and Terahertz Waves*, 39(6):561–572, 2018.

[142] Erwin Hack and Peter Zolliker. Terahertz holography for imaging amplitude and phase objects. *Optics Express*, 22(13):16079–16086, 2014.

[143] Mark Humphreys, JP Grant, Ivonne Escorcia-Carranza, Claudio Accarino, M Kenney, Yash Diptesh Shah, KG Rew, and DRS Cumming. Video-rate terahertz digital holographic imaging system. *Optics Express*, 26(20):25805–25813, 2018.

[144] Dayong Wang, Yanlin Zhao, Lu Rong, Min Wan, Xiaoyu Shi, Yunxin Wang, and John T Sheridan. Expanding the field-of-view and profile measurement of covered objects in continuous-wave terahertz reflective digital holography. *Optical Engineering*, 58(2):023111, 2019.

[145] Lu Rong, Tatiana Latychevskaia, Dayong Wang, Xun Zhou, Haochong Huang, Zeyu Li, and Yunxin Wang. Terahertz in-line digital holography of dragonfly hindwing: amplitude and phase reconstruction at enhanced resolution by extrapolation. *Optics Express*, 22(14):17236–17245, 2014.

[146] Zeyu Li, Qiang Yan, Yu Qin, Weipeng Kong, Guangbin Li, Mingrui Zou, Du Wang, Zhisheng You, and Xun Zhou. Sparsity-based continuous wave terahertz lens-free on-chip holography with sub-wavelength resolution. *Optics Express*, 27(2):702–713, 2019.

[147] Haochong Huang, Peiyao Qiu, Spozmai Panezai, Sibo Hao, Donglei Zhang, Yongqing Yang, Yuanyuan Ma, Hua Gao, Lu Gao, Zili Zhang, et al. Continuous-wave terahertz high-resolution imaging via synthetic hologram extrapolation method using pyroelectric detector. *Optics & Laser Technology*, 120:105683, 2019.

[148] Guanghao Chen and Qi Li. Markov chain Monte Carlo sampling based terahertz holography image denoising. *Applied Optics*, 54(14):4345–4351, 2015.

[149] Haochong Huang, Dayong Wang, Weihua Li, Lu Rong, Zachary D Taylor, Qinghua Deng, Bin Li, Yunxin Wang, Weidong Wu, and Spozmai Panezai. Continuous-wave terahertz multi-plane in-line digital holography. *Optics and Lasers in Engineering*, 94:76–81, 2017.

[150] Zeyu Li, Lei Li, Yu Qin, Guangbin Li, Du Wang, and Xun Zhou. Resolution and quality enhancement in terahertz in-line holography by sub-pixel sampling with double-distance reconstruction. *Optics Express*, 24(18):21134–21146, 2016.

[151] Lu Rong, Tatiana Latychevskaia, Chunhai Chen, Dayong Wang, Zhengping Yu, Xun Zhou, Zeyu Li, Haochong Huang, Yunxin Wang, and Zhou Zhou. Terahertz in-line digital holography of human hepatocellular carcinoma tissue. *Scientific reports*, 5(1):1–6, 2015.

[152] Martin S Heimbeck and Henry O Everitt. Terahertz digital holographic imaging. *Advances in Optics and Photonics*, 12(1):1–59, 2020.

[153] Massimiliano Locatelli, Marco Ravaro, Saverio Bartalini, Luigi Consolino, Miriam S Vitiello, Riccardo Cicchi, Francesco Pavone, and Paolo De Natale. Real-time terahertz digital holography with a quantum cascade laser. *Scientific reports*, 5(1):1–7, 2015.

[154] Roger Appleby and H Bruce Wallace. Standoff detection of weapons and contraband in the 100 GHz to 1 THz region. *IEEE transactions on antennas and propagation*, 55(11):2944–2956, 2007.

[155] Lu Rong, Chao Tang, Dayong Wang, Bing Li, Fangrui Tan, Yunxin Wang, and Xiaoyu Shi. Probe position correction based on overlapped object wavefront cross-correlation for continuous-wave terahertz ptychography. *Optics Express*, 27(2):938–950, 2019.

[156] Dayong Wang, Bing Li, Lu Rong, Fangrui Tan, John J Healy, Jie Zhao, and Yunxin Wang. Multi-layered full-field phase imaging using continuous-wave terahertz ptychography. *Optics Letters*, 45(6):1391–1394, 2020.

[157] Lu Rong, Fangrui Tan, Dayong Wang, Yaya Zhang, Kunlun Li, Jie Zhao, and Yunxin Wang. High-resolution terahertz ptychography using divergent illumination and extrapolation algorithm. *Optics and Lasers in Engineering*, 147:106729, 2021.

[158] Feidi Xiang, Miao Yu, Mengting Zhang, Meiyao Han, Qian Huang, Zhengang Yang, Jinsong Liu, and Kejia Wang. Terahertz ptychography using a long-distance diffraction-free beam as the probe. *Optics Letters*, 47(2):238–241, 2022.

[159] C Ozsoy-Keskinbora, CB Boothroyd, RE Dunin-Borkowski, PA Van Aken, and CT Koch. Hybridization approach to in-line and off-axis (electron) holography for superior resolution and phase sensitivity. *Scientific reports*, 4(1):1–10, 2014.

[160] Fengpeng Wang, Dayong Wang, Lu Rong, Yunxin Wang, and Jie Zhao. Single-shot dual-wavelength in-line and off-axis hybrid digital holography. *Applied Physics Letters*, 112(9):091903, 2018.

[161] Frank Dubois, Olivier Monnom, Catherine Yourassowsky, and J-C Legros. Border processing in digital holography by extension of the digital hologram and reduction of the higher spatial frequencies. *Applied optics*, 41(14):2621–2626, 2002.

[162] Etienne Cuche, Pierre Marquet, and Christian Depeursinge. Aperture apodization using cubic spline interpolation: application in digital holographic microscopy. *Optics communications*, 182(1-3):59–69, 2000.

[163] Fast thz mail scanner. http://www.orteh.pl/eng/articles/show/22, accessed: 30.06.2021.

[164] Maris Bauer, Adam Rämer, Serguei A Chevtchenko, Konstantin Y Osipov, Dovilė Čibiraitė, Sandra Pralgauskaitė, Kęstutis Ikamas, Alvydas Lisauskas, Wolfgang Heinrich, Viktor Krozer, et al. A high-sensitivity AlGaN/GaN HEMT terahertz detector with integrated broadband bow-tie antenna. *IEEE Transactions on Terahertz Science and Technology*, 9(4):430–444, 2019.

[165] Optical chopper system and chopper wheels. https://www.thorlabs.com/newgrouppage9.cfm?objectgroup_id=287, accessed: 30.03.2021.

[166] THz Materials. http://www.tydexoptics.com/products/thz_optics/thz_materials/, accessed: 30.03.2021.

[167] Dennis C Ghiglia and Louis A Romero. Robust two-dimensional weighted and unweighted phase unwrapping that uses fast transforms and iterative methods. *J. Opt. Soc. Am. A*, 11(1):107–117, Jan 1994.

[168] Alexander T Clark, John F Federici, and Ian Gatley. Effect of 3D Printing Parameters on the Refractive Index, Attenuation Coefficient, and Birefringence of Plastics in Terahertz Range. *Advances in Materials Science and Engineering*, 2021:8276378, 2021.

[169] AV Shchepetilnikov, PA Gusikhin, VM Muravev, BD Kaysin, GE Tsydynzhapov, AA Dremin, and IV Kukushkin. Linear scanning system for THz imaging. *Applied Optics*, 60(33):10448–10452, 2021.

[170] D Claus, D J Robinson, D G Chetwynd, Y Shuo, W T Pike, José J De J Toriz Garcia, and J M Rodenburg. Dual wavelength optical metrology using ptychography. *Journal of Optics*, 15(3):35702, jan 2013.

[171] Matthew D Seaberg, Bosheng Zhang, Dennis F Gardner, Elisabeth R Shanblatt, Margaret M Murnane, Henry C Kapteyn, and Daniel E Adams. Tabletop nanometer extreme ultraviolet imaging in an extended reflection mode using coherent Fresnel ptychography. *Optica*, 1(1):39–44, 2014.

[172] Peng Li and Andrew M. Maiden. Ten implementations of ptychography. *Journal of Microscopy*, 269(3):187–194, 2018.

[173] Kyoji Matsushima. Formulation of the rotational transformation of wave fields and their application to digital holography. *Applied optics*, 47(19):D110–D116, 2008.

[174] Chunpeng Wang, Zijian Xu, Haigang Liu, Yong Wang, Jian Wang, and Renzhong Tai. Background noise removal in x-ray ptychography. *Applied optics*, 56(8):2099–2111, 2017.

[175] AM Maiden, GR Morrison, B Kaulich, A Gianoncelli, and JM Rodenburg. Soft X-ray spectromicroscopy using ptychography with randomly phased illumination. *Nature communications*, 4(1):1–6, 2013.

[176] Adrien Chopard, Elizaveta Tsiplakova, Nikolay Balbekin, Olga Smolyanskaya, Jean-Baptiste Perraud, Jean-Paul Guillet, Nikolay V Petrov, and Patrick Mounaix. Single-scan multiplane phase retrieval with a radiation of terahertz quantum cascade laser. *Applied Physics B*, 128(3):1–9, 2022.

[177] Préparation d'une lame histologique. https://tinyurl.com/zr7leygx, accessed: 30.03.2021.

[178] Huibin Chang, Pablo Enfedaque, Jie Zhang, Juliane Reinhardt, Bjoern Enders, Young-Sang Yu, David Shapiro, Christian G Schroer, Tieyong Zeng, and Stefano Marchesini. Advanced denoising for x-ray ptychography. *Optics express*, 27(8):10395–10418, 2019.

[179] AP Konijnenberg, WMJ Coene, and HP Urbach. Model-independent noise-robust extension of ptychography. *Optics express*, 26(5):5857–5874, 2018.

[180] Andrew M Maiden, John M Rodenburg, and Martin J Humphry. Optical ptychography: a practical implementation with useful resolution. *Optics letters*, 35(15):2585–2587, 2010.

[181] Peng Li, Darren J Batey, Tega B Edo, Aaron D Parsons, Christoph Rau, and John M Rodenburg. Multiple mode x-ray ptychography using a lens and a fixed diffuser optic. *Journal of Optics*, 18(5):054008, 2016.

[182] Frederick Allars, Peng-Han Lu, Maximilian Kruth, Rafal E Dunin-Borkowski, John M Rodenburg, and Andrew M Maiden. Efficient large field of view electron phase imaging using near-field electron ptychography with a diffuser. *Ultramicroscopy*, 231:113257, 2021.

[183] F Hüe, JM Rodenburg, AM Maiden, and PA Midgley. Extended ptychography in the transmission electron microscope: Possibilities and limitations. *Ultramicroscopy*, 111(8):1117–1123, 2011.

[184] Mohamed Boutaayamou, Delphine Cerica, and Jacques G Verly. Terahertz pulsed imaging of dehydrated human breast cancer samples. In *2020 45th International Conference on Infrared, Millimeter, and Terahertz Waves (IRMMW-THz)*, pages 1–2. IEEE, 2020.

[185] Enrique Castro-Camus, Martin Koch, and Daniel M Mittleman. Recent advances in terahertz imaging: 1999 to 2021. *Applied Physics B*, 128(1):1–10, 2022.